DIGITAL ACCESS TO SCHOLARSHIP AT HARVARD
DASH.HARVARD.EDU

HARVARD LIBRARY
Office for Scholarly Communication

Promoter Decoding of Transcription Factor Translocation Dynamics

Citation
Hansen, Anders Sejr. 2015. Promoter Decoding of Transcription Factor Translocation Dynamics. Doctoral dissertation, Harvard University, Graduate School of Arts & Sciences.

Permanent link
http://nrs.harvard.edu/urn-3:HUL.InstRepos:17467348

Terms of Use
This article was downloaded from Harvard University's DASH repository, and is made available under the terms and conditions applicable to Other Posted Material, as set forth at http://nrs.harvard.edu/urn-3:HUL.InstRepos:dash.current.terms-of-use#LAA

Share Your Story

The Harvard community has made this article openly available.
Please share how this access benefits you. Submit a story .

Accessibility

Promoter decoding of transcription factor translocation dynamics

A dissertation presented

by

Anders Sejr Hansen

to

The Department of Chemistry and Chemical Biology

in partial fulfillment of the requirements

for the degree of

Doctor of Philosophy

in the subject of

Chemistry and Chemical Biology

Harvard University

Cambridge, Massachusetts

April, 2015

©2015 - Anders Sejr Hansen
All rights reserved

Dissertation advisor: Professor Erin K. O'Shea Anders Sejr Hansen

Promoter decoding of transcription factor translocation dynamics

Abstract

Many cellular signaling pathways exhibit a bowtie topology: multiple distinct signal inputs converge on a single master transcription factor, which controls the expression of downstream genes. Recent evidence suggests that information about signal inputs can be encoded by regulating the activation dynamics of the master transcription factor. However, it was unclear whether this is sufficient to obtain specificity in gene expression, such that each input induces a specific set of output genes. Using the budding yeast transcription factor Msn2 as a model system, we address this question.

We systematically dissect how different promoters decode transcription factor translocation dynamics in single cells (Chapter 2). We find that promoters fall into four main classes depending on the threshold of signal required for activation and on the timescale of activation. Furthermore, we provide insight into the mechanistic basis for promoter class. We show that it is possible to differentially control expression of the different promoter classes by control of Msn2 dynamics. We find that slow promoters exhibit dramatically higher noise in gene expression, but are able to filter out Msn2 oscillations. This highlights a general trade-off: for promoters, implementing a high-pass temporal filter comes at the cost of much higher noise in gene expression.

Applying tools from information theory and focusing on gene expression, we rigorously quantify the limits on information transduction through regulation of Msn2 dynamics (Chapter 3). Although we find that the amount of information transduced by Msn2 to target genes is only sufficient for reliable binary decisions, information transduction can be improved by

modulating promoter *cis*-elements or by integrating information from multiple genes. We find amplitude-encoding to be more reliable than frequency-encoding. Taken together, our results suggest that information transduction through regulation of Msn2 dynamics is limited to reliable transduction of signal identity, but not signal intensity.

The work we describe in this dissertation would not have been possible without the development of high-throughput microfluidic technologies (Chapter 4). We describe our development of a multiplexed microfluidic device, which we combine with four-color quantitative time-lapse microscopy to control nucleocytoplasmic shuttling of Msn2 and measure gene expression dynamics in single cells. We provide a detailed protocol for future studies.

Our work demonstrates that it is possible to encode multiple distinct gene expression programs in the dynamics of a single transcription factor. Nonetheless, at the level of individual genes, noise in the decoding step places an upper limit on information transduction.

Contents

List of Figures **x**

List of Tables **xii**

1 Introduction **1**
1.1 Topology of eukaryotic signal transduction networks . . . 1
1.1.1 Bowtie topology of signaling networks . . . 2
1.2 Encoding information through regulation of signaling dynamics . . . 4
1.2.1 Examples of pathways where information is encoded in signaling dynamics . . . 5
1.2.2 Msn2 and the *S. cerevisiae* stress response . . . 8
1.3 Decoding information encoded in transcription factor dynamics . . . 11
1.3.1 Signaling dynamics and control of cell fate: distinguishing cause from coincidence . . . 12
1.3.2 Control of gene expression through regulation of transcription factor dynamics . . . 15
1.3.3 Gene regulation at the single cell level is noisy . . . 17
1.4 Summary . . . 18
1.5 References . . . 19

2 Promoter decoding of transcription factor dynamics involves a trade-off between noise and control of gene expression **27**
2.1 Abstract . . . 27
2.2 Introduction . . . 28
2.3 Result . . . 31
2.3.1 Identification of specific target genes of Msn2 . . . 31
2.3.2 Systematic dissection of how different promoters decode transcription factor dynamics . . . 32
2.3.3 Using a mathematical model to cluster promoters into classes . . . 33
2.3.4 Quantitative Analysis of signal processing by LF and HS promoters . 36
2.3.5 Control of transcription factor dynamics enables differential gene expression . . . 38
2.3.6 Noise in gene expression differs markedly for different promoter classes and depends on Msn2 dynamics . . . 39

2.3.7 Encoding four gene expression programs in the dynamics of a single transcription factor . . . 42
2.3.8 The promoter activation timescale controls the noise level . . . 44
2.3.9 Slower promoter activation leads to greater noise in gene expression . 46
2.3.10 Nucleosome remodeling dynamics correlate with promoter activation dynamics . . . 48
2.4 Discussion . . . 48
2.4.1 Promoter amplitude threshold and activation timescale control how transcription factor dynamics are decoded . . . 48
2.4.2 Modulation of transcription factor dynamics enables control of gene expression . . . 49
2.4.3 Relationship between promoter class and stress-specific gene function 50
2.4.4 A trade-off between noise and control of gene expression . . . 51
2.5 Materials and methods . . . 54
2.6 Chapter 2 references . . . 59

3 Limits on information transduction through regulation of signaling dynamics 64
3.1 Abstract . . . 64
3.2 Introduction . . . 65
3.3 Results . . . 69
3.3.1 Quantifying information transduction using information theory . . . 69
3.3.2 Natural Msn2 target genes have low information transduction capacities 70
3.3.3 The promoter information transduction capacity is tunable and can be increased for natural Msn2 target genes . . . 72
3.3.4 Estimating the intrinsic information transduction capacity of promoters 75
3.3.5 Multiple gene copies reduces information loss due to intrinsic noise . 78
3.3.6 Circuits integrating the response of two genes can transduce more information than single gene circuits . . . 78
3.4 Discussion . . . 80
3.5 Materials and methods . . . 83
3.6 Chapter 3 references . . . 87

4 High-throughput microfluidics to control and measure signaling dynamics in single yeast cells 93
4.1 Abstract . . . 93
4.2 Introduction . . . 94
4.2.1 Applications of the method . . . 96
4.2.2 Comparison with other methods . . . 99
4.3 Experimental design . . . 101
4.3.1 Design and fabrication of silicon master mold . . . 101
4.3.2 Soft lithography: fabrication of microfluidic chips . . . 102
4.3.3 Setting up solenoid valves for fluid control . . . 103
4.3.4 Time-lapse microscopy . . . 104
4.3.5 Analysis of time-lapse movies . . . 105

4.3.6 Limitations . . . 106
4.4 Materials . . . 107
4.4.1 Reagents . . . 107
4.4.2 Equipment . . . 108
4.4.3 Reagent setup . . . 110
4.4.4 Equipment setup . . . 111
4.5 Procedure . . . 111
4.5.1 Photolithography: fabrication of silicon wafer master mold . . . 111
4.5.2 Soft lithography: replica molding of PDMS and fabrication of microfluidic device . . . 114
4.5.3 Setting up control valves . . . 117
4.5.4 Preparing a time-lapse microscopy experiment . . . 118
4.5.5 Setting up a time-lapse microscopy experiment . . . 118
4.5.6 Troubleshooting . . . 122
4.5.7 Anticipated results . . . 124
4.6 Chapter 4 references . . . 125

5 Discussion and future directions **132**
5.1 Discussion . . . 132
5.1.1 Motivating hypothesis behind this dissertation . . . 132
5.1.2 Development of a high-throughput microfluidic device . . . 133
5.1.3 How promoters decode Msn2 dynamics . . . 133
5.1.4 A trade-off between noise and promoter filtering . . . 135
5.1.5 Limits on information transduction through regulation of transcription factor dynamics . . . 136
5.1.6 The encoding/decoding paradigm revisited . . . 136
5.2 Future directions . . . 138
5.2.1 Msn2 and Msn4 — a coherent feed-forward motif . . . 138
5.2.2 Information encoded in Msn2/Msn4 dynamics . . . 139
5.2.3 Systematic dissection of how promoter architecture controls decoding using FACS-Seq . . . 140
5.2.4 Complete mechanism and order of events during transcriptional regulation at single promoter . . . 141
5.2.5 Promoter memory effects . . . 142
5.2.6 Dissecting timing and causality for histone modifications . . . 143
5.2.7 Msn2 dynamics and gene activation at the single-molecule level . . . 144
5.3 Final remarks . . . 145
5.4 Chapter 5 references . . . 145

A Supplementary information for Chapter 2 **148**
A.1 Supplementary figures for Chapter 2 . . . 148
A.2 Supplementary methods and results for Chapter 2 . . . 158
A.2.1 Strain construction . . . 158
A.2.2 Medium and solutions . . . 163
A.2.3 Microarray analysis . . . 164

A.2.4 Reporter gene selection . . . 165
A.2.5 *In vivo* nucleosome mapping (MNase-Seq) . . . 165
A.2.6 Microfluidic device fabrication . . . 168
A.2.7 Time-lapse microscopy . . . 169
A.2.8 Msn2 modulation range in time-lapse experiments . . . 171
A.2.9 Single-cell source data . . . 171
A.2.10 Image analysis and quantification of single-cell time traces . . . 172
A.2.11 Nuclear import and export of Msn2-mCherry . . . 174
A.2.12 Deterministic model (Figure 2.2A) . . . 175
A.2.13 Amplitude threshold and the promoter activation timescale . . . 178
A.2.14 Model fitting to natural Msn2 promoters and parameter estimation . 181
A.2.15 Noise and transcription factor dynamics: oscillations versus a single pulse . . . 184
A.2.16 Simplified model (Figure 2.5A) . . . 185
A.2.17 *in silico* promoters for the simplified model (Figure 2.5A) . . . 188
A.2.18 Synthesis of 1-NM-PP1 . . . 189
A.3 Appendix A references . . . 192

B Supplementary information for Chapter 3 195
B.1 Supplementary figures for Chapter 3 . . . 195
B.2 Materials and methods . . . 201
B.2.1 Figure legend for Figure B.3 . . . 201
B.2.2 Strain construction . . . 203
B.2.3 Microfluidic modulation of Msn2 dynamics . . . 207
B.2.4 Measurement noise and data processing . . . 207
B.2.5 Supplementary source data . . . 209
B.3 References . . . 209

C Supplementary theory for Chapter 3 211
C.1 Introduction . . . 211
C.2 Mutual information for a single reporter . . . 212
C.2.1 Shannon entropy and mutual information for a single reporter . . . 212
C.2.2 Maximal mutual information for a single reporter . . . 212
C.2.3 Computing mutual information with empirical data . . . 213
C.2.4 Comments on how to interpret maximal mutual information . . . 216
C.2.5 Comments on using a scalar for computing mutual information . . . 219
C.2.6 Comments on applying the Data Processing Inequality . . . 220
C.3 Joint mutual information for two reporters . . . 223
C.3.1 Joint mutual information for two reporters . . . 223
C.3.2 Joint maximal mutual information for two reporters . . . 224
C.3.3 Computing joint mutual information with empirical data . . . 225
C.4 Determining intrinsic mutual information . . . 226
C.4.1 Intrinsic and extrinsic contributions to gene expression noise . . . 226
C.4.2 Effect of extrinsic noise on mutual information . . . 227
C.4.3 An algorithm to estimate the intrinsic mutual information . . . 229

C.4.4 Testing the algorithm with simulated data and linear gene expression models . . . 232
C.4.5 Testing the algorithm with simulated data and nonlinear gene expression models . . . 235
C.4.6 Comments on the algorithm . . . 237
C.4.7 Computing I_{int} with empirical data . . . 238
C.5 References . . . 238

D Preliminary results for understanding how promoter architecture influences promoter decoding of Msn2 dynamics 241
D.1 Abstract . . . 241
D.2 Preliminary results . . . 242
D.2.1 Inferring the amplitude threshold and activation timescale for mutant promoters . . . 242
D.2.2 A simple calibration model for quantitative promoter class inference . . . 243
D.2.3 How Msn2 binding site number and location affects promoter class . . . 244
D.2.4 A quantitative relationship between promoter architecture and promoter class . . . 247
D.3 Discussion . . . 248

List of Figures

1.1 Overview of a typical eukaryotic signal transduction pathway 1
1.2 Bowtie topology of signaling networks 3
1.3 Encoding signal information by regulating transcription factor activation dynamics 4

2.1 Experimental set-up and systematic dissection of how different promoters decode transcription factor dynamics 34
2.2 A mathematical model for transcription factor-activated gene expression allows clustering of promoters and detailed quantitative characterization . . . 37
2.3 Control of transcription factor dynamics allows differential gene expression . 39
2.4 Noise in gene expression depends on the promoter class and on transcription factor dynamics 41
2.5 Encoding four gene expression programs in the dynamics of a single transcription factor 43
2.6 Gene expression noise depends on the promoter activation timescale 45
2.7 Slower promoter activation kinetics leads to greater noise in gene expression 47
2.8 A trade-off between noise and control of gene expression 52

3.1 Encoding and transmitting signal identity and intensity information in the dynamics of a single transcription factor 66
3.2 Information transduction by promoters with respect to amplitude and frequency modulation 73
3.3 An algorithm for estimating intrinsic mutual information 76
3.4 Integrating the response of more than one gene improves information transmission 79

4.1 Overview of microfluidic setup 96
4.2 A typical experiment 98
4.3 Device design 101
4.4 Photolithography and soft lithography overview 102
4.5 Photolithography steps: fabrication of silicon wafer master mold 112
4.6 Soft lithography steps: fabrication of microfluidic device 115
4.7 Time-lapse microscopy experiments 119

A.1 Overview of strains, microarray experiment and full gene expression heatmap 149
A.2 Comparison of model fits and raw data for *SIP18* and *DCS2* 150

A.3 Comparison of model fits and raw data for *DDR2* and *HXK1* 151
A.4 Comparison of model fits and raw data for *ALD3* and *TKL2* 152
A.5 Comparison of model fits and raw data for *RTN2* 153
A.6 Raw single-cell data for Condition A and B 154
A.7 Extrinsic noise, Noise vs. mean, YFP vs Msn2 AUC correlation and examples of bimodal gene expression 155
A.8 Surface plots showing how gene expression (mRNA AUC) and noise (mRNA AUC noise) relates to transcription factor input for the 4 *in silico* promoters 156
A.9 Expression heatmap and noise plots for *HXK1* WT, *HXK1 snf6*Δ and *HXK1 gcn5*Δ. Nucleosome occupancy at promoters 157

B.1 How time-lapse data is converted to histograms and promoter maps and noise data 196
B.2 Data processing and control of measurement noise 197
B.3 Input noise and variability in Msn2 abundance 198
B.4 Summary of results for 1x reporter diploid 199
B.5 Summary of results for 2x reporter diploid 200

C.1 Correcting I for bias 214
C.2 Interpreting I 218
C.3 Alternative YFP measures for calculating I 220
C.4 Stochastic simulation of the random telegraph model 222
C.5 Bias correction for joint mutual information, $I(R_1, R_2; S)$ 225
C.6 Inferring an estimate of I_{int} 230
C.7 Inferring the approximate intrinsic gamma distribution 231
C.8 Linear gene expression models 233
C.9 Example of the algorithm on simulated data using a linear model 234
C.10 Testing the algorithm using simulated data and linear models 235
C.11 Nonlinear gene expression models 236
C.12 Testing the algorithm using simulated data and nonlinear models 237

D.1 Inferring amplitude threshold and activation timescale from a limited set of experiments 242
D.2 A calibration model for inferring amplitude threshold and activation timescale 243
D.3 *pSIP18* promoter mutants 245
D.4 Promoter class for *pSIP18* mutants 246
D.5 Quantitative relationships between promoter architecture and class 247
D.6 A speculative mechanistic model for transcriptional control at promoters . . 249

List of Tables

4.1 Troubleshooting 122

A.1 List of strains for Chapter 2 161
A.2 Parameters for deterministic model 182

B.1 List of strains for Chapter 3 206

C.1 I_{AM} and I_{FM} for *SIP18* and *HXK1* 216
C.2 $I_{\mathrm{AM,\,joint}}(R_1, R_2; S)$ and $I_{\mathrm{FM,\,joint}}(R_1, R_2; S)$ for *SIP18* and *HXK1* 226
C.3 Empirical I_{int} 238

Acknowledgments

During graduate school I have had the privilege of working with exceptional colleagues. First, I would like to thank my advisor, Erin K. O'Shea, for support, guidance and providing a stimulating environment in which to pursue science. Having trained as a chemist, I had never taken a biology class before coming to Harvard. I thank Erin for providing me with the freedom and support to learn and venture into fields in which I had no prior experience. I have learned tremendously from Erin's approach to science.

I would also like to thank Johan Paulsson, Vlad Denic, Adam Cohen and Philippe Cluzel for serving on my committee, for advice and for stimulating discussions. Our lab's close connection to Vlad's lab has greatly enriched my doctoral training, both socially and scientifically.

In the O'Shea lab, I would especially like to thank Nan Hao who now has his own lab at UCSD. From showing me he to run a gel to introducing me to the Msn2 system, Nan patiently taught me molecular biology and helped me troubleshoot whenever I ran into problems. Moreover, I have learned immensely from our discussions. I would also like to thank Xu Zhou for being an excellent colleague and helping me with my genomics work. And I thank Mike Rust for being such a patient rotation supervisor.

The O'Shea lab is an outstanding scientific environment. I benefitted greatly from discussions with Vikram, Xu, Nan, Brian, Shankar, Ian, Kapil, Chris, Elmar, Andrian, Shankar, Rasi, Joe P. and everyone else, past and present. From coffee club and SysBio football to game nights at Shankar's, I really appreciate all of the times we have had together inside and outside of lab. I would also like to thank Peter for all his administrative help and for keeping track of the lab.

Furthermore, I would like to thank Andrew Murray and Bodo Stern for generously run-

ning the FAS Center for Systems Biology, which has been a wonderful place to be for the last 4.5 years. Through Bauer meetings and Happy Hour, I have had the opportunity to meet and discuss science with great people in a range of disciplines. In the Center, I would also like to thank Bodo and Dann Huh for critically reading my manuscripts and numerous discussions. Outside of the center, I would like to thank Raymond Cheong, Mikhail Tikhonov, Gasper Tkacik, Dougal MacLaurin, Matt Brennan and several other people for stimulating discussions. I would also like to thank Christoph Zechner for a great collaboration.

During my doctoral training, I have mentored four eminent people: three rotation students, Ryan, Tom and Jun-Han, and Jeffrey, an undergraduate. This has been a great learning experience and I wish them all the best in the future.

Outside of work, I have gotten to know some incredible people through Perkins and my program year at CCB. The kebab lunches, pot-lucks and parties have been a great part of graduate school. I would also like to thank Nashton, past and present, for four amazing years. We have had some amazing times and graduate school would have been a dull affair without you. And thanks to Noam for keeping the ASAASA going for four years — I would not know what I do about pigeons and PBR without it.

Finally, I would like to thank my family for their care and support. Most importantly, I want to thank Roshni. Without her love and warmth, none of this would have been possible.

Contributions

Chapter 1

Contributions: Anders Sejr Hansen (ASH) wrote the text.

Chapter 2

Contributions: ASH and Erin K. O'Shea (EKO) designed the project. ASH conducted the experiments and analyzed the data. ASH and EKO wrote the manuscript.

Chapter 2 has previously been published with minor changes as the following paper:

Hansen, A.S., & O'Shea, E.K. (2013). Promoter decoding of transcription factor dynamics involves a trade-off between noise and control of gene expression. *Molecular Systems Biology* **9**. doi: 10.1038/msb.2013.56

Chapter 3

Contributions: ASH: conception and design; acquisition of data; analysis and interpretation of data; drafting and revising the article. EKO: drafting or revising the article.

Chapter 3, with minor changes, is currently under peer review:

Hansen, A.S., & O'Shea, E.K. (2015). Limits on information transduction through regulation of signaling dynamics. *eLife. under review*

Chapter 4

Contributions: ASH developed the multiplexed microfluidic device, the automated fluid control system, developed MATLAB code, performed the experiments, and wrote the manuscript. Nan Hao (NH) developed the original method of using microfluidics to control analogue sensitive kinases and Msn2 localization. EKO supervised the projects. ASH, NH and EKO edited the manuscript.

Chapter 4, with minor changes, is currently under peer review:

Hansen, A.S., Hao, N., & O'Shea, E.K. (2015). High-throughput microfluidics to control and measure signaling dynamics in single yeast cells. *Nature Protocols. under review*

Chapter 5

Contributions: ASH wrote the text.

Chapter 1

Introduction

1.1 Topology of eukaryotic signal transduction networks

In order to survive, living organisms must be able to sense the external environment and respond accordingly to maintain homeostasis. It is therefore no surprise that cells have evolved sophisticated signal transduction networks that can monitor the external environment and transmit information downstream. Although the exact structure of a signaling pathway depends on the organism and the stress or signal in question, eukaryotic signal transduction networks tend to exhibit a general topology (Figure 1.1; de Nadal *et al.*, 2011).

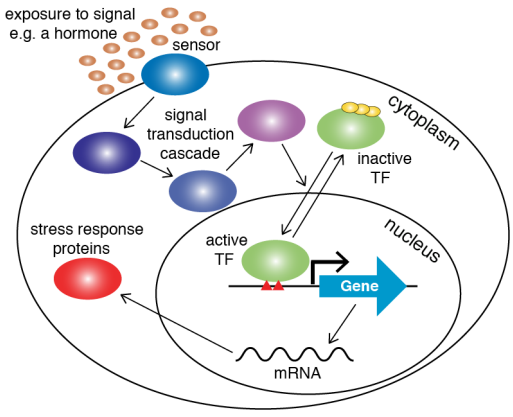

Figure 1.1: *Overview of a typical eukaryotic signal transduction pathway*
Exposure to a signal is sensed by a sensor molecule (e.g. hormone exposure or stress could be sensed by a membrane receptor). Information is then transmitted downstream and eventually leads to the activation of a transcription factor. Upon activation, the transcription factor induces expression of response genes, whose protein products mediate the desired response to the original signal.

In general, eukaryotic signal transduction pathways consist of three steps. First, a signal

(e.g. a hormone) or a stress (e.g. a change in external phosphate concentration) is sensed by a sensor molecule, such as a membrane receptor. This leads to activation of the sensor. Second, information is transmitted downstream — often through post-translational modification (e.g. phosphorylation) of downstream signaling molecules. Third, information is eventually transmitted to a regulator of gene expression, typically a transcription factor, whose activity then changes. Regulation of transcription factor activity can occur through mechanisms such as a change in post-translational modification or through a change in subcellular localization. Once active, the transcription factor will induce the expression of a series of target genes. This leads to the production of proteins, which can help protect the cell against a stress or allow the cell to respond appropriately to a signal (e.g. cell differentiation upon hormone exposure).

The simplified outline described above is the result of decades of research in signal transduction and many individual pathways are now well understood (Hynes *et al.*, 2013). While it has traditionally been thought that a cell would have a specialized pathway for each signal or stress, it turns out that the number of possible signals and stresses a cell must respond to vastly outnumber the number of signal transduction pathways available. What's more, signal transduction pathways tend to exhibit significant cross-talk: in many pathways, components are shared between multiple pathways such that activation of one pathway can influence signaling through many other pathways. This raises the general question of how specificity is achieved.

1.1.1 Bowtie topology of signaling networks

Many cellular signaling pathways exhibit a bowtie topology (Csete & Doyle, 2004), where multiple distinct signals converge on a single master regulator, which nonetheless induces

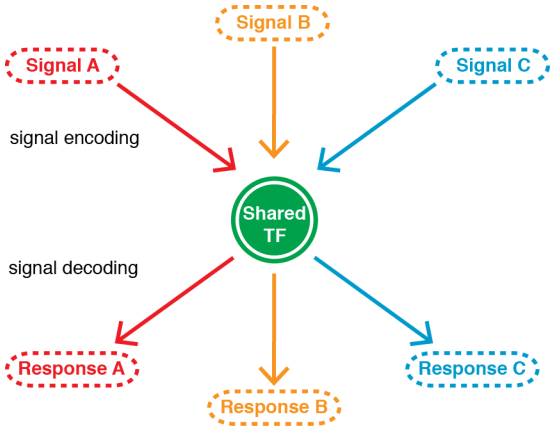

Figure 1.2: *Bowtie topology of signaling networks*
Eukaryotic signaling networks often exhibit a bowtie topology where multiple distinct signals converge on a single master regulator (e.g. a shared transcription factor), which nonetheless yields specific downstream responses.

specific downstream responses as illustrated in Figure 1.2. While a bowtie organization of signal transduction confers certain advantages such as robustness (Csete & Doyle, 2004), it raises two key biological questions. First, how can the cell encode information about multiple distinct signals by regulating the activity of a single master regulator? As illustrated in Figure 1.2, signals A, B and C all flow through the same transcription factor. Thus, to distinguish the different signals, the cell must differentially regulate the activity of the same transcription factor in a way that allows for transmission of both signal identity and signal intensity information. Second, how can this information be specifically decoded? Regardless of how the information is encoded in the shared transcription factor, downstream modules must be able to differentially decode this information such that "signal A" activates "response A", without activating the other responses. Below, we address both of these questions and discuss examples of signaling pathways that exhibit such as bowtie topology.

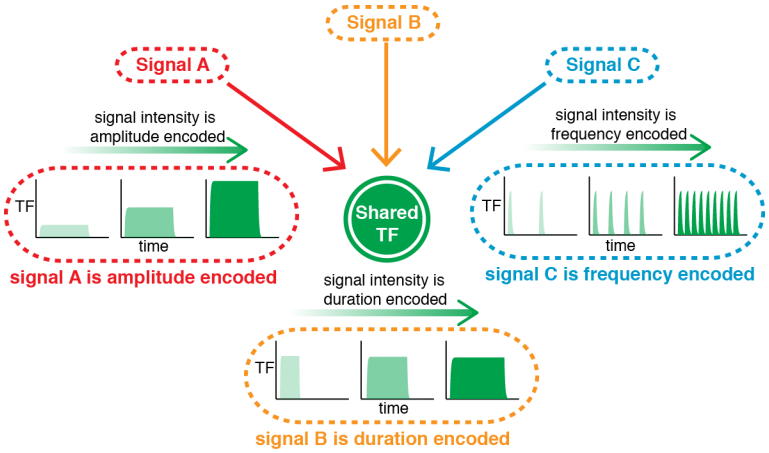

Figure 1.3: *Encoding signal information by regulating transcription factor activation dynamics*
One way the cell can encode information about multiple signals is by regulating the activation dynamics of a single, shared transcription factor (TF). By regulating the amplitude, duration and/or frequency of activation it is possible to encode both signal identity and signal intensity information in the dynamics of a single transcription factor.

1.2 Encoding information through regulation of signaling dynamics

Recent work suggests that cells can encode information about multiple distinct signals by regulating the activation dynamics of a master regulator (Behar *et al.*, 2007; Behar & Hoffmann, 2010; Levine *et al.*, 2013; Purvis & Lahav, 2013). Transcription factors are commonly activated by a change in post-translational modification such as phosphorylation and/or translocation to the nucleus, enabling cells to precisely regulate TF temporal activation dynamics. There are three general ways in which the activation dynamics can be regulated: by modulating the amplitude, the duration or the frequency of activation (Figure 1.3), or through a combination of the three. This allows the cell to encode both the identity and intensity or strength of three different signals by regulating the dynamics of a single master regulator. Below, we discuss a series of examples.

1.2.1 Examples of pathways where information is encoded in signaling dynamics

Calcium signaling (Berridge *et al.*, 2000) and growth factor signaling (Marshall, 1995) were among the first pathways studied that implicated signaling dynamics as being important for function. ERK is a mitogen-activated protein kinase and is in part responsible for mediating the cellular response to growth factors. Early studies showed that whereas nerve growth factor (NGF) lead to sustained ERK activation, epidermal growth factor (EGF) lead to transient ERK activation. In other words, growth factor identity is encoded in the duration of ERK activation (Santos *et al.*, 2007). Furthermore, NGF and EGF lead to different downstream responses and cell fates. In the neuronal cell line, PC-12, NGF treatment induces PC-12 cell differentiation, whereas EGF treatment leads to cell proliferation (Marshall, 1995). Thus, the dynamics of ERK signaling correlates with different cell fate choices.

NF-κB is an important mammalian transcription factor and a master regulator of the immune response including both the innate and adaptive immune response (Gilmore, 2006). NF-κB is also at the center of a bowtie shaped signaling pathway. For example, in response to TNFα, an adipokine signaling inflammation, NF-κB exhibits nucleocytoplasmic oscillations. In contrast, NF-κB shows sustained nuclear localization in response to bacterial lipopolysaccharides (LPS) (Hoffmann *et al.*, 2002; Nelson *et al.*, 2004; Covert *et al.*, 2005; Werner *et al.*, 2005; Hoffmann & Baltimore, 2006). Thus, the signal identity is encoded in the activation dynamics of NF-κB. In other words, by observing the dynamics of NF-κB the cell can tell what the upstream signal is: oscillations signal TNFα, whereas a sustained pulse signals LPS.

Another famous example is the transcription factor p53 which functions as a tumor suppressor and is thought to be mutated in roughly half of all cancers (Batchelor *et al.*,

2009). Referred to as the guardian of the genome (Lane, 1992), p53 coordinates processes such as cell cycle arrest, senescence and apoptosis in response to DNA damage (Batchelor *et al.*, 2008). In response to γ-irradiation, p53 shows pulses of activity (sometimes referred to as oscillations), whereas in response to UV-irradiation, p53 shows sustained activity (Lahav *et al.*, 2004; Batchelor *et al.*, 2011). Thus, the identity of the signal (γ- or UV-irradiation) is encoded in the dynamics of p53 (pulses of activity or sustained activity). When closely examined for the response not just to different signals, but also to different signal intensities, it was found that p53 dynamics also encode the signal intensity or dose. For γ-irradiation, the higher the irradiation intensity the higher the number of p53 pulses. Similarly, for UV-irradiation, the higher the irradiation intensity the higher the amplitude of the sustained pulse of p53 activation. Thus, both signal identity and signal intensity is encoded in the dynamics of p53. In other words, it appears that just by reading the dynamics of p53 the cell can tell both what signal it was exposed to and how intense this signal was.

Ca^{2+}-responsive transcription factors such as NFAT in mammalian cells (Berridge *et al.*, 2000; Crabtree & Graef, 2008; Yissachar *et al.*, 2013) and Crz1 in *S. cerevisiae* (Cai *et al.*, 2008) also exhibit complex signal-dependent dynamics. Both of these transcription factors are regulated by a conserved phosphatase, calcineurin. Calcineurin is activated by an increase in intracellular calcium concentration, after which it dephosphorylates the transcription factor which causes it to translocate to the nucleus where it regulates gene expression (Crabtree & Graef, 2008).

In *S. cerevisiae*, Crz1 exhibits bursts of nuclear localization in response to an increase in external calcium concentration — that is, Crz1 briefly translocates to the nucleus for ∼2-3 minutes before returning to the cytoplasm. These bursts appear to occur stochastically in individual cells. While the duration and amplitude of these bursts are unaffected by

the external calcium concentration, burst frequency increases with the external calcium concentration (Cai *et al.*, 2008). Thus, *S. cerevisiae* transmits information about the external calcium concentration by regulating Crz1 burst frequency. In other words, Crz1 dynamics encodes signal intensity.

In mammals, the NFAT family of transcription factors consists of five closely related genes. Yissachar *et al.* investigated the single cell dynamics of two NFAT isoforms: NFAT1 and NFAT4 (Yissachar *et al.*, 2013). In response to an increase in the external calcium concentration, NFAT4 shows brief bursts of nuclear localization with concentration-dependent frequency just like Crz1 in yeast, whereas NFAT1 does not activate. In contrast, in response to antigen both transcription factors activate. However, NFAT4 shows a briefer pulse of nuclear localization, whereas NFAT1 responds with a sustained pulse of nuclear localization where both the duration and amplitude are dose-dependent (Yissachar *et al.*, 2013). Thus, even though the NFAT transcription factors are highly similar in sequence, they exhibit very different dynamics in response to signals. This allows the cell both to encode signal identity and intensity information in NFAT dynamics, but also to discriminate different signals in a more reliable manner by having different transcription factor isoforms respond differently to the same signal.

Another illustrative example comes from neural progenitor cells. These are multipotent cells responsible for producing neurons, oligodendrocytes and astrocytes. A proper balance of neural progenitor proliferation and differentiation is critical for brain development and maintenance (Imayoshi & Kageyama, 2014). The dynamics of three basic helix-loop-helix transcription factors — Hes1, Ascl1 and Olig2 — appear to control the balance between proliferation and differentiation. Proliferating neural progenitor cells show oscillating expression of all three transcription factors. However, when expression of either Hes1, Ascl1

or Olig2 becomes sustained neural progenitor cells differentiate into astrocytes, neurons and oligodendrocytes, respectively. Thus, all three transcription factors are always expressed — and it is the dynamics of their expression that appears to control cell fate (Imayoshi *et al.*, 2013; Isomura & Kageyama, 2014).

The above examples illustrate just a subset of cellular master regulators that encode information in their dynamics. Additional examples are given elsewhere (Behar & Hoffmann, 2010; Levine *et al.*, 2013; Purvis & Lahav, 2013; Dalal *et al.*, 2014; Castillo-Hair *et al.*, 2015). In this dissertation, we will focus exclusively on the *S. cerevisiae* transcription factor Msn2, which encodes information about several stresses in its nuclear translocation dynamics, and we therefore introduce Msn2 in more detail below.

1.2.2 Msn2 and the *S. cerevisiae* stress response

Msn2 was discovered independently by two groups in 1996 as a multi-stress response transcriptional activator in yeast (Martinez-Pastor *et al.*, 1996; Schmitt & McEntee, 1996). The genes *MSN2* and *MSN4* encode homologues and partially redundant zinc finger transcription factors with the following domains: a transcription activation domain (most N-terminal), a nuclear export signal containing domain, a nuclear localization signal containing domain and finally a domain containing two Cys_2His_2-zinc fingers responsible for DNA binding (most C-terminal) (Gorner *et al.*, 2002; Boy-Marcotte *et al.*, 2006; Hao *et al.*, 2013). The consensus DNA binding motif for Msn2 is the stress-responsive element (STRE 5'-CCCCT-3') (Kobayashi & McEntee, 1993; Martinez-Pastor *et al.*, 1996; Schmitt & McEntee, 1996). In addition to this early evidence, the consensus Msn2 binding sequence has been further verified in a series of other studies. First, Msn2/4 protect the *CTT1* and *HSP104* promoters from dimethylsulphate methylation by binding to their STREs *in vivo* (Gorner *et al.*, 1998).

Second, removal of the two main STREs from the *SIP18* promoter abolishes Msn2-mediated gene induction (Figure D.3). Third, in genome-wide ChIP-Chip or ChIP-Seq experiments, Msn2 has been found to bind STREs (Huebert *et al.*, 2012; Elfving *et al.*, 2014). Finally, Msn2 binding to the STRE has been verified *in vitro* (Stewart-Ornstein *et al.*, 2013) and the *in vitro* K_{d} is ~ 23 nM for the consensus STRE sequence (Siggers *et al.*, 2014).

Early genetic studies showed that double deletion mutants (*msn2Δ msn4Δ*) are hypersensitive to stress and that strains overexpressing Msn2/4 show increased resistance to carbon starvation and heat shock (Martinez-Pastor *et al.*, 1996; Schmitt & McEntee, 1996). The activity and localization of Msn2 is negatively regulated by protein kinase A (PKA) and positively regulated by a number of known and unknown phosphatases including protein phosphatase 1 and the Psr1p/Whi2p phosphatase complex (Toda *et al.*, 1987; Smith *et al.*, 1998; Jacquet *et al.*, 2003). Msn2 contains eight serine residues that are phosphorylated by PKA (Hao *et al.*, 2013). The activity of of the nuclear export signal (NES) is regulated by two of these residues and the activity of the nuclear localization signal (NLS) is regulated by four of these residues (Hao *et al.*, 2013). When PKA is fully active, both the NES and NLS are phosphorylated. This activates the NES and inactivates the NLS causing Msn2 to reside in the cytoplasm through export from the nucleus mediated by the nuclear export receptor Msn5 (Gorner *et al.*, 2002). When PKA is fully inhibited, both the NES and NLS are dephosphorylated. This inactivates the NES and activates the NLS and Msn2 resides in the nucleus where it can activate transcription by binding to the STRE (Gorner *et al.*, 1998; Smith *et al.*, 1998; Gorner *et al.*, 2002; Hao *et al.*, 2013).

PKA itself is a heterocomplex composed of three catalytic subunits encoded by the three genes *TPK1*, *TPK2* and *TPK3* and a regulatory subunit encoded by *BCY1*. PKA activity is regulated by cyclic adenosine monophosphate (cAMP), which is synthesized by adenylate

cyclase and degraded by the phosphodiesterases Pde1 and Pde2 (Matsumoto *et al.*, 1982; Uno *et al.*, 1983; Toda *et al.*, 1987). When cAMP levels are high, cAMP binds and sequesters the regulatory PKA subunit Bcy1, which releases the catalytic PKA subunits Tpk1, Tpk2 and Tpk3 which phosphorylate Msn2. Conversely, when cAMP level are low, Bcy1 can bind and inactivate the catalytic PKA subunits: Tpk1, Tpk2 and Tpk3. Since Msn2 is then no longer actively phosphorylated, it is rapidly dephosphorylated by protein phosphatases and translocates into the nucleus within ∼1-2 min of PKA inhibition (Hao & O'Shea, 2012). Thus, Msn2 localization and activity is a dynamic steady-state between phosphorylation and dephosphorylation, with dephosphorylation and nuclear export being dominant under normal growth conditions. As a central regulator, PKA deletion (*tpk1Δ tpk2Δ tpk3Δ*) is lethal. However, cells lacking both Msn2/4 and PKA are viable (*tpk1Δ tpk2Δ tpk3Δ msn2Δ msn4Δ*; Smith *et al.*, 1998). This shows that Msn2 is one of the main targets of PKA.

Early studies showed that Msn2 exhibits complex nucleocytoplasmic translocation dynamics in response to intense excitation from a fluorescence microscope (Jacquet *et al.*, 2003; Garmendia-Torres *et al.*, 2007). A breakthrough came when Hao & O'Shea systematically investigated Msn2 dynamics in response to different stresses using an Msn2-YFP fusion protein to follow the subcellular localization of Msn2 and a microfluidic device to control stress exposure (Hao & O'Shea, 2012). They found that in response to glucose limitation, Msn2 exhibits short bursts of nuclear localization; in response to osmotic stress, Msn2 briefly translocates to the nucleus once and then returns to the cytoplasm and in response to oxidative stress, Msn2 shows sustained nuclear localization (Hao & O'Shea, 2012). Thus, the identity of three different stresses can be distinguished just by observation of Msn2 translocation dynamics. Furthermore, under glucose limitation, Msn2 burst frequency increases with stress intensity; under osmotic stress, the Msn2 pulse duration increases with stress intensity

and under oxidative stress, the nuclear concentration of Msn2 or the amplitude increases with stress intensity. Thus, as illustrated in Figure 1.3, Msn2 dynamics encode information both about three different stress identities and their intensity. Stress intensity is encoded through frequency modulation for glucose starvation, through duration modulation for osmotic stress and through amplitude modulation for oxidative stress (Hao & O'Shea, 2012). These observations have since been extended by considering additional stresses (Petrenko *et al.*, 2013) and by considering Msn2 mutants lacking proper NES or NLS phosphorylation sites, which are no longer able to fully distinguish all three stresses (Hao *et al.*, 2013).

Taken together, the number of central regulators — including Msn2 — which appear to encode information about signal identity and/or intensity in their activation dynamics begs the following question: how is this information transmitted and ultimately decoded? In the next section, we will focus on this question.

1.3 Decoding information encoded in transcription factor dynamics

As we have discussed in section 1.2, there is now extensive evidence that cells can encode information in a single master regulator by modulating the amplitude, duration and/or frequency of its activation dynamics. However, the fact the information appears to be encoded does not prove that cells actually transmit information by regulating signaling dynamics. In other words, to understand the extent to which information is transmitted by regulation of signaling dynamics we must focus on the decoding mechanism (Behar & Hoffmann, 2010).

As we will discuss in detail in Chapter 3, this argument can also be understood within the

framework of information theory (Shannon, 1948; Cover and Thomas, 2006). According to the data processing inequality, the information transduction capacity of a pathway is given by its weakest node or bottleneck. This means that no matter how much information can be transmitted through upstream arms of a pathway, the total capacity is limited by its weakest bottleneck and all additional upstream information will be lost. Thus, even if information about multiple signals and their intensities can be successfully encoded in the dynamics of a single transcription factor the encoded information will be lost if downstream decoding modules cannot fully decode this information.

Therefore, for successful information transduction a pathway must be able to both encode and decode sufficient information to elicit the desired range of responses. Below we discuss recent studies focusing on the decoding mechanism.

1.3.1 Signaling dynamics and control of cell fate: distinguishing cause from coincidence

One of the first and most famous examples implicating the dynamics of a single master regulator in control of cell fate was the mitogen-activated protein kinase, ERK (Marshall, 1995). As discussed above, EGF treatment leads to transient ERK activation and proliferation of PC-12 cells, whereas NGF treatment leads to sustained ERK activation and differentiation of PC-12 cells. Thus, ERK signaling duration correlates with cell fate. However, since EGF and NGF activate multiple and different pathways, a major challenge has been to determine whether ERK signaling duration is sufficient or even necessary to control this cell fate choice. This question has been extensively studied. For example, Santos *et al.* systematically perturbed ERK dynamics through pharmacological and RNAi-mediated perturbation of key signaling molecules during EGF and NGF treatment (Santos *et al.*, 2007).

This study provided strong evidence for the importance of ERK dynamics in controlling cell fate as well as a quantitative understanding of the signaling pathway. Nonetheless, since each perturbation targeted signaling molecules which are themselves involved in multiple feedback and feedforward loops, it has remained difficult to ascertain whether control of ERK dynamics is sufficient to control cell fate (Roskoski, 2012).

This example highlights a key experimental limitation of previous studies. To demonstrate that control of ERK dynamics is sufficient to control cell fate, a method that allows control of ERK without perturbing any other pathway is necessary. The development of optogenetics provided this capability. In three independent studies, Aoki *et al.*, Toettcher *et al.* and Zhang *et al.* used optogenetics to dynamically control protein localization with light and control ERK activity (Aoki *et al.*, 2013; Toettcher *et al.*, 2013; Zhang *et al.*, 2014). Aoki *et al.* and Zhang *et al.* used light-mediated recruitment of Raf to the membrane to control ERK activity, whereas Toettcher *et al.* used light-mediated recruitment of SOS to the membrane to activate ERK. All three groups independently confirmed that control of ERK dynamics is sufficient to control cell fate, although there is some noise in this cell fate choice.

In the case of Msn2 it is clear that different stresses lead to different nuclear translocation dynamics of Msn2 (Hao & O'Shea, 2012; Petrenko *et al.*, 2013) and different downstream gene expression programs (Gasch *et al.*, 2000). However, since different stresses activate different stress pathways in addition to inducing different dynamics of Msn2, it is unclear to what extent controlling Msn2 translocation dynamics is sufficient for controlling different gene expression programs.

The same problem of distinguishing causality from correlation has held back progress in the p53 and NF-κB fields. It is clear that TNF-α and LPS induces different NF-κB

dynamics and different downstream responses (Ashall *et al.*, 2009; Giorgetti *et al.*, 2010; Tay *et al.*, 2010), but it is unclear to what extent NF-κB dynamics are necessary or sufficient for controlling these. In the case of p53, it is clear that γ-irradiation induces p53 pulsing and cell cycle arrest, whereas UV-radiation induces sustained p53 activity, senescence and even cell apoptosis (Batchelor *et al.*, 2011; Purvis & Lahav, 2013). However, it was long unclear to what extent p53 dynamics is sufficient to explain these differences. Purvis *et al.* took a step further by combining γ-irradiation with carefully timed addition of Nutlin-3 a pharmacological inhibitor of Mdm2 — a negative regulator of p53 (Purvis *et al.*, 2012). By preventing negative feedback from Mdm2, it was possible to force sustained activity of p53 in response to γ-irradiation. This also affected cell fate: whereas cell cycle arrest is normally the major cell fate in response to γ-irradiation, senescence was now found to dominate thereby implicating p53 dynamics in control of cell fate (Purvis *et al.*, 2012).

Another remarkable example mentioned above is that of Ascl1 expression in murine neural progenitor cells (Imayoshi *et al.*, 2013). Imayoshi *et al.* found that in proliferating neural progenitors, Ascl1 expression oscillates with a period of 2-3 hours. When neural progenitor cells undergo differentiation into neurons, Ascl1 expression becomes sustained. In an impressive series of experiments, Imayoshi *et al.* developed an $\text{Ascl1}^{-/-}$ mouse that ectopically expresses Ascl1 in a light-inducible manner. With oscillatory 3 hour light stimulation in this mouse line, Ascl1 expression oscillates mimicking the natural Ascl1 expression dynamics in neural progenitors and these cells proliferate. Conversely, with sustained light stimulation, Ascl1 expression becomes sustained and the neural progenitor cells differentiate into neurons. Thus, control of Ascl1 expression dynamics is sufficient to control cell fate in neural progenitor cells.

The above examples demonstrate that controlling the signaling dynamics of a master

regulator can in several instances be sufficient to control cell fate. Thus, they provide evidence for the signal encoding/decoding paradigm, whereby information transmission can occur through an amplitude-, duration- or frequency-mediated code (Behar & Hoffmann, 2010). However, the mechanism behind the differential decoding of oscillatory and sustained signaling is not clear. In all the cases cited above, cells control cell fate by inducing different sets of genes. Although ERK is a kinase, it directly associates with and regulates the activity of several transcription factors in the cell nucleus (Roskoski, 2012). All the other examples involve transcription factors. Thus, the most parsimonious explanation would be that individual genes can somehow differentially decode transcription factor dynamics such that oscillatory transcription factor activity induces different sets of genes than sustained transcription factor activity. Or phrased differently, to what extent can the cell differentially control gene expression by controlling the dynamics of a single transcription factor? This is the motivating question behind this dissertation and the topic of the next section.

1.3.2 Control of gene expression through regulation of transcription factor dynamics

The relationship between the activity of a transcription factor and the expression level of its target genes at steady-state is sometimes referred to as the gene regulatory function (Rosenfeld *et al.*, 2005; Kim & O'Shea, 2008). This relationship has been extensively studied (Sharon *et al.*, 2012; Levo & Segal, 2014) and it is now well established that promoters can vary widely in how sensitive they are to the concentration of the transcription factor, how high their rate of transcription is and how much cell-to-cell variability in expression they exhibit (Coulon *et al.*, 2013).

Almost all previous studies of gene regulation have considered this dose-response type

relationship at steady-state. However, in order to successfully transmit information by regulating the activation dynamics of a transcription factor, gene promoters must necessarily be able to distinguish different dynamical inputs (e.g. oscillations vs. a sustained pulse). Thus, to make progress towards answering this question we needed a method that combines control of transcription factor translocation dynamics with the ability of measuring the response of individual genes. A major breakthrough came when Hao & O'Shea combined a chemical genetic method for controlling PKA activity (Bishop *et al.*, 2000; Zaman *et al.*, 2009) with microfluidics (Hersen *et al.*, 2008). By directly controlling the kinase activity of PKA with a small molecule, 1-NM-PP1, it is possible to control the phosphorylation state of Msn2. Furthermore, using microfluidics it is possible to add or remove 1-NM-PP1 within seconds and therefore control Msn2 dynamics with minute time resolution. Using this setup, Hao & O'Shea controlled the nuclear translocation dynamics of Msn2. Mimicking Msn2 dynamics under natural stresses, they studied how gene expression of a synthetic reporter gene depended on Msn2 dynamics. Importantly, they found that gene expression is not just a simple function of the integrated Msn2 level (Msn2 AUC, $\int_0^\infty [\text{Msn2}(t)]\text{d}t$). Instead, gene expression is a non-linear function of Msn2 dynamics. They extended these studies by examining expression genome-wide in response to different Msn2 dynamics using microarrays and found that promoters generally showed different activation kinetics. Although the resolution of microarray studies is more limited, this study provided evidence for the notion that controlling transcription activation dynamics can be sufficient to regulate gene expression. As such, this study motivated a more in-depth study at the single-cell level.

Encouraged by this work, we therefore decided to systematically dissect how different Msn2 target genes decode Msn2 dynamics in single cells. We describe the results of these studies in Chapter 2. By extending these studies to single cells, we discovered an important

trade-off: promoters with slow kinetics are able to filter out brief or oscillatory transcription factor input, but this comes at the cost of higher noise in gene expression. Below, we discuss how studying gene regulation at the single cell level can reveal important additional information about the transcriptional control mechanism.

1.3.3 Gene regulation at the single cell level is noisy

From early studies on bacterial chemotaxis it became clear that single bacteria exhibit non-genetic individuality and that this is due to the stochasticity inherent in biochemical reactions involving few molecules (Spudich & Koshland, 1976). Following developments in microscopy, flow cytometry and fluorescent proteins it since became possible to measure and quantitatively analyze stochasticity in gene expression in single cells (McAdams & Arkin, 1997; Tsien, 1998; Paulsson, 2004; Sanchez & Golding, 2013). These studies revealed that gene expression is surprisingly noisy — in a population of genetically identical cells, the expression levels of the same gene can vary widely between cells (Elowitz *et al.*, 2002; Raser & O'Shea, 2004). While noise in gene expression is unavoidable, studies also showed that the noise levels can differ widely between genes and that differences in promoter architectures can largely explain these differences (Newman *et al.*, 2006; Tirosh & Barkai, 2008; Choi & Kim, 2009).

However, a major limitation of many previous studies of cell-to-cell variability is that they have involved taking single time-point snapshots of unsynchronized cell populations at steady-state (Sanchez & Golding, 2013). This is important because stochastic partitioning of molecules during cell division also contributes to cell-to-cell variability and through snapshots it can be very difficult to deconvolve these two processes (Huh & Paulsson, 2011a; Huh & Paulsson, 2011b). In this dissertation, we develop methods (Chapter 4) to induce and

measure gene expression in single cells over time by controlling Msn2 dynamics and using fluorescent reporters (Chapters 2 & 3). Not only does this allow us to avoid complications arising from stochastic partitioning of molecules during cell division, this also allows us to directly relate the mechanisms of transcriptional control to measured levels of noise in gene expression (Chapter 2).

Taking noise in gene expression into account is critical for understanding information transduction since noise in gene expression represents a loss of information. For example, even though the cell appears to be able to encode information about signal identity and signal intensity for glucose limitation, osmotic and oxidative stress in the translocation dynamics of Msn2, if the decoding step — converting Msn2 dynamics into gene expression output — is too noisy, the gene expression output no longer adequately reflects the Msn2 input and the information contained in Msn2 dynamics has now been permanently lost. Thus, promoter decoding of transcription factor dynamics represents an important potential bottleneck in information transduction. In Chapter 3 of this dissertation, we study in detail how much information is lost due to gene expression noise by applying tools from information theory to the Msn2 system. We found that the Msn2 pathway reliably transmits information about signal identity for multiple different stresses. However, noise in gene expression interferes with transmission of signal intensity information.

1.4 Summary

In this Chapter we have advanced the "signal encoding/decoding" paradigm, i.e. the idea that cells make use of temporal signaling codes for information transduction across signaling networks exhibiting a bowtie topology (Behar & Hoffmann, 2010). We have argued that to understand the extent to which cells make use of temporal signaling codes, we

must focus on the decoding mechanism, since only the part of the temporal signal that can be successfully decoded can usefully be thought as truly encoding information. Additionally, we have argued that to distinguish cause from coincidence, it is crucial that studies directly control the dynamics of the transcription factor of interest rather than applying broad stresses that activate multiple pathways and therefore obscure interpretation of downstream outcomes. Furthermore, we have advanced the idea that to understand information transduction through regulation of signaling dynamics, it is crucial to study the decoding mechanism in single cells since this allows for quantitative measurements of information transduction, in bits.

Overall, in support of the "signal encoding/decoding" paradigm, we find that it is possible to encode multiple gene expression programs in the dynamics of a single transcription factor simply by modulating the amplitude threshold and activation timescales of individual promoters. At the same time, we find that noise in gene expression severely limits information transduction through regulation of signaling dynamics. Thus, while it is possible to reliably encode and transmit signal identity information (e.g. about cell fate) in the dynamics of a single transcription factor, encoding and reliably transmitting signal intensity information (e.g. fine-tuning the expression levels of genes to signal intensity) does not appear to be possible.

Our work establishes a framework for understanding information transduction through regulation of signaling dynamics. In the future it will be interesting to extend our approach to pathways beyond the Msn2 system.

1.5 References

Aoki, K., Kumagai, Y., Sakurai, A., Komatsu, N., Fujita, Y., Shionyu, C., & Matsuda, M. (2013). Stochastic ERK activation induced by noise and cell-to-cell propagation regulates

cell density-dependent proliferation. *Molecular cell*, **52**: 529-540.

Ashall, L., Horton, C.A., Nelson, D.E., Paszek, P., Harper, C.V., Sillitoe, K., Ryan, S., Spiller, D.G., Unitt, J.F., Broomhead, D.S., Kell, D.B., Rand, D.A., See, V. & White, M.R. (2009) Pulsatile stimulation determines timing and specificity of NF-kappaB-dependent transcription. *Science* **324**:242-246

Batchelor, E., Mock, C. S., Bhan, I., Loewer, A., & Lahav, G. (2008). Recurrent initiation: a mechanism for triggering p53 pulses in response to DNA damage. *Molecular cell* **30**: 277-289.

Batchelor E., Loewer, A. & Lahav, G. (2009). The ups and downs of p53: understanding protein dynamics in single cells. *Nature Reviews Cancer* **9**: 371-377

Batchelor, E., Loewer, A., Mock, C., & Lahav, G. (2011). Stimulus-dependent dynamics of p53 in single cells. *Molecular systems biology* **7**

Behar, M., Dohlman, H.G., & Elston, T.C. (2007). Kinetic insulation as an effective mechanism for achieving pathway specificity in intracellular signaling networks. *P Natl Acad Sci USA* **104**: 16146-16151.

Behar, M., & Hoffmann, A. (2010). Understanding the temporal codes of intra-cellular signals. *Curr Opin Genet Dev* **20**: 684-693.

Berridge, M.J., Lipp, P., & Bootman, M.D. (2000). The versatility and universality of calcium signalling. *Nat Rev Mol Cell Biol* **1**: 11-21.

Bishop, A.C., Ubersax, J.A., Petsch, D.T., Matheos, D.P., Gray, N.S., Blethrow, J., Shimizu, E., Tsien, J.Z., Schultz, P.G., Rose, M.D., Wood, J.L., Morgan, D.O. & Shokat, K.M. (2000) A chemical switch for inhibitor-sensitive alleles of any protein kinase. *Nature* **407**: 395-401

Boy-Marcotte, E., Garmendia, C., Garreau, H., Lallet, S., Mallet, L., & Jacquet, M. (2006). The transcriptional activation region of Msn2p, in Saccharomyces cerevisiae, is regulated by stress but is insensitive to the cAMP signalling pathway. *Mol Genet Genomics* **275**: 277-287.

Cai L., Dalal C.K. & Elowitz M.B. (2008) Frequency-modulated nuclear localization bursts coordinate gene regulation. *Nature* **455**: 485-490

Castillo-Hair, S. M., Igoshin, O. A., & Tabor, J. J. (2015). How to train your microbe: methods for dynamically characterizing gene networks, *Current Opinion in Microbiology* **24**: 113

Choi, J. K., & Kim, Y. J. (2009). Intrinsic variability of gene expression encoded in

nucleosome positioning sequences. *Nature genetics* **41**: 498-503.

Coulon, A., Chow, C.C., Singer, R.H., & Larson, D.R. (2013). Eukaryotic transcriptional dynamics: from single molecules to cell populations. *Nature reviews Genetics* **14**: 572-584.

Covert, M.W., Leung, T.H., Gaston, J.E. & Baltimore, D. (2005) Achieving stability of lipopolysaccharide induced NF-kappa B activation. *Science* **309**: 1854-1857

Cover, T.M., & Thomas, J.A. (2006). Elements of information theory, 2nd edition. Wiley-Interscience.

Crabtree, G. R., & Graef, I. A. (2008). Bursting into the Nucleus. *Science signaling* **1**, pe54.

Csete, M., & Doyle, J. (2004). Bow ties, metabolism and disease. *Trends Biotechnol* **22**: 446-450

Dalal, C.K., Cai, L., Lin, Y.H., Rahbar, K., & Elowitz, M.B. (2014). Pulsatile Dynamics in the Yeast Proteome. *Current Biology* **24**: 2189-2194.

de Nadal, E., Ammerer, G., & Posas, F. (2011). Controlling gene expression in response to stress. *Nature reviews Genetics* **12**: 833-845.

Elfving, N., Chereji, R.V., Bharatula, V., Bjorklund, S., Morozov, A.V., & Broach, J.R. (2014). A dynamic interplay of nucleosome and Msn2 binding regulates kinetics of gene activation and repression following stress. *Nucleic Acids Res* **42**: 5468-5482.

Elowitz M.B., Levine A.J., Siggia E.D., Swain P.S. (2002) Stochastic gene expression in a single cell. *Science* **297**: 1183-1186

Gasch, A. P., Spellman, P. T., Kao, C. M., Carmel-Harel, O., Eisen, M. B., Storz, G., & Brown, P. O. (2000). Genomic expression programs in the response of yeast cells to environmental changes. *Molecular biology of the cell* **11**: 4241-4257.

Garmendia-Torres, C., Goldbeter, A., & Jacquet, M. (2007). Nucleocytoplasmic oscillations of the yeast transcription factor Msn2: evidence for periodic PKA activation. *Current Biology* **17**: 1044-1049.

Gilmore T.D. (2006). Introduction to NF-κB: players, pathways, perspectives. *Oncogene* **25**: 6680-4

Giorgetti, L., Siggers, T., Tiana, G., Caprara, G., Notarbartolo, S., Corona, T., Pasparakis, M., Milani, P., Bulyk, M.L., Natoli, G. (2010) Noncooperative Interactions between Transcription Factors and Clustered DNA Binding Sites Enable Graded Transcriptional Responses to Environmental Inputs. *Molecular Cell* **37**: 418-428

Gorner, W., Durchschlag, E., Martinez-Pastor, M.T., Estruch, F., Ammerer, G., Hamilton, B., Ruis, H., & Schuller, C. (1998). Nuclear localization of the C2H2 zinc finger protein Msn2p is regulated by stress and protein kinase A activity. *Gene Dev* **12**: 586-597

Gorner, W., Durchschlag, E., Wolf, J., Brown, E.L., Ammerer, G., Ruis, H., & Schuller, C. (2002). Acute glucose starvation activates the nuclear localization signal of a stress-specific yeast transcription factor. *The EMBO journal* **21**: 135-144.

Hao, N., Budnik, B.A., Gunawardena, J., & O'Shea, E.K. (2013). Tunable Signal Processing Through Modular Control of Transcription Factor Translocation. *Science* **339**: 460-464.

Hao, N., and O'Shea, E.K. (2012). Signal-dependent dynamics of transcription factor translocation controls gene expression. *Nature structural & molecular biology* **19**: 31-U47.

Hersen P., McClean M.N., Mahadevan L. & Ramanathan S. (2008) Signal processing by the HOG MAP kinase pathway. *Proc Natl Acad Sci USA* **105**: 7165-7170

Huebert, D.J., Kuan, P.F., Keles, S., & Gasch, A.P. (2012). Dynamic changes in nucleosome occupancy are not predictive of gene expression dynamics but are linked to transcription and chromatin regulators. *Mol Cell Biol* **32**: 1645-1653

Huh, D., & Paulsson, J. (2011a). Non-genetic heterogeneity from stochastic partitioning at cell division. *Nature genetics* **43**: 95-100.

Huh, D., & Paulsson, J. (2011b). Random partitioning of molecules at cell division. *Proceedings of the National Academy of Sciences* **108**: 15004-15009.

Hoffmann, A., & Baltimore, D. (2006). Circuitry of nuclear factor κB signaling. *Immunological reviews* **210**, 171-186.

Hoffmann, A., Levchenko, A., Scott, M. L., & Baltimore, D. (2002). The IκB-NF-κB signaling module: temporal control and selective gene activation. *Science* **298**: 1241-1245.

Hynes, N. E., Ingham, P. W., Lim, W. A., Marshall, C. J., Massague, J., & Pawson, T. (2013). Signalling change: signal transduction through the decades. *Nature Reviews Molecular Cell Biology* **14**: 393-398.

Imayoshi, I., Isomura, A., Harima, Y., Kawaguchi, K., Kori, H., Miyachi, H., & Kageyama, R. (2013). Oscillatory control of factors determining multipotency and fate in mouse neural progenitors. *Science* **342**: 1203-1208.

Imayoshi, I., & Kageyama, R. (2014). Oscillatory control of bHLH factors in neural progenitors. *Trends in neurosciences*, **37**: 531-538.

Isomura, A., & Kageyama, R. (2014). Ultradian oscillations and pulses: coordinating cellular responses and cell fate decisions. *Development* **141**: 3627-3636.

Jacquet, M., Renault, G., Lallet, S., De Mey, J., & Goldbeter, A. (2003). Oscillatory nucleocytoplasmic shuttling of the general stress response transcriptional activators Msn2 and Msn4 in Saccharomyces cerevisiae. *The Journal of cell biology* **161**: 497-505.

Kim, H. D., & O'Shea, E. K. (2008). A quantitative model of transcription factor-activated gene expression. *Nature structural & molecular biology* **15**: 1192-1198.

Kobayashi, N., & McEntee, K. (1993). Identification of cis and trans components of a novel heat shock stress regulatory pathway in Saccharomyces cerevisiae. *Mol Cell Biol* **13**: 248-256.

Lahav, G., Rosenfeld, N., Sigal, A., Geva-Zatorsky, N., Levine, A. J., Elowitz, M. B., & Alon, U. (2004). Dynamics of the p53-Mdm2 feedback loop in individual cells. *Nature genetics* **36**: 147-150.

Lane, D. P. (1992). Cancer. p53, guardian of the genome. *Nature* **358**: 15-16.

Levine, J.H., Lin, Y.H., & Elowitz, M.B. (2013). Functional Roles of Pulsing in Genetic Circuits. *Science* **342**: 1193-1200.

Levo, M., & Segal, E. (2014). In pursuit of design principles of regulatory sequences. *Nature Reviews Genetics* **15**: 453-468.

Marshall, C. J. (1995). Specificity of receptor tyrosine kinase signaling: transient versus sustained extracellular signal-regulated kinase activation. *Cell* **80**: 179-185.

Matsumoto, K., Uno, I., Oshima, Y., & Ishikawa, T. (1982). Isolation and characterization of yeast mutants deficient in adenylate cyclase and cAMP-dependent protein kinase. *P Natl Acad Sci USA* **79**: 2355-2359.

Martinez-Pastor, M.T., Marchler, G., Schuller, C., Marchler-Bauer, A., Ruis, H., & Estruch, F. (1996). The Saccharomyces cerevisiae zinc finger proteins Msn2p and Msn4p are required for transcriptional induction through the stress response element (STRE). *The EMBO journal* **15**: 2227-2235.

McAdams, H. H., & Arkin, A. (1997). Stochastic mechanisms in gene expression. *P Natl Acad Sci USA* **94**: 814-819.

Nelson, D.E., Ihekwaba, A.E., Elliott, M., Johnson, J.R., Gibney, C.A., Foreman, B.E., Nelson, G., See, V., Horton, C.A., Spiller, D.G., Edwards, S.W., McDowell, H.P., Unitt, J.F., Sullivan, E., Grimley, R., Benson, N., Broomhead, D., Kell, D.B. & White, M. R.

(2004) Oscillations in NF-kappaB signaling control the dynamics of gene expression. *Science* **306**:704-708

Newman, J.R.S., Ghaemmaghami, S., Ihmels, J., Breslow, D.K., Noble, M., DeRisi, J.L., Weissman, J.S. (2006) Single-cell proteomic analysis of S. cerevisiae reveals the architecture of biological noise. *Nature* **441**:840-846

Paulsson, J. (2004). Summing up the noise in gene networks. *Nature* **427**: 415-418.

Petrenko, N., Chereji, R.V., McClean, M., Morozov, A.V., Broach, J.R. (2013) Noise and interlocking signaling pathways promote distinct transcription factor dynamics in response to different stresses. *Mol Biol Cell* **24**: 2045-2057

Purvis, J.E., Karhohs, K.W., Mock, C., Batchelor, E., Loewer, A. & Lahav, G. (2012) p53 dynamics control cell fate. *Science* **336**: 1440-1444

Purvis, J.E., & Lahav, G. (2013). Encoding and Decoding Cellular Information through Signaling Dynamics. *Cell* **152**: 945-956.

Raser, J.M., OShea, E.K. (2004) Control of stochasticity in eukaryotic gene expression. *Science* **304**: 1811-1814

Rosenfeld, N., Young, J. W., Alon, U., Swain, P. S., & Elowitz, M. B. (2005). Gene regulation at the single-cell level. *Science* **307**: 1962-1965.

Roskoski, R. Jr. (2012). ERK1/2 MAP kinases: structure, function, and regulation. *Pharmacol Res* **66**: 105

Santos, S. D., Verveer, P. J., & Bastiaens, P. I. (2007). Growth factor-induced MAPK network topology shapes Erk response determining PC-12 cell fate. *Nature cell biology* **9**: 324-330

Sanchez, A., & Golding, I. (2013). Genetic determinants and cellular constraints in noisy gene expression. *Science* **342**: 1188-1193.

Shannon, C.E. (1948). A Mathematical Theory of Communication. *At&T Tech J* **27**: 623-656.

Sharon, E., Kalma, Y., Sharp, A., Raveh-Sadka, T., Levo, M., Zeevi, D., & Segal, E. (2012). Inferring gene regulatory logic from high-throughput measurements of thousands of systematically designed promoters. *Nature biotechnology* **30**: 521-530.

Siggers, T., Reddy, J., Barron, B., & Bulyk, M. L. (2014). Diversification of transcription factor paralogs via noncanonical modularity in C2H2 zinc finger DNA binding. *Molecular cell* **55**: 640-648.

Smith, A., Ward, M.P., & Garrett, S. (1998). Yeast PKA represses Msn2p/Msn4p-dependent gene expression to regulate growth, stress response and glycogen accumulation. *The EMBO journal* **17**, 3556-3564.

Schmitt, A.P., & McEntee, K. (1996). Msn2p, a zinc finger DNA-binding protein, is the transcriptional activator of the multistress response in Saccharomyces cerevisiae. *P Natl Acad Sci USA* **93**: 5777-5782

Spudich, J. L., & Koshland Jr, D. E. (1976). Non-genetic individuality: chance in the single cell. *Nature* **262**: 467-471.

Stewart-Ornstein, J., Nelson, C., DeRisi, J., Weissman, J. S., & El-Samad, H. (2013). Msn2 coordinates a stoichiometric gene expression program. *Current Biology* **23**: 2336-2345.

Tay, S, Hughey, J.J., Lee, T.K., Lipniacki, T., Quake, S.R., Covert, M.W. (2010) Single-cell NF-kappaB dynamics reveal digital activation and analogue information processing. *Nature* **466**: 267-271

Tirosh, I., & Barkai, N. (2008). Two strategies for gene regulation by promoter nucleosomes. *Genome research* **18**: 1084-1091.

Toda, T., Cameron, S., Sass, P., Zoller, M., & Wigler, M. (1987). Three different genes in S. cerevisiae encode the catalytic subunits of the cAMP-dependent protein kinase. *Cell* **50**: 277-287.

Toettcher, J. E., Weiner, O. D., & Lim, W. A. (2013). Using optogenetics to interrogate the dynamic control of signal transmission by the Ras/Erk module. *Cell* **155**: 1422-1434.

Tsien, R. Y. (1998). The green fluorescent protein. *Annual review of biochemistry* **67**: 509-544.

Uno, I., Matsumoto, K., & Ishikawa, T. (1983). Characterization of a cyclic nucleotide phosphodiesterase-deficient mutant in yeast. *The Journal of biological chemistry* **258**: 3539-3542.

Werner, SL, Barken, D & Hoffmann, A (2005) Stimulus specificity of gene expression programs determined by temporal control of IKK activity. *Science* **309**: 1857-1861

Yissachar, N., Fischler, T.S., Cohen, A.A., Reich-Zeliger, S., Russ, D., Shifrut, E., Porat, Z. & Friedman N. (2013) Dynamic response diversity of NFAT isoforms in individual living cells. *Mol Cell* **49**:322-330

Zaman, S., Lippman, S.I., Schneper, L., Slonim, N. & Broach J.R. (2009) Glucose regulates transcription in yeast through a network of signaling pathways. *Mol Syst Biol* **5**: 245

Zhang, K., Duan, L., Ong, Q., Lin, Z., Varman, P. M., Sung, K., & Cui, B. (2014). Light-mediated kinetic control reveals the temporal effect of the Raf/MEK/ERK pathway in PC12 cell neurite outgrowth. *PloS one* **9**: e92917.

Chapter 2

Promoter decoding of transcription factor dynamics involves a trade-off between noise and control of gene expression

2.1 Abstract

Numerous transcription factors encode information about upstream signals in the dynamics of their activation, but how downstream genes decode these dynamics remains poorly understood. Using microfluidics to control the nucleocytoplasmic translocation dynamics of the budding yeast transcription factor Msn2, we elucidate the principles that govern how different promoters convert dynamical Msn2 input into gene expression output in single cells. Combining modeling and experiments, we classify promoters according to their signal-processing behavior and reveal that multiple, distinct gene expression programs can

be encoded in the dynamics of Msn2. We show that both oscillatory transcription factor dynamics and slow promoter kinetics lead to higher noise in gene expression. Furthermore, we show that the promoter activation timescale is related to nucleosome remodeling. Our findings imply a fundamental trade-off: although the cell can exploit different promoter classes to differentially control gene expression using transcription factor dynamics, gene expression noise fundamentally limits how much information can be encoded in the dynamics of a single transcription factor and reliably decoded by promoters.

2.2 Introduction

To survive in a changing environment, cells must be able to sense the environment and transmit this information through signal transduction cascades to transcription factors, which then initiate a suitable gene expression response. Whereas downstream responses to signaling have typically been understood as consequences of the strength or amplitude of the signal, emerging evidence suggests that additional information can be encoded in the temporal dynamics of these signals (Behar & Hoffmann, 2010; Purvis & Lahav, 2013).

Several mammalian transcription factors exhibit complex and signal dependent dynamics. For example, NF-$\varkappa$B, involved in controlling inflammation, undergoes nucleocytoplasmic oscillations in response to tumor necrosis factor-α (TNFα), but sustained nuclear localization in response to bacterial lipopolysaccharides (LPSs) (Nelson *et al.*, 2004; Covert *et al.*, 2005; Werner *et al.*, 2005). Thus, NF-$\varkappa$B translocation dynamics encode the signal identity (TNFα or LPS). Similarly, the tumor suppressor transcription factor p53 undergoes a dose-dependent number of nuclear pulses in response to DNA breaks, but a single sustained pulse with dose-dependent amplitude and duration in response to UV irradiation (Lahav *et al.*, 2004; Batchelor *et al.*, 2011). Thus, p53 dynamics encode both the dose (severity) and the identity

of the stress. Similarly, two transcription factor isoforms of NFAT also exhibit distinct dynamics in response to different stimuli (Yissachar *et al.*, 2013).

The activities of budding yeast transcription factors also appear to be dynamically regulated. In response to calcium, the transcription factor Crz1 exhibits short bursts of nuclear localization, where the duration is fixed but the frequency is dose-dependent (Cai *et al.*, 2008). Msn2, a zinc-finger transcription factor and regulator of the yeast multi-stress response, also exhibits oscillatory translocation dynamics (Jacquet *et al.*, 2003; Petrenko *et al.*, 2013). The identity and dose (severity) of three distinct stresses are encoded in the translocation dynamics of Msn2: in response to glucose starvation, Msn2 exhibits short bursts of nuclear localization with dose-dependent frequency; in response to osmotic stress, Msn2 translocates to the nucleus with a single initial peak with dose-dependent duration; and in response to oxidative stress, Msn2 shows sustained nuclear localization with dose-dependent amplitude (Hao & OShea, 2012).

Although it is clear that diverse signals are encoded in the dynamics of NF-κB, p53, NFAT, Crz1, Msn2, and many other transcription factors (Purvis & Lahav, 2013), we understand little about how these signals are decoded by gene promoters and converted into gene expression programs. For example, do genes differ in their sensitivity to transcription factor dynamics? And if so, what are the quantitative principles that govern this input-output relationship? Studies suggest that transcription factor dynamics can influence the gene expression response. For example, p53 dynamics may affect cell fate through differential gene regulation: p53 pulses induce only DNA repair genes, whereas a single, sustained p53 pulse leads to higher expression of senescence genes (Purvis *et al.*, 2012). Similarly, whereas some NF-κB target genes filter out low TNFα concentrations, others activate fully even in response to low TNFα concentrations (Ashall *et al.*, 2009; Giorgetti *et al.*, 2010; Tay *et al.*,

2010). In the case of Crz1, as the frequency of nuclear localization bursts increases, the ratio of the majority of the induced genes is held constant as the gene expression increases (Cai *et al.*, 2008).

In most previous studies, distinct stimuli (e.g., TNFα or LPS) were required to induce distinct transcription factor dynamics (e.g., oscillations or a sustained pulse); since these stimuli can activate a large number of other factors or responses, it is difficult to establish that differential gene regulation is caused by transcription factor dynamics instead of just being correlated with transcription factor dynamics. To overcome this limitation, we previously developed a chemical genetic system that permits direct control of Msn2 translocation dynamics. Using this experimental set-up and modeling studies, we investigated how Msn2 dynamics affects expression of a single synthetic reporter gene and predicted that promoter activation kinetics influence the response to dynamic transcription factor inputs (Hao and OShea, 2012). However, the extent to which different promoters can differentially decode Msn2 dynamics is not clear. Moreover, previous studies used population-averaged techniques (e.g., qPCR or microarrays) that cannot provide information about the effect of transcription factor dynamics on gene regulation in individual cells. This is an important limitation because gene expression is a stochastic process, such that surprisingly large differences can exist between otherwise genetically identical cells (Elowitz *et al.*, 2002; Raser & OShea, 2004; Newman *et al.*, 2006; Raj *et al.*, 2006; Raj & van Oudenaarden, 2008; Lionnet & Singer, 2012). Although cells can exploit noise in gene expression through bet-hedging such as in bacterial persistence (Balaban *et al.*, 2004), noise is by and large detrimental to the cell: given a particular signal, a specific gene expression response is generally optimal. Thus, even if information about signal dose and identity can reliably be encoded in transcription factor dynamics, the information transfer will be fundamentally limited by the fidelity with

which transcription factor dynamics is subsequently decoded by promoters (Brennan *et al.*, 2012). Hence, to understand how much of the information encoded in transcription factor dynamics is lost due to gene expression noise, a detailed single-cell study is required.

To explore and understand the relationship between transcription factor dynamics, gene expression and noise in gene expression output, we develop a method integrating high-throughput microfluidics and quantitative time-lapse microscopy to artificially control the translocation dynamics of Msn2 and measure gene expression of several Msn2 target genes at the single-cell level. Combining modeling and experiments, we predict and verify that by controlling Msn2 dynamics it is possible to differentially express genes. We show that, in theory, four different promoter classes are possible such that four gene expression programs can be encoded in the dynamics of a single transcription factor. We find that, in general, oscillatory transcription factor input leads to higher noise than single pulse input and also that some promoter classes exhibit dramatically higher levels of noise in gene expression than others as a result of a slow promoter transition step, which we show is related to slow promoter nucleosome remodeling. Thus, there is a trade-off between achieving low noise and differential gene expression. Taken together, we provide a systematic dissection of the extent to which transcription factor dynamics controls gene expression and noise.

2.3 Result

2.3.1 Identification of specific target genes of Msn2

We employed a chemical genetic strategy to control the nuclear localization and activity of Msn2 (Bishop *et al.*, 2000; Hao & OShea, 2012). Msn2 localization is regulated by protein kinase A (PKA) — when PKA is active, Msn2 is phosphorylated and cytoplasmic; when

PKA is inhibited, Msn2 is unphosphorylated and localized to the nucleus (Gorner *et al.*, 1998). We introduced analog-sensitive mutations (PKA^{as}) into all three catalytic isoforms of PKA (Tpk1, Tpk2, and Tpk3), which enabled us to selectively and reversibly inhibit PKA activity, and therefore control Msn2 localization with the small molecule 1-NM-PP1 (Zaman *et al.*, 2009; Hao and OShea, 2012). To quantify Msn2 localization, we introduced into the PKA^{as} strain an Msn2-mCherry fusion protein and a nuclear marker (Nhp6a-iRFP; Appendix Figure A.1A). To identify Msn2-specific target genes, we used microarrays to compare the gene expression response to 1-NM-PP1 in strains with and without Msn2-mCherry and identified 23 genes that showed at least five-fold upregulation in the presence of Msn2-mCherry, but no expression change in an *msn2*Δ strain (Appendix Figure A.1C). To measure both gene expression and intrinsic and extrinsic noise components, we chose seven of the most strongly induced of these genes and implemented the dual-reporter strategy (Elowitz *et al.*, 2002), replacing the native ORF with fast-maturing CFP and YFP reporters on homologous chromosomes in diploid yeast cells. Finally, although PKA^{as} inhibition might have indirect global effects on gene expression, Msn2 directly controls the transcriptional response of these seven genes: they are not induced in the absence of Msn2 and previous genome-wide ChIP experiments have shown that Msn2 directly binds their promoters (Huebert *et al.*, 2012).

2.3.2 Systematic dissection of how different promoters decode transcription factor dynamics

To systematically investigate how induction of these seven Msn2 target genes depends on Msn2 nuclear translocation dynamics, we developed a high-throughput microfluidic device (Figure 2.1A). We used this device to rapidly switch between medium with and without 1-NM-PP1 and artificially modulate Msn2 nuclear localization, enabling us to control and

measure Msn2 input dynamics and simultaneously measure gene expression output dynamics for >100,000 single cells with high temporal resolution (example experiment: Figure 2.1B). For each of the 7 promoters, we performed 30 experiments in which we systematically modulated the amplitude, duration, pulse number, and pulse interval of Msn2 nuclear localization (Appendix Figure A.1D) to mimic the naturally observed Msn2 translocation dynamics in response to stress (Hao and OShea, 2012). We observed significant differences between the promoters (Figure 2.1C): *SIP18*, *TKL2*, and *ALD3* filtered out low amplitude input (25% and 50% amplitude), short duration input and oscillatory input, and only induced in response to sustained high-amplitude input; in contrast, *HXK1*, *DCS2*, and *DDR2* responded strongly to short oscillatory input and short duration input, while showing saturation at high amplitude. In between these extremes, *RTN2* filtered out low amplitude input like *SIP18*, yet showed significant induction in response to short duration and oscillatory input like *DDR2* (Figure 2.1C). Thus, natural promoters decode the same transcription factor input differently.

2.3.3 Using a mathematical model to cluster promoters into classes

To provide a quantitative framework for understanding the input-output relationship between Msn2 dynamics and gene expression, we constructed a mathematical model for transcription factor activated gene expression using ordinary differential equations (Figure 2.2A). Rather than pursuing an all-encompassing mechanistic model that would differ between promoters, we selected from several candidates the simplest model that could accurately describe all of the promoters despite their very different behavior (see Appendix A.2.12). Models with only two promoter states could not adequately account for the long activation delay that we observe for *SIP18*, *ALD3*, and *TKL2*. Thus, our final model contains three promoter states.

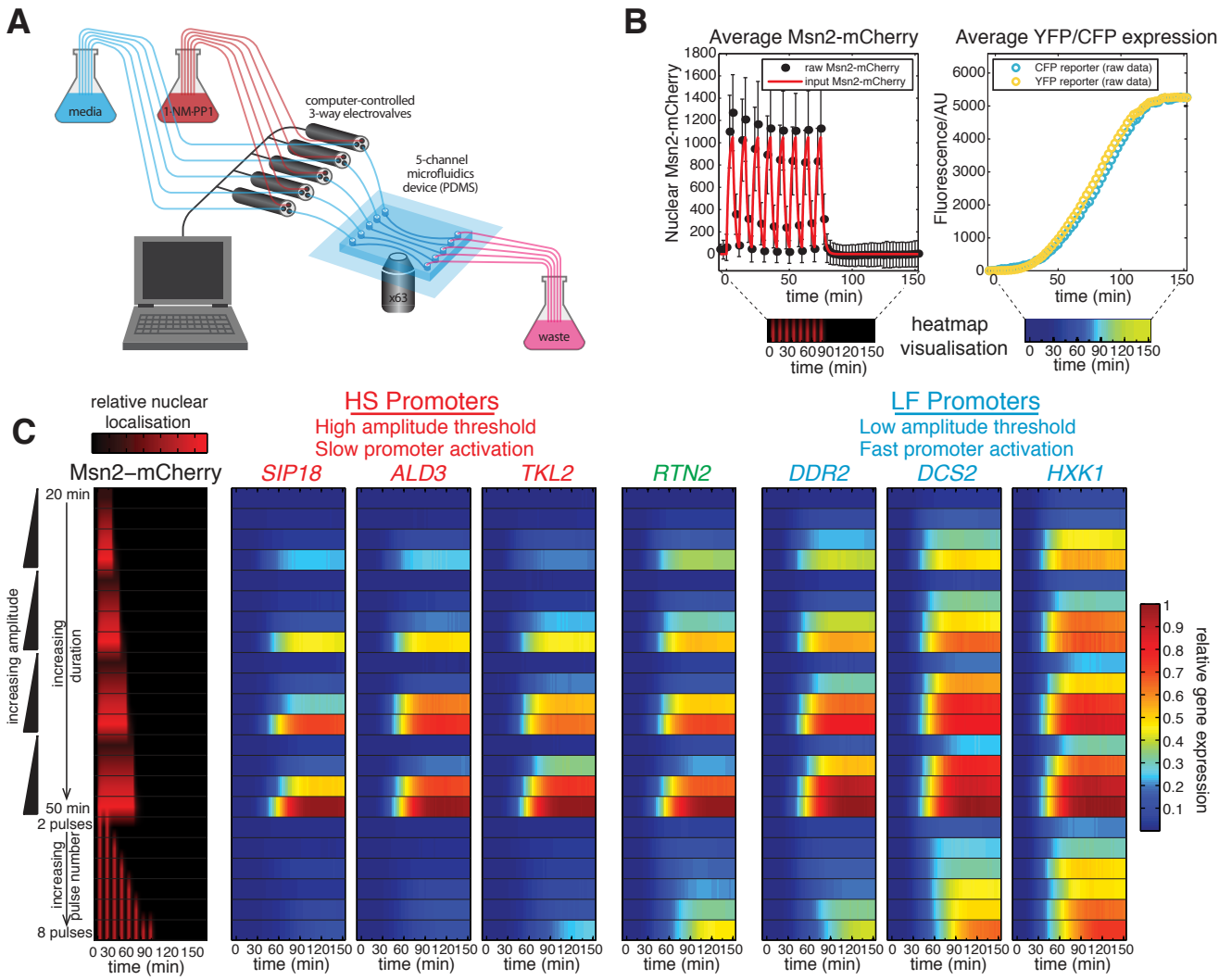

Figure 2.1: *Experimental set-up and systematic dissection of how different promoters decode transcription factor dynamics*
(A) Microfluidic set-up. Medium with or without the PKA^{as} inhibitor 1-NM-PP1 is delivered to five computer-controlled 3-way electrovalves. These control when and for how long each microfluidic channel receives 1-NM-PP1. Simultaneously, a 63x microscope objective moves between each microfluidic channel and records Msn2-mCherry translocation dynamics and gene expression in single cells.
(B) An example of an experiment (*DDR2*). Cells were treated with eight 5 min pulses of 1-NM-PP1 with 5 min intervals (red line: input Msn2-mCherry) and Msn2-mCherry translocation dynamics were monitored in single diploid cells (black dots: raw data). Gene expression was monitored with fast maturing dual CFP (SCFP3A) and YFP (mCitrineV163A) reporters.
(C) Systematic dissection of how different promoters decode transcription factor dynamics. Each row corresponds to a specific Msn2-mCherry input (left, in red) and the corresponding gene expression response for each of the seven promoters is shown on the corresponding rows on the right. The gene expression responses for each promoter are internally normalized to their maximal expression level. Each row is the per-cell average of ∼200-600 cells from at least three biological replicates. The promoter classification is derived from their clustering (Figure 2.2B). The full data sets are given in Appendix Figure A.1D. Source data for this figure is available from the *Molecular Systems Biology* website.

Although these are phenomenological variables rather than biochemically well-defined promoter states, we interpret these as unbound, bound, and active: initially, the promoter is unbound and the rate with which Msn2 binds the promoter is assumed to be proportional to the nuclear concentration of Msn2. Once bound, recruitment of factors to the promoter ($P_{\text{bound}} \rightarrow P_{\text{active}}$) is assumed to be proportional to the equilibrium fraction of Msn2 bound to the promoter and modeled as a Hill function. To account for the observation that transcription ceases when Msn2 exits the nucleus, we also model transcription as a Hill function (a full discussion of the model is given in Appendix A.2.12).

To extract quantitative information, we identified the parameter set (green parameters in Figure 2.2A) that gave the best overall fit to the full 30-experiment data set (Appendix Figures A.2-A.5) for each promoter. Global parameters (purple parameters in Figure 2.2A) were experimentally determined and found not to differ between promoters (see Appendix A.2.14). Using the model and the fitted parameters, we calculated the promoter activation timescale (time required to reach the half-maximal P_{active} level) and amplitude threshold (amplitude required to reach the half-maximal P_{active} level at steady state) for each promoter. We clustered the promoters along these two axes and observed classes of behavior (Figure 2.2B). *HXK1*, *DCS2*, and *DDR2* belong to one promoter class, which we call Low amplitude threshold, Fast promoters (LF promoters, blue): these promoters activate within a few minutes, which explains why they respond strongly to short duration oscillatory input (Figure 2.1C). Due to their low amplitude threshold, LF promoters show strong gene expression responses even to low amplitude input and show saturation at high amplitude input. At the other extreme, *SIP18*, *ALD3*, and *TKL2* belong to a class we call High amplitude threshold, Slow promoters (HS promoters, red): due to their long activation delay ($\sim$25 min), they filter out short duration input including short duration oscillatory input (Figure

2.1C). Similarly, due to their high amplitude threshold, low amplitude input is filtered out regardless of the duration. Finally, *RTN2* shows intermediate behavior: *RTN2* filters out low amplitude input like the HS promoters (Figure 2.1C) and has a promoter activation timescale (∼10 min) in between that of the LF and HS promoters, but more similar to the LF promoters. The response of *RTN2* to short oscillatory input is similar to *DDR2* (Figure 2.1C). Hence, *RTN2* exhibits much faster activation than *TKL2* and *ALD3*, but a higher amplitude threshold: this shows that amplitude threshold and promoter activation timescale can be at least partially decoupled. We therefore predict that natural promoters will show a continuum in response behavior and span the entire space of Figure 2B, including all four corners.

2.3.4 Quantitative Analysis of signal processing by LF and HS promoters

To illustrate how the HS and LF promoter classes process transcription factor signals, we quantitatively analyzed *SIP18* (HS) and *DCS2* (LF). In response to duration modulation (Figure 2.2C, dots: raw data; lines: model simulations), *SIP18* expression increases in a nonlinear, convex manner due to its slow promoter activation and shows a duration threshold below which no gene expression is seen. *DCS2* expression, on the other hand, increases linearly with duration due to its fast activation and shows no threshold. The highly convex scaling of *SIP18* in response to amplitude modulation (Figure 2.2D) shows how sensitive its expression is to the amplitude: a ∼25% increase in amplitude can more than double gene expression output. In contrast, *DCS2* shows concave scaling and begins to show saturation even at the half-maximal amplitude. When expression is plotted as a function of the Msn2 AUC (Msn2 area under the curve, $\int_0^\infty [\mathrm{Msn2}(t)]\,\mathrm{d}t$), we see a clear threshold (ca. $2 \cdot 10^4$

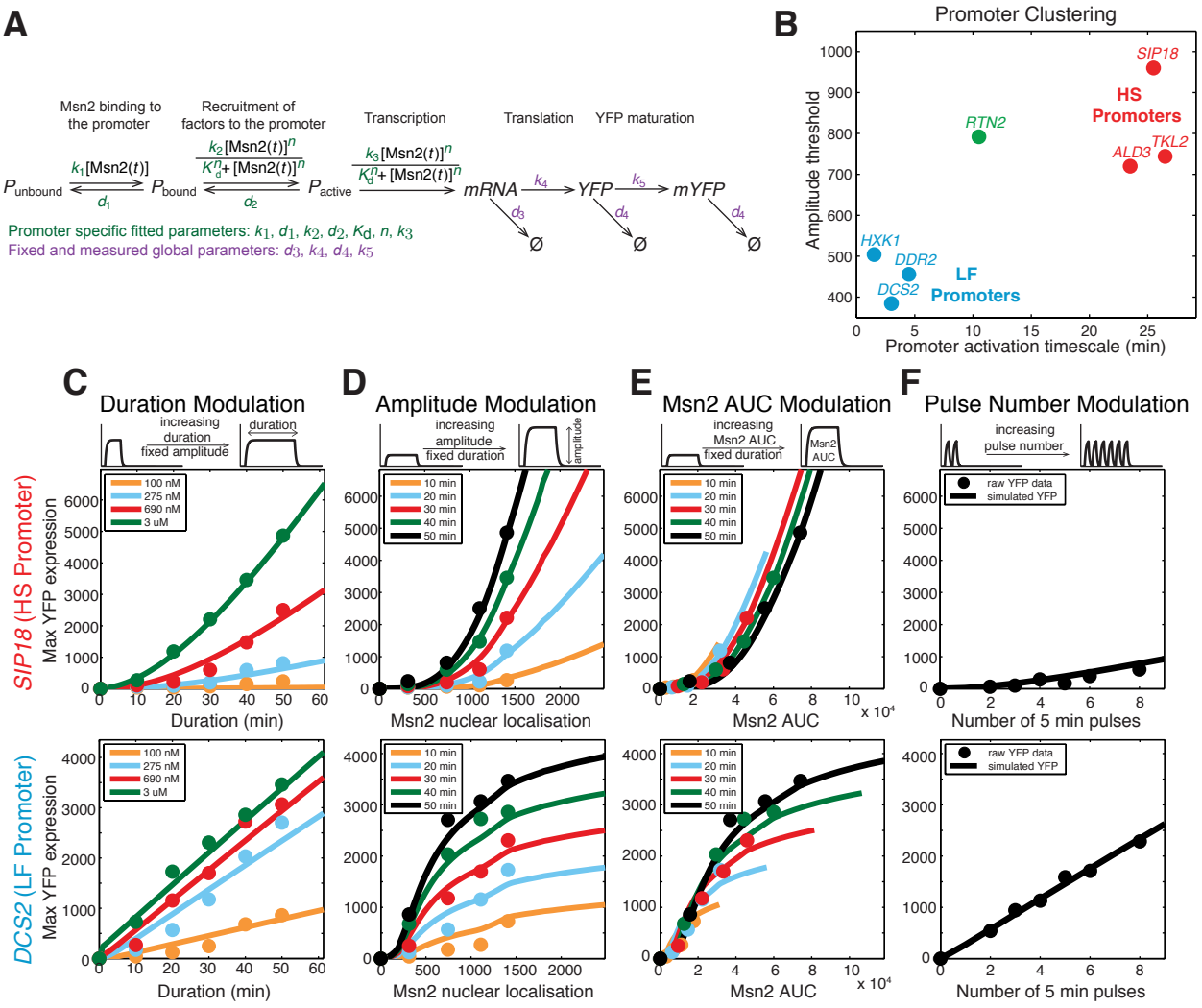

Figure 2.2: *A mathematical model for transcription factor-activated gene expression allows clustering of promoters and detailed quantitative characterization*
(A) A mathematical model (defined by the differential equations in section 2.5 (Materials and methods)). Promoter-specific parameters shown in green were obtained by least-squares global fitting to the full data set (Appendix Figure 2.1D) using the Msn2-mCherry traces as input and the YFP traces as output. Parameters shown in purple are the same for all promoters and were experimentally determined.
(B) Clustering of promoters. The amplitude threshold is defined as the nuclear Msn2-mCherry level required to reach half the P_{active} level obtained at 3 µM 1-NM-PP1 (which corresponds to the maximal nuclear Msn2-mCherry level) and obtained by mathematical simulations using the model in **(A)**. The promoter activation timescale is defined as the time (min) it takes to reach half the steady-state P_{active} level at 690 nM 1-NM-PP1 and was also obtained from model simulations.
(C-F) Illustration of how *SIP18* and *DCS2* respond to duration, amplitude, Msn2 AUC, and pulse number modulation. In all cases, the dots represent raw data (the maximum of the average YFP time trace under the specific conditions) and the curves (lines) were obtained from mathematical simulations using the best-fit parameters and the model in **(A)**. In **(C)**, 100 nM, 275 nM, 690 nM, and 3 µM are 1-NM-PP1 concentrations corresponding to ca. 25, 50, 75, and 100% Msn2-mCherry nuclear localization. In **(D, E)**, the duration was fixed to 10, 20, 30, 40, or 50 min and the amplitude increased until 2500 AU. In **(E)**, Msn2 AUC is defined as the time-integrated nuclear localization, that is, the area under the curve. In **(F)**, both the pulse duration and the pulse interval are 5 min. See Appendix Figures A.2-A.5 for full comparisons of model fitting to raw data and Appendix Table A.2 for parameters. Source data for this figure is available from the *Molecular Systems Biology* website.

Msn2 AUC, Figure 2.2E) below which *SIP18* filters out all input, whereas *DCS2* shows no such threshold. Instead, *DCS2* expression is simply proportional to the Msn2 AUC until saturation — after saturation *DCS2* expression is no longer sensitive to increasing amplitude. Thus, even for single pulse input, natural Msn2 target promoters can act as sophisticated signal processing modules with distinct decoding abilities.

Finally, in response to pulse number modulation, *DCS2* expression is simply proportional to the number of pulses (Figure 2.2F) — this is because promoter activation and deactivation are so fast that no memory effects are observed between the pulses (Hao & OShea, 2012). *SIP18*, on the other hand, displays such slow promoter activation kinetics that oscillatory input is largely filtered out regardless of the pulse number.

2.3.5 Control of transcription factor dynamics enables differential gene expression

Having established that different promoter classes decode transcription factor dynamics differently, we next investigated whether this would allow differential gene expression. Using the model (Figure 2.2A), we systematically simulated gene expression for different input dynamics (duration, amplitude, pulse number, and pulse interval) for *SIP18* and *DCS2*. The model predicts that strong induction of *DCS2* without a significant induction of *SIP18* can be achieved by using short, low frequency oscillatory input (Figure 2.3A, Condition A). Likewise, the model predicts that differential expression of *SIP18* over *DCS2* can be achieved by using a single sustained, high amplitude pulse (Figure 2.3B, Condition B). We tested these model predictions by measuring gene expression in response to these two conditions and find that the model could accurately predict gene expression responses to conditions upon which it had not been trained (Figure 2.3). This demonstrates that significant differential gene

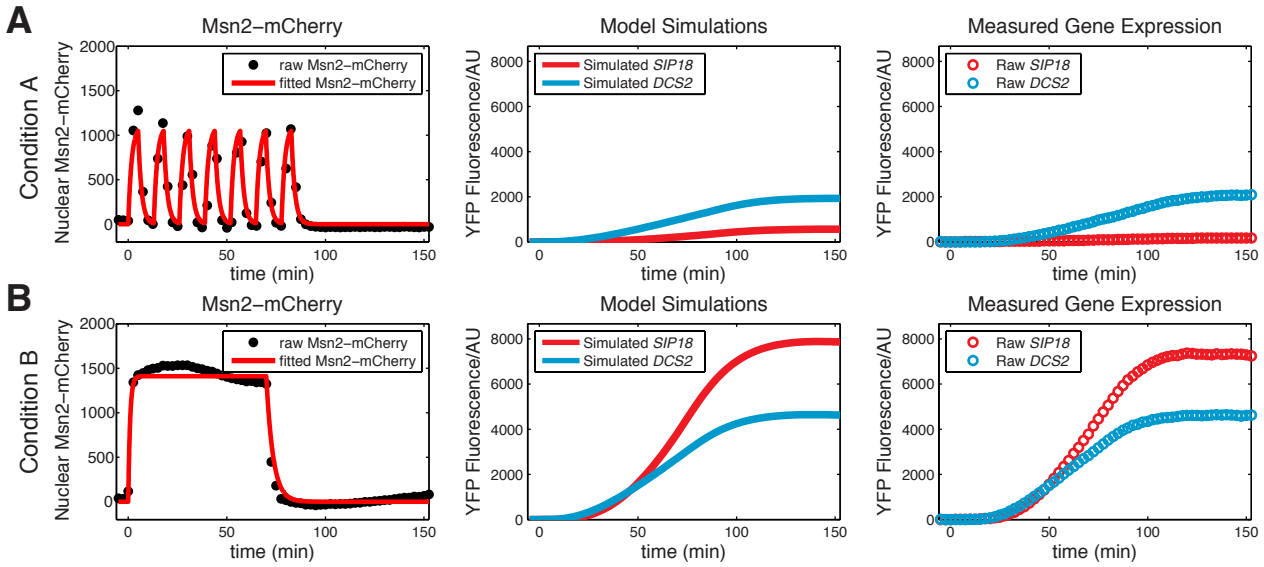

Figure 2.3: *Control of transcription factor dynamics allows differential gene expression*
(A, B) The left column shows the Msn2-mCherry input; the middle column shows the predicted gene expression responses to that Msn2-mCherry input (simulated using the model in Figure 2.2A) and the right column shows the raw experimentally measured gene expression data for the *SIP18* and *DCS2* reporters (per-cell average of ∼300-500 cells). Condition A: seven 5 min pulses separated by 7.95 min at 690 nM 1-NM-PP1. Condition B: a single 70-min pulse at 3 μM 1-NM-PP1. See Appendix Figure A.6 for raw single-cell data. Source data for this figure is available from the *Molecular Systems Biology* website.

expression between LF and HS promoters at an absolute level is possible just by controlling transcription factor dynamics. Thus, the cell can exploit this mechanism to encode multiple, distinct gene expression programs in the translocation dynamics of a single transcription factor.

2.3.6 Noise in gene expression differs markedly for different promoter classes and depends on Msn2 dynamics

Having analyzed how gene expression responses depend on Msn2 input at the population level, we next investigated single-cell behavior. Since the dual CFP and YFP reporters share the same cellular environment, the degree to which they correlate allows us to discern two sources of cell-to-cell variability (Elowitz *et al.*, 2002): variability caused by the shared environment, such as differences in the number of Msn2 molecules or ribosomes between cells, which affect both CFP and YFP equally (extrinsic noise); and the remaining intrinsic

variability that is not accounted for by the shared environment, which may stem from factors such as stochastic binding events at individual promoters (intrinsic noise) (Hilfinger & Paulsson, 2011).

We first investigated how total (Figure 2.4A) and intrinsic (Figure 2.4B) noise ($\frac{\sigma^2}{\mu^2}$) scale with transcription factor input (Msn2 AUC) for all experiments for all seven promoters (each dot in Figure 2.4A and B corresponds to the gene expression noise for a given Msn2 input for a single promoter (colored by class)). Although noise generally decreases with increasing Msn2 AUC, we observed substantial differences in total and intrinsic noise between the promoter classes: for a given Msn2 AUC, noise in gene expression was significantly higher for the slow (HS) promoters than the fast (LF) promoters. Since the Msn2 input, mRNA transcript (coding region and 3'-UTR) and protein are the same for all promoters, differences in intrinsic noise between promoters should primarily originate from promoter transitions and transcription. Therefore, different promoter classes exhibit inherently different levels of noise in gene expression. For example, even when *SIP18* (HS) expression robustly exceeds *DCS2* (LF) expression at the population level (Figure 2.3B), *SIP18* still exhibits more than two-fold higher noise than *DCS2* (Appendix Figure A.6B). To determine whether noise in gene expression depends on transcription factor dynamics, we compared the total noise for a single 40-min pulse with eight 5 min oscillatory pulses (Figure 2.4C) such that the Msn2 AUC, total duration, and amplitude were constant. We find that noise in gene expression is higher in response to oscillatory input than in response to a single pulse. Furthermore, the extent to which oscillatory input results in higher noise seems to depend on the promoter class: HS promoters are much noisier in general, but also show greater differences between oscillatory input and single pulse input. This contrasts with a recent theoretical study (Tostevin *et al.*, 2012), which found that at steady state, oscillatory input could lead to lower noise

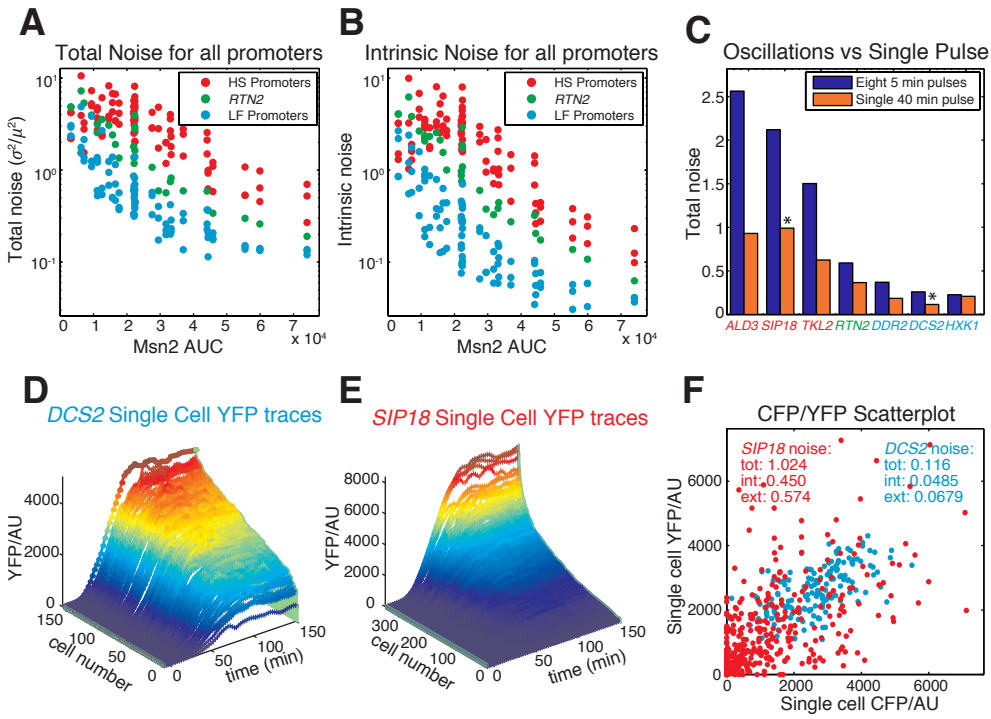

Figure 2.4: *Noise in gene expression depends on the promoter class and on transcription factor dynamics*
(A, B) Total noise **(A)** ($\frac{\sigma^2}{\mu^2}$) and intrinsic **(B)** noise (defined in section 2.5 (Materials and methods)) is plotted against the Msn2 AUC (red, green, and blue denotes HS (*SIP18*, *ALD3* and *TKL2*), *RTN2*, and LF (*DDR2*, *DCS2*, and *HXK1*) promoters, respectively). Each dot corresponds to the noise (mean noise across time points after gene expression has reached a plateau) for a single experiment: that is, a single Msn2 input for a single promoter.
(C) transcription factor dynamics and noise. The total noise for a 40-min pulse at 690 nM 1-NM-PP1 (purple) is compared with the total noise for eight pulses with 5 min duration and 5 min interval at 690 nM 1-NM-PP1 (orange) such that the total Msn2 AUC is constant.
(D, E) Single-cell YFP time traces for *DCS2* and *SIP18* in response to a single 40-min pulse at 690 nM 1-NM-PP1 corresponding to the orange bar graphs for *DCS2* and *SIP18* in **(C)** that are highlighted with an asterisk (*). The traces show raw single-cell YFP data (smoothed by a 3-point moving average).
(F) YFP/CFP scatterplot. Each dot corresponds to the raw CFP (x-axis) and YFP (y-axis) fluorescence in a single cell at 150 min from **(D)** and **(E)**. *SIP18*: red dots. *DCS2*: blue dots. Spread along the diagonal is due to extrinsic noise effects and spread orthogonal to the diagonal is due to intrinsic noise effects. See also Appendix Figure A.7 for examples of bimodal gene expression, noise versus mean, extrinsic noise and additional plots. Source data for this figure is available from the *Molecular Systems Biology* website.

than constant input. However, this discrepancy is likely due to differences in comparisons: that study used a much higher amplitude for oscillatory input than for constant input such that the promoter activation timescale was shorter for oscillatory input (see also Appendix A.2.15).

Notably, the only promoter that shows a negligible noise difference between oscillatory and single pulse input is *HXK1*, which also has the fastest activation timescale (∼1.3 min). In fact, the noise (Figure 2.4C, orange bars) is significantly correlated with the promoter activation timescale ($\rho = 0.919$; $P < 0.005$; Pearson's correlation), such that the slower the

promoter activation, the higher the noise.

Single-cell time traces (Figure 2.4D and E) and a CFP/YFP scatterplot (Figure 2.4F) for *DCS2* and *SIP18* illustrate how substantial the noise differences are between the HS and LF promoters. We find that both intrinsic and extrinsic noise contribute significantly to the total noise. For *DCS2*, gene expression is remarkably reliable with low variation between cells. For *SIP18*, however, we observe bimodal gene expression: some cells induce very strongly, whereas a large proportion of cells show no expression at all. In general, we observe many cases of bimodal gene expression for the HS promoters when the signal is close to the threshold (Appendix Figure A.7H and J), which further underscores how noisy these promoters are.

Taken together, our results reveal that oscillatory transcription factor input leads to higher noise in gene expression and that noise is significantly correlated with the promoter activation timescale. That HS promoters suffer from significantly higher total and intrinsic noise than LF promoters furthermore implies an inherent trade-off: employing HS and LF promoters enables differential gene expression by controlling transcription factor dynamics; but for the HS promoter, high noise means that the information encoded in transcription factor dynamics is decoded with low fidelity.

2.3.7 Encoding four gene expression programs in the dynamics of a single transcription factor

Previously, we showed that natural promoters differ in their amplitude threshold and promoter activation timescale and, importantly, that these two properties can be decoupled (Figure 2.2B). On the basis of these observations, four promoter classes exist in theory: promoters can have either a low or a high amplitude threshold (H or L) and exhibit either fast

or slow activation (F or S). To theoretically investigate whether differential expression of all four classes is possible by controlling transcription factor dynamics, we consider the simplest formulation of the deterministic model (Figure 2.5A) that can capture differences in both the amplitude threshold and promoter activation timescales of the full model (Figure 2.2A). We quantify gene expression as the mRNA AUC (Figure 2.5B), which will be proportional to the protein level after it has reached a plateau since the mRNA lifetime is much shorter than the protein lifetime.

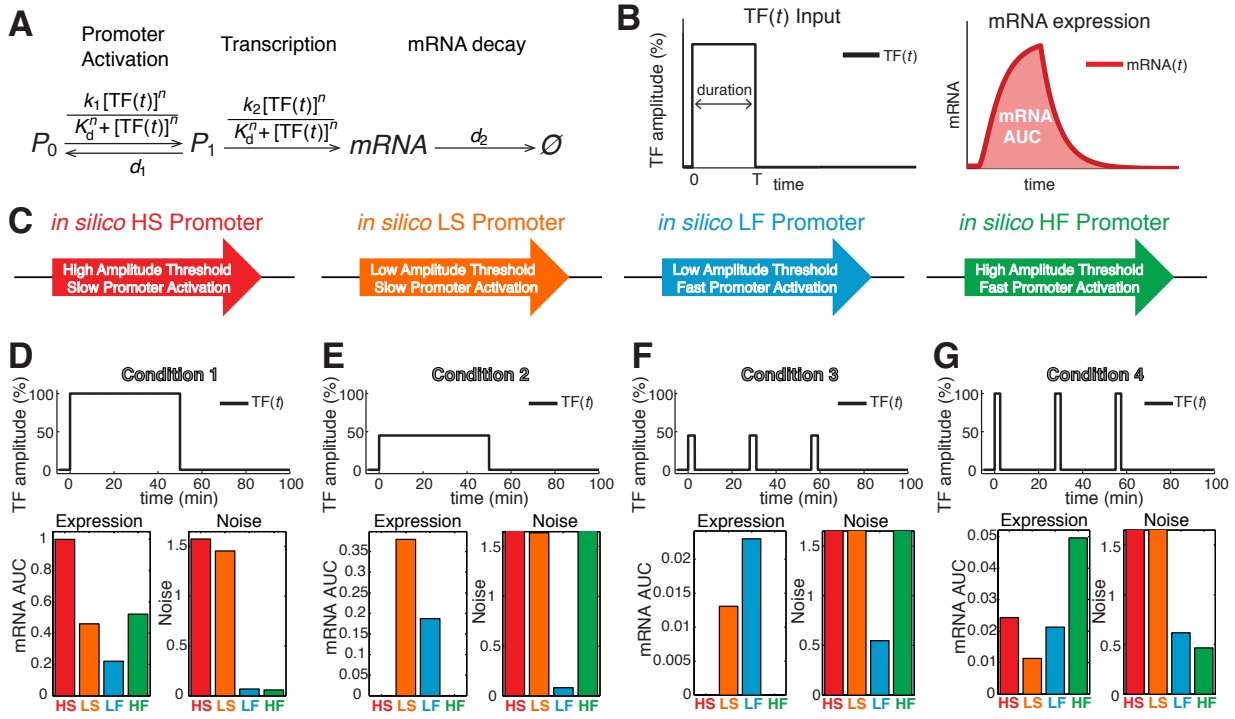

Figure 2.5: *Encoding four gene expression programs in the dynamics of a single transcription factor*
(A) A simplified model.
(B) transcription factor input (left) and gene expression output (mRNA AUC, right) for the model in **(A)**. Nuclear translocation is modeled as a step function and gene expression is quantified as the mRNA AUC.
(C) Analysis of *in silico* promoters. Four hypothetical promoters were generated *in silico* and their sensitivity to transcription factor dynamics analyzed. Parameters were chosen such that the timescale of the promoter transition for the slow and fast promoters were on as same order as *SIP18* (∼30 min) and *HXK1* (∼1 min), respectively. The following parameters were used: $k_1 = d_1 = 0.0167$ (HS, LS), $k_1 = d_1 = 0.5$ (HF, LF), $K_d = 75, n = 8$ (HS, HF), $K_d = 20, n = 2.5$ (HS, HF), $k_2 = 30$ (HS), $k_2 = 12$ (LS), $k_2 = 3$ (LF), $k_2 = 8$ (HF), $d_2 = 0.12\text{min}^{-1}$(for all).
(D-G) Differential gene expression and noise. Four conditions were chosen such that each of the four promoters would show higher gene expression (mRNA AUC, left bar graph) than the other three under one condition. The gene expression values were globally normalized to one, such that the differences shown are absolute and not just relative. The mRNA AUC noise ($\frac{\sigma^2}{\mu^2}$, right bar graph in **(D-G)**) was obtained from exact discrete-time stochastic simulations (10^5 iterations) of the model in **(A)** for each condition and promoter. The noise y-axis maximum was set to 1.65 in all cases because under multiple conditions (e.g., Condition 2 and 3 for HS), the gene expression is essentially zero and the noise essentially infinite. Full surface plots showing how gene expression and noise scale with transcription factor amplitude, nuclear duration, pulse duration and interval can be found in Appendix Figure A.8. A discussion of the model and its solution is given in Appendix A.2.16.

Next, we generate representative promoters for each of the four classes *in silico* that differ only in their amplitude threshold and promoter activation timescale (Figure 2.5C). We analytically solve the model for the mRNA AUC (see Appendix A.2.16) and then systematically investigate how gene expression depends on duration, amplitude, pulse interval, and pulse duration (Appendix Figure A.8A-C). By searching this space, we identify four conditions where differential expression of the four promoters at an absolute level is possible. The HS promoter dominates in response to a single sustained, high-amplitude pulse (Figure 2.5D, left), the LS promoter dominates in response to a single sustained, low-amplitude pulse (Figure 2.5E), the LF promoter dominates in response to low amplitude, low frequency oscillations (Figure 2.5F), and finally, the HF promoter dominates in response to high amplitude, low frequency oscillations (Figure 2.5G). Thus, it is possible to encode four distinct gene expression programs in the translocation dynamics of a single transcription factor.

2.3.8 The promoter activation timescale controls the noise level

Experimentally, we observed a strong positive correlation between noise and the promoter activation timescale. Consistent with this result, in the case of the four *in silico* promoters (Figure 2.5D-G, right and Appendix Figure A.8D-F), the LF promoter always exhibits lower noise than the LS promoter and the HF promoter always exhibits lower noise than the HS promoter. Furthermore, the noise levels we observe for the slow promoters (Figure 2.4) are substantially higher than those typically seen in steady-state studies (Bar-Even *et al.*, 2006; Newman *et al.*, 2006). To understand why, consider a fast (HF or LF) and a slow (LS or HS) promoter exposed to a single, transient pulse: for all but the briefest pulses, all fast promoters in a population will activate and approach a new steady state, whereas for a slow promoter a substantial fraction will not even activate in response to a sustained pulse (50

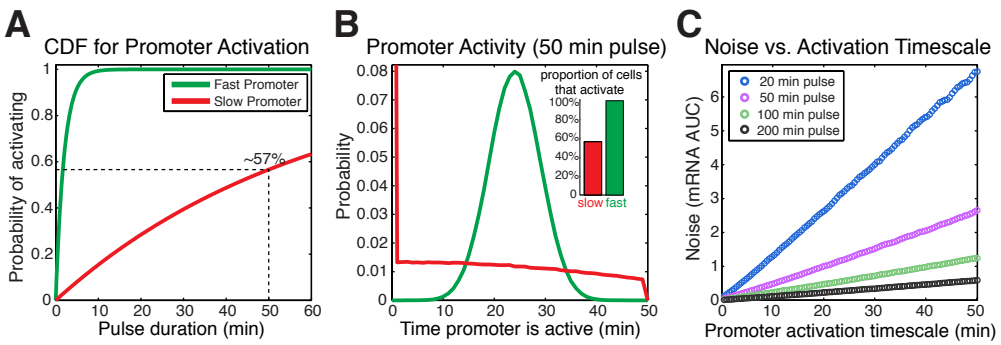

Figure 2.6: *Gene expression noise depends on the promoter activation timescale*
(A) Cumulative distribution function (CDF) versus pulse length. The CDF describes the proportion of cells that activate at least once during a pulse. Parameters: fast promoter ($k_1 = d_1 = 0.5$); slow promoter ($k_1 = d_1 = 0.0167$).
(B) Promoter activity histogram. For a 50-min pulse, the histogram shows the variability in the amount of time the fast (green) and slow (red) promoters are active. For the slow promoter, 43% of cells fail to activate at all. Simulated using the Gillespie algorithm (10^6 iterations).
(C) Noise versus activation timescale. Using the model in (Figure 2.5A) and $k_1 = d_1 = [0.0098; 1.00], K_{\mathrm{d}} = 20, n = 2.5, k2 =$ from 3 and upwards, $d_2 = 0.12$ min^{-1}. Each data point is from discrete time stochastic simulations ($5 \cdot 10^4$ iterations). k_2 was chosen such that, for a given pulse duration, the mean expression is constant for all activation timescales.

min, Figure 2.6A). During a 50-min pulse, the fast promoter will frequently switch between the ON and the OFF states, such that although there is variability in the amount of time it is active during the pulse, the variability between cells is relatively modest (Figure 2.6B): all promoters are active for at least 10 min, but none for >40 min. For the slow promoter, however, 43% of cells fail to activate at all (Figure 2.6B); and among the fraction that do activate, because of the slow switching frequency, the variability in the amount of time the promoter is active is huge (Figure 2.6B). This explains why slow promoter kinetics leads to such high noise.

This is also consistent with many previous steady-state studies that have shown that genes with high transcriptional burst frequency but small burst sizes exhibit lower noise than genes with low burst frequency but large burst sizes (Raj & van Oudenaarden, 2008; Hornung *et al.*, 2012; Lionnet & Singer, 2012; Dadiani *et al.*, 2013). Comparing promoters with the same mean expression, but different kinetics, we find that noise scales strongly with the activation timescale (Figure 2.6C). But as the pulse duration approaches that of two cell divisions (∼200 min, steady-state behavior), the effect of the promoter activation timescale

on noise is greatly reduced. Therefore, whereas at steady state the effects of promoter kinetics (burst frequency) are modest because of averaging due to the long lifetimes of proteins, the consequences are dramatic when the pulse is transient (Figure 2.6C). Thus, the promoter activation timescale controls noise in gene expression and this underscores the importance of promoter kinetics when considering transient transcription factor dynamics.

2.3.9 Slower promoter activation leads to greater noise in gene expression

A key prediction of our theory is that slowing down promoter activation will lead to higher noise. Since transcription factors generally cannot bind to binding sites in the promoter that are occupied by nucleosomes (Lam *et al.*, 2008; Zhou & OShea, 2011) and nucleosome removal often accompanies gene induction (Shivaswamy *et al.*, 2008; Bai *et al.*, 2010), we hypothesized that interfering with chromatin remodeling would slow down promoter activation. To test this, we generated strains lacking either the SWI/SNF (*snf6*Δ) or SAGA (*gcn5*Δ) chromatin remodeling complexes (Raser & OShea, 2004) and containing the *SIP18* and *HXK1* expression reporters.

For the *SIP18* reporter, both complexes are required for induction (Appendix Figure A.9C). For the SWI/SNF and SAGA mutants of the *HXK1* reporter strain, the expression level is not substantially affected so we repeated all 30 experiments (Appendix Figure A.9A) and fit the model (Figure 2.2A) to the data to obtain parameters from which we inferred the amplitude threshold and promoter activation timescale (Figure 2.7A). Both mutants showed slower promoter activation (Figure 2.7A) and higher noise (Figure 2.7B-D) consistent with our previous observations (Figure 2.4) and theoretical predictions (Figures 2.5 and 2.6). Furthermore, as observed for the natural promoters (Figure 2.4C), the slower *HXK1*

mutants now show higher noise in response to oscillatory than single pulse input, whereas the faster WT strain does not (Figure 2.7D). Overall, we conclude that the promoter activation timescale is a key determinant of noise in gene expression.

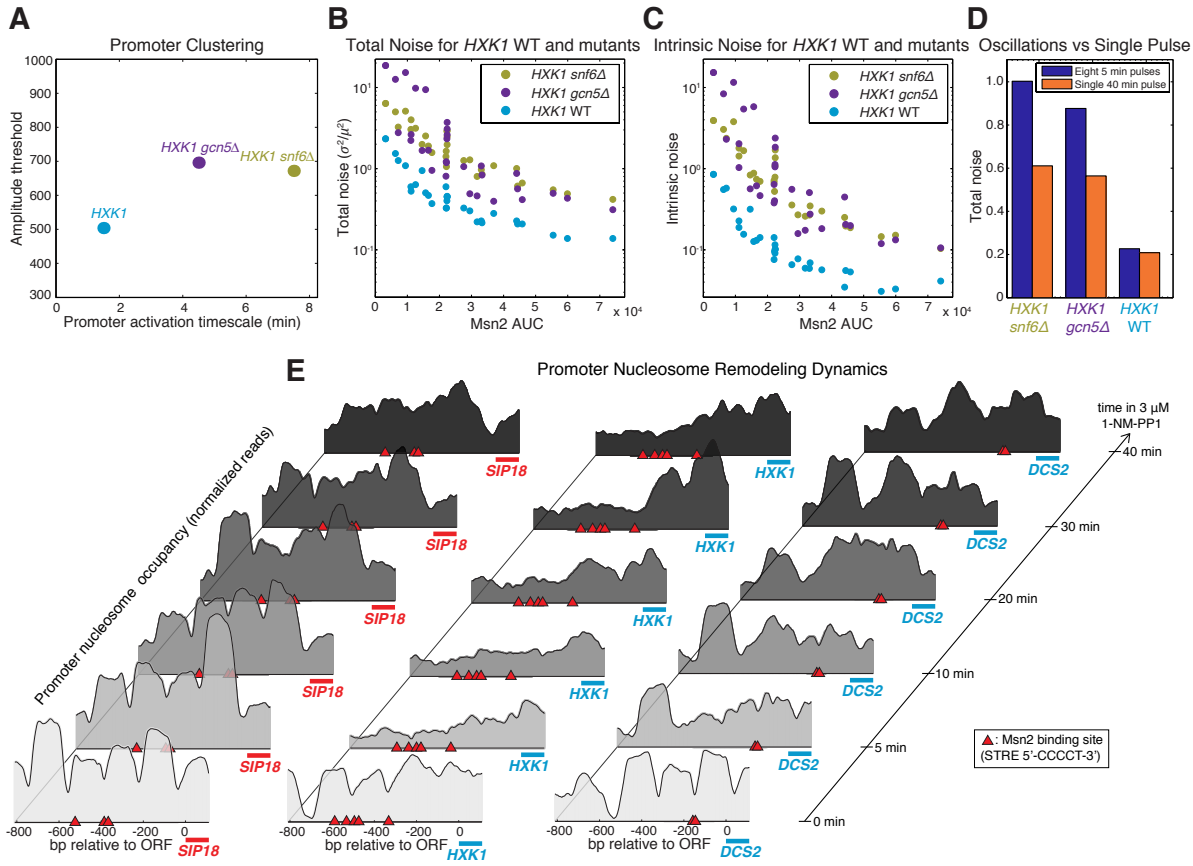

Figure 2.7: *Slower promoter activation kinetics leads to greater noise in gene expression*
(A) Promoter clustering of chromatin remodeling complex mutants (SWI/SNF (*snf6*Δ) and SAGA (*gcn5*Δ)). All 30 experiments (Appendix Figure A.9A) were repeated in biological triplicate for the mutant strains and their amplitude threshold and promoter activation timescale obtained from fitting to the deterministic model in (Figure 2.2A).
(B, C) Total **(B)** and intrinsic noise **(C)** *HXK1* WT, *HXK1 snf6*Δ and *HXK1 gcn5*Δ strains as a function of Msn2 AUC.
(D) The total noise for a 40-min pulse at 690 nM 1-NM-PP1 (purple) is compared with the total noise for eight pulses with 5 min duration and interval at 690 nM 1-NM-PP1 (orange) such that the total Msn2 AUC is constant.
(E) Nucleosome remodeling dynamics. Promoter nucleosome occupancy in response to 3 μM 1-NM-PP1 was profiled using MNase-Seq (see Appendix A.2.5). See also Appendix Figure A.9 for the full data sets and additional nucleosome data. Source data for this figure is available from the *Molecular Systems Biology* website.

2.3.10 Nucleosome remodeling dynamics correlate with promoter activation dynamics

The observation that chromatin remodeling complex mutants slow down promoter activation led us to hypothesize that nucleosome remodeling might be rate-limiting for promoter activation. To test this, we used micrococcal nuclease digestion coupled with high-throughput sequencing (MNase-Seq) to follow nucleosome remodeling dynamics in response to Msn2 activation (Figure 2.7E). We find that whereas all promoters have clearly positioned nucleosomes initially, nucleosome positioning collapses within 5 min for the fast *HXK1* and *DCS2* promoters (a hallmark of transcriptional activation; Zhou & OShea, 2011). In contrast, slow promoters such as *SIP18* have higher nucleosome occupancy initially and the nucleosomes remain clearly positioned until the 20-30 min time points which is very similar to the activation timescale we inferred using modeling (∼25 min, Figure 2.2B). The observed correlation between nucleosome remodeling and promoter activation is consistent with a model where the promoter activation timescale is controlled by the position and stability of promoter nucleosomes.

2.4 Discussion

2.4.1 Promoter amplitude threshold and activation timescale control how transcription factor dynamics are decoded

The expanding list of transcription factors that exhibit complicated dose- and signal-dependent dynamics prompted us to systematically investigate the quantitative principles that govern how gene promoters decode such dynamics. We demonstrate that the amplitude

threshold and promoter activation timescale govern how transcription factor dynamics are decoded. But at the mechanistic level, what determines these two properties? From previous steady-state studies, it appears that the amplitude threshold depends at least in part on the binding affinity of the promoter for the transcription factor; that is, the affinity and number of transcription factor binding sites and chromatin structure (Lam *et al.*, 2008; Sharon *et al.*, 2012). This is also consistent with our observations: LF promoters tend to have multiple clustered Msn2 binding sites, whereas *RTN2* and HS promoters tend to have only one or two isolated sites (Appendix Figure A.9D). Much less is known about what determines the promoter activation timescale. We show here that the model-inferred promoter activation timescales largely match the observed nucleosome remodeling timescales. Furthermore, we show that the SWI/SNF and SAGA chromatin remodeling complexes are required for the induction of *SIP18* and that deleting them significantly slows down activation of the *HXK1* promoter (Figure 2.7). Taken together, a coarse grained model emerges where the amplitude threshold is related to transcription factor binding sites and the promoter activation timescale to nucleosome organization. Detailed mechanistic studies are now required to elucidate the details of what determines the amplitude threshold and promoter activation timescale at individual promoters. Such studies should be greatly facilitated by the high-throughput technologies developed here.

2.4.2 Modulation of transcription factor dynamics enables control of gene expression

Using mathematical modeling, we predict and experimentally verify conditions where differential expression of two promoters is possible at an absolute level (Figure 2.3), providing evidence that transcription factor dynamics is an important mechanism for control of gene

expression. We extend this result to four promoter classes by showing theoretically (Figure 2.5D-G) how absolute differential expression of the HS, LS, LF, and HF promoter classes can be achieved by controlling only transcription factor dynamics. Mammalian transcription factors appear to be constrained in the number of distinct binding sites that can be evolved (Berger *et al.*, 2008). Thus, in addition to combinatorial regulation, an economical way of overcoming this limitation might be for the cell to encode multiple gene expression programs in the dynamics of a single transcription factor rather than evolving multiple transcription factors with distinct binding site specificities.

2.4.3 Relationship between promoter class and stress-specific gene function

Msn2 dynamics qualitatively differ in response to glucose starvation, osmotic and oxidative stress (Hao & O'Shea, 2012). Although the genes in this study were chosen because their transcriptional response is strong and Msn2 specific, is there a relationship between gene function and promoter class? For two of the genes we studied, based on the gene function, we can rationalize why a given gene might belong to a given class. For example, the HS promoter *SIP18* will filter out the brief pulses of nuclear Msn2 during glucose starvation, and will induce only during prolonged nuclear accumulation of Msn2 that occurs in oxidative stress, where the protein appears to protect against reactive oxygen species (Rodriguez-Porrata *et al.*, 2012). Conversely, the fast LF promoter *HXK1* responds strongly to brief pulses and will induce strongly during glucose starvation, where the protein catalyzes phosphorylation of glucose and facilitates growth on non-fermentable carbon sources (Herrero *et al.*, 1995). For several of the other genes, the function or stress requirement is unclear. Thus, while the correlation between gene function and promoter class is intuitive for *SIP18* and *HXK1*, a

larger sample size will be necessary to determine whether this correlation is general rather than anecdotal.

Using our synthetic PKA^{as} system, we studied the causal input-output relationship between artificially controlled Msn2 dynamics and the promoter-controlled gene expression response. However, in response to natural stresses, factors other than Msn2 will be activated and the regulation may be partly post-transcriptional. Thus, while we show that exploiting the four promoter classes is sufficient to encode four gene expression programs in the dynamics of a single transcription factor, complementary approaches will be required to determine how much of the physiological regulation for natural stresses is promoter class controlled and how much is post-transcriptional or Msn2 independent.

2.4.4 A trade-off between noise and control of gene expression

Previous studies on transcription factor dynamics did not consider gene expression noise (Cai *et al.*, 2008; Hao & O'Shea, 2012). Here we provide a link between transcription factor dynamics and control of noise in gene expression: for constant amplitude, total duration, and transcription factor AUC, oscillatory input gives rise to higher noise in gene expression than a single pulse. This shows that noise depends on transcription factor dynamics and that the function of transcription factor oscillations is unlikely to be the reduction of noise in gene expression (Tostevin *et al.*, 2012). Instead, given that low frequency oscillations enables the cell to induce LF and HF promoters without inducing LS and HS promoters, it is likely that this advantage of low frequency oscillations overrides the cost of higher noise in gene expression.

Furthermore, noise also depends on the promoter class — the slower the promoter activation timescale, the greater the noise in gene expression. These promoter class-specific

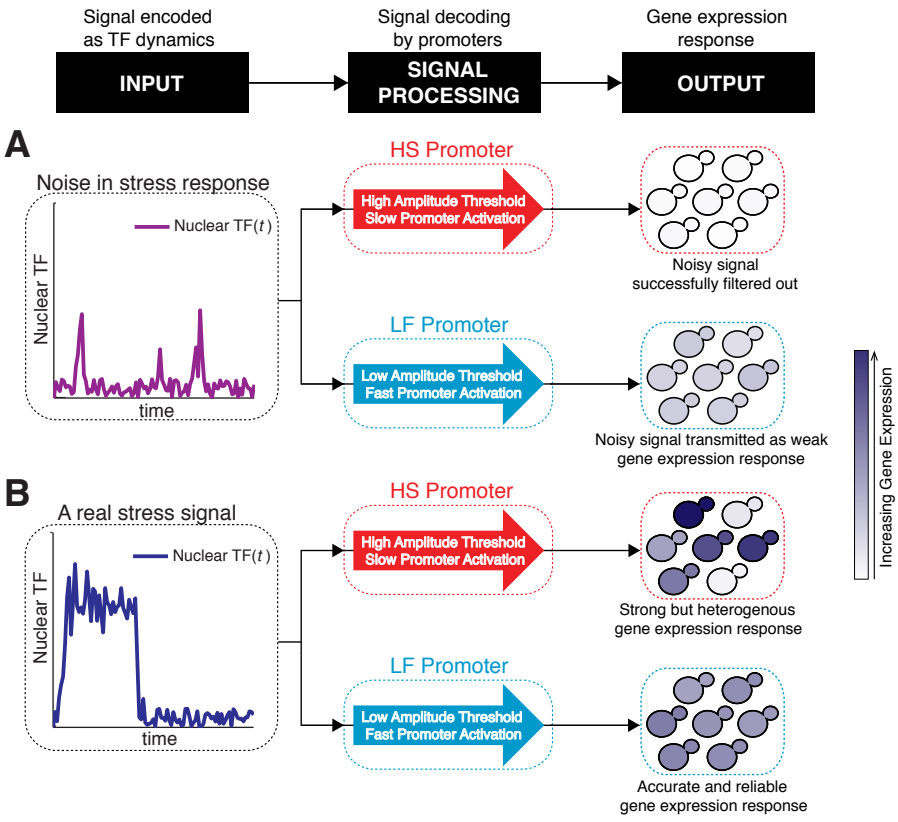

Figure 2.8: *A trade-off between noise and control of gene expression*
(A) Natural variation along the baseline in a stress response signal transduction pathway can lead to spurious activation of a transcription factor (signaling noise). The high-threshold HS promoter filters out such noise, whereas the fast LF promoter transmits such upstream noise as a weak gene expression response.
(B) A real stress signal is transmitted for decoding by both promoters. The LF promoter is inherently less noisy and yields a strong and accurate gene expression response. The HS promoter is inherently noisy and yields a strong, but heterogenous gene expression response.

noise and decoding properties highlight a key trade-off for the cell (Figure 2.8). Any signal transduction pathway has to distinguish real signals from noise and transmit the intensity of the signal. This invariably carries the risk of false signals being transmitted. HS promoters have filtering abilities when decoding signals and reliably filter out such noise up to a threshold. In contrast, LF promoters are activated immediately and transmit such signaling noise (Figure 2.8A). Conversely, HS promoters respond strongly to a real signal, but with high gene expression noise. LF promoters, on the other hand, are inherently less noisy and respond reliably with low noise (Figure 2.8B). Thus, there is a clear trade-off between promoters having filtering abilities and low noise in gene expression. This further reveals that the cell faces an important trade-off between encoding multiple gene expression programs in

transcription factor dynamics and having them decoded with high fidelity (low noise): with four promoter classes, cells can encode up to four distinct gene expression programs in the dynamics of a single transcription factor. Yet, the two slow promoter classes (LS and HS) inherently suffer from high noise in gene expression, which severely limits their decoding fidelity.

Previous work on p53 and NF-κB have divided their target genes into 'early' versus 'late' categories depending on their qPCR-measured induction dynamics (Tay *et al.*, 2010; Purvis *et al.*, 2012). In the case of p53, the 'late' genes are associated with terminal cell fates such as senescence and apoptosis (Purvis *et al.*, 2012). The results presented here would place these 'late' genes in the HS or LS classes and predict that they would filter out the sporadic pulses that have been shown to occur in cycling cells (Loewer *et al.*, 2010) and thereby avoid the aberrant induction of apoptosis, but also that they would suffer from high noise in gene expression when actually induced. Since the failure to induce these terminal cell fate genes could result in the development of cancer and the death of the organism, this further underscores how serious this trade-off between noise and control of gene expression can be (Figure 2.8).

One of the central challenges that the cell faces is how to transmit information in such a way that the desired responses are elicited. Systems engineering faces much the same challenge. We show here that individual promoters can serve as discrete signal-processing modules that the cell can exploit to decode transcription factor dynamics: by tuning their amplitude threshold promoters can filter out low amplitude input (*SIP18*), simply integrate the signal (*DCS2* before saturation) or filter out high amplitude input (*DCS2* after saturation); by tuning their promoter activation timescale promoters can serve as high-pass filters (low frequency transcription factor input is filtered out), signal integrators (fast promoters),

or duration filters (slow promoters). Furthermore, we connect each signal-processing module (promoter class) with signal decoding fidelity: the ability to filter out short duration and low frequency transcription factor input comes at the cost of high noise in gene expression. Hence, although the cell can choose between several distinct signal-processing modules when decoding transcription factor dynamics, there is a trade-off between noise and control of gene expression.

2.5 Materials and methods

Strains

The yeast strains used in this study are in the W303 background and a full list can be found in Appendix Table A.1. Full details on strain construction are given in Appendix A.2.1.

Microarray analysis and reporter gene selection

To determine the transcriptional target genes of Msn2, genome-wide gene expression levels in response to 3 μM of 1-NM-PP1 were analyzed in a diploid Msn2-mCherry strain and compared with a diploid *msn2*Δ strain. Cells were grown overnight at 30°C to an $OD_{600\ nm}$ of 0.15 and 1-NMPP1 was added to a final concentration of 3 μM. Cells were harvested at time points 0, 10, 20, and 40 min and RNA extraction, cDNA synthesis, microarray hybridization (Agilent 8_15 K S. cerevisiae two-color arrays), and data normalization performed as previously described (Zhou & OShea, 2011). Genes that showed at least five-fold upregulation in response to 1-NM-PP1 in the Msn2-mCherry diploid, but no expression change in the msn2Δ diploid (Appendix Figure A.1C) and no serious deletion phenotype were selected and their endogenous ORF replaced by SCFP3A or mCitrineV163A followed by the *ADH1* terminator

and dual-reporter diploids formed by mating. Of these diploid strains, seven showed strong enough expression for reliable detection by microscopy. All seven promoters are known to directly bind Msn2 (Huebert *et al.*, 2012). Full details are given in Appendix A.2.4.

Microfluidic device

The high-throughput device developed here was loosely inspired by a previously reported low-throughput device (Hersen *et al.*, 2008). Briefly, the SU8 master wafer was fabricated using standard photolithography technology and custom transparency masks and the PDMS-based microfluidic device produced by replica molding using standard soft lithography techniques. Each microfluidic channel has a width of 400 μm and a height of ca. 111 μm. The design for the transparency mask is available upon request. Full details are given in Appendix A.2.6.

Time-lapse microscopy

Yeast cells were grown overnight at 30°C to an $OD_{600\ nm}$ of 0.1, quickly collected by filtration and loaded into a microfluidic device pre-treated with concanavalin A. Five 3-way electrovalves (LFYA1228032H Y-valve in perfluoroelastomer, the Lee Company) control whether normal medium or medium with 1-NM-PP1 is delivered to each of the five microfluidic channels and the flow (ca. 1 μL/s per channel) driven by gravity. The valves can be computationally switched within milliseconds and the medium inside the microfluidic channel changed within seconds. The device was loaded on a Zeiss AxioObserver Z1 inverted microscope with an EM-CCD camera and the entire system was kept at 30°C. Images were acquired with an oil-immersion objective (63x, NA 1.4, oil Ph3, Plan-Apochromat) with 2.5 min resolution for 64 frames. The automated microscope stage moves between the positions, maintains focus, and acquires phase contrast, YFP, CFP, iRFP, and RFP images.

To monitor Msn2-mCherry nuclear localization, a z-stack series (focal plane ±1.75 mm) was acquired. The electrovalves were programmed with custom-written software (`MATLAB`) that is available upon request. Full details are given in Appendix A.2.7.

Image analysis

Image analysis was performed using custom-written software (`MATLAB`) that automatically segments, tracks, and quantifies single cells. Briefly, the cell segmentation algorithm fits the best ellipse from a library to the cell boundary. The background subtraction algorithm uses the mode in each channel. The tracking algorithm proceeds by matching closest cells between frames subject to a series of constraints. The nucleus is segmented by thresholding the NHP6a-iRFP nuclear marker. Quantification of nuclear Msn2-mCherry is done by considering the brightest pixels in a maximum-intensity projection of an Msn2-mCherry z-stack series. CFP (SCFP3A) and YFP (mCitrineV163A) reporter expression was adjusted for photobleaching and quantified as the mean pixel intensity of the entire cell. The image analysis code is available upon request. Full details are given in Appendix A.2.10.

Deterministic model (Figure 2A)

The model (Figure 2.2A) consists of the three promoter states, mRNA, pre-mature YFP and mature YFP, and is described by the following six ordinary differential equations:

$$\frac{\mathrm{d}P_{\mathrm{unbound}}}{\mathrm{d}t} = d_1 P_{\mathrm{bound}} - k_1[\mathrm{Msn2}(t)]P_{\mathrm{bound}} \tag{2.1}$$

$$\frac{\mathrm{d}P_{\mathrm{bound}}}{\mathrm{d}t} = k_1[\mathrm{Msn2}(t)]P_{\mathrm{bound}} + d_2 P_{\mathrm{active}} - \left(d_1 + \frac{k_2[\mathrm{Msn2}(t)]^n}{K_{\mathrm{d}}^n + [\mathrm{Msn2}(t)]^n}\right) P_{\mathrm{bound}} \tag{2.2}$$

$$\frac{\mathrm{d}P_{\mathrm{active}}}{\mathrm{d}t} = \frac{k_2[\mathrm{Msn2}(t)]^n}{K_{\mathrm{d}}^n + [\mathrm{Msn2}(t)]^n} P_{\mathrm{bound}} - d_2 P_{\mathrm{active}} \tag{2.3}$$

$$\frac{\mathrm{d}[\mathrm{mRNA}]}{\mathrm{d}t} = \frac{k_3[\mathrm{Msn2}(t)]^n}{K_{\mathrm{d}}^n + [\mathrm{Msn2}(t)]^n} P_{\mathrm{active}} - d_3[\mathrm{mRNA}] \tag{2.4}$$

$$\frac{\mathrm{d}[\mathrm{YFP}]}{\mathrm{d}t} = k_4[\mathrm{mRNA}] - (d_4 + k_5)\,[\mathrm{YFP}] \tag{2.5}$$

$$\frac{\mathrm{d}[\mathrm{mYFP}]}{\mathrm{d}t} = k_5[\mathrm{YFP}] - d_4[\mathrm{mYFP}] \tag{2.6}$$

The input function is [Msn2(t)], which is a continuous function that describes how Msn2 nuclear localization changes with time and the output is mYFP. A full discussion of the model and how the fitting was performed is given in Appendix A.2.14. The parameters for each promoter are listed in Appendix Table A.2.

Gene expression noise definitions

Following the dual-reporter convention for two reporters x and y (Elowitz *et al.*, 2002), the total, extrinsic, and intrinsic noise are defined as:

$$\eta^2_{\mathrm{total}} = \frac{\langle x^2 + y^2\rangle - 2\langle x\rangle\langle y\rangle}{2\langle x\rangle\langle y\rangle} \tag{2.7}$$

$$\eta^2_{\mathrm{ext}} = \frac{\langle xy\rangle - \langle x\rangle\langle y\rangle}{\langle x\rangle\langle y\rangle} \tag{2.8}$$

$$\eta^2_{\mathrm{int}} = \frac{\langle (x-y)^2\rangle}{2\langle x\rangle\langle y\rangle} \tag{2.9}$$

where the angled brackets denote averaging over the entire cell population. In all cases where noise is reported in this study, the noise is the mean of multiple time points after

the gene expression trace has reached its plateau. For the dual-reporter system to work, the CFP and YFP reporters must be statistically identically distributed. Due to inherent differences in brightness and exposure times, it is necessary to rescale the CFP values by multiplication of a constant factor. This resulted in the CFP and YFP reporters having the same mean and distributions.

In vivo nucleosome mapping (MNase-Seq)

Cells were grown overnight at 30°C to an $OD_{600\,nm}$ of 0.15 and 1-NM-PP1 was added to a final concentration of 3 μM. Cells were harvested at time points 0, 5, 10, 20, 30, and 40 min. Crosslinking, lysis, MNase digestion, mononucleosome purification, and sequencing library preparation were performed as previously described (Zhou & OShea, 2011). Paired-end libraries were sequenced on an Illumina Hiseq 2000 and bioinformatic analysis performed using `Perl`, `Python`, and `MATLAB`. Full details are given in Appendix A.2.5.

Synthesis of 1-NM-PP1

1-NM-PP1 was synthesized from 1-naphthaleneacetic acid in five chemical steps at a gram-scale (>99% pure by NMR) using standard methods from organic synthesis. Full synthetic details are given in Appendix A.2.18.

Accession codes

Illumina sequencing data are available in the ArrayExpress (www.ebi.ac.uk/arrayexpress) database under accession number E-MTAB-1950. Microarray data are available in the ArrayExpress database under accession number E-MTAB-1945.

Supplementary Information

Supplementary information is given in Appendix A.

Acknowledgements

We thank N. Hao for insightful discussions. We thank X. Zhou, S. Mukherji, R.V. Wadhwani, D. MacLaurin and members of the O'Shea lab for discussions. We thank J. Paulsson, B. Stern, D. Huh, V. Denic and members of the O'Shea lab for critically reading the manuscript. This work was performed in part at the Center for Nanoscale Systems at Harvard University, a member of the National Nanotechnology Infrastructure Network (NNIN), which is supported by the National Science Foundation under NSF award no. ECS-0335765. The Howard Hughes Medical Institute supported this work.

Author contributions

ASH and EKO designed the project. ASH conducted the experiments and analyzed the data. ASH and EKO wrote the manuscript.

Conflict of interest

The authors declare that they have no conflict of interest.

2.6 Chapter 2 references

Ashall L, Horton CA, Nelson DE, Paszek P, Harper CV, Sillitoe K, Ryan S, Spiller DG, Unitt JF, Broomhead DS, Kell DB, Rand DA, See V, White MR (2009) Pulsatile stimulation determines timing and specificity of NF-kappaB-dependent transcription. *Science* **324**:242-246

Bai L, Charvin G, Siggia ED, Cross FR (2010) Nucleosome-depleted regions in cell-cycle-regulated promoters ensure reliable gene expression in every cell cycle. *Dev Cell* **18**: 544-555

Balaban NQ, Merrin J, Chait R, Kowalik L, Leibler S (2004) Bacterial persistence as a phenotypic switch. *Science* **305**: 1622-1625

Bar-Even A, Paulsson J, Maheshri N, Carmi M, OShea E, Pilpel Y, Barkai N (2006) Noise in protein expression scales with natural protein abundance. *Nat Genet* **38**: 636-643

Batchelor E, Loewer A, Mock C, Lahav G (2011) Stimulus-dependent dynamics of p53 in single cells. *Mol Syst Biol* **7**: 488

Behar M, Hoffmann A (2010) Understanding the temporal codes of intra-cellular signals. *Curr Opin Genet Dev* **20**: 684-693

Berger MF, Badis G, Gehrke AR, Talukder S, Philippakis AA, Pena-Castillo L, Alleyne TM, Mnaimneh S, Botvinnik OB, Chan ET, Khalid F, ZhangW, Newburger D, Jaeger SA, Morris QD, Bulyk ML, Hughes TR (2008) Variation in homeodomain DNA binding revealed by high-resolution analysis of sequence preferences. *Cell* **133**: 1266-1276

Bishop AC, Ubersax JA, Petsch DT, Matheos DP, Gray NS, Blethrow J, Shimizu E, Tsien JZ, Schultz PG, Rose MD, Wood JL, Morgan DO, Shokat KM (2000) A chemical switch for inhibitor-sensitive alleles of any protein kinase. *Nature* **407**: 395-401

Brennan MD, Cheong R, Levchenko A (2012) How information theory handles cell signaling and uncertainty. *Science* **338**: 334-335

Cai L, Dalal CK, Elowitz MB (2008) Frequency-modulated nuclear localization bursts coordinate gene regulation. *Nature* **455**: 485-490

Covert MW, Leung TH, Gaston JE, Baltimore D (2005) Achieving stability of lipopolysaccharide-induced NF-kappa B activation. *Science* **309**: 1854-1857

Dadiani M, van Dijk D, Segal B, Field Y, Ben-Artzi G, Raveh-Sadka T, Levo M, Kaplow I,Weinberger A, Segal E (2013) Two DNA-encoded strategies for increasing expressionwith opposing effects on promoter dynamics and transcriptional noise. *Genome Res* **23**: 966-976

Elowitz MB, Levine AJ, Siggia ED, Swain PS (2002) Stochastic gene expression in a single cell. *Science* **297**: 1183-1186

Giorgetti L, Siggers T, Tiana G, Caprara G, Notarbartolo S, Corona T, Pasparakis M, Milani P, Bulyk ML, Natoli G (2010) Noncooperative Interactions between Transcription Factors and Clustered DNA Binding Sites Enable Graded Transcriptional Responses to Environmental Inputs. *Mol Cell* **37**: 418-428

Gorner W, Durchschlag E, Martinez-Pastor MT, Estruch F, Ammerer G, Hamilton B, Ruis H, Schuller C (1998) Nuclear localization of the C2H2 zinc finger protein Msn2p is regulated by stress and protein kinase A activity. *Gene Dev* **12**: 586-597

Hao N, OShea EK (2012) Signal-dependent dynamics of transcription factor translocation controls gene expression. *Nat Struct Mol Biol* **19**: 31-U47

Herrero P, Galindez J, Ruiz N, Martinezcampa C, Moreno F (1995) Transcriptional regulation of the Saccharomyces cerevisiae Hxk1, Hxk2 and Glk1 genes. *Yeast* **11**: 137-144

Hersen P, McClean MN, Mahadevan L, Ramanathan S (2008) Signal processing by the HOG MAP kinase pathway. *Proc Natl Acad Sci USA* **105**: 7165-7170

Hilfinger A, Paulsson J (2011) Separating intrinsic from extrinsic fluctuations in dynamic biological systems. *Proc Natl Acad Sci USA* **108**: 12167-12172

Hornung G, Bar-Ziv R, Rosin D, Tokuriki N, Tawfik DS, OrenM, Barkai N (2012) Noise-mean relationship in mutated promoters. *Genome Res* **22**: 2409-2417

Huebert DJ, Kuan PF, Keles S, Gasch AP (2012) Dynamic changes in nucleosome occupancy are not predictive of gene expression dynamics but are linked to transcription and chromatin regulators. *Mol Cell Biol* **32**: 1645-1653

Jacquet M, Renault G, Lallet S, De Mey J, Goldbeter A (2003) Oscillatory nucleocytoplasmic shuttling of the general stress response transcriptional activators Msn2 and Msn4 in Saccharomyces cerevisiae. *J Cell Biol* **161**: 497-505

Lahav G, Rosenfeld N, Sigal A, Geva-ZatorskyN, Levine AJ, ElowitzMB, Alon U (2004) Dynamics of the p53-Mdm2 feedback loop in individual cells. *Nat Genet* **36**: 147-150

Lam FH, Steger DJ, OShea EK (2008) Chromatin decouples promoter threshold from dynamic range. *Nature* **453**: 246-U216

Lionnet T, Singer RH (2012) Transcription goes digital. *EMBO Rep* **13**: 313-321

Loewer A, Batchelor E, Gaglia G, LahavG (2010) Basal dynamics of p53 reveal transcriptionally attenuated pulses in cycling cells. *Cell* **142**: 89-100

Nelson DE, Ihekwaba AE, Elliott M, Johnson JR, Gibney CA Foreman BE, Nelson G, See V, Horton CA, Spiller DG, Edwards SW, McDowell HP, Unitt JF, Sullivan E, Grimley R, Benson N, Broomhead D, Kell DB, WhiteMR(2004) Oscillations in NF-kappaB signaling control the dynamics of gene expression. *Science* **306**:704-708

Newman JRS, Ghaemmaghami S, Ihmels J, Breslow DK, Noble M, DeRisi JL, Weissman JS (2006) Single-cell proteomic analysis of S. cerevisiae reveals the architecture of biological

noise. *Nature* **441**:840-846

Petrenko N, Chereji RV, McClean M, Morozov AV, Broach JR (2013) Noise and interlocking signaling pathways promote distinct transcription factor dynamics in response to different stresses. *Mol Biol Cell* **24**: 2045-2057

Purvis JE, Karhohs KW, Mock C, Batchelor E, Loewer A, Lahav G (2012) p53 dynamics control cell fate. *Science* **336**: 1440-1444

Purvis JE, Lahav G (2013) Encoding and decoding cellular information through signaling dynamics. *Cell* **152**: 945-956

Raj A, Peskin CS, Tranchina D, Vargas DY, Tyagi S (2006) Stochastic mRNA synthesis in mammalian cells. *PLoS Biol* **4**: 1707-1719

Raj A, van Oudenaarden A (2008) Nature, nurture, or chance: stochastic gene expression and its consequences. *Cell* **135**: 216-226

Raser JM, OShea EK (2004) Control of stochasticity in eukaryotic gene expression. *Science* **304**: 1811-1814

Rodriguez-Porrata B, Carmona-Gutierrez D, Reisenbichler A, Bauer M, Lopez G, Escote X, Mas A, Madeo F, Cordero-Otero R (2012) Sip18 hydrophilin prevents yeast cell death during desiccation stress. *J Appl Microbiol* **112**: 512-525

Sharon E, Kalma Y, Sharp A, Raveh-Sadka T, Levo M, Zeevi D, Keren L, Yakhini Z, Weinberger A, Segal E (2012) Inferring gene regulatory logic from high-throughput measurements of thousands of systematically designed promoters. *Nat Biotechnol* **30**: 521-530

Shivaswamy S, Bhinge A, Zhao YJ, Jones S, Hirst M, Iyer VR (2008) Dynamic remodeling of individual nucleosomes across a eukaryotic genome in response to transcriptional perturbation. *PLoS Biol* **6**: 618-630

Tay S, Hughey JJ, Lee TK, Lipniacki T, Quake SR, Covert MW (2010) Single-cell NF-kappaB dynamics reveal digital activation and analogue information processing. *Nature* **466**: 267-271

Tostevin F, de Ronde W, Ten Wolde PR (2012) Reliability of frequency and amplitude decoding in gene regulation. *Phys Rev Lett* **108**:108104

Werner SL, Barken D, Hoffmann A (2005) Stimulus specificity of gene expression programs determined by temporal control of IKK activity. *Science* **309**: 1857-1861

Yissachar N, Fischler TS, Cohen AA, Reich-Zeliger S, Russ D Shifrut E, Porat Z, Friedman N (2013) Dynamic response diversity of NFAT isoforms in individual living cells. *Mol*

Cell **49**:322-330

Zaman S, Lippman SI, Schneper L, Slonim N, Broach JR (2009) Glucose regulates transcription in yeast through a network of signaling pathways. *Mol Syst Biol* **5**: 245

Zhou X, OShea EK (2011) Integrated approaches reveal determinants of genome-wide binding and function of the transcription factor Pho4. *Mol Cell* **42**: 826-836

Chapter 3

Limits on information transduction through regulation of signaling dynamics

3.1 Abstract

Signaling pathways often transmit multiple signals through a single shared transcription factor (TF) and encode signal information by differentially regulating TF dynamics. However, signal information will be lost unless it can be reliably decoded by downstream genes. To understand the limits on dynamic information transduction, we apply information theory to quantify how much gene expression information the yeast TF Msn2 can transduce to target genes in the amplitude or frequency of its activation dynamics. We find that although the amount of information transmitted by Msn2 to single target genes is limited, information transduction can be increased by modulating promoter *cis*-elements or by integrating information from multiple genes. By correcting for extrinsic noise, we estimate an upper

bound on information transduction. Overall, we find that information transduction through amplitude and frequency regulation of Msn2 is limited to error-free transduction of signal identity, but not signal intensity information.

3.2 Introduction

Cellular signaling pathways often exhibit a bowtie topology (Csete & Doyle, 2004): multiple distinct signal inputs converge on a single master regulator, typically a transcription factor, which then controls the expression of partially overlapping sets of downstream target genes. This raises two general questions: first, how can the cell encode information about different signals in the activity of a single master transcription factor? Second, can this information be decoded by target genes to elicit a specific output for each input?

One way the cell can encode signal information is by regulating the activation dynamics of a single master transcription factor (Figure 3.1A). For example, p53, a tumor suppressor transcription factor, exhibits an intensity-dependent number of nuclear pulses in response to γ-radiation, but a sustained pulse of nuclear localization with intensity-dependent amplitude during UV-radiation (Batchelor *et al.*, 2011; Lahav *et al.*, 2004). Akin to p53, the yeast multi-stress response transcription factor Msn2 exhibits short pulses of nuclear localization with intensity-dependent frequency under glucose limitation, but sustained nuclear localization with intensity-dependent amplitude under oxidative stress (Hao *et al.*, 2013; Hao & O'Shea, 2012; Jacquet *et al.*, 2003; Petrenko *et al.*, 2013). Thus, p53 and Msn2 dynamics encode both signal identity and signal intensity. Beyond p53 and Msn2, amplitude- or frequency encoding of signal identity and intensity information is conserved throughout eukaryotic signaling pathways (see also (Albeck *et al.*, 2013; Aoki *et al.*, 2013; Berridge *et al.*, 2000; Cai *et al.*, 2008; Dalal *et al.*, 2014; Harima *et al.*, 2014; Imayoshi *et al.*, 2013;

Warmflash *et al.*, 2012; Werner *et al.*, 2005)). Such encoding of signal identity and intensity information in transcription factor activation dynamics has led to the hypothesis that transcription factor target genes can reliably decode this dynamical information to elicit distinct gene expression programs with fine-tuned expression levels (Figure 3.1A) (Behar *et al.*, 2007; Behar & Hoffmann, 2010; de Ronde & ten Wolde, 2014; Hansen & O'Shea, 2013; Levine *et al.*, 2013; Purvis & Lahav, 2013; Yosef & Regev, 2011).

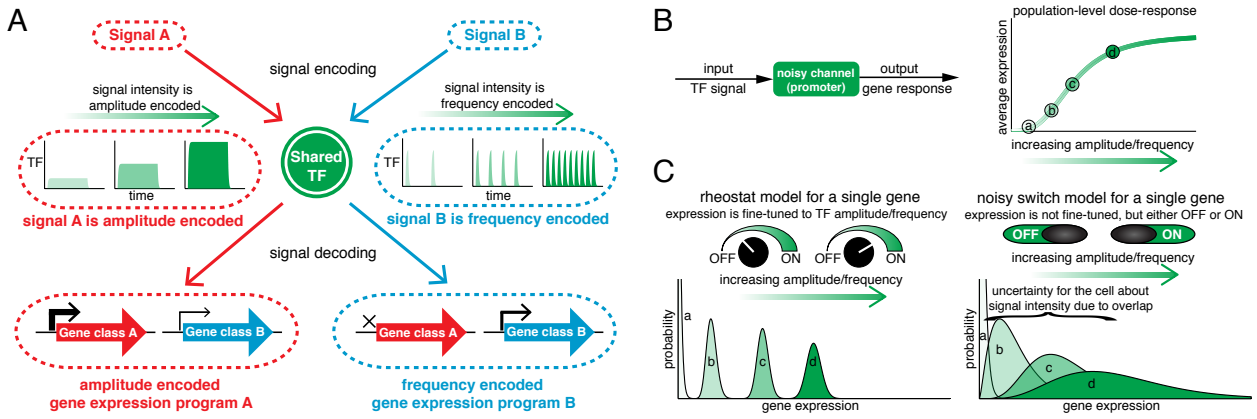

Figure 3.1: *Encoding and transmitting signal identity and intensity information in the dynamics of a single transcription factor*
(A) Different signals (e.g. stress or ligand exposure) can be encoded in the dynamics of a single transcription factor (TF). Signal identity is encoded in the type of transcription factor dynamics: a sustained pulse (signal A) or nuclear pulsing (signal B). Signal intensity (e.g. ligand concentration) is encoded in the amplitude for signal A, but in the frequency for signal B. Different dynamical patterns of TF activation can activate distinct, but specific, downstream gene expression programs.
(B) Applying an information theoretic framework to cell signaling, a gene promoter can be considered a channel. A graded population-level dose-response belies the complexity of the single-cell response: it shows the mean expression at points a, b, c and d, but not the width or variance of their distributions.
(C) Two extreme models. In the rheostat model, signal intensity information encoded in the frequency or amplitude of a TF leads to non-overlapping gene expression distributions (a, b, c and d). Thus, by reading the gene expression output the cell can accurately determine the input signal intensity and high information transmission is achieved. Conversely, in the noisy switch model, as a consequence of overlapping gene expression distributions (a, b, c and d) information about signal intensity is permanently lost: the cell can distinguish ON/OFF (signal identity), but the expression of a target gene cannot be fine-tuned to the stress intensity.

However, non-genetic cell-to-cell variability (noise) in gene expression limits the fidelity with which information can be decoded by transcription factor target genes (Coulon *et al.*, 2013; Sanchez & Golding, 2013). This is important because the capacity of any signaling pathway for information transduction is limited by the capacity of its weakest node or bottleneck (Cover & Thomas, 2006). Thus, even though information can reliably be encoded in transcription factor activation dynamics (Selimkhanov *et al.*, 2014), this information will be lost unless genes can reliably decode it. We therefore focus on the response of single

genes and ask: can cells reliably transmit both signal identity and intensity information in the amplitude and frequency of transcription factors to target genes in the presence of biochemical noise? In other words, what are the limits on amplitude- and frequency-mediated information transduction? We investigate this by applying tools from information theory to quantify how much of the information (in bits) encoded in the amplitude and frequency of a transcription factor can be transmitted through gene promoters to fine-tune the gene expression level.

Originally developed by Claude Shannon for communication systems (Shannon, 1948), information theory has recently been applied to cell signaling (reviewed in (Bowsher & Swain, 2014; Levchenko & Nemenman, 2014; Mc Mahon *et al.*, 2014; Nemenman, 2012; Rhee *et al.*, 2012; Tkacik & Walczak, 2011; Waltermann & Klipp, 2011)). Mutual information quantifies how much information an output can carry about an input across a noisy channel (Figure 3.1B). Mathematically, information is quantified in bits: to resolve two different signal intensities without error requires at least 1 bit of information, to resolve four different signal intensities without error requires at least 2 bit of information and so forth. However, 1 bit of information does not guarantee that two intensities can be distinguished without error. Similarly, 1 bit may allow multiple intensities to be distinguished, albeit with some associated error (Bowsher & Swain, 2014). As an example of how information theory can be applied, consider a dose-response relationship (Figure 3.1B). A graded population-level dose-response can belie the complexity of the single-cell response (Ferrell & Machleder, 1998). For example, if different transcription factor amplitudes or frequencies lead to distinguishable gene expression outputs (points a, b, c and d), signal intensity information is accurately transmitted and the cell can fine-tune the expression of stress genes to the stress intensity like a rheostat (Figure 3.1C, rheostat model). However, biochemical noise can degrade signal

information: if gene expression outputs are no longer resolvable, the cell can no longer fine-tune the expression level of stress genes to stress intensity (Figure 3.1C, noisy switch model). In the noisy switch model, the cell can distinguish no stimulus (point a, OFF) from maximal stimulus (point d, ON) — but intermediate stimuli (points b and c) cannot reliably be distinguished based on the gene expression output and signal intensity information has been lost (Figure 3.1C). Information theory provides a framework for capturing and quantifying these differences. Thus, we can distinguish these two models by measuring information transduction by promoters: the noisy switch model requires ∼1 bit, whereas the rheostat model requires substantially higher mutual information.

Previous applications of information theory have been theoretical (Bowsher & Swain, 2012; de Ronde *et al.*, 2011; Lestas *et al.*, 2010; Rieckh & Tkacik, 2014; Tostevin & ten Wolde, 2009; Ziv *et al.*, 2007) or have focused on upstream signaling and development (Cheong *et al.*, 2011; Dubuis *et al.*, 2013; Gregor *et al.*, 2007; Mehta *et al.*, 2009; Selimkhanov *et al.*, 2014; Skerker *et al.*, 2008; Tkacik *et al.*, 2008; Tkacik *et al.*, 2009; Tostevin *et al.*, 2007; Uda *et al.*, 2013; Voliotis *et al.*, 2014). However, despite gene expression being the final bottleneck in cell signaling, gene expression has received little attention. Estimating an upper limit on the information transduction capacity of a gene has not previously been possible due to extrinsic noise: even when studying genetically identical single cells, the cells can exhibit non-genetic differences, e.g. in cell cycle phase or variability in TF concentration, which means the measured mutual information will be an underestimate (Elowitz *et al.*, 2002; Toettcher *et al.*, 2013). Here we overcome this limitation through a combined experimental and theoretical approach that corrects for extrinsic noise and allows us to estimate an upper limit on the information transduction capacity of individual Msn2 target genes.

We combine high-throughput microfluidics to control the amplitude and frequency of

Msn2 nuclear translocation with information theory to determine the information transduction capacity of Msn2 target genes. We find that Msn2 target genes can transduce just over 1 bit of information, consistent with the noisy switch model. Although individual Msn2 target genes can only transduce little information, we illustrate how the cell can improve information transduction capacity by modulating promoter *cis*-elements, by integrating the response of more than one gene, or by having multiple copies of the same gene. We show that more information can be transduced through amplitude than through frequency modulation of Msn2 activation dynamics. Nevertheless, while previous studies have shown that significant amounts of information can be encoded in TF activation dynamics (Selimkhanov *et al.*, 2014), we find that noise in the decoding step severely limits information transduction. Specifically, our results indicate that information about signal identity, but not signal intensity, can be transmitted nearly without error in the amplitude and frequency of Msn2 and decoded by Msn2-responsive promoters.

3.3 Results

3.3.1 Quantifying information transduction using information theory

Information theory quantifies information transduction across a channel between a signal and a response (Cover & Thomas, 2006; Shannon, 1948). If a channel is noisy, a given signal input will give rise to a distribution of response outputs. This represents a loss of information since the signal input can no longer reliably be learned from observing the response output (Figure 3.1B-C). A black-box-framework, information theory was originally developed for telecommunication channels, but it can also be applied to other channels such

as gene promoters or cell signaling pathways provided that the signal input (here amplitude or frequency of Msn2 activation) can be precisely controlled and the response output distribution precisely measured (here single-cell gene expression). Mutual information, $MI(R;S)$, measured in bits, quantifies the amount of information about the signal input (S) that can be obtained by observing the response output (R) and, given discretized data, is defined as:

$$MI(R;S) = \sum_{i,j} P(R_i, S_j) \log_2 \left(\frac{P(R_i, S_j)}{P(R_i)P(S_j)} \right) \tag{3.1}$$

The response distribution, $P(R)$, is the experimentally measured distribution of gene expression output. The signal distribution, $P(S)$, is the relative probability of each Msn2 amplitude or frequency. Since $MI(R;S)$ depends on $P(S)$ and since $P(S)$, e.g. how often a cell might be exposed to a particular intensity of oxidative stress, is unknowable, hereafter we consider the maximal mutual information, I ($I(R;S) = \max_{P(S)}[MI(R;S)]$) which is the maximal amount of information that can be transduced through a promoter channel. I can be thought of as a channel capacity, though a gene promoter is effectively a single-use channel and I therefore has units of bits, whereas messages are sent repeatedly through a Shannon channel and, accordingly, the channel capacity has units of bits/s ((Bowsher & Swain, 2014); a detailed discussion is given in Appendix C).

3.3.2 Natural Msn2 target genes have low information transduction capacities

To measure how much information Msn2 target genes can transduce, we took advantage of a pharmacological method for controlling Msn2 nuclear localization using a small

molecule, 1-NM-PP1, (Bishop *et al.*, 2000; Hao & O'Shea, 2012; Zaman *et al.*, 2009) and high-throughput microfluidics coupled to quantitative time-lapse microscopy (Chapter 4; Hansen & O'Shea, 2013). With this setup (Figure B.1A), we can control and measure the amplitude and frequency of activation of an Msn2-mCherry fusion protein over time and generate single-cell traces that mimic the natural Msn2 dynamics under oxidative stress (a sustained nuclear pulse with signal intensity-dependent amplitude; Figure 3.2A) and glucose limitation (short pulses with signal intensity-dependent frequency; Figure 3.2B) (Hao & O'Shea, 2012; Petrenko *et al.*, 2013). To measure stress-relevant gene expression, we use CFP/YFP fluorescent reporters and focus on two specific Msn2 target genes: *HXK1*, which is induced under glucose limitation (Herrero *et al.*, 1995) and *SIP18*, which is induced in response to oxidative stress (Rodriguez-Porrata *et al.*, 2012). Using this setup, we have previously shown that, at the population level, individual genes differentially decode Msn2 dynamics (Hansen & O'Shea, 2013; Hao & O'Shea, 2012): oscillatory Msn2 activation induces gene class B (e.g. *HXK1*) without inducing gene class A (e.g. *SIP18*), whereas sustained Msn2 activation preferentially induces gene class A (Figure 3.1A). Thus, this represents an ideal setup for studying promoter decoding of Msn2 dynamics in single cells, which enables us to quantify information transduction.

To measure information transduction through the *HXK1* and *SIP18* promoters with respect to amplitude modulation (I_{AM}), we exposed thousands of cells to increasing amplitudes of a 70 min Msn2 pulse to mimic oxidative stress, measured the single-cell distribution of responses for each amplitude with minimal measurement noise (see Appendix B and Figure B.2), and determined the population-averaged dose-response (Figure 3.2A; all raw single-cell data is available online at Dryad Digital Depository in (Hansen & O'Shea, 2015); see also Figure B.1B). We quantify gene expression as the maximal YFP concentration after

the YFP time-trace has reached a plateau (Appendix C). Surprisingly, for both *HXK1* and *SIP18*, I_{AM} was 1.2-1.3 bits — enough to distinguish ON from OFF without error (the 'no Msn2 input' and the 'brown' distributions are clearly distinguishable; Figure 3.2A), but with limited ability to distinguish signal intensities. One way to think about this result is to ask, given the *HXK1* YFP expression output, how much information does that provide about the input amplitude? For example, considering the *HXK1* AM histograms in Figure 3.2A, for most YFP outputs the cell can exclude the 'no Msn2 input' condition, but appears to be unable to discern which of the other amplitudes it was exposed to without a high error rate. Consequently, *HXK1* and *SIP18* can distinguish no stress from high oxidative stress (high Msn2 amplitude) without error, but cannot accurately transmit information about stress intensity.

Next, we measured information transduction of *HXK1* and *SIP18* with respect to frequency modulation (I_{FM}) using 5-min Msn2 pulses at frequencies similar to those observed under glucose limitation (Figure 3.2B). Even though *HXK1* is physiologically induced during Msn2 pulsing, I_{FM} was only 1.11 bits — again enough for distinguishing ON from OFF essentially without error like a noisy switch, but insufficient to accurately fine-tune the *HXK1* expression level to each Msn2 frequency like a rheostat. *SIP18*, required only under oxidative stress, largely filters out Msn2 pulsing and therefore has a negligible I_{FM}.

3.3.3 The promoter information transduction capacity is tunable and can be increased for natural Msn2 target genes

It is generally assumed that gene expression levels are fine-tuned (de Nadal *et al.*, 2011), but the very low I_{AM} and I_{FM} of *HXK1* and *SIP18* are incompatible with this idea. One possibility is that mutual information for promoters is biophysically constrained to ∼1.0-

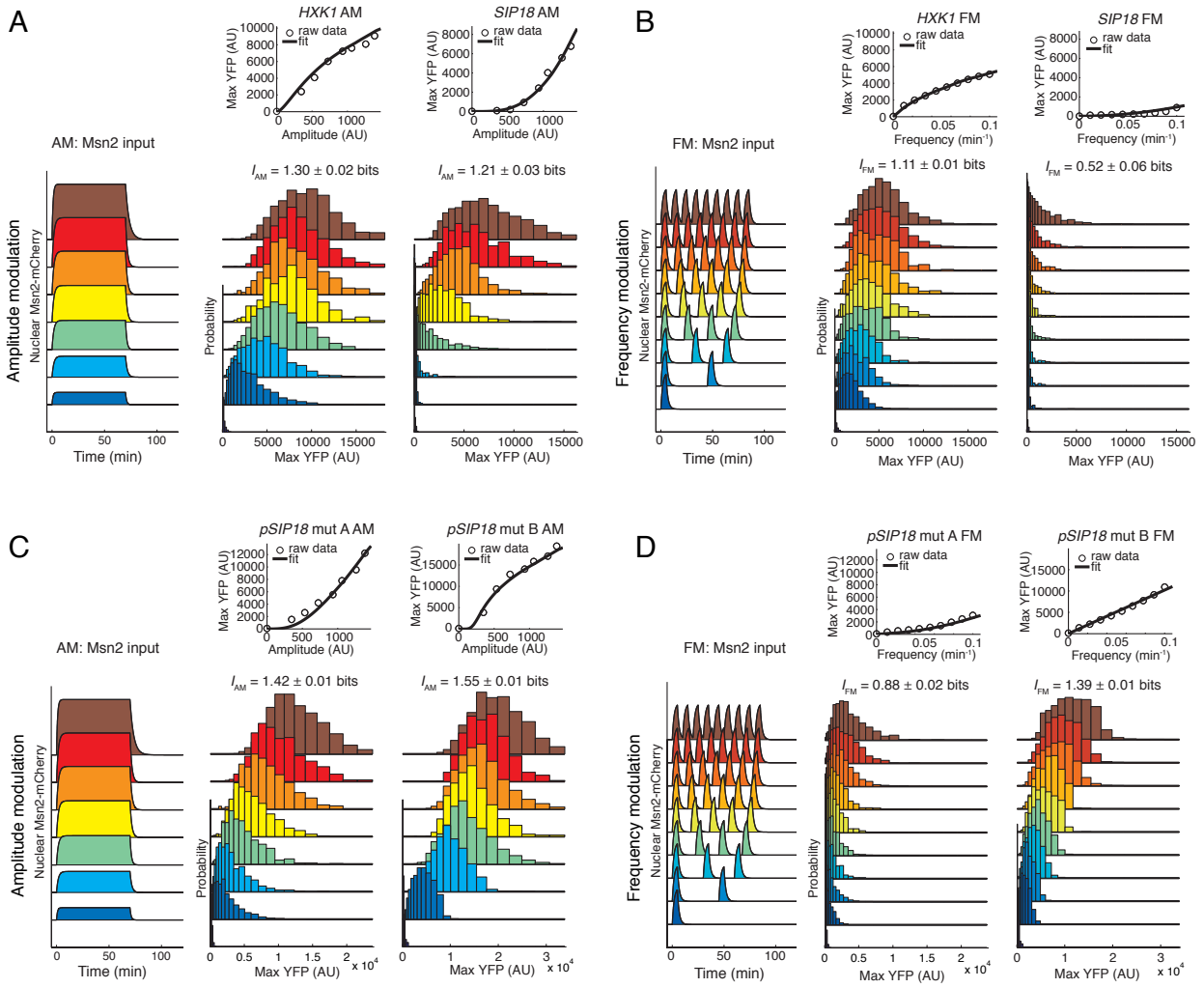

Figure 3.2: *Information transduction by promoters with respect to amplitude and frequency modulation*
(A) Cells containing either the *hxk1*::YFP or *sip18*::YFP reporter were exposed to either no activation or a 70-min pulse of seven increasing amplitudes from ca. 25% (100 nM 1-NM-PP1) to 100% (3 µM 1-NM-PP1) of maximal Msn2-mCherry nuclear localization and single-cell gene expression monitored. For each single-cell time-trace, YFP concentration is converted to a scalar by taking the maximal YFP value after smoothing. For each Msn2-mCherry input (a fit to the raw data is shown on the left (AM: Msn2 input)), the gene expression distribution is plotted as a histogram of the same color on the right for *HXK1* and *SIP18*. The population-averaged dose-response (top) is obtained by calculating the YFP histogram mean for each Msn2 input condition.
(B) Cells containing either the *hxk1*::YFP or *sip18*::YFP reporter were exposed to either no activation or from one to nine 5-min pulses of Msn2-mCherry nuclear localization (ca. 75% of maximal nuclear Msn2-mCherry, 690 nM 1-NM-PP1) at increasing frequency. All calculations were performed as in **(A)**.
(C) Cells containing either the *pSIP18* mut A::YFP reporter or the *pSIP18* mut B::YFP reporter were exposed to amplitude modulation as in **(A)**.
(D) Cells containing either the *pSIP18* mut A::YFP reporter or the *pSIP18* mut B::YFP reporter were exposed to frequency modulation as in **(B)**.
Mutual information, I, and its error are calculated as described in Appenix C. Full details on data processing are given in Appendix B. Each plot of an Msn2 input pulse and YFP expression is based on data from ca. 1000 cells from at least three biological replicates. All raw single-cell time-lapse microscopy source data for *HXK1* (15259 cells), *SIP18* (21242 cells), *pSIP18* mut A (18203 cells) and *pSIP18* mut B (17655 cells) for this figure is available online at Dryad Digital Repository (Hansen & O'Shea, 2015).

1.3 bit, but another possibility is that *HXK1* and *SIP18* are not optimized for AM- and FM-mediated information transduction. To investigate this and explore the relationship between promoter *cis*-elements and information transduction we focused on *SIP18*, which has the lowest I and suffers from high gene expression noise (Figure B.1D), and asked if altering promoter architecture could improve information transduction. We removed the two functional Msn2 binding sites in the *SIP18* promoter and added three and four new binding sites in the nucleosome-free region closer to the transcription start site (promoter architecture maps are shown in Figure B.1C) to generate *pSIP18* mut A and *pSIP18* mut B, which differ from the wild-type *SIP18* promoter by 14 and 18 nucleotides, respectively. We then repeated the experiments for mut A and mut B to measure their I_{AM} and I_{FM}.

With respect to amplitude modulation (AM), both mutants had significantly higher I_{AM} of 1.42 bits (mut A) and 1.55 bits (mut B) (Figure 3.2C). We attribute this increase to a combination of three factors: a more linear dose-response, a higher dynamic range and significantly lower gene expression noise (Figure B.1D).

The wild-type *SIP18* promoter filters out oscillatory input and therefore has a negligible I_{FM}. In contrast, with respect to frequency modulation (FM) mut A shows a slightly higher I_{FM} of 0.88 bits and mut B a significantly higher I_{FM} of 1.39 bits (Figure 3.2D). Notably, although *HXK1* presumably evolved to decode Msn2 pulsing, as is observed under glucose limitation, mut B now shows a higher I_{FM} than even *HXK1*. These results show that natural Msn2 target genes do not have their maximal I. Thus, beyond the ability to distinguish no stress from high stress as in the noisy switch model, Msn2 target genes are not optimized for fine-tuning their expression to the stress intensity even though promoters with higher $I_{\mathrm{AM/FM}}$ are only a few mutations away. Furthermore, I_{AM} exceeds I_{FM} for all four promoters, which shows that, at least in these four cases, transmitting gene expression information in the

amplitude of transcription factor activation dynamics is more reliable than transmitting it in the frequency. Thus, the promoter information transduction capacity is tunable in *cis*: by modulating Msn2 binding sites, we can control both how a promoter decodes transcription factor dynamics and how much information it can transmit.

3.3.4 Estimating the intrinsic information transduction capacity of promoters

Natural Msn2 target promoters appear to have $I \leq 1.3$ bits. Thus, we observe high information loss during gene expression. Information loss comes from two sources: gene-intrinsic and gene-extrinsic noise (Elowitz *et al.*, 2002). Intrinsic noise originates from the inherently stochastic nature of biochemical reactions, such as stochastic binding of Msn2 at individual promoters. Information loss due to intrinsic noise is therefore unavoidable for the cell. Extrinsic noise comes from the intracellular environment, which may differ between cells in a population. Even though we consider genetically identical cells grown in a microfluidic chemostat, the cell population could exhibit non-genetic differences in cell-cycle phase and Msn2 abundance or dynamics etc. This could cause the dose-response to be different between single cells (Figure 3.3A), as was observed in a recent study on Ras/ERK signaling (Toettcher *et al.*, 2013). For example, a cell with a higher-than-average Msn2 abundance might show higher gene expression. When we carefully quantify Msn2-mCherry dynamics, we observe loss of information between the microfluidic 1-NM-PP1 input and nuclear Msn2 due to variability in Msn2 abundance between cells (Figure B.3). Likewise, the cell cycle is a major source of extrinsic gene expression noise (Zopf *et al.*, 2013). Therefore, measuring mutual information in a cell population subject to extrinsic noise, as we did in Figure 3.2, underestimates the intrinsic information transduction capacity of a promoter.

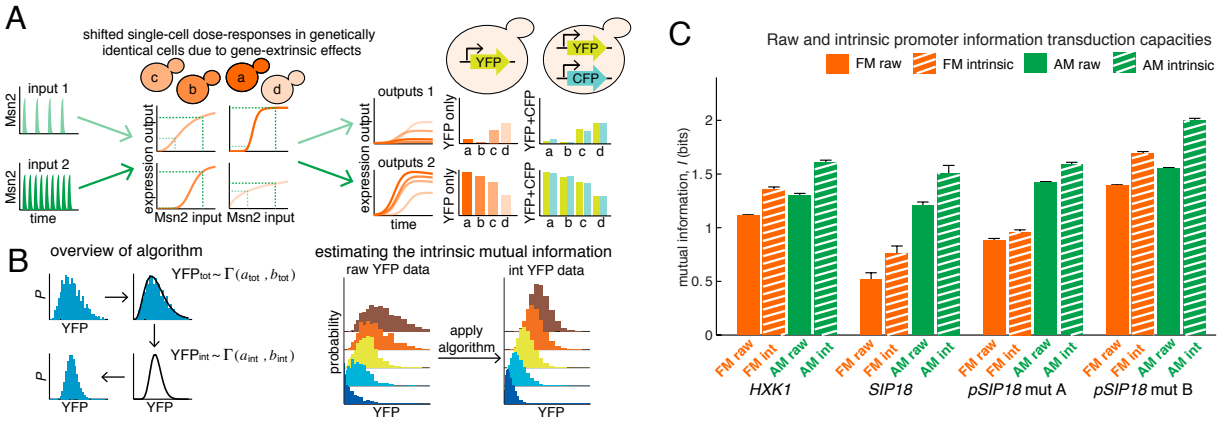

Figure 3.3: *An algorithm for estimating intrinsic mutual information*
(A) Genetically identical cells can have shifted single-cell dose-responses due to gene-extrinsic effects such as variation in Msn2 abundance and cell cycle phase. Measuring the response of a single reporter (YFP) therefore underestimates mutual information. By introducing an additional equivalent reporter (CFP), we can distinguish extrinsic noise such as a shifted dose-response since this affects both CFP and YFP equally, from true intrinsic stochasticity.
(B) Overview of algorithm. By fitting a gamma distribution to the raw YFP data, calculating the CFP/YFP covariance and filtering this component out of the total variance, an intrinsic YFP distribution can be estimated (left). By repeating this for each dose-response distribution, intrinsic mutual information can be estimated (right). Full details on the algorithm are given in Appendix C.
(C) By applying the algorithm to the data from Figure 3.2 (solid bars), we can estimate intrinsic mutual information (hatched bars).

Although it is in principle possible to correct for cell cycle phase, Msn2 abundance and other gene-extrinsic factors individually, it is impossible to correct for all factors. To overcome this limitation and estimate the intrinsic I (I_{int}), we developed a method based on the dual-reporter approach (Elowitz *et al.*, 2002; Hilfinger & Paulsson, 2011; Swain *et al.*, 2002). By having two gene expression reporters in diploid cells on homologous chromosomes that differ only by their color (CFP and YFP) but share the same intracellular environment, the extent to which they co-vary in the same cell allows us to infer how much gene-extrinsic factors such as cell-cycle phase and Msn2 variability etc. contribute altogether (extrinsic noise), without having to specify each factor. Or phrased differently, if the dose-response is shifted in a cell, both the CFP and YFP reporter will be affected in a correlated manner and their covariance allows us to quantify this (Figure 3.3A). Therefore, we developed an algorithm that uses the CFP/YFP covariance to estimate what the intrinsic I (I_{int}) would have been in the absence of extrinsic noise. Briefly, our algorithm takes the following steps: First, the raw

YFP histogram is fitted to a gamma distribution (YFP $\sim \Gamma(a, b)$). Second, the extrinsic component (covariance) of the total variance is determined ($\sigma^2_{\text{ext}} = \langle \text{CFP} \cdot \text{YFP} \rangle - \langle \text{CFP} \rangle \langle \text{YFP} \rangle$). Third, keeping the mean constant, a new gamma distribution without the extrinsic component is inferred ($\text{YFP}_{\text{int}} \sim \Gamma(a_{\text{int}}, b_{\text{int}})$). Fourth, this is repeated for each Msn2 input (e.g. amplitude or frequency). Finally, this inferred dataset is discretized and then used to estimate I_{int} (Figure 3.3B; a detailed discussion of the algorithm is given in Appendix C). We verified our algorithm *in silico* by systematically simulating five linear and five non-linear gene expression models with and without extrinsic noise and compared the true I_{int} to the algorithm-inferred I_{int}. The algorithm tended to slightly underestimate the true I_{int}, but the mean error was less than 2% and the error was always less than 5% (see Appendix C.4).

Therefore, by using dual-reporter strains we can determine how much of the information loss is extrinsic, apply the algorithm and estimate I_{int} in each case ($I_{\text{AM,int}}$ and $I_{\text{FM,int}}$). We find that filtering out extrinsic noise significantly increases I (hatched bars, Figure 3.3C). Since the cell most likely incorporates some gene-extrinsic factors into a decision, but most likely does not incorporate all gene-extrinsic factors, we interpret I_{raw} and I_{int} as a lower and upper bound, respectively, on the true I. Thus, our approach allows us to estimate an upper bound, I_{int}, on a promoters information transduction capacity.

Even after correcting for extrinsic noise, $I_{\text{AM,int}}$ for *HXK1* and *SIP18* only reach ∼1.5-1.6 bits (Figure 3.3C). And $I_{\text{FM,int}}$ for *HXK1* is just 1.36 bits — that is, three ranges of inputs can only be distinguished with some associated error. Thus, even when considering I_{int}, which is the upper limit on the maximal mutual information, neither natural Msn2 target gene can transmit information about stress intensity without some error. That is, consistent with the noisy switch model, expression of *HXK1* and *SIP18* is not reliably fine-tuned to stress intensity. In contrast, for mut B $I_{\text{FM,int}}$ is 1.55 bits and $I_{\text{AM,int}}$ is ∼2 bits (Figure 3.3C).

Thus, mut B almost approaches a range where information about both signal identity and intensity could conceivably be transduced nearly without error like a rheostat, though the natural Msn2 target genes, *HXK1* and *SIP18*, do not.

3.3.5 Multiple gene copies reduces information loss due to intrinsic noise

Filtering out extrinsic noise substantially increases I (Figure 3.3C). Next, we considered how reducing intrinsic noise might increase I. In principle, as the number of gene copies increases, information loss due to intrinsic noise decreases due to simple ensemble averaging and mutual information increases — in the limit of infinite copies, intrinsic noise is zero and all information loss is due to extrinsic noise (Cheong *et al.*, 2011). To test this we generated diploid strains with either one (1x) or two (2x) copies of the *hxk1*::CFP and *sip18*::YFP reporters in the same cell.

We repeated the AM and FM experiments for the 1x and 2x diploids (Figures B.4 and B.5). Comparing the 1x and 2x diploids (Figure 3.4A), we see that having two copies of a gene generally improves I by ∼0.05-0.20 bits. For example, on going from haploid (1x) to diploid (2x), *HXK1* I_{AM} increases from 1.30 to 1.47 bits. Therefore, in terms of information transduction, being diploid confers a small but robust advantage.

3.3.6 Circuits integrating the response of two genes can transduce more information than single gene circuits

So far we have considered information transduction from Msn2 to a single gene. Yet, Msn2 controls the expression of hundreds of genes in response to different stresses (Elfving *et al.*, 2014; Hao & O'Shea, 2012; Huebert *et al.*, 2012). We therefore extend our approach

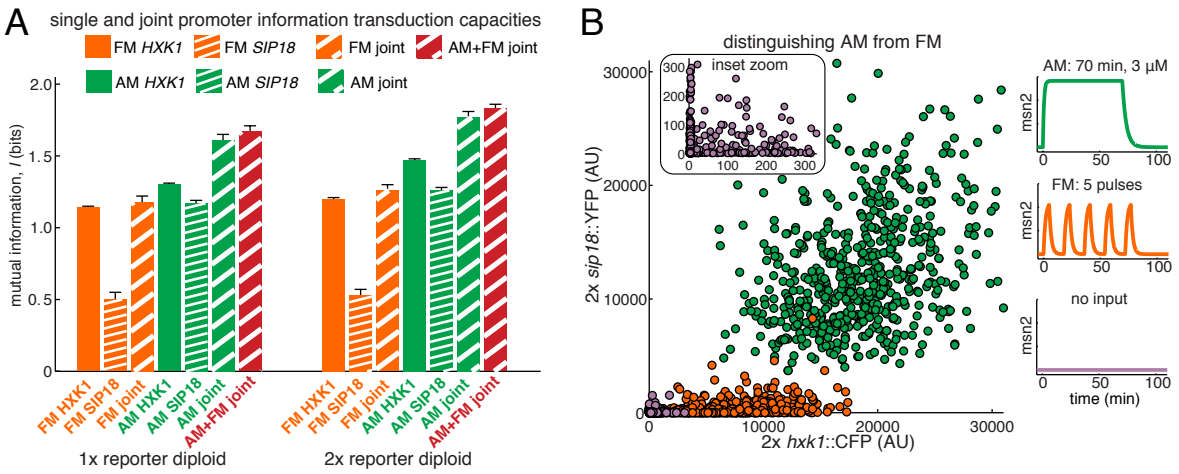

Figure 3.4: *Integrating the response of more than one gene improves information transmission*
(A) The AM and FM experiments (Figure 3.2) were repeated for diploid strains containing either one copy (1x) of the *hxk1*::CFP and *sip18*::YFP reporters or two copies (2x) of the *hxk1*::CFP and *sip18*::YFP reporters and individual and joint mutual information determined (full details on calculations are given in Appendix C).
(B) 2x *sip18*::YFP vs. 2x *hxk1*::CFP scatterplot showing expression for three experiments: no input (light purple), five 5-min pulses of 690 nM 1-NM-PP1 separated by 13-min intervals (orange) or one 70-min pulse of 3 μM 1-NM-PP1 (green). For each condition, 600 cells are shown. The YFP/CFP expression is the maximal value after each time-trace has reached a plateau. The inset shows a zoom-in highlighting the 'no input' condition.
All raw single-cell time-lapse microscopy source data for the 1x reporter diploid (21236 cells) and 2x reporter diploid (19222 cells) for this figure is available online at Dryad Digital Repository (Hansen & O'Shea, 2015).

to information transduction from Msn2 to multiple genes. We next asked whether one way the cell might overcome the low I of individual genes would be to integrate the response of two or more different genes. To simulate and test this, we used diploid strains with both *hxk1*::CFP and *sip18*::YFP in the same cell, which allows us to measure the joint mutual information, $I(R_1, R_2; S)$.

We find that the AM joint mutual information ($I_{\mathrm{AM,joint}}$) is significantly higher in both the 1x and 2x cases than the individual I_{AM} of *HXK1* and *SIP18* (Figure 3.4A). For example, the total joint mutual information ($I_{\mathrm{AM+FM,joint}}$; combining both the AM and FM responses) is 1.67 bits and 1.83 bits for the 1x and 2x diploids, respectively (Figure 3.4A). For example, although *HXK1* and *SIP18* individually can only distinguish ON from OFF without error (Figure 3.2A), their joint response can distinguish three inputs (no input, FM or AM) nearly without error (Figure 3.4B).

Thus, these results show that although the information transduction capacities of individ-

ual genes may be low, by integrating the response of two different genes the cell can improve information transduction. Therefore, by integrating the response of even more than two genes, the cell could potentially substantially improve the information transduction capacity of a pathway.

3.4 Discussion

Here we use information theory to investigate the hypothesis that cells can transduce both signal identity and signal intensity information in the amplitude and frequency of TF activation dynamics to control gene expression. As a conceptual framework, we introduce two extreme models of information transmission (Figure 3.1C): in the noisy switch model, the cell only transmits information sufficient to turn ON or OFF particular genes or pathways in response to external signals or stresses, whereas in the rheostat model the cell is accurately fine-tuning the expression levels of relevant genes to the intensity of a signal or stress. For a TF responding to multiple stresses, we can extend this framework beyond a single gene. Extending the noisy switch model to two genes, the stress-relevant gene *HXK1* is reliably induced during FM pulsing of Msn2 (as seen under glucose limitation), whereas both *HXK1* and the stress-relevant *SIP18* gene are reliably induced during AM activation of Msn2 (as seen under oxidative stress) (Figure 3.4B). Therefore, three inputs (no input, FM or AM) can be distinguished essentially without error (Figure 3.4B). However, given the modest joint information transduction capacities with respect to AM and FM combined ($I_{\mathrm{AM+FM,joint}}$; Figure 3.4A), the cell cannot fine-tune *HXK1* and *SIP18* expression levels to stress intensity without significant error. Thus, signal identity information for two distinct stresses can be transduced in the amplitude and frequency of Msn2 essentially without error, but intensity information can only be transduced with high error.

A central result in information theory is that the information transduction capacity of a signaling pathway is limited by and equal to the capacity of its weakest node or bottleneck (see also Appendix C for a discussion). In other words, once information has been lost, no amount of post-processing can recover it, as is seen in the game of broken telephone. Therefore, by measuring information transduction of individual Msn2 target genes to be ∼1.0-1.3 bits, we can establish that the expression of Msn2 target genes cannot transduce stress signal intensity information without significant error at least for the AM and FM signals studied here — we can draw this conclusion without knowing all the relevant upstream components of the signaling pathway, how they mechanistically interact and how much information they can transmit. Thus, this approach can provide insight into the purpose of a pathway (e.g. noisy switch vs. rheostat) and can readily be applied to other signaling pathways.

Why does information transduction by Msn2 resemble a noisy switch rather than a rheostat? Or phrased differently, why should the cell not fine-tune the expression level of stress genes to the stress intensity? One possibility is that the stochasticity inherent in the biophysical process of transcription fundamentally constrains information transduction by a promoter to ∼1.0-1.3 bit. However, since the information transduction capacity of *SIP18* can be substantially increased by modulating promoter *cis*-elements (Figure 3.2 and 3.3), the low I of natural Msn2 target genes is not solely due to inherent biophysical constraints. Another speculative possibility is that variability is selected for: since evolutionary selection works at the population-level, variability in gene expression can create phenotypic diversity within an isogenic population (Balaban *et al.*, 2004; Blake *et al.*, 2006). It is also important to note that under natural stress a network of factors could be activated, whereas here we study the limits on amplitude- and frequency-mediated transduction of gene expression

information in the dynamics of a single master transcription factor.

Many biological signaling pathways transmit information through the amplitude or frequency of a shared signaling molecule (Figure 3.1A) and this has raised the long-standing question: can more information be transmitted through the amplitude or the frequency of a signaling molecule (Li & Goldbeter, 1989; Rapp *et al.*, 1981)? This question has not previously been experimentally addressed for transcription factors responding to multiple signals in an amplitude- or frequency-dependent manner. We show that more gene expression information can be transduced through the amplitude than through the frequency of Msn2 activation dynamics for all genes studied here (Figure 3.2 and 3.3). Although the FM dose-responses tend to be more linear, the AM dose-responses have higher dynamic range and lower noise (Figure 3.2 and Figure B.1D). While we show that gene promoters have higher information transduction capacities for amplitude- than frequency-encoded information (Figure 3.2 and 3.3), maximal information transduction can be achieved for transcription factors that exhibit both amplitude- and frequency-encoding (Figure 3.4).

The amount of information promoters measured in this study can transmit is limited (Figure 3.2-3.4); yet we stress that for many "house-keeping" genes or genes expressed at steady-state information transduction is likely significantly higher, in part due to time-averaging. Indeed, the gene expression response to a transient signal is noisier than a response at steady-state (Hansen & O'Shea, 2013) and inducible genes tend to show higher expression noise (Bar-Even *et al.*, 2006; Newman *et al.*, 2006). One way the cell can improve information transduction is by integrating the response of more than one gene (Figure 3.4) or by having multiple copies of a gene (Figure 3.4B). An example of this is ribosome biogenesis where, by having multiple copies of each gene encoding a subunit and employing elaborate feedback control, the cell can fine-tune its translational capability to its growth and energy status

(Lempiainen & Shore, 2009). Another example is morphogen or cytokine secretion: although the amount produced by each single cell might be noisy, the average amount produced by a large number of cells can be highly precise (Cheong *et al.*, 2011; Gregor *et al.*, 2007). Hence, a number of strategies for increasing information transmission exist.

In conclusion, we have investigated the reliability of transmitting gene expression information in the amplitude and frequency of a TF. We show that the information transduction capacity of a gene can be tuned in *cis* and the amount of information transmitted increased by integrating the response of multiple genes. Nonetheless, for individual genes our results are consistent with the Msn2 pathway transmitting essentially error-free signal identity information, but unreliable signal intensity information, and therefore functioning more like a noisy switch than a rheostat. Since many similar master regulators, such as p53, NF-$\varkappa$B, ERK and Hes1, also transduce information through regulation of signaling dynamics, it will be interesting to investigate whether dynamic cell signaling is generally limited to error-free transduction of only signal identity information.

3.5 Materials and methods

Strains

All *Saccharomyces cerevisiae* strains used in this work are in the W303 background and a list of strains is given in table B.1. Information about how they were constructed is given in Appendix B.2.2.

Microfluidics and time-lapse microscopy

The microscopy experiments were performed essentially as described elsewhere (Hansen & O'Shea, 2013; Chapter 4). Briefly, yeast cells were grown overnight at 30°C with shaking

at 180 RPM to an $OD_{600\,nm}$ of ca. 0.1 in low fluorescence medium, quickly collected by suction filtration, loaded into the five channels of a microfluidics device pretreated with concanavalin A and the setup mounted on a Zeiss AxioObserver Z1 inverted fluorescence microscope equipped with an Evolve EM-CCD camera (Photometrics), 63x oil-immersion objective (NA 1.4, Plan-Apochromat), Zeiss Colibri LEDs and an incubation chamber kept at 30°C. Solenoid valves programmed using custom-written software (MATLAB) control whether medium with or without 1-NM-PP1 is delivered to each microfluidic channel and the flow (ca. 1 μL/s) was driven by gravity. Control of 1-NM-PP1 delivery enables control of Msn2 pulsing (Figure 3.2) and a unique pulse sequence can be delivered to each of the five microfluidics channels. The microscope maintains focus and moves between each channel to acquire phase-contrast, YFP, CFP, RFP and iRFP images for 64 frames with a 2.5 min time resolution. Full details are given in Chapter 4. Control software for the microfluidic device is available upon request. All raw single-cell data is available online at Dryad Digital Repository (Hansen & O'Shea, 2015).

Image analysis

Image analysis was performed using custom-written software (`MATLAB`) that segments, tracks and quantifies single-cell time-traces. To convert time-series data into a scalar (max YFP in Figure 3.2), the single-cell time-traces were smoothed using moving-average smoothing and the fluorescence (in AU) is the mean pixel-intensity per cell corresponding to the YFP concentration. Image analysis software is available upon request. Full details are given in Appendix A.2.10 and Chapter 4.

Computation of mutual information

The mutual information for a single reporter is defined in equation 3.1 and the maximal mutual information given by:

$$I\left(R;S\right)=\max_{P(S)}\left[MI\left(R;S\right)\right]\quad\text{for}\quad\sum_{i}P(S_i)=1;\quad P(S_i)\geq 0 \tag{3.2}$$

The $P(S)$ that maximizes the mutual information is determined using the iterative Blahut-Arimoto algorithm. An unbiased I was estimated using jackknife sampling to correct for undersampling as has previously been described (Cheong et al., 2011; Slonim et al., 2005; Strong et al., 1998). The data were discretized by binning as shown in Figure 3.2. Maximal mutual information, I, and its error are reported as the mean and standard deviation, respectively, from calculating the unbiased I using 15 to 35 bins, inclusive. To determine the maximal joint mutual information, I (Figure 3.4B), first consider the joint mutual information between the signal S and two responses R_1 (e.g. YFP) and R_2 (e.g. CFP):

$$MI\left(R_1,R_2;S\right)=MI\left(R_1;S\right)+MI\left(R_2;S|R_1\right) \tag{3.3}$$

Where $MI(R_1;S)$ is known from equation 3.1 and $MI(R_2;S|R_1)$ is given by:

$$\begin{aligned}MI\left(R_2;S|R_1\right)=&\sum_{i}\sum_{j}\sum_{k}P\left(R_1=r_i,R_2=r_j,S=s_k\right)\\&\cdot\log_2\left(\frac{P\left(R_1=r_i\right)P\left(R_1=r_i,R_2=r_j,S=s_k\right)}{P\left(R_1=r_i,R_2=r_j\right)P\left(R_1=r_i,S=s_k\right)}\right)\end{aligned} \tag{3.4}$$

The maximal joint mutual information is then given by:

$$I\left(R_1,R_2;S\right)=\max_{P(S)}\left[MI\left(R_1,R_2;S\right)\right]\quad\text{for}\quad\sum_{i}P(S_i)=1;\quad P(S_i)\geq 0 \tag{3.5}$$

As before, $P(S)$ is obtained using the Blahut-Arimoto algorithm and the mean and error of I is obtained as for a single reporter, except using 8 to 20 bins, inclusive. Full details are given in Appendix C.

Algorithm to estimate the intrinsic mutual information

Briefly, the total, intrinsic and extrinsic noise for each condition is calculated using dual-reporters (CFP/YFP) (Elowitz *et al.*, 2002; Swain *et al.*, 2002). The expression distributions in the absence of extrinsic noise are required to determine I_{int}. This is an intractable problem (Hilfinger & Paulsson, 2011). To estimate it, the raw, empirical YFP distribution is fitted to a gamma distribution ($X \sim \Gamma(a, b)$). Keeping the mean fixed, a new gamma distribution representing the YFP response in the absence of extrinsic noise is then inferred by filtering out the extrinsic contribution to the variance. This is repeated for each condition, each distribution is then discretized and the maximal mutual information, I, determined as above.

The accuracy of the algorithm was tested by simulating five linear and five non-linear stochastic gene expression models for both a fast and a slow promoter using the Gillespie algorithm under amplitude modulation (10 conditions). Extrinsic noise is added by picking the translation rate and transcription factor concentration for each iteration from a gamma distribution. The algorithm was then applied to each data set with extrinsic noise and compared to simulation results with only intrinsic noise and the error calculated. In all 80 cases (10 models, 2 promoters, 4 levels of extrinsic noise), the error was less than 5% (in bits) and the mean error was less than 2%. Full details are given in Appendix C.

Acknowledgements

We thank Raymond Cheong, Gasper Tkacik and Mikhail Tikhonov for insightful discussions. We thank Nan Hao, Dann Huh, Arvind Subramaniam, Matthew Brennan, Roshni Wadhwani, Andrian Gutu, Shankar Mukherji, Kapil Amarnath, Bodo Stern, Sharad Ramanathan and members of the O'Shea lab for discussions and critically reading the manuscript. This work was performed in part at the Center for Nanoscale Systems at Harvard Univer-

sity, a member of the National Nanotechnology Infrastructure Network (NNIN), which is supported by the National Science Foundation under NSF award no. ECS-0335765. Image analysis and model simulations were run on the Odyssey cluster supported by the FAS Division of Science, Research Computing Group at Harvard University. The Howard Hughes Medical Institute supported this work.

3.6 Chapter 3 references

Albeck, J.G., Mills, G.B., & Brugge, J.S. (2013). Frequency-modulated pulses of ERK activity transmit quantitative proliferation signals. *Mol Cell* **49**: 249-261.

Aoki, K., Kamioka, Y., & Matsuda, M. (2013). Fluorescence resonance energy transfer imaging of cell signaling from in vitro to in vivo: basis of biosensor construction, live imaging, and image processing. *Dev Growth Differ* **55**: 515-522.

Balaban, N.Q., Merrin, J., Chait, R., Kowalik, L., & Leibler, S. (2004). Bacterial persistence as a phenotypic switch. *Science* **305**: 1622-1625.

Bar-Even, A., Paulsson, J., Maheshri, N., Carmi, M., O'Shea, E., Pilpel, Y., & Barkai, N. (2006). Noise in protein expression scales with natural protein abundance. *Nat Genet* **38**: 636-643.

Batchelor, E., Loewer, A., Mock, C., & Lahav, G. (2011). Stimulus-dependent dynamics of p53 in single cells. *Mol Syst Biol* **7**.

Behar, M., Dohlman, H.G., & Elston, T.C. (2007). Kinetic insulation as an effective mechanism for achieving pathway specificity in intracellular signaling networks. *P Natl Acad Sci USA* **104**: 16146-16151.

Behar, M., & Hoffmann, A. (2010). Understanding the temporal codes of intra-cellular signals. *Curr Opin Genet Dev* **20**: 684-693.

Berridge, M.J., Lipp, P., & Bootman, M.D. (2000). The versatility and universality of calcium signalling. *Nat Rev Mol Cell Biol* **1**: 11-21.

Bishop, A.C., Ubersax, J.A., Petsch, D.T., Matheos, D.P., Gray, N.S., Blethrow, J., Shimizu, E., Tsien, J.Z., Schultz, P.G., Rose, M.D., *et al.* (2000). A chemical switch for inhibitor-sensitive alleles of any protein kinase. *Nature* **407**, 395-401.

Blake, W.J., Balazsi, G., Kohanski, M.A., Isaacs, F.J., Murphy, K.F., Kuang, Y., Cantor, C.R., Walt, D.R., & Collins, J.J. (2006). Phenotypic consequences of promoter-mediated transcriptional noise. *Mol Cell* **24**: 853-865.

Bowsher, C.G., & Swain, P.S. (2012). Identifying sources of variation and the flow of information in biochemical networks. *P Natl Acad Sci USA* **109**: E1320-E1328.

Bowsher, C.G., & Swain, P.S. (2014). Environmental sensing, information transfer, and cellular decision-making. *Curr Opin Biotech* **28**: 149-155.

Cai, L., Dalal, C.K., & Elowitz, M.B. (2008). Frequency-modulated nuclear localization bursts coordinate gene regulation. *Nature* **455**: 485-490.

Cheong, R., Rhee, A., Wang, C.J., Nemenman, I., & Levchenko, A. (2011). Information transduction capacity of noisy biochemical signaling networks. *Science* **334**: 354-358.

Coulon, A., Chow, C.C., Singer, R.H., & Larson, D.R. (2013). Eukaryotic transcriptional dynamics: from single molecules to cell populations. *Nature reviews Genetics* **14**: 572-584.

Cover, T.M., & Thomas, J.A. (2006). Elements of information theory. 2nd edition (Hoboken, N.J., Wiley-Interscience).

Csete, M., & Doyle, J. (2004). Bow ties, metabolism and disease. *Trends Biotechnol* **22**: 446-450.

Dalal, C.K., Cai, L., Lin, Y.H., Rahbar, K., & Elowitz, M.B. (2014). Pulsatile Dynamics in the Yeast Proteome. *Current Biology* **24**: 2189-2194.

de Nadal, E., Ammerer, G., & Posas, F. (2011). Controlling gene expression in response to stress. *Nature reviews Genetics* **12**: 833-845.

de Ronde, W., & ten Wolde, P.R. (2014). Multiplexing oscillatory biochemical signals. *Phys Biol* **11**.

de Ronde, W., Tostevin, F., & ten Wolde, P.R. (2011). Multiplexing biochemical signals. *Phys Rev Lett* **107**: 048101.

Dubuis, J.O., Tkacik, G., Wieschaus, E.F., Gregor, T., & Bialek, W. (2013). Positional information, in bits. *P Natl Acad Sci USA* **110**: 16301-16308.

Elfving, N., Chereji, R.V., Bharatula, V., Bjorklund, S., Morozov, A.V., & Broach, J.R. (2014). A dynamic interplay of nucleosome and Msn2 binding regulates kinetics of gene activation and repression following stress. *Nucleic Acids Res* **42**: 5468-5482.

Elowitz, M.B., Levine, A.J., Siggia, E.D., & Swain, P.S. (2002). Stochastic gene expression in a single cell. *Science* **297**: 1183-1186.

Ferrell, J.E., Jr., & Machleder, E.M. (1998). The biochemical basis of an all-or-none cell fate switch in Xenopus oocytes. *Science* **280**: 895-898.

Gregor, T., Tank, D.W., Wieschaus, E.F., & Bialek, W. (2007). Probing the limits to positional information. *Cell* **130**: 153-164.

Hansen, A.S., & O'Shea, E.K. (2013). Promoter decoding of transcription factor dynamics involves a trade-off between noise and control of gene expression. *Mol Syst Biol* **9**.

Hansen, A.S., & O'Shea, E.K. (2015). Data from: Limits on information transduction through regulation of signaling dynamics. *Dryad Digital Repository*.

Hao, N., Budnik, B.A., Gunawardena, J., & O'Shea, E.K. (2013). Tunable Signal Processing Through Modular Control of Transcription Factor Translocation. *Science* **339**: 460-464.

Hao, N., & O'Shea, E.K. (2012). Signal-dependent dynamics of transcription factor translocation controls gene expression. *Nat Struct Mol Biol* **19**: 31-39.

Harima, Y., Imayoshi, I., Shimojo, H., Kobayashi, T., & Kageyama, R. (2014). The roles and mechanism of ultradian oscillatory expression of the mouse Hes genes. *Semin Cell Dev Biol* **34**: 85-90.

Herrero, P., Galindez, J., Ruiz, N., Martinezcampa, C., & Moreno, F. (1995). Transcriptional Regulation of the Saccharomyces-Cerevisiae Hxk1, Hxk2 and Glk1 Genes. *Yeast* **11**: 137-144.

Hilfinger, A., & Paulsson, J. (2011). Separating intrinsic from extrinsic fluctuations in dynamic biological systems. *P Natl Acad Sci USA* **108**: 12167-12172.

Huebert, D.J., Kuan, P.F., Keles, S., & Gasch, A.P. (2012). Dynamic Changes in Nucleosome Occupancy Are Not Predictive of Gene Expression Dynamics but Are Linked to Transcription and Chromatin Regulators. *Mol Cell Biol* **32**: 1645-1653.

Imayoshi, I., Isomura, A., Harima, Y., Kawaguchi, K., Kori, H., Miyachi, H., Fujiwara, T., Ishidate, F., & Kageyama, R. (2013). Oscillatory Control of Factors Determining Multipotency and Fate in Mouse Neural Progenitors. *Science* **342**: 1203-1208.

Jacquet, M., Renault, G., Lallet, S., De Mey, J., & Goldbeter, A. (2003). Oscillatory nucleocytoplasmic shuttling of the general stress response transcriptional activators Msn2 and Msn4 in Saccharomyces cerevisiae. *The Journal of cell biology* **161**: 497-505.

Lahav, G., Rosenfeld, N., Sigal, A., Geva-Zatorsky, N., Levine, A.J., Elowitz, M.B., & Alon, U. (2004). Dynamics of the p53-Mdm2 feedback loop in individual cells. *Nat Genet* **36**: 147-150.

Lempiainen, H., & Shore, D. (2009). Growth control and ribosome biogenesis. *Curr Opin Cell Biol* **21**: 855-863.

Lestas, I., Vinnicombe, G., & Paulsson, J. (2010). Fundamental limits on the suppression of molecular fluctuations. *Nature* **467**: 174-178.

Levchenko, A., & Nemenman, I. (2014). Cellular noise and information transmission. *Curr Opin Biotech* **28**: 156-164.

Levine, J.H., Lin, Y.H., & Elowitz, M.B. (2013). Functional Roles of Pulsing in Genetic Circuits. *Science* **342**: 1193-1200.

Li, Y., & Goldbeter, A. (1989). Frequency specificity in intercellular communication. Influence of patterns of periodic signaling on target cell responsiveness. *Biophys J* **55**: 125-145.

Mc Mahon, S.S., Sim, A., Filippi, S., Johnson, R., Liepe, J., Smith, D., & Stumpf, M.P. (2014). Information theory and signal transduction systems: From molecular information processing to network inference. *Semin Cell Dev Biol* **35**: 98-108.

Mehta, P., Goyal, S., Long, T., Bassler, B.L., & Wingreen, N.S. (2009). Information processing and signal integration in bacterial quorum sensing. *Mol Syst Biol* **5**: 325.

Nemenman, I. (2012). Information theory and adaptation. In *Quantitative Biology: From Molecular to Cellular Systems*, M.E. Wall, ed. (CRC Press).

Newman, J.R.S., Ghaemmaghami, S., Ihmels, J., Breslow, D.K., Noble, M., DeRisi, J.L., & Weissman, J.S. (2006). Single-cell proteomic analysis of S-cerevisiae reveals the architecture of biological noise. *Nature* **441**: 840-846.

Petrenko, N., Chereji, R.V., McClean, M.N., Morozov, A.V., & Broach, J.R. (2013). Noise and interlocking signaling pathways promote distinct transcription factor dynamics in response to different stresses. *Mol Biol Cell* **24**: 2045-2057.

Purvis, J.E., & Lahav, G. (2013). Encoding and Decoding Cellular Information through Signaling Dynamics. *Cell* **152**: 945-956.

Rapp, P.E., Mees, A.I., & Sparrow, C.T. (1981). Frequency encoded biochemical regulation is more accurate than amplitude dependent control. *J Theor Biol* **90**: 531-544.

Rhee, A., Cheong, R., & Levchenko, A. (2012). The application of information theory to biochemical signaling systems. *Phys Biol* **9**, 045011.

Rieckh, G., & Tkacik, G. (2014). Noise and information transmission in promoters with multiple internal States. *Biophys J* **106**: 1194-1204.

Rodriguez-Porrata, B., Carmona-Gutierrez, D., Reisenbichler, A., Bauer, M., Lopez, G., Escote, X., Mas, A., Madeo, F., & Cordero-Otero, R. (2012). Sip18 hydrophilin prevents yeast cell death during desiccation stress. *J Appl Microbiol* **112**: 512-525.

Sanchez, A., & Golding, I. (2013). Genetic determinants and cellular constraints in noisy gene expression. *Science* **342**: 1188-1193.

Selimkhanov, J., Taylor, B., Yao, J., Pilko, A., Albeck, J., Hoffmann, A., Tsimring, L., & Wollman, R. (2014). Accurate information transmission through dynamic biochemical signaling networks. *Science* **346**: 1370-1373.

Shannon, C.E. (1948). A Mathematical Theory of Communication. *AT&T Tech J* **27**: 623-656.

Skerker, J.M., Perchuk, B.S., Siryaporn, A., Lubin, E.A., Ashenberg, O., Goulian, M., & Laub, M.T. (2008). Rewiring the specificity of two-component signal transduction systems. *Cell* **133**: 1043-1054.

Slonim, N., Atwal, G.S., Tkacik, G., & Bialek, W. (2005). Information-based clustering. *P Natl Acad Sci USA* **102**: 18297-18302.

Strong, S.P., Koberle, R., van Steveninck, R.R.D., & Bialek, W. (1998). Entropy and information in neural spike trains. *Phys Rev Lett* **80**: 197-200.

Swain, P.S., Elowitz, M.B., & Siggia, E.D. (2002). Intrinsic and extrinsic contributions to stochasticity in gene expression. *P Natl Acad Sci USA* **99**: 12795-12800.

Tkacik, G., Callan, C.G., Jr., & Bialek, W. (2008). Information flow and optimization in transcriptional regulation. *P Natl Acad Sci USA* **105**: 12265-12270.

Tkacik, G., & Walczak, A.M. (2011). Information transmission in genetic regulatory networks: a review. *J Phys Condens Matter* **23**: 153102.

Tkacik, G., Walczak, A.M., & Bialek, W. (2009). Optimizing information flow in small genetic networks. *Phys Rev E* **80**.

Toettcher, J.E., Weiner, O.D., & Lim, W.A. (2013). Using optogenetics to interrogate the dynamic control of signal transmission by the Ras/Erk module. *Cell* **155**: 1422-1434.

Tostevin, F., & ten Wolde, P.R. (2009). Mutual information between input and output trajectories of biochemical networks. *Phys Rev Lett* **102**: 218-101.

Tostevin, F., ten Wolde, P.R., & Howard, M. (2007). Fundamental limits to position determination by concentration gradients. *PLoS Comput Biol* **3**: e78.

Uda, S., Saito, T.H., Kudo, T., Kokaji, T., Tsuchiya, T., Kubota, H., Komori, Y., Ozaki, Y., & Kuroda, S. (2013). Robustness and compensation of information transmission of signaling pathways. *Science* **341**: 558-561.

Voliotis, M., Perrett, R.M., McWilliams, C., McArdle, C.A., & Bowsher, C.G. (2014). Information transfer by leaky, heterogeneous, protein kinase signaling systems. *P Natl Acad Sci USA* **111**: E326-333.

Waltermann, C., & Klipp, E. (2011). Information theory based approaches to cellular signaling. *Biochim Biophys Acta* **1810**: 924-932.

Warmflash, A., Zhang, Q.X., Sorre, B., Vonica, A., Siggia, E.D., & Brivanlou, A.H. (2012). Dynamics of TGF-beta signaling reveal adaptive and pulsatile behaviors reflected in the nuclear localization of transcription factor Smad4. *P Natl Acad Sci USA* **109**: E1947-E1956.

Werner, S.L., Barken, D., & Hoffmann, A. (2005). Stimulus specificity of gene expression programs determined by temporal control of IKK activity. *Science* **309**: 1857-1861.

Yosef, N., & Regev, A. (2011). Impulse Control: Temporal Dynamics in Gene Transcription. *Cell* **144**: 886-896.

Zaman, S., Lippman, S.I., Schneper, L., Slonim, N., & Broach, J.R. (2009). Glucose regulates transcription in yeast through a network of signaling pathways. *Mol Syst Biol* **5**.

Ziv, E., Nemenman, I., & Wiggins, C.H. (2007). Optimal signal processing in small stochastic biochemical networks. *Plos One* **2**: e1077.

Chapter 4

High-throughput microfluidics to control and measure signaling dynamics in single yeast cells

4.1 Abstract

Microfluidics coupled to quantitative time-lapse fluorescence microscopy is transforming our ability to control, measure, and understand signaling dynamics in single living cells. Here we describe a pipeline that incorporates high-throughput microfluidic cell culture, automated programmable fluid handling for cell stimulation, quantitative time-lapse microscopy, and computational analysis of time-lapse movies. We illustrate how this setup can be used to control the nuclear localization of the budding yeast transcription factor Msn2. Using this protocol, we generate oscillations of Msn2 localization and measure the dynamic gene expression response of individual genes in single cells. The protocol allows a single researcher to perform up to 20 different experiments in a single day, whilst collecting data for thousands

of single cells. The protocol can be widely used to control and monitor single-cell signaling dynamics in other signal transduction systems in microorganisms.

4.2 Introduction

Fluorescence microscopy has become a standard laboratory tool and live-cell imaging of signaling dynamics (Batchelor *et al.*, 2011; Selimkhanov *et al.*, 2014), protein translocation (Cai *et al.*, 2014; Cai *et al.*, 2008; Hao *et al.*, 2013; Yissachar *et al.*, 2013), and cell-fate choice (Imayoshi *et al.*, 2013) is increasingly becoming routine (Spiller *et al.*, 2010). This has led to a greater appreciation of the importance of dynamics in signal transduction, control of cell fate (Behar & Hoffmann, 2010; Castillo-Hair *et al.*, 2015; Levine *et al.*, 2013; Purvis & Lahav, 2013), and heterogeneity (Sanchez & Golding, 2013). However, traditional live-cell imaging approaches suffer from an inability to maintain constant extracellular conditions and cannot make precisely controlled perturbations.

Microfluidics largely overcomes these limitations by combining chemostatic cell culture with the ability to make perturbations with exquisite spatiotemporal control (Bennett & Hasty, 2009; Ferry *et al.*, 2011; Sackmann *et al.*, 2014). Additionally, since microfluidics is highly amenable to automation and only requires small culture medium volumes, it is ideally suited for multiplexing, which vastly improves reliability and throughput (Denervaud *et al.*, 2013; Hansen & O'Shea, 2013). Combined with automated image analysis, it is therefore possible to obtain time-lapse data sets of cell signaling at an unprecedented scale (Denervaud *et al.*, 2013; Hansen & O'Shea, 2013; Selimkhanov *et al.*, 2014; Tseng *et al.*, 2014). From a synthetic biology point-of-view, microfluidics provides unprecedented control of cellular behavior (Prindle et al., 2014) including long-term control of gene expression in single cells (Menolascina *et al.*, 2014; Uhlendorf *et al.*, 2012). Applications of microfluidics coupled to

time-lapse microscopy have yielded important insights into signaling dynamics (Hao *et al.*, 2008; Hao & O'Shea, 2012; Hersen *et al.*, 2008; Mettetal *et al.*, 2008; Sorre *et al.*, 2014), spatial control of gene expression (Cohen *et al.*, 2012) and how cells monitor and respond to changes in their environment (Bennett *et al.*, 2008). More widespread adoption of microfluidics coupled to time-lapse microscopy is therefore set to transform our understanding of signaling dynamics inside living cells.

Combining microfluidics (Hersen *et al.*, 2008) with time-lapse microscopy, we previously discovered that the budding yeast general stress response transcription factor, Msn2, encodes information about external stresses in its translocation dynamics (Hao *et al.*, 2013; Hao & O'Shea, 2012; Petrenko *et al.*, 2013). To systematically investigate how downstream genes respond to different Msn2 dynamics, we developed an automated high-throughput microfluidic device, which we describe in this protocol (Figure 4.1). The device enabled us to perform 4-color quantitative time-lapse microscopy, where we followed more than 100,000 single cells over time and controlled and quantified Msn2-mCherry translocation dynamics while measuring gene expression dynamics using fluorescent reporters (CFP and YFP) at high time-resolution (Hansen & O'Shea, 2013). From these studies, we found that it is possible to induce multiple distinct gene expression programs simply by regulating the dynamics of Msn2 (Hansen & O'Shea, 2013).

Here we provide our protocol. We describe how to design and fabricate the microfluidic device, how to set up control valves for automated fluid handling, and provide software to interface valves with `MATLAB`. We describe how to set up automated time-lapse microscopy experiments and analyze the resulting time-lapse movies. Compared to other approaches, this protocol is simple and easy to adopt. With this protocol it is possible to conduct 20 different time-lapse experiments in a single day generating data for thousands of single cells.

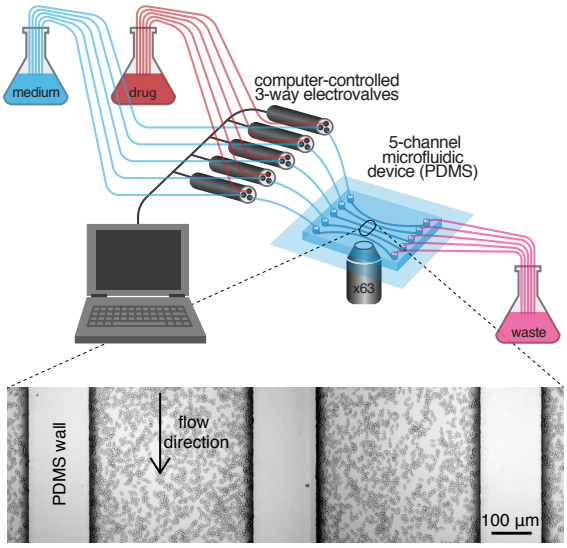

Figure 4.1: *Overview of microfluidic setup*
Microfluidic device. Five computer-controlled solenoid valves control whether normal medium or stress medium (e.g. with drug) is delivered to yeast cells grown in five microfluidic channels. Simultaneously, protein translocation dynamics and/or gene expression responses are recorded from all five channels using time-lapse microscopy. Thus, five separate perturbations can be multiplexed in a single experiment. Below, a cropped brightfield image of budding yeast cells growing in microfluidic channels (two images stitched horizontally together). Two full and two partial microfluidic channels (400 µm wide) are shown with a high density of cells growing in them. Each microfluidic channel is separated by PDMS walls (150 µm wide) and the direction of medium flow is from top to bottom.
Adapted from Hansen & OShea (Hansen & O'Shea, 2013) with permission from *EMBO*.

4.2.1 Applications of the method

In this protocol we describe how to use a multiplexed microfluidics device to investigate signaling dynamics in *S. cerevisiae* (Figure 4.1). This protocol will be useful for any short-to-medium term (≤5-6 h) perturbation experiment (involving e.g. a change in medium such as osmotic shock exposure or exposure to a drug) with a fluorescent readout (e.g. a change in gene expression or subcellular localization). Cells are grown in five microfluidic channels that can be independently controlled: thus perturbation and control experiments can be performed side-by-side or multiple conditions for the same or different strains can be investigated in a single experiment.

As an example application we describe here a typical experiment. Msn2 localization is regulated by PKA phosphorylation. By expanding the ATP binding pocket of PKA, we can inhibit PKA kinase activity with a small molecule, 1-NM-PP1 (Bishop *et al.*, 2000;

Zaman *et al.*, 2009). Addition of 1-NM-PP1 leads to rapid nuclear localization of Msn2 and by controlling 1-NM-PP1 exposure, we have full control of Msn2 localization (Hansen & O'Shea, 2013; Hao *et al.*, 2013; Hao & O'Shea, 2012). To quantify Msn2 localization we use an Msn2-mCherry fusion protein and to segment the nucleus we use an infrared nuclear marker (NHP6a-iRFP) (Filonov *et al.*, 2011; Hansen & O'Shea, 2013). To quantify gene expression and intrinsic and extrinsic noise (Elowitz *et al.*, 2002), we replace the ORF of Msn2 target genes with fast-maturing CFP and YFP fluorescent proteins ($\tau_{\text{maturation}} \sim 8-10$ min at 30°C) in diploid cells. A typical experiment is shown in Figure 4.2. Cells were exposed to six 5-min pulses of 690 nM 1-NM-PP1 with 10-min intervals (Figure 4.2B) and YFP (Figure 4.2C) and CFP (Figure 4.2D) gene expression measured in each of ∼100 single cells over time with minimal measurement noise. In addition to studying the average level of gene expression, from these measurements we can also quantify intrinsic and extrinsic noise (Elowitz *et al.*, 2002) in gene expression (Figure 4.2E).

To retain cells during time-lapse experiments, we coat the cover glass with concanavalin A — a lectin that binds cell surface saccharides (Agrawal & Goldstein, 1968; Bisaria *et al.*, 2014; Senear & Teller, 1981). This works well for yeast but is also suitable for other microorganisms including cyanobacteria. With the ever-increasing number of fluorescence-based sensors and reporters (Bermejo *et al.*, 2011; Dean & Palmer, 2014; Huh *et al.*, 2003; Strack *et al.*, 2014), our method is therefore applicable to studies involving changes in gene expression (Hansen & O'Shea, 2013; Hao & O'Shea, 2012), changes in protein localization (Hao & O'Shea, 2012; Petrenko *et al.*, 2013), changes in RNA localization (Zid & O'Shea, 2014), changes in metabolite levels (Paige *et al.*, 2012) or any other process with a fluorescent read-out in a range of microorganisms.

Finally, we highlight that the analogue-sensitive kinase strategy (Bishop *et al.*, 2000)

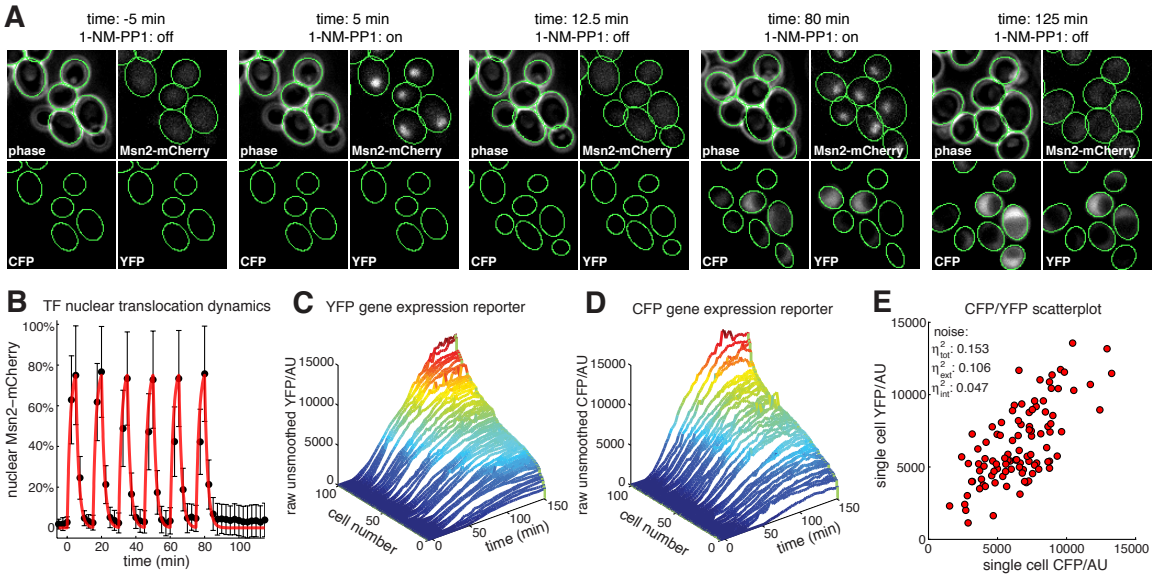

Figure 4.2: *A typical experiment*
(A) Raw phase contrast (top left), Msn2-mCherry (top right), CFP expression (bottom left), and YFP expression (bottom right) images are shown for five timepoints. Small (99 x 99 pixels) sections of full images are shown. The cell segmentation is overlaid in green. The raw data in **(A)** and the quantified data in **(B-E)** are from the same time-lapse experiment. Images have been contrast adjusted, but not adjusted for photobleaching, which is why later Msn2-mCherry and YFP images appear less bright. CFP shows much lower photobleaching than YFP and therefore appears brighter in later frames. Msn2-mCherry nuclear localization is visible as nuclear foci in frame 2 and 4. Cell growth and movement is visible between frames. The cell segmentation algorithm fits the yeast cell phase ring to an ellipse. Frames with slight segmentation errors are deliberately shown to illustrate the limits of our segmentation algorithm. Since the phase ring is outside the cell, for quantification of CFP and YFP expression ellipses with 3 pixels smaller a and b values are used. This is why the bottom panel ellipses are smaller than the upper panel ellipses. Cell-to-cell variability in CFP and YFP expression is detectable both in the raw data and in **(C-E)**.
(B) Protein translocation dynamics. In this example, Msn2-mCherry translocation dynamics in response to six 5-min pulses of 690 nM 1-NM-PP1 separated by 10-min intervals which leads to 75% of maximal nuclear localization is shown. Raw data (black dots) and errorbars (standard deviation) are from 101 single cells and the red line shows a fit to the data. Much of the observed variability is due to the nucleus moving in and out of focus.
(C-D) Single cell time traces of the YFP (b) and CFP (c) gene expression reporters. Raw, unsmoothed data is shown. Thus, the dynamics of promoter activity can be reliably inferred from time-traces (Zechner et al., 2014).
(E) By following both CFP and YFP gene expression dynamics in the same single cell, their co-variance can be computed. Thus, we can calculate both intrinsic and extrinsic noise(Elowitz et al., 2002). Each dot in the scatterplot, is the max CFP and YFP from one single cell.
The above experiment was performed with strain EY2967/ASH189 using data from Hansen & OShea, 2015 (Hansen & O'Shea, 2015).

in combination with microfluidics and microscopy can be generally applied to control the activity of any kinase of interest with exquisite spatiotemporal resolution and investigate downstream responses. The analogue-sensitive mutations (such as Met→Gly for PKA (Zaman *et al.*, 2009)) have been generated for a number of kinases including MAP kinases such as Hog1 (Westfall & Thorner, 2006), kinases involved in transcription such as Cdk7/Kin28 (Liu *et al.*, 2004) and Srb10/Cdk8 (Liu *et al.*, 2004) and other important kinases such as Pho85 (Carroll *et al.*, 2001), Fus3 (Bishop *et al.*, 2000), Cdc28 (Bishop *et al.*, 2000) and Snf1 (Shirra *et al.*, 2008) (a partial list is given elsewhere (Elphick *et al.*, 2007)). Thus, this is

a powerful method for investigating the dynamic regulation of any kinase-driven signaling pathway. Furthermore, our microfluidic method can be combined with other developments in pharmacological control of protein activity and localization (McIsaac *et al.*, 2011; Rakhit *et al.*, 2014) such as the anchor-away method (Belshaw *et al.*, 1996; Geda *et al.*, 2008; Haruki *et al.*, 2008) to control and monitor the dynamics of kinase-independent signaling pathways.

4.2.2 Comparison with other methods

Several microfluidic methods have been described for yeast (Bennett *et al.*, 2008; Crane *et al.*, 2014; Hersen *et al.*, 2008; Huberts *et al.*, 2013; Mettetal *et al.*, 2008; Rowat *et al.*, 2009; Taylor *et al.*, 2009; Uhlendorf *et al.*, 2012) and mammalian cells (Kellogg *et al.*, 2014). In the case of yeast, most other methods either address very specific questions (Bennett *et al.*, 2008; Denervaud *et al.*, 2013; Ferry *et al.*, 2011; Uhlendorf *et al.*, 2012) or focus on very long-term imaging, e.g. for measurements of replicative life-span (Crane *et al.*, 2014; Huberts *et al.*, 2013; Lee *et al.*, 2012; Ryley & Pereira-Smith, 2006; Xie *et al.*, 2012; Zhang *et al.*, 2012). This highlights a trade-off between specialization on the one hand and generality, simplicity, and easy-of-use on the other hand. For example, a recent massively parallel microfluidic device (Denervaud *et al.*, 2013) allows for analysis of 1,152 different strains from the yeast GFP library (Huh *et al.*, 2003) in a single experiment. However, while this is clearly a technical breakthrough such setups require extensive know-how and infrastructure beyond the capabilities of most labs and are beyond the requirements of most experiments. There are also expensive commercial systems available such as the ONIX system from CellAsic (Lee *et al.*, 2008). However, in this device cells are retained through squeezing which induces a stress response and hydrophobic inhibitors such as 1-NM-PP1 absorb into the material and therefore cannot be washed out again.

Most other reported microfluidic devices are multi-layered, which complicates the photolithography process by requiring accurate alignment. Our device is simply a single layer and once the silicon master is fabricated or obtained from a company, no specialized equipment is required for the production of microfluidic chips. The development of our device is inspired by a previously reported single Y-channel device (Bisaria *et al.*, 2014; Hersen *et al.*, 2008). By adding five channels, our adaptation allows for more high-throughput measurements of multiple strains or conditions, and by automating fluid handling using solenoid valves, our setup is entirely automated and once set up will run automatically. Furthermore, our automated fluid handling system is relatively simple to set up and can be controlled through `MATLAB`. Also importantly, our fluid handling system is made of chemically inert perfluoroelastomer. This is essential when working with hydrophobic inhibitors such as 1-NM-PP1, which absorb into most other materials.

Another advantage of a simple setup is lower failure probability and that the time to set up each experiment is greatly reduced. For short-to-medium term experiments ($\leq$5-6 h), this is crucial. We routinely perform four $\sim$2.5 h time-lapse experiments per day, thereby sampling 20 conditions or strains in a day. Furthermore, for flow rate control many other approaches (summarized in Crane *et al.*, 2014) use air pressure or syringe pumps. Our setup simply uses gravity — by adjusting the relative height difference between the input medium flask and waste flask, the flow rate can be accurately controlled. Finally, by eliminating the demands for specialized equipment, our method is easy to adopt and very cheap — the total cost per experiment is less than $5.

4.3 Experimental design

4.3.1 Design and fabrication of silicon master mold

A silicon wafer master mold is used for making PDMS chips. To fabricate the silicon master, a mask is required. Our negative transparency mask is available upon request and several companies print masks at a resolution sufficient for photolithography (5080 dpi is sufficient). Our design consists of five 400 μm-wide channels separated by 150 μm-wide walls (Figure 4.3), but can also readily modified to include more or fewer channels depending on multiplexing requirements.

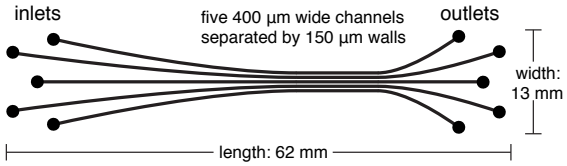

Figure 4.3: *Device design*
The transparency mask with annotation is shown. The device consists of five 400 μm wide channels, where cells are grown, separated by 150 μm walls. It is a negative mask, so areas in black are exposed to UV during photolithography.

Once the mask has been obtained from a company (e.g. CAD/Art Services), the silicon master mold can be fabricated in a clean room. Since our device contains only a single layer, no mask alignment is necessary during photolithography and the silicon master is therefore simply produced by spin-coasting a 4" silicon wafer with SU-8 photoresist, exposing to UV under the transparency mask and developing in PGMEA (an organic solvent) to give the final silicon master mold (Figure 4.4). SU-8 photoresist cross-links under UV exposure, such that any unexposed SU-8 will be washed away during development leaving only the desired pattern. Most universities will have clean room facilities. However the fabrication of a silicon master can also be out-sourced to companies (e.g. SIMTech). We use SU-8 2100 to generate a pattern with a height of ∼100 μm, but should a different height be desired this can simply be obtained by using another photoresist and changing the spin-coating program accordingly

(e.g. SU-8 2050 for a height of ∼50 µm). In general, smaller heights leads to lower flow rates. Higher flow rates enable more rapid washout of 1-NM-PP1, but also slightly higher cell loss during the experiment. At ∼100 µm height, we have never observed clogging during an experiment — something that can be a common issue with very low heights (≤10 µm). Following post-exposure baking, if the recommended hard-bake (step 12) and silanization (step 14) steps are included, the resulting silicon master mold is indefinitely stable and can be used for PDMS replica molding for years.

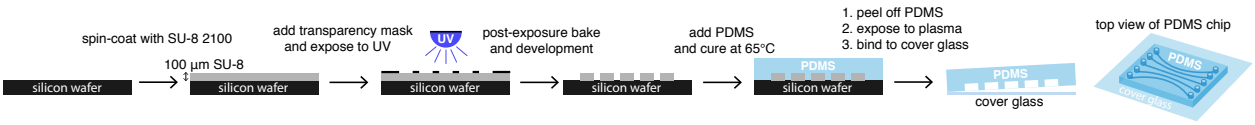

Figure 4.4: *Photolithography and soft lithography overview*
Overview of protcol steps 2-26. During the photolithography steps a 4" Si wafer is spin-coated with SU-8 photoresist to a height of ∼100 µm. Subsequently, it is exposed to UV light under a transparency mask. The photoresist pattern exposed to UV cross-links, whereas the unexposed photoresist is washed away during development to give the desired channel pattern. During the soft lithography steps, PDMS is poured over the silicon master mold, cured and then peeled off and holes punched for inlets and outlets. Following plasma exposure, PDMS is bonded to a cover glass to yield the final microfluidic device (right most).

4.3.2 Soft lithography: fabrication of microfluidic chips

Once the silicon master mold has been obtained, the microfluidic device is fabricated through replica molding of PDMS elastomer (Qin *et al.*, 2010). For PDMS replica molding we use Sylgard 184 (Dow Corning): PDMS is mixed with curing agent in a 1:10 (w/w) ratio, poured over the silicon master, degassed and cured at 65°C (Figure 4.4). Once cured, PDMS adopts a permanent and stable solid structure. Cured PDMS is then carefully peeled off the silicon master and holes are punched for inlets and outlets. Next, the PDMS chip is bonded to the cover glass. Following exposure to O_2-plasma both the PDMS chip and a cover glass will undergo surface activation (Hillborg *et al.*, 2000; McDonald *et al.*, 2000) and they can subsequently be permanently bonded to form the desired microfluidic device (Figure 4.4). Following baking at 65°C, we then insert "adaptor-tubing" into the inlets and outlets and

seal these with PDMS. This greatly eases insertion of tubing when setting up microscopy experiments and also prevents leaks from occurring during time-lapse experiments.

As a material, PDMS is optically transparent from the near-UV range into the infrared range and therefore compatible with all standard fluorescent reporters. In addition, it is gas permeable, cheap, hydrophobic, very easy to work with and biocompatible (Qin *et al.*, 2010). PDMS is therefore well suited for both cell culture and fluorescence microscopy.

Once a microfluidic device has been made, it can be stored for months (in a petri dish to avoid dust accumulation). We find it more efficient to make a large number of devices at once and storing them, than making a new device for each experiment.

4.3.3 Setting up solenoid valves for fluid control

We use 3-way solenoid valves and an electronic board to independently control fluid delivery to each of the five channels in which cells are grown. Normal medium and perturbation medium (e.g. with 1-NM-PP1) is delivered through PE tubing to the two valve inlets and the electronic board then controls which of the two inlets leads out through the outlet which is connected to the microfluidic device through ismaprene tubing. A number of electro-fluidic solenoid valves are available. We use LFYA1228032H from The Lee Company. These valves benefit from a minimal internal volume (22 μL) and excellent chemical resistance (made from FFKM perfluoroelastomer). This is essential when working with hydrophobic inhibitors such as 1-NM-PP1, which absorb into most hydrophobic materials (e.g. PE tubing) and subsequently slowly releases preventing true medium switching. We provide a simple step-by-step tutorial online aimed at researchers without previous electronics experience on how to set up the valve control system and interface it with `MATLAB`. In total, it should take ∼1 h to set up and once set up it can be re-used for years. Subsequently, the valves are simply controlled

in MATLAB (see also Box 1).

4.3.4 Time-lapse microscopy

For live-cell imaging, we grow ∼50 mL of cells overnight in low fluorescence medium with amino acids (LFM) (Hansen & O'Shea, 2013; Sheff & Thorn, 2004) to an $OD_{600\ nm}$∼0.1. Since Msn2 activity is extremely sensitive to the glucose concentration (Hao & O'Shea, 2012), we recommend keeping cells at a low $OD_{600\ nm}$ to avoid leaky activation due to glucose deprivation, but for other purposes higher $OD_{600\ nm}$ may be preferable. Since it can be difficult to spin down cells in LFM, we prefer to collect cells by suction filtration.

A microfluidic device is then washed, incubated with concanavalin A (ConA) and cells are loaded into the microfluidic channels. Following a brief incubation, the microfluidic device is loaded on the microscope stage and the flow is started. It is important to be quick and careful here since the Msn2 pathway is very sensitive and seemingly small perturbations can cause Msn2 nuclear localization. For example, mechanical perturbations such as bumping of the microfluidic device or tubing can cause Msn2 nuclear localization. However, if care is taken Msn2 will be entirely cytoplasmic at the beginning of an experiment. Furthermore, care must be taken when inserting tubing into the microfluidic inlets and outlets. It is important to keep a constant medium flow to avoid introducing air bubbles and important to securely insert the tubing to avoid leakage during an experiment.

During time-lapse experiments there is a trade-off between time-resolution and the number of stage positions that can be recorded at. On our microscope (Zeiss AxioObserver Z1), it takes ∼13.5 s for the microscope stage to move to a position, focus and collect phase contrast images and images in four fluorescent channels (including a z-stack of Msn2-mCherry). Since we collect two stage positions per microfluidic channel, this limits our time-resolution

to ∼2.5 min during time-lapse acquisition. This is sufficient for quantifying gene expression dynamics, but for other purposes such as natural transcription factor dynamics during stress exposure a finer time-resolution may be necessary (Cai *et al.*, 2008; Hao *et al.*, 2013; Hao & O'Shea, 2012; Petrenko *et al.*, 2013). Furthermore, it is important to incorporate this delay into the pre-programmed valve control script in `MATLAB`. In our case, we use a 27 s delay between 1-NM-PP1 treatment in one microfluidic channel and the next to account for the time required to image two stage positions in each channel. In general, it can be useful to include one channel as a no treatment control.

4.3.5 Analysis of time-lapse movies

The multiplexed nature of this protocol means that each experiment can generate gigabytes of images with time-lapse information about thousands of cells. Thus, it is highly desirable to automate the image analysis process, which includes segmentation of cells, tracking between frames and quantification of fluorescence. A number of open-source programs are available for this (Gordon *et al.*, 2007; Lamprecht *et al.*, 2007), although in many cases it is worth investing the time to develop code optimized for a more specialized purpose. We use our own custom-written code in `MATLAB`. Yeast cells are relatively simple to segment from phase contrast images, since their contours show up as a bright, white phase ring. We segment by fitting ellipses to this phase ring. Although computationally expensive, this is very robust. The optimal tracking algorithm will depend on how much movement is observed during the movie and since cells are occasionally lost due to flow, it is essential to allow for cell loss in the tracking algorithm. We simply match closest cells between frames.

For quantification of nuclear localization, one approach is to segment the nucleus using a nuclear marker (we use Nhp6a-iRFP (Hansen & O'Shea, 2013)) and then quantify the

mean transcription factor intensity (e.g. Msn2-mCherry) inside the nucleus. This approach is sensitive to slight errors in nucleus segmentation. Instead, we find the approach (Cai *et al.*, 2008; Hao & O'Shea, 2012) of quantifying nuclear localization using the 10 (or 15 for diploids) brightest pixels in the cell much more robust. A lot of the variability observed in nuclear localization in diploid cells (the errorbars in Figure 4.2B) is due to the nucleus moving in and out of focus during image acquisition and this can partially be overcome by recording a z-stack series. To quantify gene expression one approach is to quantify total fluorescence per cell. We quantify gene expression as the mean pixel-intensity across the entire cell for several reasons. First, what matters to the cell is generally the protein concentration, not the absolute number. Second, any slight segmentation error will strongly affect total fluorescence, but have a minimal effect on mean fluorescence since the fluorescent reporter is evenly distributed throughout the cytoplasm. Third, when considering cell-to-cell variability, if total fluorescence is used a lot of the observed variability is due to cell size variation rather than noise in gene expression.

4.3.6 Limitations

The main limitation of this protocol is cell retention for long-term imaging (>6 h). Long-term imaging is challenging because even a single cell eventually generates a very large colony and for this purpose approaches that selectively retain only mother cells are recommended (Crane *et al.*, 2014; Huberts *et al.*, 2013; Lee *et al.*, 2012; Xie *et al.*, 2012; Zhang *et al.*, 2012). Furthermore, for more complicated applications such as generation of precisely defined gradients (Bennett *et al.*, 2008; Ferry *et al.*, 2011) or sub-second medium switching (Hersen *et al.*, 2008) other approaches are superior. Although microfluidics coupled to time-lapse microscopy is a generally powerful technique, the inclusion of microfluidics does complicate

the experiment setup. However, the current protocol should be relatively simple to set up. We have verified this method for budding yeast and cyanobacteria and the method is likely to work for most microorganisms, but we have not tested it.

4.4 Materials

4.4.1 Reagents

Photolithography

- SU-8 photoresist (SU-8 2100, MicroChem)
  CAUTION: SU-8 photoresist is toxic and flammable. Wear appropriate PPE, handle in fume hood and avoid contact.
- PGMEA (Propylene Glycol Methyl Ether Acetate) (Sigma-Aldrich, item 484431) or SU-8 developer (Product Y020100, MicroChem).
- Isopropanol (e.g. item W292907 from Sigma-Aldrich)
- Acetone (e.g. item 439126 from Sigma-Aldrich)
- Methanol (e.g. item 32213 from Sigma-Aldrich)
  CAUTION: organic solvents (PGMEA, methanol etc.) are toxic and flammable. Handle in fume hood and wear appropriate PPE.
- Silanization agent (1,1,2,2-tetrahydro(perfluorooctyl) trichlorosilane item 448931, Sigma-Aldrich).
  CAUTION. The silanization agent is toxic, corrosive and can cause serious eye damage. Ensure that you wear PPE and work in a fume hood.

Soft lithography: fabrication of microfluidic device in PDMS

- PDMS and curing agent (Sylgard®184 silicone elastomer kit from Dow Corning)
- Microscope cover glasses (60x85 mm, No 1.5H (170 μm High Precision) from Paul Marienfeld GmbH & Co.KG). Can be bought through Azer Scientific in the US.
- Razer blades (e.g. item from D109727 VWR)
- Adapter tubing (polyethylene, 1.57ODx1.14ID PE-160/10 item 64-0755 from Warner Instruments)

Time-lapse microscopy

- Low fluorescence medium (LFM) with amino acids (Per liter, this medium contains: 20 g glucose (2% glucose), 5 g $(NH_4)_2SO_4$, 1 g KH_2PO_4, 500 mg $MgSO_4{\cdot}7H_2O$, 100 mg NaCl, 100 mg $CaCl_2{\cdot}2H_2O$, 500 µg H_3BO_3, 40 µg $CuSO_4$, 100 µg KI, 200 µg $FeCl_3$, 400 µg $MnSO_4$, 200 µg $Na_2MoO_4{\cdot}2H_2O$, 400 µg $ZnSO_4$, 2 µg biotin, 400 µg calcium pantothenate, 2 mg myo-inositol, 400 µg niacin/nicotinic acid, 200 µg *p*-aminobenzoic acid, 400 µg pyroxidine·HCl, 400 µg thiamine·HCl, 30 mg L-isoleucine, 150 mg L-valine, 40 mg adenine, 20 mg L-arginine, 20 mg L-histidine, 100 mg L-leucine, 30 mg L-lysine, 20 mg L-methionine, 50 mg L-phenylalanine, 200 mg L-threonine, 30 mg L-tryptophan, 30 mg L-tyrosine and 20 mg uracil). All ingredients were purchased from Sigma-Aldrich.

- 1-NM-PP1 (Commercially available from Cayman Chemical as item 13330. We synthesize it from 1-naphteleneacetic acid in large quantities as previous described (Hansen & O'Shea, 2013)).

- Concanavalin A (1 g, Type IV from *Canavalia ensiformis* as a lyophilized powder, item C2010-1g from Sigma-Aldrich).
  CRITICAL: ConA from different sources can vary in activity. Type IV from Sigma-Aldrich works well in our hands.

- PBS solution (Dulbecco's phosphate buffered saline, item D8537 from Sigma-Aldrich).

- Ethanol or reagent alcohol (e.g. item 362808 from Sigma-Aldrich).

- Yeast strain with suitable fluorescent reporters. In this example, we make use of our previously reported diploid strain (Hansen & O'Shea, 2013) in the W303 (*trp1 leu2 ura3 his3 can1 GAL*$^+$ *psi*$^+$) background (EY2813/ASH94): *TPK1*^{M164G} *TPK2*^{M147G} *TPK3*^{M165G} *msn4*Δ::TRP1/LEU2 *MSN2*-mCherry NHP6a-iRFP::KAN *sip18*::mCitrineV163A/SCFP3a-spHIS5

- Plasmids encoding fluorescent proteins are available from AddGene:

  - Fast-folding codon-optimized (Grote *et al.*, 2005) YFP mCitrineV163A in a pKT vector (Sheff & Thorn, 2004): pKT-mCitrineV163A-HIS available from AddGene.
  - Fast-folding codon-optimized(Grote *et al.*, 2005) CFP SCFP3A (Kremers *et al.*, 2006) in a pKT vector (Sheff & Thorn, 2004): pKT-SCFP3A-HIS available from AddGene.
  - Codon-optimized (Grote *et al.*, 2005) infrared iRFP (Filonov *et al.*, 2011) in a pKT vector (Sheff & Thorn, 2004): pKT-iRFP-KAN available from AddGene.

4.4.2 Equipment

Photolithography

Most clean rooms will have all necessary equipment. For reference, the equipment we use is given below:

- Spin coater (e.g. Headway Spin Coater model PWM32).

- Silicon wafers (4-inch diameter, 0-100 Ω·cm, 500 μm thickness, Test grade, item 452 at University Wafers, South Boston, MA).
- Hot plates (e.g. HP30 hot plates from Torrey Pines Scientific).
- Mask aligner (e.g. Karl Suss MJB4 from SUSS MicroTec).
- Profilometer (e.g. P-16+ Contact Stylus Profiler from KLA-Tencor).
- Optical microscope (e.g. Eclipse ME600L from Nikon).
- Petri dishes (e.g. 145/20 mm petri dishes item 639102 from Greiner Bio-One GmbH or item 82050-596 from VWR).
- Appropriate design software (e.g. Auto Cad, Adobe Illustrator etc. This is only necessary if a modified design is desired).

Solenoid valve control

- Soldering iron and solder (any will work).
- Wire cutter (any will work).
- Heat shrink tubing (recommended).
- Computer (either PC or Mac) with USB port and MATLAB software (The Mathworks).
- Serial-to-USB converter (Tripp-lite USA-19HS - Keyspan High-Speed USB to Serial Adapter. Can be purchased from CDW as item 555201). See also: `www.tripplite.com/high-speed-usb-to-serial-adapter-keyspan~USA19HS/`
- Control board (F81 RS-232 8-Channel 1-Amp N-Channel FET Controller Board (item F81) from National Control Devices, LLC. See also: `www.controlanything.com`).
- Quick start kit with power supply, serial cable and RSIO serial interface board (QS12 +12 Volt Quick start kit (item QS12) from National Control Devices, LLC). See also: `www.controlanything.com`
- Solenoid valves (3-way 12 volts LFYA1228032H Y-valve in perfluoroelastomer, the Lee Company).
  CRITICAL: While other valves are available, LFYA1228032H valves have a low internal volume (22 μL) and are inert to hydrophobic inhibitors like 1-NM-PP1, which can absorb into other materials.

Soft lithography: fabrication of microfluidic device in PDMS

- Planetary mixer and degasser with disposable cups (e.g. THINKY ARE-250 Mixer from THINKY USA Inc.).
- Oven with level surfaces (any lab grade oven with adjustable temperature settings will work).
- Plasma exposure (we use a Plasma-PrepTM II plasma etcher from SPI).

- Cutting mat (any will work, but one with a grid pattern is helpful. We use an ALVIN® cutting mat).
- Hole puncher (Harris Uni-Core 2.00 sold e.g. as item 15076 from Ted Pella Inc).
- Tweezers (e.g. 5-SA tweezers, S95307 Aven Tools 18062ER from Fisher Scientific).
- Dissection scissors (e.g. item 25874-105 from VWR).
- Vacuum desiccator attached to vacuum pump (e.g. item 250-028 from Jencons but any will work).

Time-lapse microscopy

- Ismaprene tubing (Ismatec PharMed BPT (ID 0.51 mm, wall 0.85 mm), item SC0305 from IDEX Corporation).
- PE tubing (Polyethylene tubing, 0.050" OD/0.034" ID, item BPE-T90 from Instech Solomon).
- Valve adaptor tubing (Polyethylene tubing (1.57OD x 1.14ID), PE-160/10. Cat 64-0755 from Warner Instruments).
- 20G needle (PrecisionGlide^{TM} needle 20G (0.9 mm x 25 mm) REF 305175 from BD).
- Immersion Oil (use immersion oil appropriate for microscope and objective. We use Carl Zeiss Immersol immersion oil 518F, item 12-624-66A from Fisher Scientific).
- 1 mL Luer-Lok^{TM} disposable syringes (item 309628 from BD).
- Suitable inverted fluorescence microscope with environmental incubation chamber, automated stage, and auto-focus function. Any such microscope should work. We use a Zeiss AxioObserver Z1 inverted microscope with both LED and Lamp excitation and Zeiss Definite Focus for focusing. Our setup uses an EM-CCD camera (Evolve 512, Photometrics) and an oil-immersion objective (63x, NA 1.4, oil Ph3, Plan-Apochromat).

4.4.3 Reagent setup

- ConA solution. Prepare and filter-sterilize a 1 M $CaCl_2$ solution in water and a 1 M $MnCl_2$ solution in water. Obtain 1 g of ConA (Agrawal & Goldstein, 1968; Senear & Teller, 1981) (type IV from Sigma-Aldrich C2010). Adjust PBS solution pH to 6.5. On ice, gently dissolve ConA powder in 45 mL PBS at pH 6.5, 2.5 mL 1 M $CaCl_2$ solution and 1 M $MnCl_2$ solution. Once fully dissolved, aliquot the 20 mg/mL ConA solution into 200 µL aliquots and store these at -20°C or -80°C.
  CRITICAL: ConA activity can vary from batch to batch and proper activity is essential to maintain cells under flow during the microfluidic experiments. If activity is too high or low, adjust the concentration accordingly. Handle powder gently on ice and carefully adjust the pH (a pH between 6 and 7 is important for high ConA activity (Agrawal & Goldstein, 1968; Bisaria *et al.*, 2014; Senear & Teller, 1981)). Freeze thawing or long-term storage at 4°C leads to loss of activity.
- 70% ethanol. Mix ethanol or reagent alcohol with water in 70:30 (v/v) ratio.

- 1-NM-PP1 stock. We prepare 1-NM-PP1 stocks in DMSO at 1000x concentration (e.g. a 3 mM stock for experiments where a 3 μM concentration is needed) and store these as aliquots at -20°C. 1-NM-PP1 is extremely stable and can be freeze-thawed without degrading.

4.4.4 Equipment setup

Transparency mask for photolithography Obtain negative film photolithography transparency mask from a company. Our mask file is available online and several companies offer this service (we use CAD/Art Services, `http://www.outputcity.com`).

Device holder for microscopy We use a metal holder to hold microfluidic device. Any machine shop should be able to prepare this. The dimensions for our holder are given online.

Suction filtration setup We use a Millipore system (Millipore kit item XX1002530 contains everything needed) with nitrocellulose filters (mixed cellulose esters, 0.8 μm, 25 mm, item AAWG02500 from Millipore).

Silicon wafer master mold Steps 2-14 describe how to fabricate the silicon wafer master mold. If desired, these steps can also be out-sourced to a company and once a master mold has been obtained it can be re-used indefinitely. SIMTech offers these services, as do a number of other companies. Since the companies that offer this service are constantly changing, for an up-to-date list see also:
`http://en.wikipedia.org/wiki/List_of_microfluidics_related_companies`
`http://www.simtech.a-star.edu.sg/smf/`
`http://stanford.edu/group/foundry/Services.html`

4.5 Procedure

4.5.1 Photolithography: fabrication of silicon wafer master mold

1. Obtain photolithography transparency mask from company (we use CAD/Art Services). Steps 2-14 for fabrication of silicon wafers can also be outsourced to companies (see above).

2. Choose an SU-8 photoresist appropriate for the desired height. We recommend SU-8 2050 for ∼50 μm height and SU-8 2100 for ∼100 μm height. Instructions are available from the MicroChem website (`http://www.microchem.com/Prod-SU82000.htm`). Below, we detail the steps for obtaining microfluidic channels of ∼100 μm height using SU-8 2100.

CRITICAL. Steps 3-14 need to be performed in a clean room to prevent contamination by dust etc. Avoid introducing air bubbles when working with SU-8 and make sure

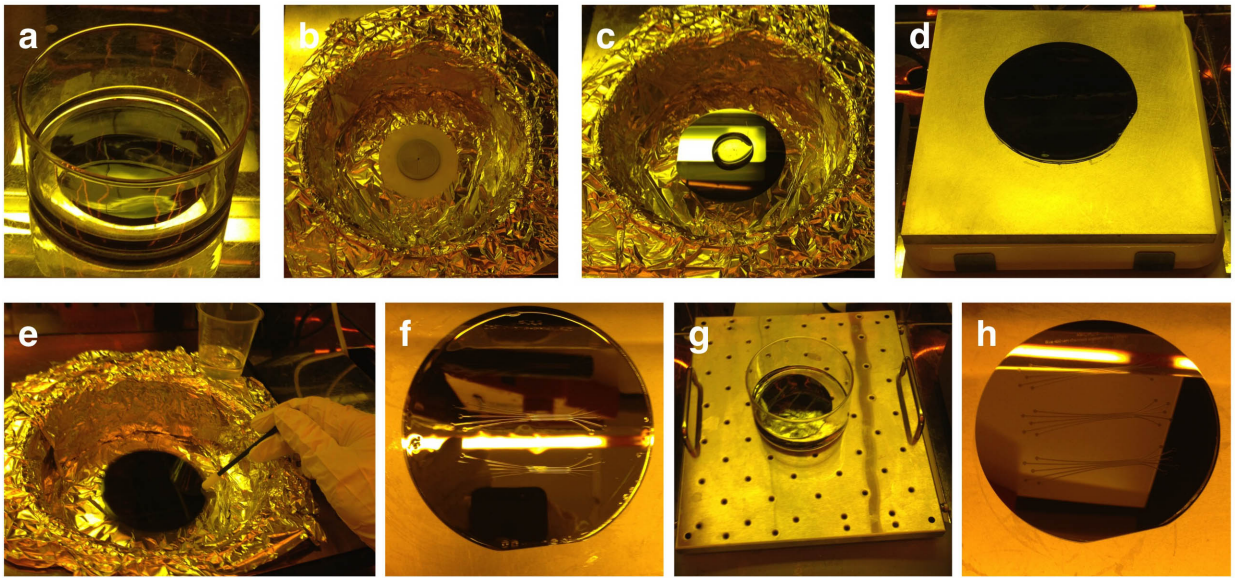

Figure 4.5: *Photolithography steps: fabrication of silicon wafer master mold*
a) Step 3: clean wafer in acetone.
b) Step 4: Prepare spin coater. Line bowl with aluminium foil to facilitate cleaning.
c) Step 5: Pour ca. 4-5 mL SU-8 2100 on 4" wafer and spin.
d) Step 6: Soft bake. Place spin-coated wafer on level hot plate and bake. Be sure to remove any air bubbles by tapping with the tip of e.g. a needle.
e) Step 7: Edge bead removal. Spin wafer at 1000 rpm and remove edge by pressing a cue tip soaked in PGMEA against the wafer edge as illustrated.
f) Step 9: Post-exposure bake. Place wafer on level 65°C hotplate and then ramp up to 95°C for 11 min. Features will begin to appear.
g) Step 10: Development. Place wafer in PGMEA bath with shaking and incubate for 10 min or until development is complete.
h) Step 12: Hard bake. After development, perform hard bake. The wafer is now finished.

that all surfaces (e.g. hot plates) are level.

CAUTION. SU-8 photoresists are toxic and flammable. Make sure that you wear proper PPE and work inside a fume hood.

3. (Recommended) Clean wafer by incubation in an acetone bath ideally with sonication for 5 min (Figure 4.5a). Wash wafer with methanol and then isopropanol. Dry wafer with nitrogen gun and then bake at 200°C for 5 min to remove any leftover solvent.

4. Prepare spin coater. Line the bowl of the spin coater with aluminium foil to facilitate cleaning (Figure 4.5b) and place the wafer on the chuck center and make sure that it sticks by applying vacuum.

5. Spin coating. To obtain a thickness of ∼100 μm we use SU-8 2100. Add ca. 4-5 mL SU-8 2100 to the centre of the wafer (Figure 4.5c). Use the following spin program: Ramp up to 500 rpm at 100 rpm/s acceleration. Hold for 5 s. Ramp up to 3000 rpm at 300 rpm/s acceleration. Hold for 45 s. Then ramp down.

6. Soft bake. Pre-bake the wafer on level 65°C hot plate for 5 min, then soft-bake at 95°C for 20 min and cool down to 65°C before proceeding (Figure 4.5d).
CRITICAL: any air bubbles should be removed during the soft-bake by tapping with needle tip or tip of tweezers.

7. (Recommended) Edge bead removal. Place the coated wafer back on the chuck of the spin coater and spin at 400 rpm for 60 s. As the wafer is spinning remove edge by placing a cue tip soaked in PGMEA or SU-8 developer on the edge (Figure 4.5e). Re-soak the cue tip as necessary. Bake wafer on 65°C hot plate for 2 min to remove any residual PGMEA.

8. Exposure. Exact conditions will depend on instrument and the UV source power, but should be performed according to MicroChem guidelines which can be found at: `http://www.microchem.com/Prod-SU82000.htm` To eliminate radiation below 350 nm, we use a 360 nm long-pass filter and an exposure energy of 430 mJ/cm^2 (a lower exposure energy should be used if a long-pass filter is not used). On the mask aligner we use, this works out to an exposure time of ∼21 s. Place transparency mask on top of substrate and add 360 nm long-pass filter and expose.

9. Post-exposure bake. Place the wafer on a level 65°C hot plate. Ramp hot plate up to 95°C and hold for 11 min. Latent visible image should appear during post-exposure bake (Figure 4.5f).
CRITICAL: cool down wafer slowly — rapid cooling can cause cracks in the SU-8 film.

10. Development. Prepare PGMEA bath for development and place on shaker. Submerge wafer with the SU-8 coated side facing upwards. Gently rock the PGMEA bath with wafer at 90 rpm for 10 min (Figure 4.5g). To check whether development is complete remove wafer and use spray bottle to spray isopropanol on wafer. If a white film is observed, this indicates underdevelopment. In that case, put the wafer back into the PGMEA bath and develop for longer.

11. Once development is complete, rinse with isopropanol and dry with nitrogen gun.

12. (Recommended) Hard bake. Performing hard bake will increase durability and can heal any surface cracks. Place wafer on level hot plate and heat to 150°C for 20 min and then cool down (Figure 4.5h).

13. (Recommended) Characterization. To ensure that mold pattern is without defect, the wafer mold should be inspected using a simple transmitted light microscope and a profilometer to characterize height etc.

14. (Recommended) Silanization. Place wafer in petri dish without lid inside desiccator together with a small vial containing ∼500 µL silanization agent 1,1,2,2-tetrahydro-(perfluorooctyl)trichlorosilane. Incubate in dessicator under reduced pressure overnight. CAUTION. Silanization agent is toxic and corrosive. Wear PPE and work in fume hood.

PAUSE POINT. After these steps, the wafer mold is stable and can be used and stored for years.

4.5.2 Soft lithography: replica molding of PDMS and fabrication of microfluidic device

CAUTION: The following steps involve organic solvents and elastomers, which are flammable, toxic and carcinogenic. Use proper PPE, work in a fume hood if possible and wear gloves.

15. Place wafer in petri dish with mold pattern facing up.

16. Mix PDMS and curing agent in a 10:1 ratio (w/w) in disposable plastic cup. If a planetary mixer is available use this for mixing and degassing (we use a THINKY ARE-250 mixer with a 30 s mixing and 30 s degassing program and 100 mL disposable cups). If not, manually mix extensively with disposable plastic spoon and degas in vacuum desiccator.

17. Pour mixed PDMS over wafer in petri dish to a height of 5 mm (Figure 4.6a). Pour gently to avoid forming air bubbles. More PDMS will be needed the first time since you have to cover the entire petri dish. Subsequently ∼30 mL PDMS is suitable for a ∼5 mm height. Degas in vacuum dessicator until air bubbles disappear. This often takes ∼20 min.

18. (Recommended) Cover glass cleaning. Pour ∼300 mL isopropanol into beaker (enough to fully submerge cover glasses. Wash cover glasses in acetone and then store in

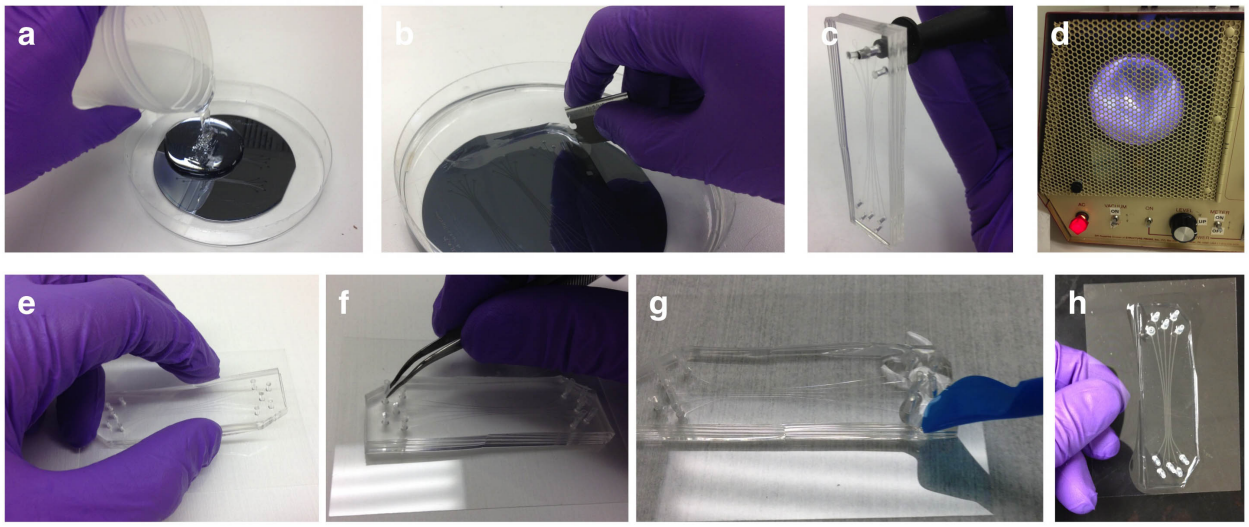

Figure 4.6: *Soft lithography steps: fabrication of microfluidic device*
a) Step 17: Pour mixed PDMS on silicon wafer master mold in petri dish.
b) Step 20: Once cured at 65°C, cut out PDMS chip with razor blade taking care not to cut the SU-8 pattern.
v) Step 21: Punch holes for inlets and outlets using Harris Uni-Core 2.00 to finish the PDMS chip.
d) Step 23: Expose both PDMS chips and cover glasses to oxygen plasma to activate surfaces.
e) Step 23-24: After plasma treatment, place PDMS chip featured-side down on cover glass and gently press. Then incubate at 65°C for >1 h. **f)** Step 25: Insert a small piece (∼8-10 mm) of "adaptor tubing" into each inlet and outlet.
g) Step 26: Following incubation at 65°C for >2 h, the final microfluidic device is obtained.
h) Close-up of final device.

isopropanol bath until needed in step 22. Cleaning cover glasses improves plasma bonding to PDMS.

19. Once PDMS degassing is complete, place lid over petri dish containing wafer and PDMS and place petri in an oven at 65°C. Make sure the surface is level. Cure in oven for at least 2 h.

PAUSE POINT. After curing, the whole petri dish can be stored indefinitely at room temperature.

20. After curing, take petri dish out of oven and wait a couple of minutes for it to cool down. With a razor blade, cut through PDMS against wafer and circle the entire SU-8 pattern (Figure 4.6b). Be careful to keep ∼1 cm from cutting area to SU-8 pattern since accidentally cutting SU-8 pattern with razor blade can destroy it. Once you have cut a circle around the SU-8 pattern, carefully wedge the blade under the PDMS until you can grab PDMS with a finger. Then carefully peel off PDMS mold from the master surface.

CRITICAL. It is important to be careful during PDMS peeling to leave the SU-8 pattern intact. If this part is done carefully, the same SU-8 master can be used for

years.

21. After PDMS peeling, place on cutting mat with channel features facing up. Cut each device into a PDMS rectangle leaving ∼5 mm between the PDMS edge and the edge-most channels. Punch holes with Harris Uni-Core 2.00 (Figure 4.6c). Be careful to punch straight holes at the exact end of each channel and make sure the punched out PDMS is fully removed. Repeat for all inlet and outlet holes.

22. Hold each hole-punched PDMS chip with tweezers and wash with acetone and then isopropanol. Then dry with nitrogen gun. For each PDMS device, also dry a cleaned cover glass from step 18 with nitrogen gun.

23. Plasma treatment. The exact protocol will depend on the plasma instrument available. We use a Plasma-Prep II (from SPI) and the following protocol: Carefully place cleaned PDMS devices and cover glasses upright with the side to be bonded exposed inside plasma chamber. Close plasma chamber and turn on vacuum. Switch gas to pure oxygen. Wait until a pressure of 300 Torr (400 mbar) is reached. Turn on oxygen plasma and tune instrument. Expose for 12 s (Figure 4.6d). Turn off vacuum and wait for instrument to reach standard pressure. As soon as possible, take out plasma chamber and carefully place PDMS devices on cover glasses (Figure 4.6e). The channel side should face cover glass. Place on soft material (e.g. layers of paper tissues) and gently press PDMS device against cover glass until fully bound.
CAUTION. Cover glasses are very thin and can break when PDMS device is pressed against them, so take great care.

24. Place each plasma-bonded microfluidic device in oven at 65°C for at least 1 h.

25. Cut adapter tubing (PE-160/10, Warner Instruments) into pieces of ∼8-10 mm in length. Take out microfluidic device and place on soft material. Gently press one piece of tubing into each inlet and each outlet (Figure 4.6f). Then with a plastic spoon, pour small amount of mixed PDMS (from step 16) around each inlet and outlet to seal tubing (Figure 4.6g).

26. Place each microfluidic device with sealed inlet and outlet tubing in oven at 65°C for at least 2 h, but preferably overnight.
PAUSE POINT. Microfluidic device fabrication is now complete (Figure 4.6h) and they

can be stored for months. It is more efficient to make a large number of devices in a single setting. Store devices in petri dish to avoid dust accumulation. Steps 15-26 should be repeated whenever more microfluidic devices are needed.

4.5.3 Setting up control valves

27. Setting up the valve control system requires a small amount of soldering. We provide a detailed tutorial aimed at someone without previous soldering and electronics experience (available online). Setting up the control valves should take ∼1 h and needs only to be done once. An example of how to interface valves with `MATLAB` is shown in Box 1.

Box 1

To use `MATLAB` to control electrovalves, make sure the board is plugged in and the USB connection inserted into the computer (see also online tutorial for more detailed guidelines). The first step is establishing a serial connection. Run script "`Windows_open_valves.m`" if on a Windows-based computer and run script "`Mac_open_valves.m`" if on a Mac. Once this is done, a serial connection (`s1`) is established and the valves can be controlled through `MATLAB`. To close the serial connection again use: `fclose(s1)`.

The valves are programmed by sending ASCII characters. First ASCII character 254 is sent to enter command mode and then an ASCII character of 0-15 is sent to turn ON/OFF the desired valve. The function `toggleValves.m` takes care of all of this. For example to switch ON all valves use:

```
>> toggleValves([0,0,1],s1)
```

Or to switch OFF all valves use:

```
>> toggleValves([0,0,0],s1)
```

To switch ON/OFF a single valve use (e.g. turn valve 3 ON):

```
>> toggleValves([3,1],s1)
```

Or to turn valve 4 OFF use:

```
>> toggleValves([4,0],s1)
```

Combining the `toggleValves.m` function with the `pause` function in MATLAB, fluid delivery programs are easily made. E.g. the simple program

```
for i=1:6
     toggleValves([0,0,1],s1); %all ON
     pause(300);
     toggleValves([0,0,0],s1); %all OFF
     pause(600);
end
```

delivers six 5-min pulses (5 min = 300 s) of treatment followed by 10-min intervals. This is the 1-NM-PP1 delivery program used to generate Figure 4.2a.

4.5.4 Preparing a time-lapse microscopy experiment

To prepare a time-lapse experiment the following steps should be performed the day before.

28. In the morning, inoculate the relevant yeast strain in low fluorescence medium and grow for >8 h at 30°C. At night, calculate how many cells to add to a 250 mL conical flask containing 50 mL low fluorescence medium so that the culture reaches an $OD_{600\ nm}$ of 0.1 at the desired time the following day assuming a doubling time of 90 min. Grow this culture overnight at 30°C with shaking at 180 rpm.

29. Prepare all media. For a ∼3 h, five-channel experiment, ∼100-150 mL of medium is needed depending on flow rate. Prepare a flask with medium without treatment and flasks for each treatment (e.g. 1-NM-PP1). Also prepare a flask for outlet waste. Incubate these overnight at 30°C.

CRITICAL. Incubating medium overnight at 30°C is essential to avoid air bubbles forming during the experiment.

4.5.5 Setting up a time-lapse microscopy experiment

30. Take out a tube containing 20 mg/mL ConA solution from freezer and gently thaw on ice at least 1 h before experiment. Once fully thawed, add 200 µL PBS (pH 6.5) and 600 µL H_2O to the 200 µL ConA solution and mix to obtain 1 mL final solution of 4 mg/mL ConA.

CRITICAL. It is important to gently and slowly thaw ConA on ice to prevent a loss of activity. If ConA is stored at 4°C, the solution should be relatively fresh (<1 month old) to ensure optimal immobilizing activity.

31. Prepare microscope set-up at least 1 h before experiment. Turn on microscope and heat up incubation chamber to 30°C. Connect valve control system to computer, open `MATLAB` and establish serial connection to valves. Cut PE tubing for inlets and outlets (Figure 4.7a). 5 pieces are needed for each inlet and outlet, so 15 total. These should be around 50-100 cm long depending on microscope setup. We keep flasks with inlet medium and outlet waste outside of microscope incubation chamber, so tubing must be long enough to reach these. Cut 5 pieces of ismaprene tubing (∼12 cm) and attach

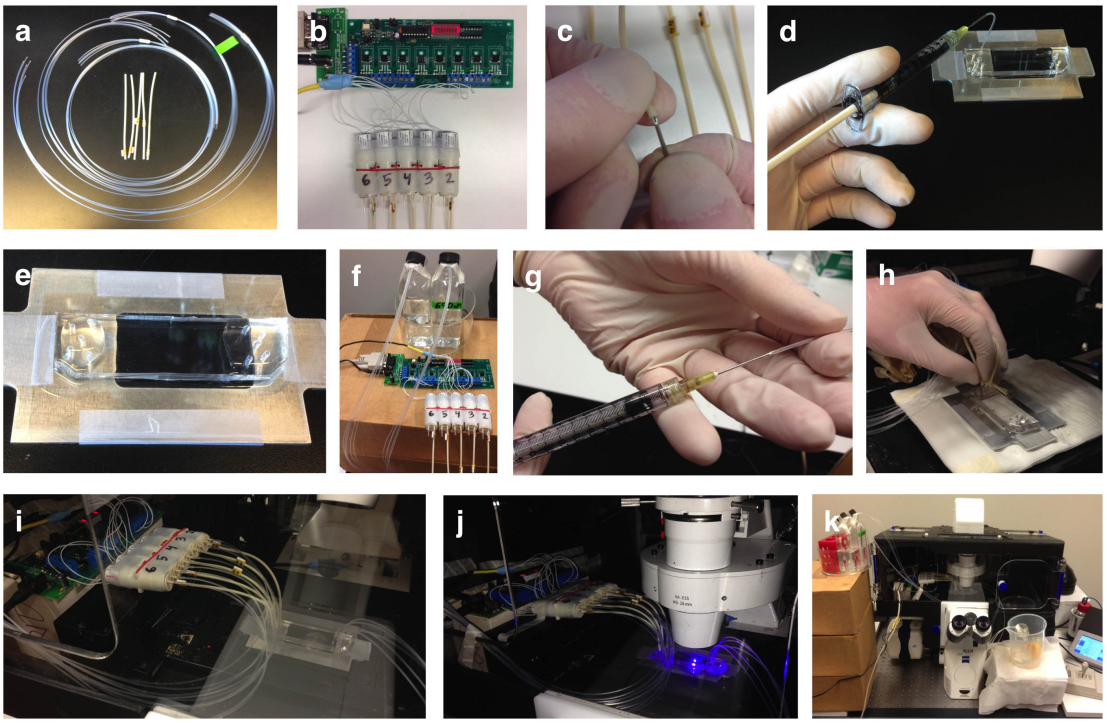

Figure 4.7: *Time-lapse microscopy experiments*
a) Step 31: prepare PE tubing for inlets and outlets and ismaprene tubing for valves.
b) Step 31: Attach ismaprene tubing to valve outlets.
c) Step 31: Insert a small piece of PE tubing on 20G needle and the insert PE tubing piece into ismaprene tubing. This is the piece that goes into the microfluidic device inlets and should be short (∼5 mm).
d) Step 33: Wash microfluidic device using 1 mL syringe with 20G needle and PE tubing attached to needle by gently flushing each channel with 70% ethanol, water and then loading ConA solution.
e) Step 33: Ideally always keep inlets and outlets covered with liquid to avoid introducing air bubbles.
f) Step 34: Insert PE tubing into medium and safely tape everything stuck.
g) Step 34: To start flow from medium, insert syringe with 20G needle into PE tubing end and pull. Then insert PE tubing into the solenoid valve inlets.
h) Step 36: Move board, valves and microfluidic device into microscope chamber and insert ismaprene tubing with PE ends into the microfluidic device inlets taking care to avoid air bubbles.
i) Step 37: Once the outlets have been connected via PE tubing to waste flask the setup should look like this.
j) Step 39: illustration of setup during time-lapse acquisition.
k) Full view of setup. Flow rate is controlled by height difference between inlet medium and waste flask.

to valve outlets (Figure 4.7b). Cut small pieces of PE tubing and attach to other end of ismaprene tubing with 20G needle (Figure 4.7c).

32. Prepare microfluidic device. Tape the microfluidic device to a microscope holder with Scotch tape. Cut off excess adaptor tubing so that it is level with PDMS. Cut a piece of PE tubing (∼10-15 cm), attach to 20G needle and attach needle to 1 mL syringe. Cut tubing in such a way that the end is diagonal rather than blunt — this greatly eases insertion.

33. Wash microfluidic device. Wash each microfluidic channel with ∼200 µL 70% ethanol by inserting syringe through PE tubing and gently pushing liquid through channels

(Figure 4.7d). Then wash each channel with ∼200 µL H_2O. Dry off excess liquid with Kim wipes. Finally load each channel with ∼200 µL 4 mg/mL ConA solution. Ensure that all inlets and outlets are fully covered by ConA solution (Figure 4.7e) and incubate at room temperature for at least 5 min before loading cells.

CRITICAL. Avoid introducing air bubbles — as an air bubble travels through the channel it will take out all adhered cells with it. During wash steps, apply gentle pressure from syringe — too high pressure can break the PDMS walls between the channels.

34. Prepare tubing and medium for inlets and outlets. Add 1-NM-PP1 or equivalent to stress medium at the desired concentration (we store 1-NM-PP1 as a 1000x stock in DMSO at -20°C and add it just before use). Connect PE tubing with flasks containing medium. Tape tubing stuck to flasks (Figure 4.7f). To start flow, insert 1 mL syringe with 20G needle into PE tubing and draw out liquid (Figure 4.7g). Then attach PE tubing to valve inlets and outlets. Flow rate is controlled by gravity. Switch between inlets a few times using `togglevalves.m` script in `MATLAB` to remove any air bubbles. Ensure that valves are off before proceeding.

CRITICAL. Avoid reusing PE tubing for 1-NM-PP1 treatments; Old PE tubing will cause the release of residual 1-NM-PP1 into medium. It is important to tape PE tubing stuck to medium flasks (Figure 4.7f). If tubing moves above medium, air will be sucked in and when these air bubbles reach microfluidic channels, cells will be lost.

35. Load cells into microfluidic device. Collect cells when they have reached the right $OD_{600\ nm}$ (we use 50 mL at $OD_{600\ nm}$∼0.1 so 5 OD units of cells). We prefer collecting cells by suction filtration rather than centrifugation. Collect cells and quickly re-suspend in 500 µL fresh medium. Wash away all ConA using fresh medium (∼200 µL per channel) and then load cell suspension using syringe. Incubate cells in the microfluidic device for 5 min at room temperature. After 5 min, wash each microfluidic channel with fresh medium. The pressure with which cells are washed with fresh medium determines subsequent cell density in each channel.

CRITICAL. After this step, the microfluidic device should immediately be loaded onto microscope with flow of fresh medium to keep cells in a chemostatic environment and to avoid stress.

36. Load microfluidic device on microscope. Carefully, place microfluidic device on holder inside microscope incubation chamber on paper towels to absorb any spillage. Carefully, move board and valves into incubation chamber — take care not to detach any tubing. Attach each ismaprene tubing outlet to microfluidic device inlets under constant medium flow (Figure 4.7h). Dry off any spillage.

CRITICAL. When inserting ismaprene tubing into device inlets, make sure the medium is constantly flowing from ismaprene tubing to avoid introducing air bubbles.

37. Attach outlets. Attach PE tubing to outlet waste flask and tape it stuck. Move flask above microscope chamber and start flow by drawing liquid from PE tubing with syringe (Figure 4.7g). Carefully attach outlet PE tubing to microfluidic device outlets — make sure PE tubing is stably inserted to avoid leakage. Move outlet flask to below microscope chamber (Figure 4.7i). The flow rate is controlled by gravity — the height difference between the inlet and outlet flasks governs this. A height different of $\sim$30 cm yields a flow rate of $\sim$1μL/s per channel in our hands.

38. Begin microscopy. Add immersion oil to objective. Move objective to the straight part of the microfluidic channels and focus to find cells. Tape tubing and valves to chamber so that nothing moves during image acquisition.

CRITICAL. Cell handling and loading will inevitably introduce some stresses. Therefore, before starting the microscope acquisition, allow cells stay in the device with constant medium flow for at least 20-30 min to recover from stress and adapt to the microfluidic culturing condition.

39. Pick stage positions. Use microscope software (we use Zeiss AxioVision 4.8) to pick stage positions in each microfluidic channel and the auto-focus function to maintain focus (we use Zeiss Definite Focus). Pick positions as close as possible to each other to avoid excessive stage movement during time-lapse acquisition. We use $\sim$5 fields-of-view as separation between positions. We avoid positions right next to the PDMS wall of the microfluidic channel.

40. Time-lapse movie acquisition (Figure 4.7j-k). This will depend on the microscope, software and experiment in question. For reference, in a typical experiment we acquire two field-of-view positions per microfluidic channel at 2.5 min time resolution (10 positions total) using the following exposure settings: phase-contrast (10 ms), YFP (50 ms, Zeiss

Colibri LED at 505 nm excitation using Zeiss filter cube HE 46 (EX BP 500/20, BS FT 515, EM BP 535/30), intensity: 100%), CFP (100 ms, Zeiss Colibri LED at 445 nm using Zeiss filter cube HE 47 (EX BP 436/25, BS FT 455, EM BP 480/40), intensity: 100%), iRFP (400 ms, Sutter DG-4 lamp using filter cube 32 Alexa fluor 680/Cy5.5 (EX BP 665/45, BS FT 695, EM BP 725/50)), RFP (3 x 400 ms z-stack series (focal plane ± 1.75 μm), Zeiss Colibri LED at 590 nm using Zeiss filter cube HE 64 (EX BP 587/25, BS FT 605, EM BP 647/70), intensity: 100%).

41. Clean up. Save images and remove and dispose of the microfluidic device. Clean objective with lens cleaner. We recommend disposing of tubing that has been in contact with 1-NM-PP1, but all other tubing can be re-used. Wash valves and ismaprene tubing with 70% ethanol in between experiments.

4.5.6 Troubleshooting

Table 4.1: Troubleshooting

Step/Problem	**Possible reason**	**Solution**
step 9: Cracks in SU-8 pattern	Rapid cooling can cause thermal stress	In all steps involving heating on hot plates, slowly ramp the temperature up or down to avoid thermal stress.
step 20: Detachment of SU-8 pattern	Insufficient adhesion of SU-8 to wafer	Include additional wafer cleaning step before step 4. We sometimes perform oxygen plasma cleaning of wafer immediately prior to SU-8 coating (150 mTorr O_2 at 60 W for 2 min with a Technics Plasma Stripper Model 220).
	SU-8 pattern detaches during PDMS peeling	Ensure that razor blade cut is complete and be more gently whilst peeling off PDMS. Perform recommended hard bake (step 12) and silanization (step 14).
step 33: Walls between microfluidic channels break down during washing steps	Too much pressure or too weak bonding.	Apply only gently pressure on syringe during wash steps. Perform all recommended cleaning steps during soft-lithography (step 18) and optimize oxygen plasma exposure time (step 23).

step 40: Excessive cell loss or movement during time-lapse experiment	High flow rate	Lower flow rate by reducing height difference between inlet and outlet flasks. Unless very quick medium switching is required, a much lower flow rate may be fine.
	Defect ConA	Change ConA stock. We sometimes observe dramatic batch-to-batch variation in activity.
step 40: Sudden loss of all cells in field-of-view	Air bubble	Make sure all medium is pre-heated before experiments.
	Air bubble	When washing microfluidic device and loading cells, take care not to introduce air bubbles. These can sit around and only move through microfluidic channels during time-lapse experiments.
step 40: Focus is lost during time-lapse acquisition	Thermal expansion of microfludic device holder	Pre-warm microfluidic device holder. Wait for 20-30 min before starting time-lapse acquisition to allow everything to heat up.
	Unstable setup during stage movement	If the stage positions are too far apart or if device holder or tubing is not stable during acquisition this can happen. Tape everything stuck.
step 40: Leakage during experiment	Tubing coming loose during experiment	Securely attach PE tubing to microfluidic device. Cutting PE tubing ends sharply and diagonally makes secure insertion much easier. Avoid blunt ends.
step 40: PDMS delamination	Insufficient bonding of PDMS to cover glass	Properly clean PDMS and cover glasses prior to plasma exposure. It may be necessary to optimize oxygen plasma exposure time (both too brief and too long exposure times can cause this). When sealing adapter tubing in step 25, also add mixed PDMS around PDMS chip to seal it to glass.

step 40: Msn2 is nuclear prior to 1-NM-PP1 treatment	Leftover 1-NM-PP1 from previous experiment absorbed into tubing	Do not re-use PE-tubing that has been exposed to 1-NM-PP1. If an extremely high concentration of 1-NM-PP1 has been used (e.g. >10 μM) it may be necessary to also replace ismaprene tubing.
	Clogged tubing	Occasionally, we observe nuclear Msn2 if tubing is clogged or improperly positioned. Change tubing and keep tubing path straight.
step 40: Too few (or too many) cells in microfluidic channels	Improper cell loading	Load more (or fewer cells) during step 35. Apply less (or more) pressure when washing with fresh medium during step 35.
step 40: Washout of 1-NM-PP1 is too slow	Flow rate is too low	Washout of 1-NM-PP1, as measured by Msn2 localization, should not take more than 2-3 min. If it takes longer, increase flow rate.

4.5.7 Anticipated results

The anticipated results will depend on the experiment in question. Using the analogue sensitive PKA^{as}-system to control Msn2 dynamics and measure gene expression (Figure 4.2) as an example this protocol should allow a single researcher to expose cells to e.g. five different Msn2 pulse frequencies (Figure 4.2B) in a single experiment whilst collecting two fields-of-view per channel and ∼200 cells per field-of-view, thus generating data for ∼2000 cells in a single experiment. With a good image acquisition system, reporter gene expression can be quantified with minimal measurement noise (Figure 4.2C-D). If experiments are well planned a single researcher readily can set up four experiments in a day, sampling 20 different experimental conditions or strains whilst obtaining time-lapse data for up to 10,000 single cells. With this amount of data it becomes possible to not just study the average behavior of a cell population, but to take the entire probability distribution into account (Hansen & O'Shea, 2013; Chapters 2 and 3).

Acknowledgements

We thank M. McClean and S. Ramanathan for help with setting up the microfluidic device. We thank D. MacLaurin and E. Zwiebach-Cohen for discussions. We thank the O'Shea lab for discussions and comments on the manuscript. This work was performed in part at the Center for Nanoscale Systems at Harvard University, a member of the National Nanotechnology Infrastructure Network (NNIN), which is supported by the National Science Foundation under NSF award no. ECS-0335765. The Howard Hughes Medical Institute supported this work.

4.6 Chapter 4 references

Agrawal, B.B.L., & Goldstein, I. (1968). Protein-Carbohydrate Interaction: 7. Physical and Chemical Studies on Concanavalin a Hemagglutinin of Jack Bean. *Arch Biochem Biophys* **124**: 218-229.

Batchelor, E., Loewer, A., Mock, C., & Lahav, G. (2011). Stimulus-dependent dynamics of p53 in single cells. *Mol Syst Biol* **7**.

Behar, M., & Hoffmann, A. (2010). Understanding the temporal codes of intra-cellular signals. *Curr Opin Genet Dev* **20**: 684-693.

Belshaw, P.J., Ho, S.N., Crabtree, G.R., & Schreiber, S.L. (1996). Controlling protein association and subcellular localization with a synthetic ligand that induces heterodimerization of proteins. *P Natl Acad Sci USA* **93**: 4604-4607.

Bennett, M.R., & Hasty, J. (2009). Microfluidic devices for measuring gene network dynamics in single cells. *Nat Rev Genet* **10**: 628-638.

Bennett, M.R., Pang, W.L., Ostroff, N.A., Baumgartner, B.L., Nayak, S., Tsimring, L.S., & Hasty, J. (2008). Metabolic gene regulation in a dynamically changing environment. *Nature* **454**: 1119-1122.

Bermejo, C., Haerizadeh, F., Takanaga, H., Chermak, D., & Frommer, W.B. (2011). Optical sensors for measuring dynamic changes of cytosolic metabolite levels in yeast. *Nat Protoc* **6**: 1806-1817.

Bisaria, A., Hersen, P., & McClean, M.N. (2014). Microfluidic Platforms for Generating Dynamic Environmental Perturbations to Study the Responses of Single Yeast Cells. *Methods Mol Biol* **1205**: 111-129.

Bishop, A.C., Ubersax, J.A., Petsch, D.T., Matheos, D.P., Gray, N.S., Blethrow, J., Shimizu, E., Tsien, J.Z., Schultz, P.G., Rose, M.D., *et al.* (2000). A chemical switch for inhibitor-sensitive alleles of any protein kinase. *Nature* **407**: 395-401.

Cai, H.Q., Katoh-Kurasawa, M., Muramoto, T., Santhanam, B., Long, Y., Li, L., Ueda, M., Iglesias, P.A., Shaulsky, G., & Devreotes, P.N. (2014). Nucleocytoplasmic Shuttling of a GATA Transcription Factor Functions as a Development Timer. *Science* **343**, 1249531.

Cai, L., Dalal, C.K., & Elowitz, M.B. (2008). Frequency-modulated nuclear localization bursts coordinate gene regulation. *Nature* **455**: 485-490.

Carroll, A.S., Bishop, A.C., DeRisi, J.L., Shokat, K.M., & O'Shea, E.K. (2001). Chemical inhibition of the Pho85 cyclin-dependent kinase reveals a role in the environmental stress response. *P Natl Acad Sci USA* **98**: 12578-12583.

Castillo-Hair, S.M., Igoshin, O.A., & Tabor, J.J. (2015). How to train your microbe: methods for dynamically characterizing gene networks. *Curr Opin Microbiol* **24**: 113-123.

Cohen, M.S., Ghosh, A.K., Kim, H.J., Jeon, N.L., & Jaffrey, S.R. (2012). Chemical Genetic-Mediated Spatial Regulation of Protein Expression in Neurons Reveals an Axonal Function for Wld(S). *Chem Biol* **19**: 179-187.

Crane, M.M., Clark, I.B., Bakker, E., Smith, S., & Swain, P.S. (2014). A microfluidic system for studying ageing and dynamic single-cell responses in budding yeast. *Plos One* **9**: e100042.

Dean, K.M., & Palmer, A.E. (2014). Advances in fluorescence labeling strategies for dynamic cellular imaging. *Nat Chem Biol* **10**: 512-523.

Denervaud, N., Becker, J., Delgado-Gonzalo, R., Damay, P., Rajkumar, A.S., Unser, M., Shore, D., Naef, F., & Maerkl, S.J. (2013). A chemostat array enables the spatio-temporal analysis of the yeast proteome. *P Natl Acad Sci USA* **110**, 15842-15847.

Elowitz, M.B., Levine, A.J., Siggia, E.D., & Swain, P.S. (2002). Stochastic gene expression in a single cell. *Science* **297**: 1183-1186.

Elphick, L.M., Lee, S.E., Gouverneur, V., & Mann, D.J. (2007). Using chemical genetics and ATP analogues to dissect protein kinase function. *ACS Chem Biol* **2**: 299-314.

Ferry, M.S., Razinkov, I.A., and Hasty, J. (2011). Microfluidics for Synthetic Biology: From Design to Execution. *Methods in Enzymology* **497**: 295-372.

Filonov, G.S., Piatkevich, K.D., Ting, L.M., Zhang, J.H., Kim, K., & Verkhusha, V.V. (2011). Bright and stable near-infrared fluorescent protein for in vivo imaging. *Nat Biotechnol* **29**: 757-U133.

Geda, P., Patury, S., Ma, J., Bharucha, N., Dobry, C.J., Lawson, S.K., Gestwicki, J.E., & Kumar, A. (2008). A small molecule-directed approach to control protein localization and function. *Yeast* **25**: 577-594.

Gordon, A., Colman-Lerner, A., Chin, T.E., Benjamin, K.R., Yu, R.C., & Brent, R. (2007). Single-cell quantification of molecules and rates using open-source microscope-based cytometry. *Nat Methods* **4**: 175-181.

Grote, A., Hiller, K., Scheer, M., Munch, R., Nortemann, B., Hempel, D.C., & Jahn, D. (2005). JCat: a novel tool to adapt codon usage of a target gene to its potential expression host. *Nucleic Acids Res* **33**: W526-W531.

Hansen, A.S., & O'Shea, E.K. (2013). Promoter decoding of transcription factor dynamics involves a trade-off between noise and control of gene expression. *Mol Syst Biol* **9**.

Hansen, A.S., & O'Shea, E.K. (2015). Data from: Limits on information transduction through regulation of signaling dynamics. *Dryad Digital Repository*: doi:10.5061/dryad.97vt8

Hao, N., Budnik, B.A., Gunawardena, J., & O'Shea, E.K. (2013). Tunable Signal Processing Through Modular Control of Transcription Factor Translocation. *Science* **339**: 460-464.

Hao, N., Nayak, S., Behar, M., Shanks, R.H., Nagiec, M.J., Errede, B., Hasty, J., Elston, T.C., & Dohlman, H.G. (2008). Regulation of cell signaling dynamics by the protein kinase-scaffold Ste5. *Mol Cell* **30**: 649-656.

Hao, N., & O'Shea, E.K. (2012). Signal-dependent dynamics of transcription factor translocation controls gene expression. *Nat Struct Mol Biol* **19**: 31-39.

Haruki, H., Nishikawa, J., & Laemmli, U.K. (2008). The anchor-away technique: Rapid, conditional establishment of yeast mutant phenotypes. *Mol Cell* **31**: 925-932.

Hersen, P., McClean, M.N., Mahadevan, L., & Ramanathan, S. (2008). Signal processing by the HOG MAP kinase pathway. *P Natl Acad Sci USA* **105**: 7165-7170.

Hillborg, H., Ankner, J.F., Gedde, U.W., Smith, G.D., Yasuda, H.K., & Wikstrom, K. (2000). Crosslinked polydimethylsiloxane exposed to oxygen plasma studied by neutron reflectometry and other surface specific techniques. *Polymer* **41**: 6851-6863.

Huberts, D.H.E.W., Lee, S.S., Gonzalez, J., Janssens, G.E., Avalos Vizcarra, I., & Heinemann, M. (2013). Construction and use of a microfluidic dissection platform for long-term imaging of cellular processes in budding yeast. *Nat Protoc* **8**: 1019-1027.

Huh, W.K., Falvo, J.V., Gerke, L.C., Carroll, A.S., Howson, R.W., Weissman, J.S., & O'Shea, E.K. (2003). Global analysis of protein localization in budding yeast. *Nature* **425**: 686-691.

Imayoshi, I., Isomura, A., Harima, Y., Kawaguchi, K., Kori, H., Miyachi, H., Fujiwara, T., Ishidate, F., & Kageyama, R. (2013). Oscillatory Control of Factors Determining Multipotency and Fate in Mouse Neural Progenitors. *Science* **342**: 1203-1208.

Kellogg, R.A., Gomez-Sjoberg, R., Leyrat, A.A., & Tay, S. (2014). High-throughput microfluidic single-cell analysis pipeline for studies of signaling dynamics. *Nat Protoc* **9**: 1713-1726.

Kremers, G.J., Goedhart, J., van Munster, E.B., & Gadella, T.W.J. (2006). Cyan and yellow super fluorescent proteins with improved brightness, protein folding, and FRET Forster radius. *Biochemistry* **45**: 6570-6580.

Lamprecht, M.R., Sabatini, D.M., & Carpenter, A.E. (2007). CellProfiler(TM): free, versatile software for automated biological image analysis. *Biotechniques* **42**: 71-75.

Lee, P.J., Helman, N.C., Lim, W.A., & Hung, P.J. (2008). A microfluidic system for dynamic yeast cell imaging. *Biotechniques* **44**: 91-95.

Lee, S.S., Avalos Vizcarra, I., Huberts, D.H., Lee, L.P., & Heinemann, M. (2012). Whole lifespan microscopic observation of budding yeast aging through a microfluidic dissection platform. *P Natl Acad Sci USA* **109**: 4916-4920.

Levine, J.H., Lin, Y.H., and Elowitz, M.B. (2013). Functional Roles of Pulsing in Genetic Circuits. *Science* **342**: 1193-1200.

Liu, Y., Kung, C., Fishburn, J., Ansari, A.Z., Shokat, K.M., & Hahn, S. (2004). Two cyclin-dependent kinases promote RNA polymerase II transcription and formation of the scaffold complex. *Mol Cell Biol* **24**: 1721-1735.

McDonald, J.C., Duffy, D.C., Anderson, J.R., Chiu, D.T., Wu, H.K., Schueller, O.J.A., & Whitesides, G.M. (2000). Fabrication of microfluidic systems in poly(dimethylsiloxane). *Electrophoresis* **21**: 27-40.

McIsaac, R.S., Silverman, S.J., McClean, M.N., Gibney, P.A., Macinskas, J., Hickman, M.J., Petti, A.A., & Botstein, D. (2011). Fast-acting and nearly gratuitous induction of gene expression and protein depletion in *Saccharomyces cerevisiae*. *Mol Biol Cell* **22**: 4447-4459.

Menolascina, F., Fiore, G., Orabona, E., De Stefano, L., Ferry, M., Hasty, J., di Bernardo, M., & di Bernardo, D. (2014). In-vivo real-time control of protein expression from endogenous and synthetic gene networks. *PLoS Comput Biol* **10**: e1003625.

Mettetal, J.T., Muzzey, D., Gomez-Uribe, C., & van Oudenaarden, A. (2008). The frequency dependence of osmo-adaptation in Saccharomyces cerevisiae. *Science* **319**: 482-484.

Paige, J.S., Nguyen-Duc, T., Song, W.J., & Jaffrey, S.R. (2012). Fluorescence Imaging of Cellular Metabolites with RNA. *Science* **335**: 1194-1194.

Petrenko, N., Chereji, R.V., McClean, M.N., Morozov, A.V., & Broach, J.R. (2013). Noise and interlocking signaling pathways promote distinct transcription factor dynamics in response to different stresses. *Mol Biol Cell* **24**: 2045-2057.

Prindle, A., Selimkhanov, J., Li, H., Razinkov, I., Tsimring, L.S., & Hasty, J. (2014). Rapid and tunable post-translational coupling of genetic circuits. *Nature*: **508**: 387-391.

Purvis, J.E., & Lahav, G. (2013). Encoding and Decoding Cellular Information through Signaling Dynamics. *Cell* **152**: 945-956.

Qin, D., Xia, Y., & Whitesides, G.M. (2010). Soft lithography for micro- and nanoscale patterning. *Nat Protoc* **5**: 491-502.

Rakhit, R., Navarro, R., & Wandless, T.J. (2014). Chemical Biology Strategies for Post-translational Control of Protein Function. *Chem Biol* **21**: 1238-1252.

Rowat, A.C., Bird, J.C., Agresti, J.J., Rando, O.J., & Weitz, D.A. (2009). Tracking lineages of single cells in lines using a microfluidic device. *P Natl Acad Sci USA* **106**: 18149-18154.

Ryley, J., & Pereira-Smith, O.M. (2006). Microfluidics device for single cell gene expression analysis in Saccharomyces cerevisiae. *Yeast* **23**: 1065-1073.

Sackmann, E.K., Fulton, A.L., & Beebe, D.J. (2014). The present and future role of microfluidics in biomedical research. *Nature 507*: 181-189.

Sanchez, A., & Golding, I. (2013). Genetic determinants and cellular constraints in noisy gene expression. *Science* **342**: 1188-1193.

Selimkhanov, J., Taylor, B., Yao, J., Pilko, A., Albeck, J., Hoffmann, A., Tsimring, L., & Wollman, R. (2014). Accurate information transmission through dynamic biochemical signaling networks. *Science* **346**: 1370-1373.

Senear, D.F., & Teller, D.C. (1981). Thermodynamics of Concanavalin A Dimer-Tetramer Self-Association — Sedimentation Equilibrium Studies. *Biochemistry* **20**: 3076-3083.

Sheff, M.A., & Thorn, K.S. (2004). Optimized cassettes for fluorescent protein tagging in *Saccharomyces cerevisiae*. *Yeast* **21**: 661-670.

Shirra, M.K., McCartney, R.R., Zhang, C., Shokat, K.M., Schmidt, M.C., & Arndt, K.M. (2008). A chemical genomics study identifies Snf1 as a repressor of GCN4 translation. *The Journal of biological chemistry* **283**: 35889-35898.

Sorre, B., Warmflash, A., Brivanlou, A.H., & Siggia, E.D. (2014). Encoding of Temporal Signals by the TGF-beta Pathway and Implications for Embryonic Patterning. *Dev Cell* **30**: 334-342.

Spiller, D.G., Wood, C.D., Rand, D.A., & White, M.R.H. (2010). Measurement of single-cell dynamics. *Nature* **465**: 736-745.

Strack, R.L., Song, W.J., & Jaffrey, S.R. (2014). Using Spinach-based sensors for fluorescence imaging of intracellular metabolites and proteins in living bacteria. *Nat Protoc* **9**: 146-155.

Taylor, R.J., Falconnet, D., Niemisto, A., Ramsey, S.A., Prinz, S., Shmulevich, I., Galitski, T., & Hansen, C.L. (2009). Dynamic analysis of MAPK signaling using a high-throughput microfluidic single-cell imaging platform. *P Natl Acad Sci USA* **106**: 3758-3763.

Tseng, P., Weaver, W.M., Masaeli, M., Owsley, K., & Di Carlo, D. (2014). Research highlights: microfluidics meets big data. *Lab Chip* **14**: 828-832.

Uhlendorf, J., Miermont, A., Delaveau, T., Charvin, G., Fages, F., Bottani, S., Batt, G., & Hersen, P. (2012). Long-term model predictive control of gene expression at the population and single-cell levels. *P Natl Acad Sci USA* **109**: 14271-14276.

Westfall, P.J., & Thorner, J. (2006). Analysis of mitogen-activated protein kinase signaling specificity in response to hyperosmotic stress: use of an analog-sensitive HOG1 allele. *Eukaryot Cell* **5**: 1215-1228.

Xie, Z., Zhang, Y., Zou, K., Brandman, O., Luo, C., Ouyang, Q., & Li, H. (2012). Molecular phenotyping of aging in single yeast cells using a novel microfluidic device. *Aging Cell* **11**: 599-606.

Yissachar, N., Fischler, T.S., Cohen, A.A., Reich-Zeliger, S., Russ, D., Shifrut, E., Porat, Z., & Friedman, N. (2013). Dynamic Response Diversity of NFAT Isoforms in Individual Living Cells. *Mol Cell* **49**: 322-330.

Zaman, S., Lippman, S.I., Schneper, L., Slonim, N., & Broach, J.R. (2009). Glucose regulates transcription in yeast through a network of signaling pathways. *Mol Syst Biol* **5**.

Zechner, C., Unger, M., Pelet, S., Peter, M., & Koeppl, H. (2014). Scalable inference of heterogeneous reaction kinetics from pooled single-cell recordings. *Nat Methods* **11**: 197-202.

Zhang, Y., Luo, C., Zou, K., Xie, Z., Brandman, O., Ouyang, Q., & Li, H. (2012). Single cell analysis of yeast replicative aging using a new generation of microfluidic device. *Plos One* **7**: e48275.

Zid, B.M., & O'Shea, E.K. (2014). Promoter sequences direct cytoplasmic localization and translation of mRNAs during starvation in yeast. *Nature* **514**: 117-121.

Chapter 5

Discussion and future directions

5.1 Discussion

5.1.1 Motivating hypothesis behind this dissertation

As we have discussed in Chapter 1, cellular signaling networks tend to exhibit a bowtie topology (Figure 1.2) in which multiple distinct signals converge on a single master regulator, typically a transcription factor, which then regulates distinct downstream gene expression programs. Furthermore, the master regulator transcription factor often shows different activation dynamics in response to different signals. Thus, the motivating hypothesis behind this dissertation has been that genes can differentially decode transcription factor dynamics. For example, oscillations could predominantly induce one set of genes, whereas sustained transcription factor activation would predominantly induce a different set of genes. If true, this could possibly explain how a single master regulator transcription factor can induce different sets of genes in response to different signals or stresses. Early evidence that this might be true came from the original study by Hao & O'Shea on Msn2, which indicated that different yeast promoters decode Msn2 dynamics differently (Hao & O'Shea, 2012).

To systematically dissect how different promoters decode TF dynamics, we therefore developed high-throughput microfluidic technologies coupled to quantitative time-lapse microscopy (Chapter 4). We discuss these efforts below.

5.1.2 Development of a high-throughput microfluidic device

A major technical advance from this dissertation work is the development of the high-throughput microfluidic device detailed in Chapter 4. This device took us around two years to develop because several technical challenges had to be overcome. First, Msn2 is extremely sensitive to stress and just slightly curved microfluidic channels can lead to Msn2 activation. We designed and tested around thirty different microfluidic devices before we found a design that could: multiplex five experiments; enable rapid medium switching; and did not aberrantly activate Msn2. Second, the inhibitor 1-NM-PP1 absorbs into essentially all hydrophobic materials, including valves, PDMS and tubing, prohibiting wash-out. By solving these technical problems (Chapter 4) and developing an automated fluid control system, we can now perform twenty different time-lapse experiments in a regular work day whilst collecting time-course data for thousands of cells. Furthermore, we wrote image analysis software that allowed us to largely automate the analysis of time-lapse movies. Together, this dissertation contains multidimensional time-course data for around half a million single cells under different dynamical Msn2 perturbations — a dataset of unprecedented size and quality.

5.1.3 How promoters decode Msn2 dynamics

Following the development of our high-throughput microfluidic device, we tackled the problem of how different promoters decode transcription factor dynamics in single cells.

Previous approaches suffered from an inability to directly control transcription factor activity — which is necessary to distinguish causation from correlation — and from considering only the population average (Nelson *et al.*, 2004; Ashall *et al.*, 2009; Tay *et al.*, 2010).

By systematically dissecting how natural Msn2-dependent promoters decode Msn2 dynamics (Figure 2.1), we found that two properties can largely explain differences in the promoter responses: the promoter amplitude threshold and the promoter activation timescale. Since promoters can either have a low or high threshold and either be fast or slow, we propose that promoters can usefully be classified as belonging to one of four extreme promoter classes (Figure 2.2B). Furthermore, we show theoretically that given these four different promoter classes, it is in principle possible for the cell to encode four distinct gene expression programs in the dynamics of a single transcription factor (Figure 2.5).

What then determines which class a promoter falls into? We show that the activation timescale correlates with the nucleosome remodeling timescale (Figure 2.7E). Further, we show that chromatin remodeling is causally important for setting the promoter activation timescale: deletion of either the SWI/SNF or SAGA complex significantly slows down a fast promoter and abolishes gene induction from a slow promoter. The amplitude threshold is in part determined by the number, strength and accessibility of Msn2 binding sites. In ongoing work we outline in Appendix D, we have shown that simply by modulating the number and location of Msn2 binding sites, we can convert the HS gene, *SIP18*, into either the LF or LS class. The mechanistic basis for each promoter class will be an interesting and promising avenue to explore in more detail in the future.

By showing that gene promoters can fall into at least four extreme promoter classes and that each class can be preferentially induced just by regulating the dynamics of the master regulator transcription factor, we provide significant support for the encoding/decoding

paradigm in this dissertation. It is possible to preferentially transmit at least four distinct gene expression programs through a bowtie-shaped signal transduction pathway. However, when considering gene induction at the single cell level, we found an important trade-off which we will discuss in the next section.

5.1.4 A trade-off between noise and promoter filtering

By considering how different promoter classes decode Msn2 dynamics in single cells, we found that gene expression noise differs dramatically between different promoter classes (Figure 2.4). Specifically, we found that slow promoters suffer from dramatically higher noise than fast promoters. This can also be rationalized theoretically (Figure 2.6). Furthermore, we also found that only by being slow can a promoter filter out transient Msn2 input or Msn2 pulses. Thus, these results highlight a previously unappreciated trade-off (Figure 2.8). Slow promoters have filtering properties and therefore avoid leaky induction due to signaling noise. However, this comes at the cost of dramatically higher noise in gene expression — when slow promoters do induce, there is so much noise that a significant fraction of the population often fails to respond at all. Conversely, fast promoters have much lower noise in gene expression and can respond more reliably to upstream signals. However, this comes at the cost of leakiness and an inability to filter out upstream signaling noise. Thus, for promoters there is a trade-off between reducing noise and having filtering abilities.

The unexpectedly high levels of cell-to-cell variability that we observed motivated us to rigorously investigate information transduction through regulation of the dynamics of a single transcription factor.

5.1.5 Limits on information transduction through regulation of transcription factor dynamics

Cell signaling is fundamentally about information transduction (e.g. transducing information about hormone exposure to induce a specific cell fate), yet cell signaling is typically studied in very qualitative terms. For example, the biochemical targets of many pathways are now well understood (Hynes *et al.*, 2013). But there is still not a single pathway for which we know quantitatively how much information it can transduce (in bits).

Although we have shown that it is possible for a bowtie-shaped pathway to give rise to at least four different downstream fates at a population-averaged level, we wanted to know how much information it is possible to transmit through a bowtie-shaped pathway by regulating the dynamics of a single transcription factor. As we discuss in Chapter 3, we find that gene expression noise severely limits information transduction such that in the absence of other network motifs, only information about signal identity, but not signal intensity, can be transduced simply by regulating the dynamics of Msn2.

Instead, in order to increase the information transduction capacity it is necessary to either average over multiple genes or multiple cells to reduce the effects of noise. Furthermore, we find that the information transduction capacity of a gene can be tuned in *cis*. Nonetheless, at the level of an individual cell, information about different signal identities can be transduced through a gene, but not information about signal intensity.

5.1.6 The encoding/decoding paradigm revisited

In Chapter 1 we introduced the "encoding/decoding paradigm". Recently, this idea has been the topic of intense interest (Behar & Hoffmann, 2010; Levine *et al.*, 2013; Purvis and Lahav, 2013). In this dissertation, we have attempted to rigorously test this paradigm by

quantifying the limits on information transduction through regulating the temporal activation dynamics of transcription factors.

Taken together, our findings are consistent with the general idea of the "encoding/decoding paradigm". A large number of studies have shown that cells encode information by regulating the dynamics of transcription factors (Chapter 1) and we find that individual genes are capable of differentially decoding transcription factor dynamics. We find that there is significant loss of information at the decoding step, but that differential decoding is possible in single cells. For example it should be possible to reliably have a single transcription factor control two different cell fates in response to an inducing signal simply by differentially regulating its dynamics. This strongly supports the idea that regulation of signaling dynamics is sufficient to control cell fate. However, based on our results on the Msn2 system, moving beyond two different cells fates does not appear to be possible.

In the future it will be interesting to apply the approach described in this dissertation to other systems including those in mammalian cells. Furthermore, we have exclusively considered the transcription factor input — gene expression output relationship. If the gene product itself is involved in feedback or feed-forward interactions, more sophisticated control of cell fate may be possible. Additionally, we have only considered the case of a single transcription factor even though combinatorial control is clearly important, especially in higher eukaryotes. This dissertation therefore suggests a number of interesting future directions, which we will briefly discuss below.

5.2 Future directions

5.2.1 Msn2 and Msn4 — a coherent feed-forward motif

In this dissertation we have exclusively considered Msn2. However, in budding yeast the general stress response is mediated by the two partially redundant and highly similar transcription factors, Msn2 and Msn4. This system is complicated by the fact that whereas Msn2 expression is constant and constitutive, Msn4 is itself a target of Msn2 (Gasch *et al.*, 2000). Thus, the general stress response exhibits memory — a cell recently exposed to stress will have higher levels of Msn4 and therefore induce the environmental stress response more strongly than a cell not previously exposed to stress. In fact, the Msn2/Msn4 motif forms a type 1 coherent feed-forward loop. The properties of type 1 coherent feed-forward loops depend in part on whether the downstream module is an AND gate or an OR gate (Alon, 2007). This dissertation suggests that, depending on the amplitude threshold of promoters, a promoter could serve as both an AND or an OR gate. Thus, it will be important in the future to dissect what role this type 1 coherent feed-forward loop plays in the yeast general stress response. Given that coherent feed-forward loops exhibit memory and that promoters also exhibit memory as we have shown in Chapter 2, the interplay between the two will be very interesting and is likely to exhibit non-trivial dynamics.

In addition to the decoding step, characterizing the dynamics of Msn4 under natural stress will also be critical. Superficially, since Msn2 and Msn4 are highly similar in sequence and since both are regulated by PKA, one might expect Msn4 dynamics to identically match Msn2 dynamics during stress. However, this might not be so. Hao & O'Shea showed that Msn2 dynamics under stress can be tuned by controlling the nuclear localization signal and the nuclear export signal (Hao *et al.*, 2013). They found that both nuclear localization signal

mutants and nuclear export signal mutants could not fully distinguish glucose limitation, oxidative and osmotic stress like the wild-type Msn2 protein. Thus, if the kinetics of nuclear import or nuclear export for Msn4 are different, Msn2 and Msn4 may show very different dynamics under natural stress. Along these lines, NFAT1 and NFAT4 also show different dynamics in response to the same signal despite being highly similar in sequence (Yissachar *et al.*, 2013).

Thus, both at the upstream level (Msn2 and Msn4 dynamics during stress) and at the downstream level (gene induction by Msn2 and Msn4), the interplay between Msn2 and Msn4 remains entirely unexplored. We highlight this as a very interesting avenue for future studies.

5.2.2 Information encoded in Msn2/Msn4 dynamics

As emphasized above, characterizing the dynamics of both Msn2 and Msn4 in response to stress is a promising future direction. It would also be interesting to apply information theory to this problem. In Chapter 3, we implicitly assume that Msn2 translocation dynamics encode much more information about stress identity and intensity than can be decoded by individual genes. This assumption is strongly supported by previous studies (Hao & O'Shea, 2012; Hao *et al.*, 2013). However, it remains unclear how much information about environmental stresses Msn2 dynamics encodes and how many different stresses can be reliably distinguished based on Msn2 dynamics. It would be interesting to measure the joint mutual information for Msn2 and Msn4 under natural stresses. This is a challenging problem, which requires both extensive high-quality time-lapse data and careful calculation to adjust for bias in the mutual information calculations. However, recent studies on information encoding in the dynamics of mammalian transcription factors and kinases could provide a foundation

(Selimkhanov *et al.*, 2014). As in Chapter 3, the underlying motivation is that by putting a number on information transduction we can quantitatively understand what is and what is not possible for signal transduction pathways and understand the limits on information transduction through regulation of signaling dynamics.

5.2.3 Systematic dissection of how promoter architecture controls decoding using FACS-Seq

As discussed above, our work highlights the importance of the promoter amplitude threshold and activation timescale in controlling how promoters decode transcription factor dynamics. This begs the question of what determines the amplitude threshold and activation timescale, mechanistically. The ultimate goal would be to be able to predict the promoter class from DNA sequence alone.

In ongoing studies we outline in Appendix D, we have systematically dissected how the distribution and number of Msn2 binding sites in the *SIP18* promoter affect promoter class. From these studies, we find that just two variables can quantitatively explain >90% of the variance we see in the promoter amplitude threshold: 1) the number of clustered binding sites and 2) the nucleosome occupancy over these binding sites (Figure D.5). Similarly, just three variables are necessary to quantitatively explain >90% of the variance we see in the promoter activation timescale: 1) the number of clustered binding sites; 2) the nucleosome occupancy over these binding sites and 3) the distance from these binding sites to the transcription start site (Figure D.5). Furthermore, we find that we can convert *SIP18* into both the LF and LS classes simply by modulating the number and location of binding sites in the promoter (see also Appendix D and Figures D.3 & D.4).

Although these studies have given significant insight into the mechanistic basis for pro-

moter class, this approach is very labor-intensive and limited to the study of at most a few promoters. To fully understand this relationship, it would be necessary to determine the amplitude threshold and activation timescale for thousands of systematically designed promoters. By combining recent developments in combinatorial synthesis of long DNA fragments based on microarray technology with FACS-Seq (Sharon *et al.*, 2012), this is now possible. Thus, an important follow-up project from this work would be to initiate a study where the response of thousands of systematically designed promoters to transcription factor dynamics is determined using FACS-Seq. Such a study would likely advance our understanding of the relationship between promoter class and DNA sequence significantly.

5.2.4 Complete mechanism and order of events during transcriptional regulation at single promoter

In this dissertation we have characterized and measured the amplitude threshold and activation timescale for several natural Msn2 target promoters. We have also shown that some Msn2 binding sites and the SWI/SNF and SAGA complex are required for induction of *SIP18*. Yet, we are still very far from a mechanistic understanding of the order of events that take place at any individual promoter. For example, does nucleosome remodeling take place before or after Msn2 binding? All promoters studied in this work have multiple Msn2 binding sites. But which site is bound first? And how does binding at one site affect binding at another? Furthermore, we have not yet investigated several aspects of chromatin. For example, which nucleosome in a promoter is evicted first? What histone modifications change during promoter activation and in which order? What are the histone modifying enzymes that are recruited to each promoter and in which order do these events take place? How is RNA Pol II recruited to a promoter? Furthermore, since we observe memory effects

under Msn2 pulsing, how is this memory stored? The most likely explanation would be in histone modifications and nucleosome positioning, but which histone modifications? And how quickly does this memory decay?

Most of these questions can be addressed through chromatin immuno-precipitation experiments combined with our chemical genetic method for controlling Msn2 localization and activity. By dissecting the order of events, it should be possible to develop and test a full mechanistic model for the order of events during gene activation. This could advance our understanding of the transcriptional control mechanism.

5.2.5 Promoter memory effects

We observe widespread memory effects during gene activation (Figure 2.1C). For example, in response to Msn2 pulsing, the gene expression output is not simply proportional to the number of pulses. One way this can be rationalized is through the "head-start" effect (Hao & O'Shea, 2012). To illustrate this idea, consider the following. During the first pulse, even if no mRNA is produced, chromatin remodeling and histone modifications might take place at a promoter. For example, a nucleosome could be evicted making it easier for Msn2 to bind in the future. This means that during the second pulse, Msn2 it more likely to be able to activate gene expression and transcription is more likely to occur. Thus, there is a head-start effect after the first pulse.

At the same time, a head-start effect is only observed if the interval between the first and second pulses is shorter than the decay time. Our microfluidic platform allows for full control of Msn2 translocation dynamics and measurement of the gene expression time-traces. Additionally, from our deterministic modeling work (Figure 2.2A) we found that at least three promoter states are necessary to account for the delays in gene activation that we

observe. Thus, it could be interesting to quantitatively characterize these promoter memory effects and ask questions such as: How is promoter memory stored and how quickly does it decay? How different is this for different promoters? Can we change promoter memory by modulating promoter architecture? All of these are interesting questions that could take our understanding of gene regulation beyond the classical two-state random telegraph model (Ko 1991; Peccoud & Ycart, 1995).

5.2.6 Dissecting timing and causality for histone modifications

One of the main limitations of chromatin research is that almost all studies are correlative in nature. At this stage, a host of specific histone modifications are described and whether they correlate with repression or activation is now known (Bannister & Kouzarides, 2011). For example, it is known that H3K9me3 tends to mark repressed genes, but it is unclear whether H3K9me3 is a cause or consequence of gene repression. Phrased differently, if one were to deposit H3K9me3 on a gene, what would happen to gene activity?

Recent developments in programmable DNA binding protein engineering (Hsu *et al.* combined with small molecule-mediated control of protein localization (Geda *et al.*, 2008; Haruko *et al.*, 2008; McIsaac *et al.*, 2012; Rakhit *et al.*, 2014), now makes it possible to control recruitment of chromatin remodeling enzymes to specific loci using small molecules (Hathaway *et al.*, 2012). When combined with our microfluidic system, it should be possible to independently control both Msn2 localization and chromatin remodeling with exquisite spatiotemporal resolution. Using gene expression as a read-out, it is therefore possible to quantitatively dissect the effect of specific histone modifications on gene expression. For example, how would gene activation be affected if a repressive or activating mark was placed on a promoter just prior to Msn2 activation?

This combination would allow for an elegant dissection of questions such as this one and could improve our understanding of what effect different histone modifications causally have on gene expression.

5.2.7 Msn2 dynamics and gene activation at the single-molecule level

To fully understand the steps involved in gene activation, it will be necessary to describe these steps as probabilistic events. For example, what is the probability that a promoter will produce an mRNA within the first five minutes of Msn2 activation? In principle, since we have extensive single-cell time trace data for the YFP and CFP gene expression reporters, it should be possible to infer the underlying promoter transition dynamics using inference approaches (Zechner *et al.*, 2014).

Another more direct approach would be to observe transcription as it takes place in real time at the single molecule level. Pioneering work from Robert Singer and colleagues using the MS2 system now makes it possible to count every time a gene transcribes an mRNA inside living yeast cells in real time (Larson *et al.*, 2011). Combined with our microfluidic system to control Msn2 activity, it is therefore possible to pulse Msn2 in and out of the nucleus and count every time an mRNA is produced. By circumventing the need for inferring promoter activity from fluorescent protein measurements, this would allow direct observation of the transcription process. Furthermore, if such data could be obtained it would also be possible to constrain and distinguish stochastic models of gene expression. Such studies could profoundly increase our understanding of the transcription control mechanism.

5.3 Final remarks

The work described in this thesis was motivated by the hypothesis that cells transmit information by differentially regulating the dynamics of transcription factors. We provide the first systematic dissection of how different promoters decode transcription factor dynamics in single cells. Our work yields new insight into gene regulation and the limits on information transduction through regulation of signaling dynamics. However, as is often the case, while we have answered some questions, we have also raised several new ones. We therefore hope that our approach, which emphasizes dissecting causal relationships and rigorously quantifying information transduction, will inspire future work in the fields of signaling dynamics and gene regulation.

5.4 Chapter 5 references

Alon, U. (2007). Network motifs: theory and experimental approaches. *Nature Reviews Genetics* **8**: 450-461.

Ashall, L., Horton, C.A., Nelson, D.E., Paszek, P., Harper, C.V., Sillitoe, K., Ryan, S., Spiller, D.G., Unitt, J.F., Broomhead, D.S., Kell, D.B., Rand, D.A., See, V. & White, M.R. (2009) Pulsatile stimulation determines timing and specificity of NF-kappaB-dependent transcription. *Science* **324**:242-246

Bannister, A. J., & Kouzarides, T. (2011). Regulation of chromatin by histone modifications. *Cell research* **21**: 381-395.

Behar, M., & Hoffmann, A. (2010). Understanding the temporal codes of intra-cellular signals. *Curr Opin Genet Dev* **20**: 684-693.

Gasch, A. P., Spellman, P. T., Kao, C. M., Carmel-Harel, O., Eisen, M. B., Storz, G., Botstein, D. & Brown, P. O. (2000). Genomic expression programs in the response of yeast cells to environmental changes. *Molecular biology of the cell* **11**: 4241-4257.

Geda, P., Patury, S., Ma, J., Bharucha, N., Dobry, C. J., Lawson, S. K., Gestwicki, J. E., & Kumar, A. (2008). A small molecule-directed approach to control protein localization and function. *Yeast* **25**: 577-594.

Hathaway, N. A., Bell, O., Hodges, C., Miller, E. L., Neel, D. S., & Crabtree, G. R. (2012). Dynamics and memory of heterochromatin in living cells. *Cell* **149**: 1447-1460.

Hao, N., & O'Shea, E.K. (2012). Signal-dependent dynamics of transcription factor translocation controls gene expression. *Nature structural & molecular biology* **19**: 31-U47.

Hao, N., Budnik, B.A., Gunawardena, J., & O'Shea, E.K. (2013). Tunable Signal Processing Through Modular Control of Transcription Factor Translocation. *Science* **339**: 460-464.

Haruki, H., Nishikawa, J., & Laemmli, U. K. (2008). The anchor-away technique: rapid, conditional establishment of yeast mutant phenotypes. *Molecular cell* **31**: 925-932.

Hynes, N. E., Ingham, P. W., Lim, W. A., Marshall, C. J., Massague, J., & Pawson, T. (2013). Signalling change: signal transduction through the decades. *Nature Reviews Molecular Cell Biology* **14**: 393-398.

Hsu, P. D., Lander, E. S., & Zhang, F. (2014). Development and applications of CRISPR-Cas9 for genome engineering. *Cell* **157** 1262-1278.

Ko M. S. H. (1991). A stochastic model for gene induction. *Journal of Theoretical Biology* **153**: 181-194.

Larson, D. R., Zenklusen, D., Wu, B., Chao, J. A., & Singer, R. H. (2011). Real-time observation of transcription initiation and elongation on an endogenous yeast gene. *Science* **332**: 475-478.

Levine, J.H., Lin, Y.H., & Elowitz, M.B. (2013). Functional Roles of Pulsing in Genetic Circuits. *Science* **342**: 1193-1200.

McIsaac, R. S., Silverman, S. J., McClean, M. N., Gibney, P. A., Macinskas, J., Hickman, M. J., Petti, A. N., & Botstein, D. (2011). Fast-acting and nearly gratuitous induction of gene expression and protein depletion in Saccharomyces cerevisiae. *Molecular biology of the cell* **22**: 4447-4459.

Nelson, D.E., Ihekwaba, A.E., Elliott, M., Johnson, J.R., Gibney, C.A., Foreman, B.E., Nelson, G., See, V., Horton, C.A., Spiller, D.G., Edwards, S.W., McDowell, H.P., Unitt, J.F., Sullivan, E., Grimley, R., Benson, N., Broomhead, D., Kell, D.B. & White, M. R. (2004) Oscillations in NF-kappaB signaling control the dynamics of gene expression. *Science* **306**:704-708

Peccoud, J. & Ycart, B. (1995). Markovian Modeling of Gene Product Synthesis. *Theor Popul Biol* **48**: 222-234.

Purvis, J.E., & Lahav, G. (2013). Encoding and Decoding Cellular Information through Signaling Dynamics. *Cell* **152**: 945-956.

Rakhit, R., Navarro, R., & Wandless, T. J. (2014). Chemical Biology Strategies for Post-translational Control of Protein Function. *Chemistry & biology* **21**: 1238-1252.

Sharon, E., Kalma, Y., Sharp, A., Raveh-Sadka, T., Levo, M., Zeevi, D., Keren, L., Yakhini, Z., Weinberger, A., Segal, E. (2012) Inferring gene regulatory logic from high-throughput measurements of thousands of systematically designed promoters. *Nat Biotechnol* **30**: 521-530

Selimkhanov, J., Taylor, B., Yao, J., Pilko, A., Albeck, J., Hoffmann, A., Tsimring, L., & Wollman, R. (2014). Accurate information transmission through dynamic biochemical signaling networks. *Science* **346**: 1370-1373.

Tay, S, Hughey, J.J., Lee, T.K., Lipniacki, T., Quake, S.R., Covert, M.W. (2010) Single-cell NF-kappaB dynamics reveal digital activation and analogue information processing. *Nature* **466**: 267-271

Yissachar, N., Fischler, T.S., Cohen, A.A., Reich-Zeliger, S., Russ, D., Shifrut, E., Porat, Z. & Friedman N. (2013) Dynamic response diversity of NFAT isoforms in individual living cells. *Mol Cell* **49**:322-330

Zechner, C., Unger, M., Pelet, S., Peter, M., & Koeppl, H. (2014). Scalable inference of heterogeneous reaction kinetics from pooled single-cell recordings. *Nature methods* **11**: 197-202.

Appendix A

Supplementary information for Chapter 2

A.1 Supplementary figures for Chapter 2

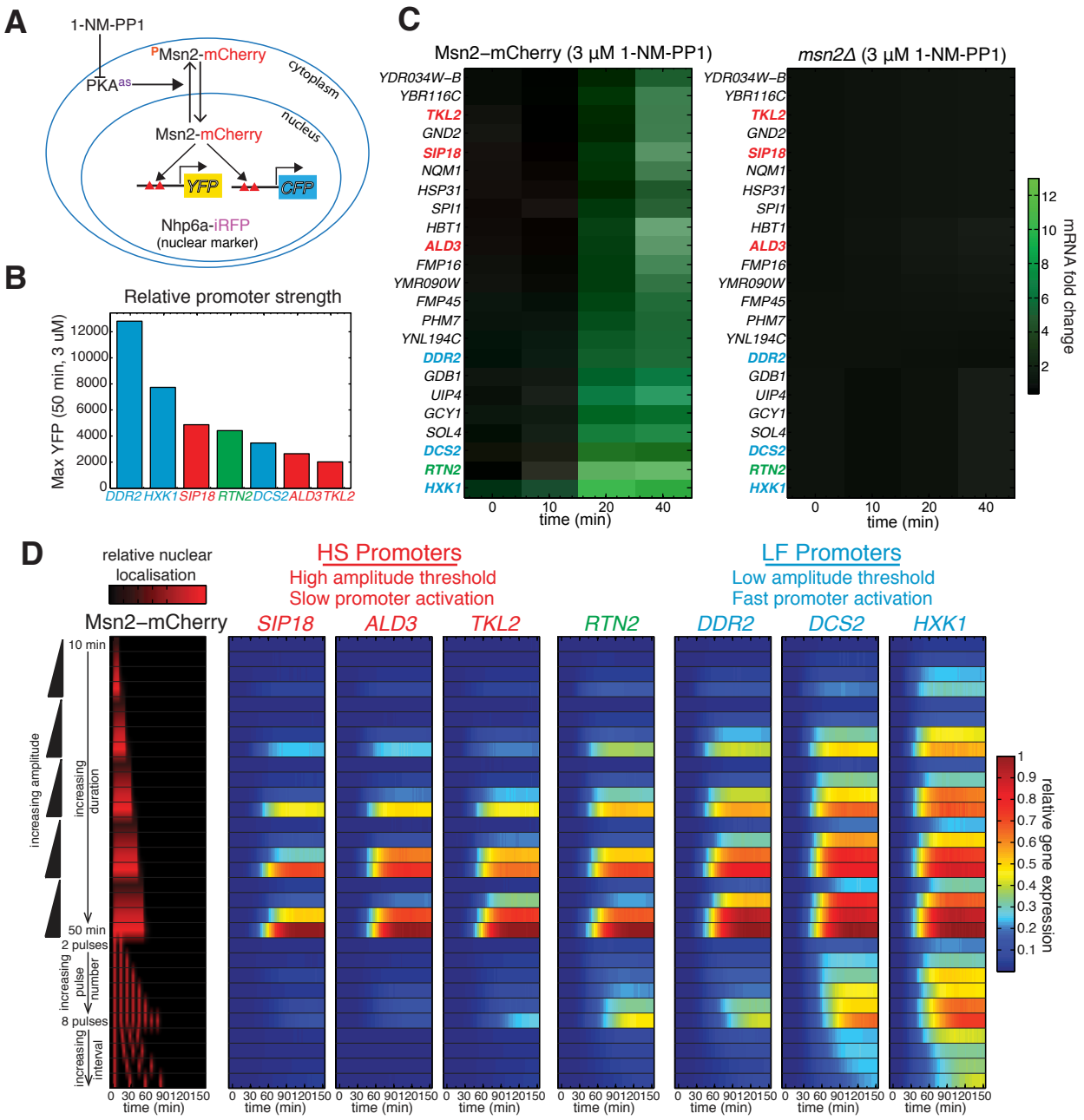

Figure A.1: *Overview of strains, microarray experiment and full gene expression heatmap*
(A) Overview of strains. Diploid strains were used for all experiments. Each of the 3 catalytic subunits of PKA has been mutated to contain an analogue-sensitive mutation (M→G) in the ATP binding pocket that renders it selectively and reversibly inhibitable with the small-molecule inhibitor 1-NM-PP1. Msn2 is C-terminally tagged with mCherry. Thus, when 1-NM-PP1 is added to the cells, PKA^{as} is inhibited, Msn2-mCherry dephosphorylated and translocated to the nucleus where it activates the expression of target genes. The ORF of Msn2 target genes were replaced with YFP (mCitrineV163A) in haploid *MAT***a** strains and CFP (SCFP3A) in haploid *MAT*α strains and mated. The diploid strains therefore have the Msn2 target gene replaced with YFP on one chromosome and CFP on the other. The nuclear protein Nhp6a was C-terminally tagged with the infrared fluorescent protein iRFP to allow easy segmentation of the cell nucleus. All strains are *msn4*Δ.
(B) Relative promoter strengths. As an approximate measure for promoter strength, the gene expression response to a single 50 min pulse with 3 μM 1-NM-PP1 was used, which yields high induction for all the promoters.
(C) Identification of Msn2 target genes. 3 μM 1-NM-PP1 was added to diploids with Msn2 (Msn2-mCherry, right) or without (*msn2*Δ, left) and global gene expression monitored by microarray profiling at time points 0, 10, 20 and 40 min. Shown is the fold change in mRNA levels. 23 genes (each row is a gene) showed strong induction at the mRNA level in the presence of Msn2-mCherry, but no induction in the absence of Msn2.
(D) Systematic dissection of how different promoters decode transcription factor dynamics. Each row corresponds to a specific Msn2-mCherry input (left, in red) and the corresponding gene expression response for each of the 7 promoters is shown on the corresponding rows on the right. The gene expression responses for each promoter are internally normalized to their maximal expression level. Each row is the per-cell average of ∼200-600 cells from at least three biological replicates. This heatmap shows all 210 experiments. The heatmap in Figure 2.1C only shows a subset.

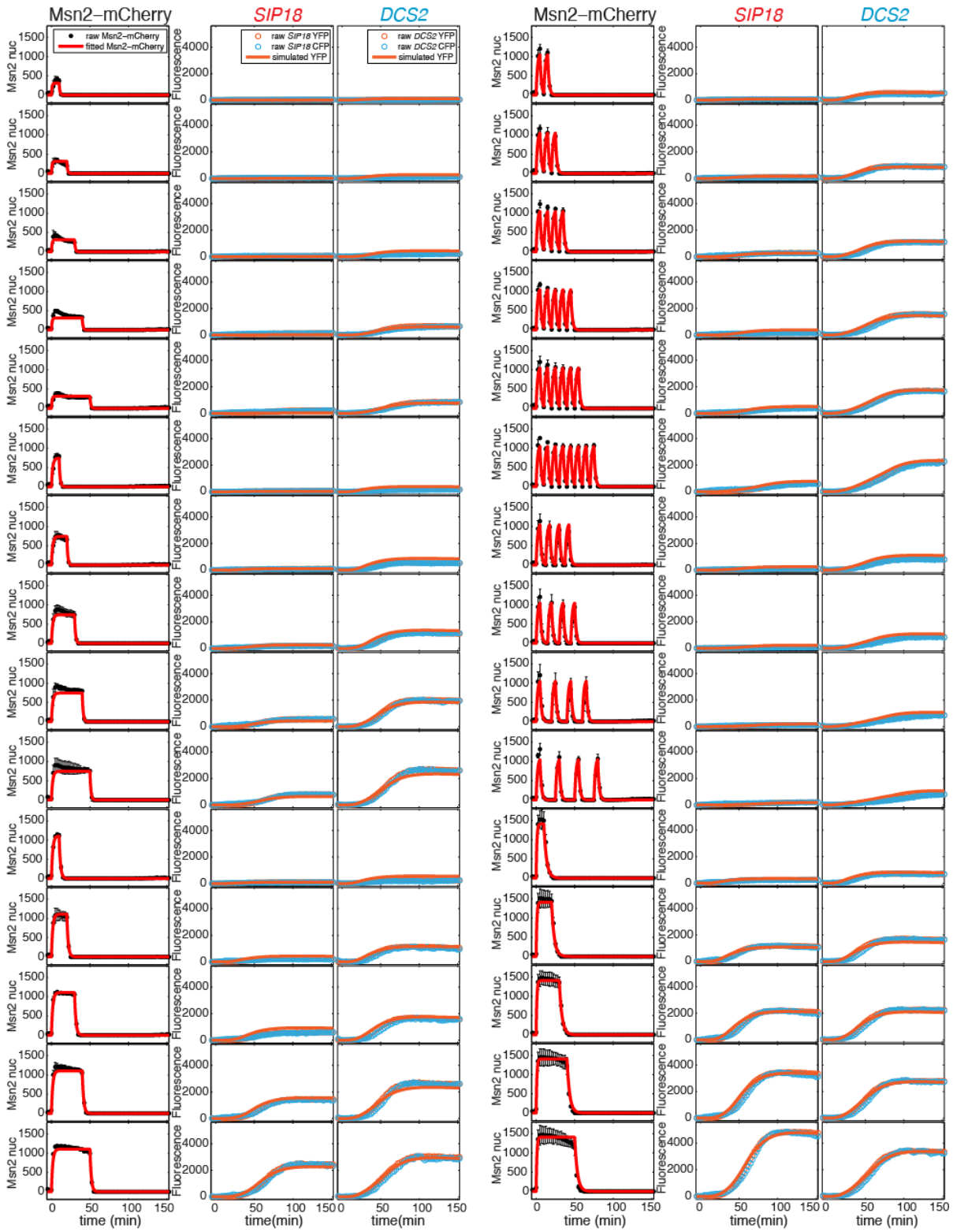

Figure A.2: *Comparison of model fits and raw data for SIP18 and DCS2*
Comparison of model fits and raw data for *SIP18* and *DCS2*. Msn2-mCherry input (1st and 4th columns), per-cell average *SIP18* (2nd and 5th columns) and *DCS2* (3rd and 6th columns) are shown. For Msn2-mCherry, the black dots depict raw data. For *SIP18* and *DCS2* the open orange and cyan circles depict raw YFP and CFP data, respectively. The solid orange line depicts the global model fit to the raw YFP data. The fitting was done by fitting the model in Figure 2.2A using the solid red lines as Msn2-mCherry input and computing the parameters that globally minimized the least-squares error between the model output and the raw YFP data. The dots in Figure 2.2C-F are the maxima of the raw YFP data (orange open circles) shown in this figure.

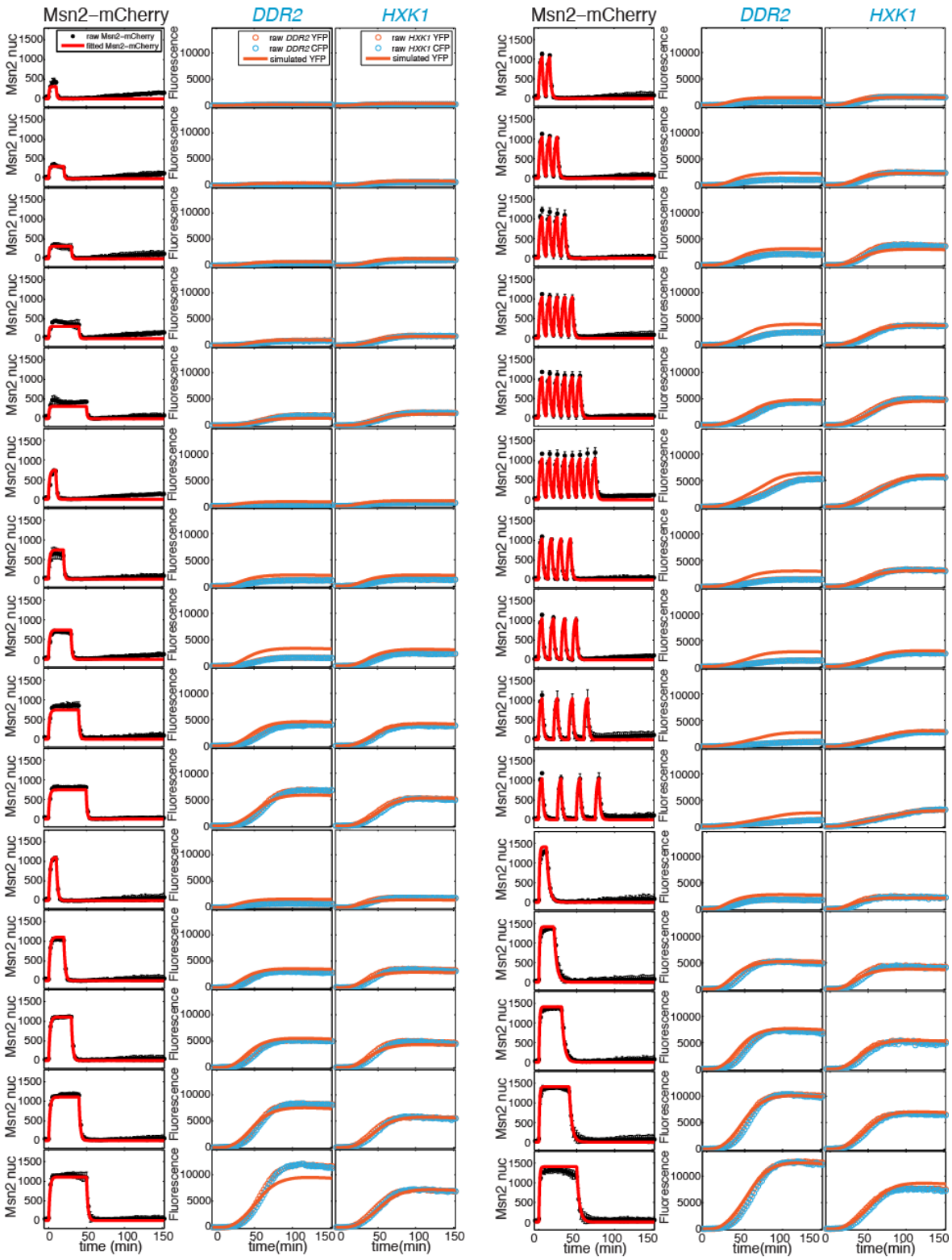

Figure A.3: *Comparison of model fits and raw data for DDR2 and HXK1*
Comparison of model fits and raw data for *DDR2* and *HXK1*. Msn2-mCherry input (1st and 4th columns), per-cell average *DDR2* (2nd and 5th columns) and *HXK1* (3rd and 6th columns) are shown. For Msn2-mCherry, the black dots depict raw data. For *DDR2* and *HXK1* the open orange and cyan circles depict raw YFP and CFP data, respectively. The solid orange line depicts the global model fit to the raw YFP data. The fitting was done by fitting the model in Figure 2.2A using the solid red lines as Msn2-mCherry input and computing the parameters that globally minimized the least-squares error between the model output and the raw YFP data.

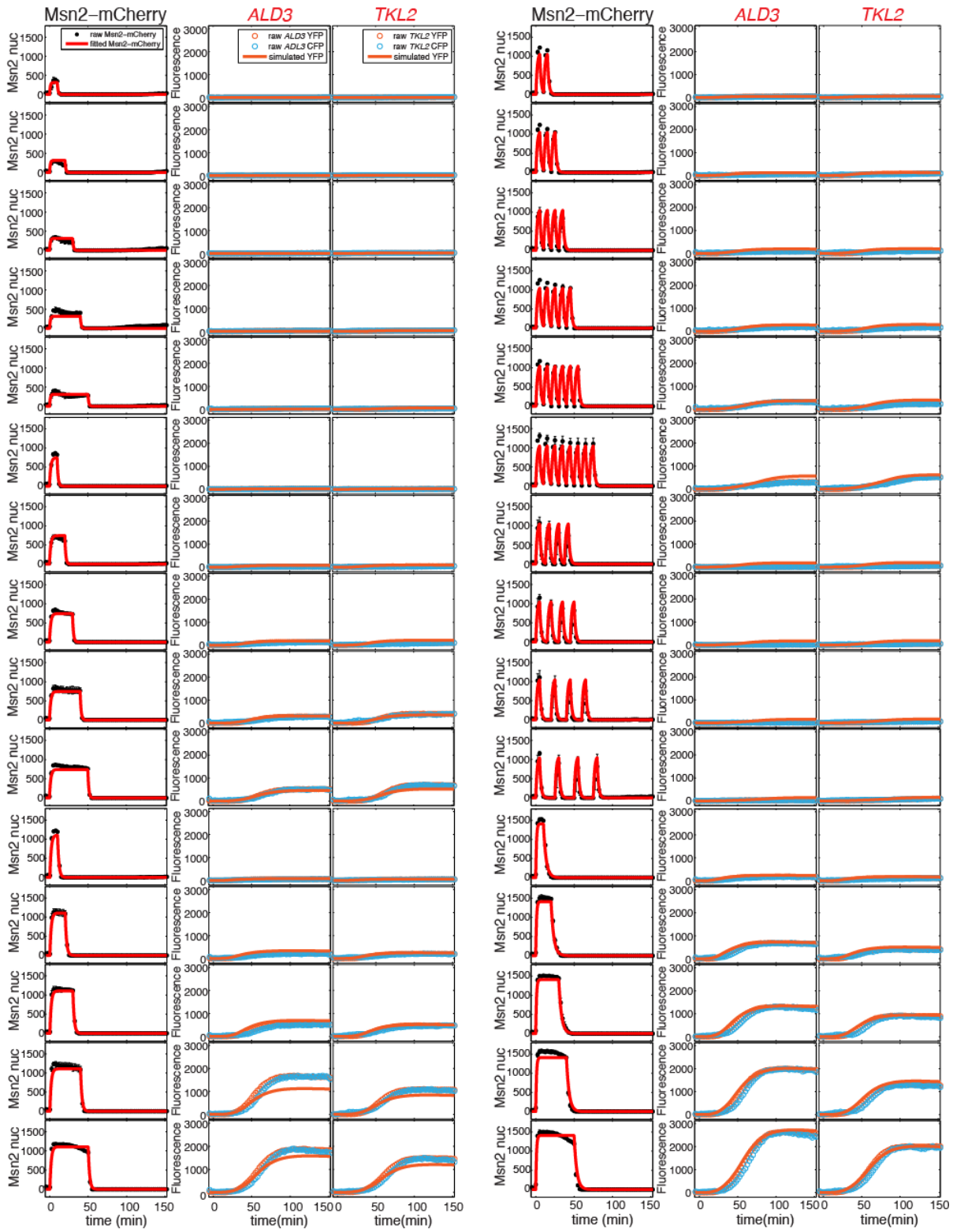

Figure A.4: *Comparison of model fits and raw data for ALD3 and TKL2*
Comparison of model fits and raw data for *ALD3* and *TKL2*. Msn2-mCherry input (1st and 4th columns), per-cell average *ALD3* (2nd and 5th columns) and *TKL2* (3rd and 6th columns) are shown. For Msn2-mCherry, the black dots depict raw data. For *ALD3* and *TKL2* the open orange and cyan circles depict raw YFP and CFP data, respectively. The solid orange line depicts the global model fit to the raw YFP data. The fitting was done by fitting the model in Figure 2.2A using the solid red lines as Msn2-mCherry input and computing the parameters that globally minimized the least-squares error between the model output and the raw YFP data.

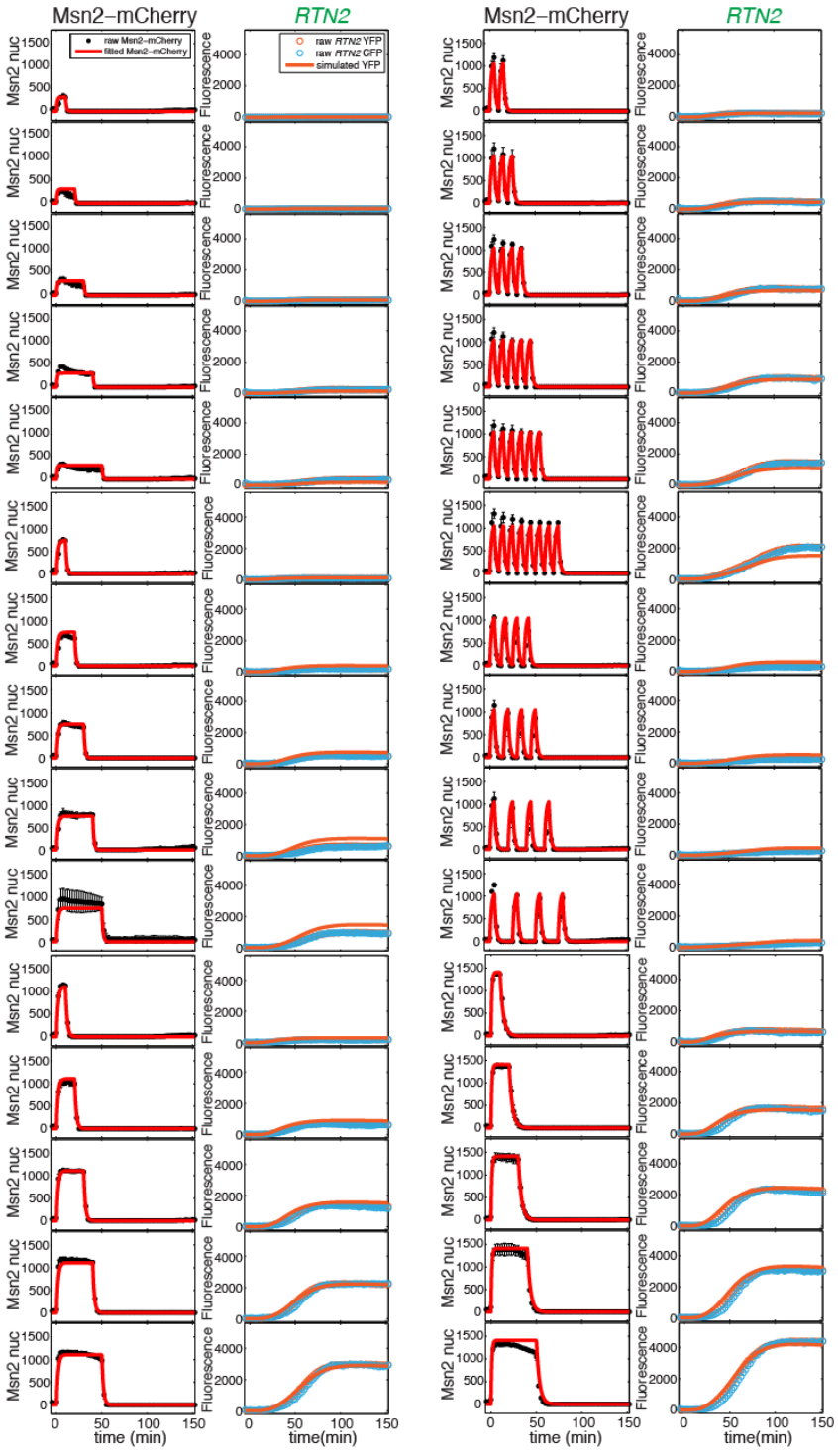

Figure A.5: *Comparison of model fits and raw data for RTN2*
Comparison of model fits and raw data for *RTN2*. Msn2-mCherry input (1st and 3rd columns) and per-cell average *RTN2* (2nd and 4th columns) are shown. For Msn2-mCherry, the black dots depict raw data. For *RTN2* the open orange and cyan circles depict raw YFP and CFP data, respectively. The solid orange line depicts the global model fit to the raw YFP data. The fitting was done by fitting the model in Figure 2.2A using the solid red lines as Msn2-mCherry input and computing the parameters that globally minimized the leastsquares error between the model output and the raw YFP data.

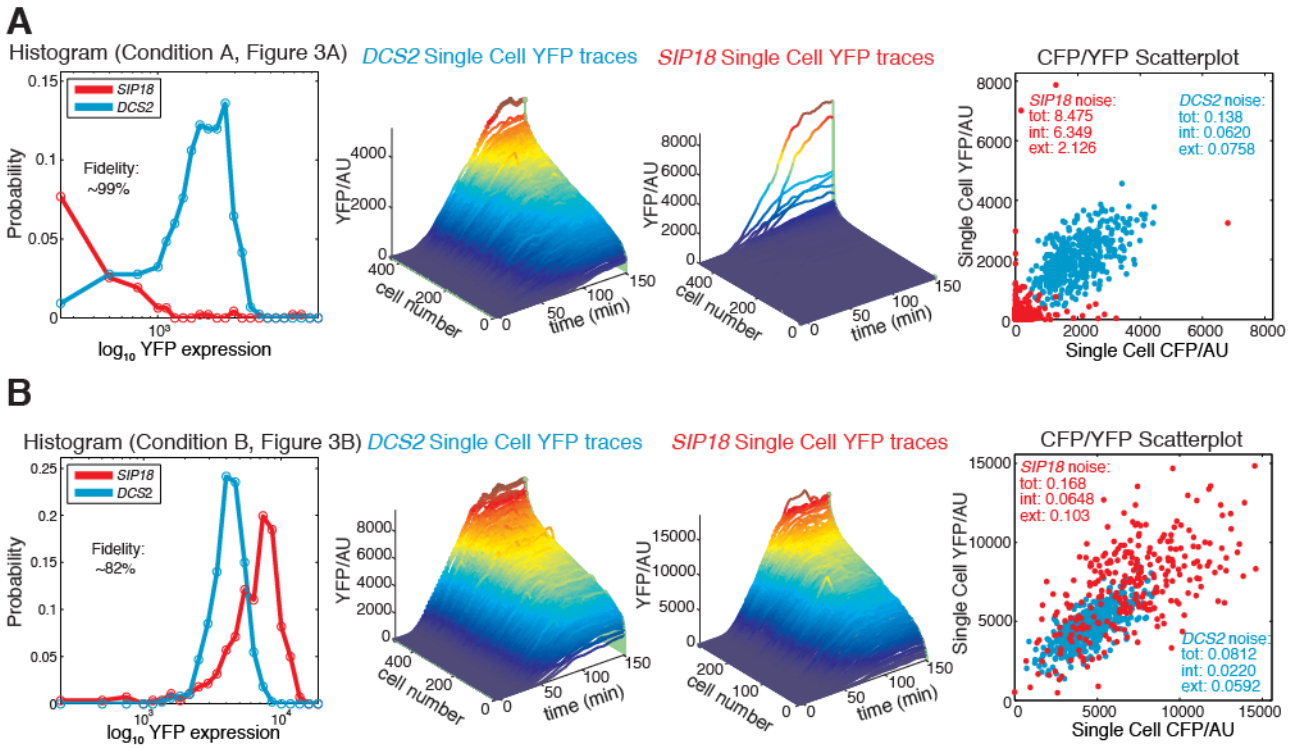

Figure A.6: *Raw single-cell data for Condition A and B*
(A) *DCS2* and *SIP18* under Condition A (Figure 2.3A). Histogram, single-cell YFP traces and CFP/YFP scatterplot (showing total, intrinsic and extrinsic noise) under Condition A (Figure 2.3A, seven 5 min pulses separated by 7.95 min intervals with 690 nM 1-NM-PP1). The fidelity is defined as the probability (99%) that *DCS2* expression will be higher than *SIP18* expression in a single cell and is calculated from the empirical probability distributions.
(B) *DCS2* and *SIP18* under Condition B (Figure 2.3B). Histogram, single-cell YFP traces and CFP/YFP scatterplot (showing total, intrinsic and extrinsic noise) under Condition B (Figure 2.3B, single 70 min pulse with 3 μM 1-NM-PP1). The fidelity is defined as the probability (82%) that *SIP18* expression will be higher than *DCS2* expression in a single cell and is calculated from the empirical probability distributions.

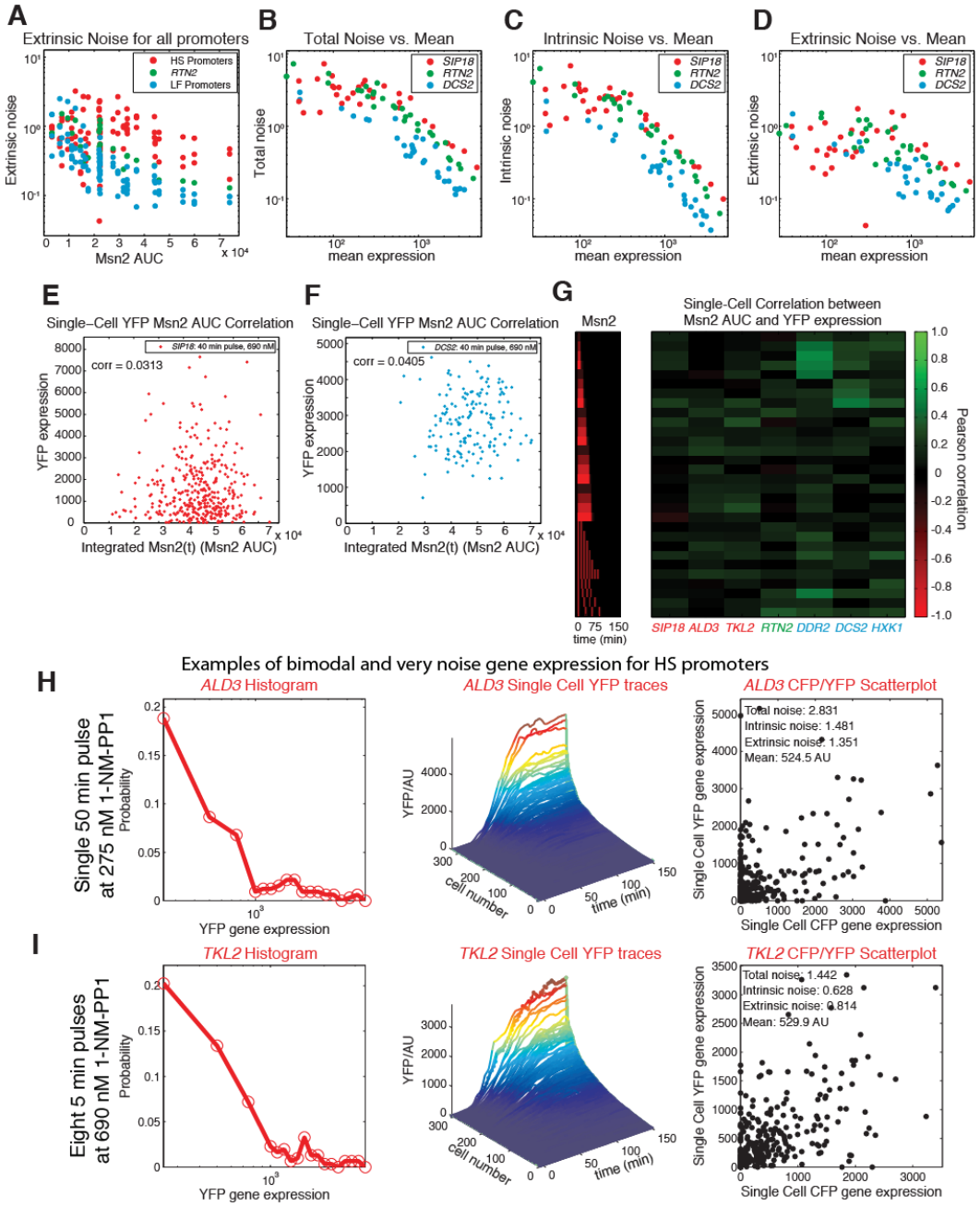

Figure A.7: *Extrinsic noise, Noise vs. mean, YFP vs Msn2 AUC correlation and examples of bimodal gene expression*
(A) Extrinsic noise **(A)** is plotted against the Msn2 AUC (Red, green and blue denotes HS (*SIP18*, *ALD3* and *TKL2*), *RTN2* and LF (*DDR2*, *DCS2* and *HXK1*) promoters, respectively). Each dot corresponds to the noise (mean across timepoints after gene expression has reached a plateau) for a single experiment: that is, a single Msn2 input for a single promoter.
(B-D) Total noise **(B)** ($\frac{\sigma^2}{\mu^2}$), intrinsic **(C)** and extrinsic noise **(D)** is plotted against the mean expression. Each dot corresponds to the noise (mean across timepoints after gene expression has reached a plateau) for a single experiment: that is, a single Msn2 input for a single promoter. *SIP18*, *RTN2* and *DCS2* have similar maximal expression means (Appendix Figure A.1B).
(E-G) Variability in Msn2 levels between cells can only explain very little variability in gene expression. **(E)** and **(F)** show two examples of the correlation between single-cell YFP and cumulative Msn2 levels (Msn2 AUC). **(E)** corresponds to Figure 2.4E, **(F)** to Figure 2.4D. **(G)** shows heatmap of correlation between YFP and Msn2 AUC for all 210 experiments. The correlation varied between ca. −0.2 to +0.5 with a median value of 0.1. Overall, the correlation was modest (29/210 instances of negative correlation). This indicates that most of the gene expression noise is not simply due to variability in Msn2 levels between cells and is consistent with the observation that Msn2 levels show little variability between cells.
(H) *ALD3*: example of bimodal gene expression. Histogram (x-scale is $\log_{10}$) and single-cell traces for YFP for *ALD3* (single 50 min pulse with 275 nM 1-NM-PP1) and CFP/YFP scatter plot showing total, intrinsic and extrinsic noise.
(I) *TKL2*: example of bimodal gene expression. Histogram (x-scale is $\log_{10}$) and single-cell traces for YFP for *TKL2* (eight 5 min pulses with 5 min interval and 690 nM 1-NM-PP1) and CFP/YFP scatter plot showing total, intrinsic and extrinsic noise.

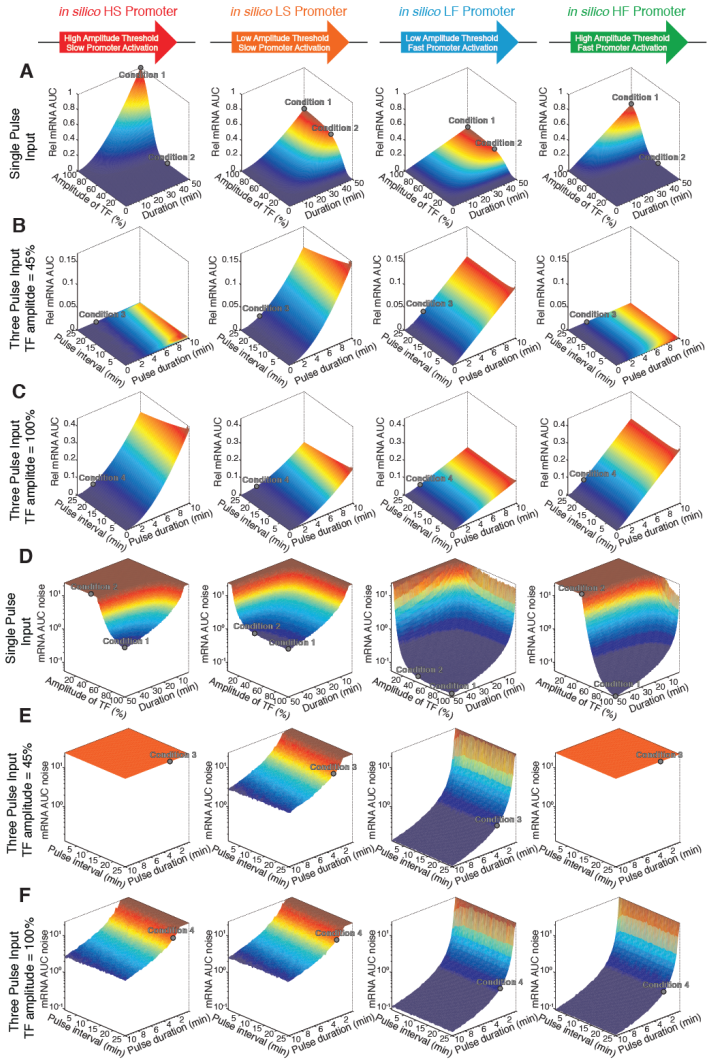

Figure A.8: *Surface plots showing how gene expression (mRNA AUC) and noise (mRNA AUC noise) relates to transcription factor input for the 4 in silico promoters*

(A) How gene expression scales with TF amplitude and nuclear duration for a single pulse. The surface plots show how gene expression scales with TF amplitude and nuclear duration for a single pulse for each of the 4 *in silico* promoters with the parameters given in the Figure 2.5 figure legend. The expression bar graphs in Figure 2.5D, E are quantifications of the points labeled Condition 1 and Condition 2 on the surface plots in **(A)** for each of the 4 promoters.

(B) How gene expression scales with pulse interval and duration at low TF amplitude. These surface plots show how gene expression scales with pulse interval and duration for oscillatory input with 3 pulses and TF=45%. The expression bar graph in Figure 2.5F, is the quantification of the points labeled with Condition 3 on the surface plots in **(B)** for each of the 4 promoters.

(C) How gene expression scales with pulse interval and duration at low TF amplitude. These surface plots show how gene expression scales with pulse interval and duration for oscillatory input with 3 pulses and TF=100%. The expression bar graph in Figure 2.5G, is the quantification of the points labeled with Condition 4 on the surface plots in **(C)** for each of the 4 promoters.

(D) How gene expression noise scales with TF amplitude and nuclear duration for a single pulse. The surface plots show how noise scales with TF amplitude and nuclear duration for a single pulse for each of the 4 *in silico* promoters with the parameters given in the Figure 2.5 figure legend. The noise bar graphs in Figure 2.5D, E are quantifications of the points labeled Condition 1 and Condition 2 on the surface plots in **(D)** for each of the 4 promoters.

(E) How gene expression noise scales with pulse interval and duration at low TF amplitude. These surface plots show how noise scales with pulse interval and duration for oscillatory input with 3 pulses and TF=45%. The noise bar graph in Figure 2.5F, is the quantification of the points labeled with Condition 3 on the surface plots in **(E)** for each of the 4 promoters. For the HS and HF promoters, expression is essentially zero and the noise effectively infinite. All values were capped at 25, which is why they appear flat.

(F) How gene expression noise scales with pulse interval and duration at low TF amplitude. These surface plots show how noise scales with pulse interval and duration for oscillatory input with 3 pulses and TF=100%. The noise bar graph in Figure 2.5G, is the quantification of the points labeled with Condition 4 on the surface plots in **(F)** for each of the 4 promoters.

Each column in **(A-F)** refer to one promoter. E.g. the surface plots in the 3rd column are all for the LF promoter. The noise is in some case almost infinite and in all surface plots above, all values greater than 25, were set to 25 for ease of visualization. Thus, the noise does not plateau. The noise surface plots were calculated using discrete time stochastic simulations.

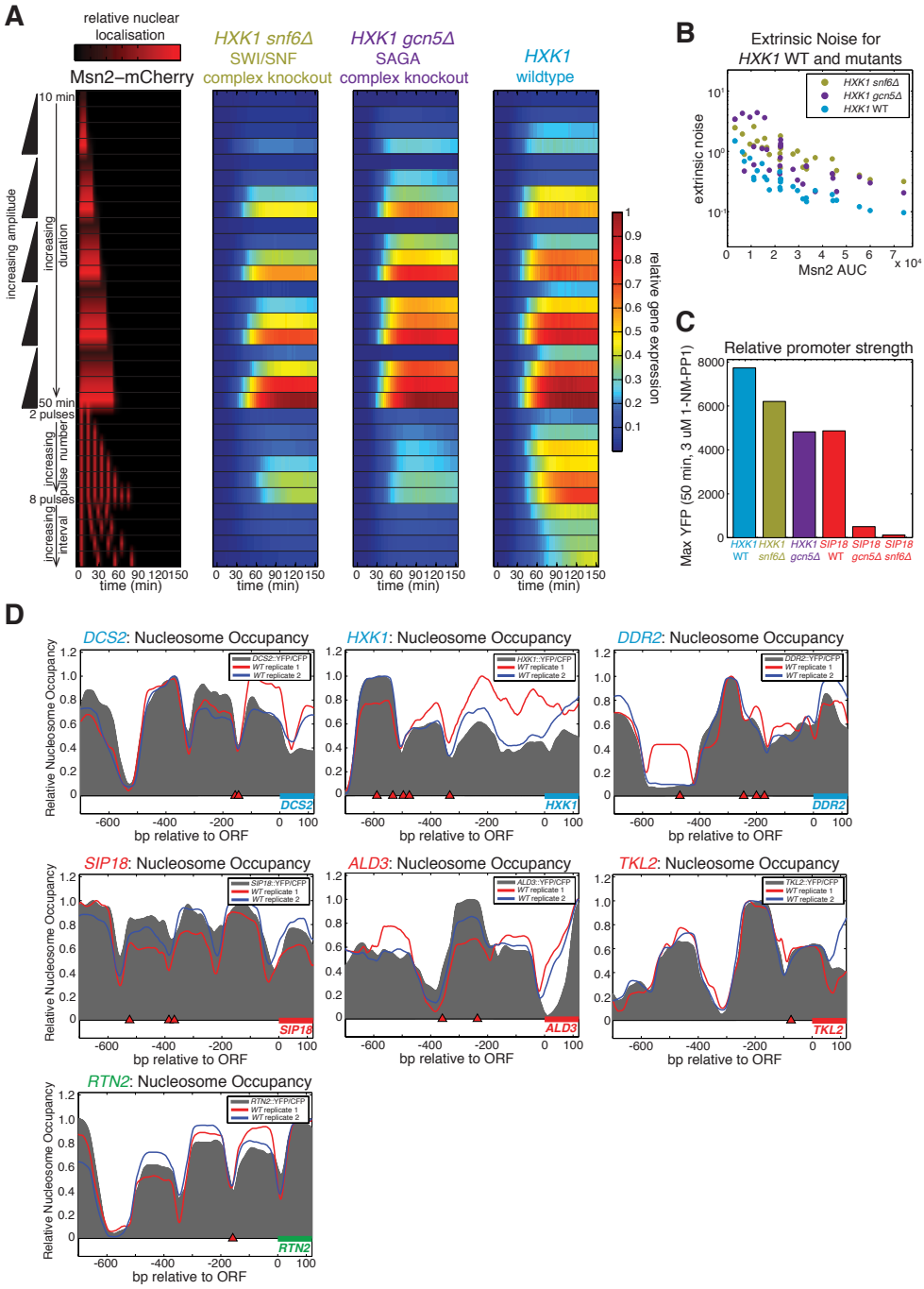

Figure A.9: *Expression heatmap and noise plots for HXK1 WT, HXK1 gcn5Δ and HXK1 snf6Δ. Nucleosome occupancy at promoters*

(A) Comparison of gene expression responses for wildtype *HXK1* and chromatin remodeling mutants. Each row corresponds to a specific Msn2-mCherry input (left, in red) and the corresponding gene expression response for the wildtype and the mutant strains is shown on the corresponding rows on the right. The gene expression responses for each promoter are internally normalized to their maximal expression level. Each row is the per-cell average of ∼200-600 cells from at least three biological replicates.

(B) Extrinsic noise for *HXK1* WT, *HXK1 snf6*Δ and *HXK1 gcn5*Δ strains as a function of Msn2 AUC. In all cases, the noise shown is the mean across all timepoints after the gene expression traces has reached a plateau.

(C) Relative promoter strengths WT and mutant strains. As an approximate measure for promoter strength, the gene expression response to a single 50 min pulse with 3 μM 1-NM-PP1 was used, which yields high induction.

(D) Replacing the native ORF with the CFP/YFP reporters does not significantly alter the nucleosome occupancy in the promoter. The nucleosome occupancy in the ORF::CFP/YFP strain (grey bar graph) is compared to biological replicates of the wildtype strain (EY2807/ASH79) (blue and red lines show full biological replicates). The wildtype strain was used for the nucleosome remodeling time-course shown in Chapter 2 (Figure 2.7E). In **(D)** the maximal nucleosome occupancy is normalized to 1 for each promoter for each data sets. The red triangles signify the position of the Msn2 binding sites (5'-CCCCT-3' or the reverse complement) in the promoter.

A.2 Supplementary methods and results for Chapter 2

A.2.1 Strain construction

Standard methods for growing and genetically manipulating yeast were used in this study. The *Saccharomyces cerevisiae* strains used in this study are from an ADE^+ strain in the W303 background (*MAT***a** and *MAT*$\boldsymbol{\alpha}$ *trp1 leu2 ura3 his3 can1* GAL^+ psi^+). All manipulations were done identically in both haploid mating types unless otherwise stated and followed by mating to form diploids.

The analog-sensititve mutations in all three isoforms of PKA, *TPK1*$^{\mathrm{M164G}}$, *TPK2*$^{\mathrm{M147G}}$ and *TPK3*$^{\mathrm{M165G}}$, were introduced by replacing the codon of interest with *URA3* and followed by replacing *URA3* with a PCR generated DNA fragment containing the analog-sensitive mutation and counterselection against *URA3*. All mutations were verified by sequencing. Msn4 binds the same DNA sequence (the stress response element, STRE) as Msn2 and is under the transcriptional control of Msn2. Here we focus solely on Msn2-dependent transcription, so the *MSN4* gene was deleted in all subsequent strains. *MSN4* was deleted by replacing the endogenous ORF with a *TRP1* PCR fragment in the *MAT***a** mating type and with a *LEU2* PCR fragment *MAT*$\boldsymbol{\alpha}$ mating type. These deletions were verified by PCR.

Msn2 was C-terminally tagged with a yeast codon-optimized mCherry from a pKT vector (Sheff & Thorn, 2004), by replacing the endogenous stop codon of the *MSN2* locus first with *URA3* and then by replacing *URA3* with a linker-mCherry PCR fragment such that the endogenous terminator of Msn2 was unchanged. The pKT linker is the amino acid sequence GDGAGLIN (Sheff & Thorn, 2004) and Msn2-linker-FP fusion proteins have previously been shown to be functional (Hao & O'Shea, 2012).

In order to segment the nucleus, the nuclear protein Nhp6a was C-terminally tagged with the recently developed infrared fluorescent protein iRFP (Filonov *et al.*, 2011) using a linker-iRFP::*KAN* MX fragment generated by PCR amplification from a pKT vector (pKT-iRFP-*KAN* MX). iRFP was yeast codon-optimised (Grote *et al.*, 2005) and the linker sequence is again GDGAGLIN. The strains were then verified by sequencing. For reference, the codon-optimized iRFP sequence is given below:

```
>> iRFP
   ATGGCTGAAGGTTCTGTTGCTAGACAACCAGACTTGTTGACTTGTGACGACGAACCAATCCAC
   ATCCCAGGTGCTATCCAACCACACGGTTTGTTGTTGGCTTTGGCTGCTGACATGACTATCGTT
   GCTGGTTCTGACAACTTGCCAGAATTGACTGGTTTGGCTATCGGTGCTTTGATCGGTAGATCT
   GCTGCTGACGTTTTCGACTCTGAAACTCACAACAGATTGACTATCGCTTTGGCTGAACCAGGT
   GCTGCTGTTGGTGCTCCAATCACTGTTGGTTTCACTATGAGAAAGGACGCTGGTTTCATCGGT
   TCTTGGCACAGACACGACCAATTGATCTTCTTGGAATTGGAACCACCACAAAGAGACGTTGCT
   GAACCACAAGCTTTCTTCAGAAGAACTAACTCTGCTATCAGAAGATTGCAAGCTGCTGAAACT
   TTGGAATCTGCTTGTGCTGCTGCTGCTCAAGAAGTTAGAAAGATCACTGGTTTCGACAGAGTT
   ATGATCTACAGATTCGCTTCTGACTTCTCTGGTGAAGTTATCGCTGAAGACAGATGTGCTGAA
   GTTGAATCTAAGTTGGGTTTGCACTACCCAGCTTCTACTGTTCCAGCTCAAGCTAGAAGATTG
   TACACTATCAACCCAGTTAGAATCATCCCAGACATCAACTACAGACCAGTTCCAGTTACTCCA
   GACTTGAACCCAGTTACTGGTAGACCAATCGACTTGTCTTTCGCTATCTTGAGATCTGTTTCT
   CCAGTTCACTTGGAATTCATGAGAAACATCGGTATGCACGGTACTATGTCTATCTCTATCTTG
   AGAGGTGAAAGATTGTGGGGTTTGATCGTTTGTCACCACAGAACTCCATACTACGTTGACTTG
   GACGGTAGACAAGCTTGTGAATTGGTTGCTCAAGTTTTGGCTTGGCAAATCGGTGTTATGGAA
   GAATAA
```

For the reporter genes, we replaced the entire endogenous ORF with a PCR fragment containing the relevant fluorescent protein (CFP or YFP) followed by the *ADH1* terminator and *spHIS5* selection marker generated by PCR amplification from a pKT vector (either pKT-mCitrineV163A-*spHIS5* or pKT-SCFP3A-*spHIS5*) using the primers:

Forward: 5'-(gene-specific)-ATGTCTAAGGGTGAAGAATTGTTC-3'

Reverse: 5'-(gene-specific)-TCGATGAATTCGAGCTCG-3'

Thus, the entire endogenous promoter of the gene of interest up until the start codon is preserved, but all gene reporters have the same 3'-UTR and terminator sequence. The

CFP reporter is SCFP3A (Kremers *et al.*, 2006) and the YFP reporter is mCitrineV163A and both have been yeast codon-optimized (Grote *et al.*, 2005). These two cyan and yellow fluorescent proteins were identified by screening numerous CFP and YFP variants for their brightness, photobleaching and maturation time properties and identifying the two with the fastest and most similar maturation times. For reference, the full codon-optimized nucleotide sequence of SCFP3A and mCitrineV163A are given below:

```
>> SCFP3A
   ATGTCTAAGGGTGAAGAATTGTTCACTGGTGTTGTTCCAATCTTGGTTGAATTGGACGGTGAC
   GTTAACGGTCACAAGTTCTCTGTTTCTGGTGAAGGTGAAGGTGACGCTACTTACGGTAAGTTG
   ACTTTGAAGTTCATCTGTACTACTGGTAAGTTGCCAGTTCCATGGCCAACTTTGGTTACTACT
   TTGACTTGGGGTGTTCAATGTTTCGCTAGATACCCAGACCACATGAAGCAACACGACTTCTTC
   AAGTCTGCTATGCCAGAAGGTTACGTTCAAGAAAGAACTATCTTCTTCAAGGACGACGGTAAC
   TACAAGACTAGAGCTGAAGTTAAGTTCGAAGGTGACACTTTGGTTAACAGAATCGAATTGAAG
   GGTATCGACTTCAAGGAAGACGGTAACATCTTGGGTCACAAGTTGGAATACAACTACATCTCT
   GACAACGTTTACATCACTGCTGACAAGCAAAAGAACGGTATCAAGGCTAACTTCAAGATCAGA
   CACAACATCGAAGACGGTGGTGTTCAATTGGCTGACCACTACCAACAAAACACTCCAATCGGT
   GACGGTCCAGTTTTGTTGCCAGACAACCACTACTTGTCTACTCAATCTAAGTTGTCTAAGGAC
   CCAAACGAAAAGAGAGACCACATGGTTTTGTTGGAATTCGTTACTGCTGCTGGTATCACTTTG
   GGTATGGACGAATTGTACAAGTAA

>> mCitrineV163A
   ATGTCTAAGGGTGAAGAATTGTTCACTGGTGTTGTTCCAATCTTGGTTGAATTGGACGGTGAC
   GTTAACGGTCACAAGTTCTCTGTTTCTGGTGAAGGTGAAGGTGACGCTACTTACGGTAAGTTG
   ACTTTGAAGTTCATCTGTACTACTGGTAAGTTGCCAGTTCCATGGCCAACTTTGGTTACTACT
   TTGGGTTACGGTTTGATGTGTTTCGCTAGATACCCAGACCACATGAAGCAACACGACTTCTTC
   AAGTCTGCTATGCCAGAAGGTTACGTTCAAGAAAGAACTATCTTCTTCAAGGACGACGGTAAC
   TACAAGACTAGAGCTGAAGTTAAGTTCGAAGGTGACACTTTGGTTAACAGAATCGAATTGAAG
   GGTATCGACTTCAAGGAAGACGGTAACATCTTGGGTCACAAGTTGGAATACAACTACAACTCT
   CACAACGTTTACATCATGGCTGACAAGCAAAAGAACGGTATCAAGGCTAACTTCAAGATCAGA
   CACAACATCGAAGACGGTTCTGTTCAATTGGCTGACCACTACCAACAAAACACTCCAATCGGT
   GACGGTCCAGTTTTGTTGCCAGACAACCACTACTTGTCTTACCAATCTAAGTTGTCTAAGGAC
   CCAAACGAAAAGAGAGACCACATGGTTTTGTTGGAATTCGTTACTGCTGCTGGTATCACTCAC
   GGTATGGACGAATTGTACAAGTAA
```

All reporter diploids had a doubling time of 89 min (± 1 min) when grown in bulk, which was indistinguishable from their ancestor strains (ASH079 and ASH019).

For the chromatin remodeling complex mutants, the function of either the SWI/SNF or

the SAGA chromatin remodeling complex was abolished by deletion of the *SNF6* or *GCN5* genes, respectively (Raser & O'Shea, 2004). This was done in both the *MAT***a** and *MAT*$\boldsymbol{\alpha}$ mating types of the *HXK1* (ASH89 and ASH90) and *SIP18* (ASH92 and ASH93) strains by replacing the entire ORF of either *SNF6* or *GCN5* with a *URA3* PCR fragment and followed by mating to generate diploids.

Since the *MSN4* gene has been deleted and replaced with *TRP1* in the *MAT***a** mating type and with *LEU2* in the *MAT*$\boldsymbol{\alpha}$ mating type, mating was done simply by mixing both haploids and growing them in YEPD medium overnight, washing them and then plating on double-selection plates (-*TRP-LEU*) and picking a single colony to obtain diploids. That cells were really diploid after mating was verified by tetrad analysis.

A list of the strains constructed and used in this study is given in Appendix Table A.1. All strains are derived from EY0690 and EY0691.

Table A.1: List of strains for Chapter 2.

Strains	**Type**	**Strain genotype**
EY0690	*MAT***a**	W303 *trp1 leu2 ura3 his3 can1 GAL*$^+$ *psi*$^+$ (not generated in this study)
EY0691	*MAT*$\boldsymbol{\alpha}$	W303 *trp1 leu2 ura3 his3 can1 GAL*$^+$ *psi*$^+$ (not generated in this study)
EY2795/ASH06	*MAT***a**	*TPK1*^{M164G} *TPK2*^{M147G} *TPK3*^{M165G}
EY2796/ASH07	*MAT*$\boldsymbol{\alpha}$	*TPK1*^{M164G} *TPK2*^{M147G} *TPK3*^{M165G}
EY2797/ASH08	*MAT***a**	*TPK1*^{M164G} *TPK2*^{M147G} *TPK3*^{M165G} *msn4*Δ::TRP1
EY2798/ASH09	*MAT*$\boldsymbol{\alpha}$	*TPK1*^{M164G} *TPK2*^{M147G} *TPK3*^{M165G} *msn4*Δ::LEU2
EY2799/ASH11	*MAT***a**	*TPK1*^{M164G} *TPK2*^{M147G} *TPK3*^{M165G} *msn4*Δ::TRP1 *msn2*Δ::natMX
EY2780/ASH12	*MAT*$\boldsymbol{\alpha}$	*TPK1*^{M164G} *TPK2*^{M147G} *TPK3*^{M165G} *msn4*Δ::LEU2 *msn2*Δ::natMX
EY2781/ASH13	diploid	*TPK1*^{M164G} *TPK2*^{M147G} *TPK3*^{M165G} *msn4*Δ::TRP1/LEU2 *msn2*Δ::natMX
EY2802/ASH17	*MAT***a**	*TPK1*^{M164G} *TPK2*^{M147G} *TPK3*^{M165G} *msn4*Δ::TRP1 *MSN2*-mCherry
EY2803/ASH18	*MAT*$\boldsymbol{\alpha}$	*TPK1*^{M164G} *TPK2*^{M147G} *TPK3*^{M165G} *msn4*Δ::LEU2 *MSN2*-mCherry
EY2804/ASH19	diploid	*TPK1*^{M164G} *TPK2*^{M147G} *TPK3*^{M165G} *msn4*Δ::TRP1/LEU2 *MSN2*-mCherry
EY2805/ASH77	*MAT***a**	*TPK1*^{M164G} *TPK2*^{M147G} *TPK3*^{M165G} *msn4*Δ::TRP1 *MSN2*-mCherry NHP6a-iRFP::KAN
EY2806/ASH78	*MAT*$\boldsymbol{\alpha}$	*TPK1*^{M164G} *TPK2*^{M147G} *TPK3*^{M165G} *msn4*Δ::LEU2 *MSN2*-mCherry NHP6a-iRFP::KAN
EY2807/ASH79	diploid	*TPK1*^{M164G} *TPK2*^{M147G} *TPK3*^{M165G} *msn4*Δ::TRP1/LEU2 *MSN2*-mCherry NHP6a-iRFP::KAN
EY2808/ASH89	*MAT***a**	*TPK1*^{M164G} *TPK2*^{M147G} *TPK3*^{M165G} *msn4*Δ::TRP1 *MSN2*-mCherry NHP6a-iRFP::KAN *hxk1*::mCitrineV163A-spHIS5
EY2809/ASH90	*MAT*$\boldsymbol{\alpha}$	*TPK1*^{M164G} *TPK2*^{M147G} *TPK3*^{M165G} *msn4*Δ::LEU2 *MSN2*-mCherry

		NHP6a-iRFP::KAN *hxk1*::SCFP3A-spHIS5
EY2810/ASH91	diploid	*TPK1*^{M164G} *TPK2*^{M147G} *TPK3*^{M165G} *msn4*Δ::TRP1/LEU2 *MSN2*-mCherry
		NHP6a-iRFP::KAN *hxk1*::mCitrineV163A/SCFP3a-spHIS5
EY2811/ASH92	*MAT***a**	*TPK1*^{M164G} *TPK2*^{M147G} *TPK3*^{M165G} *msn4*Δ::TRP1 *MSN2*-mCherry
		NHP6a-iRFP::KAN *sip18*::mCitrineV163A-spHIS5
EY2812/ASH93	*MAT*α	*TPK1*^{M164G} *TPK2*^{M147G} *TPK3*^{M165G} *msn4*Δ::LEU2 *MSN2*-mCherry
		NHP6a-iRFP::KAN *sip18*::SCFP3A-spHIS5
EY2813/ASH94	diploid	*TPK1*^{M164G} *TPK2*^{M147G} *TPK3*^{M165G} *msn4*Δ::TRP1/LEU2 *MSN2*-mCherry
		NHP6a-iRFP::KAN *sip18*::mCitrineV163A/SCFP3a-spHIS5
EY2814/ASH95	*MAT***a**	*TPK1*^{M164G} *TPK2*^{M147G} *TPK3*^{M165G} *msn4*Δ::TRP1 *MSN2*-mCherry
		NHP6a-iRFP::KAN *rtn2*::mCitrineV163A-spHIS5
EY2815/ASH96	*MAT*α	*TPK1*^{M164G} *TPK2*^{M147G} *TPK3*^{M165G} *msn4*Δ::LEU2 *MSN2*-mCherry
		NHP6a-iRFP::KAN *rtn2*::SCFP3A-spHIS5
EY2816/ASH97	diploid	*TPK1*^{M164G} *TPK2*^{M147G} *TPK3*^{M165G} *msn4*Δ::TRP1/LEU2 *MSN2*-mCherry
		NHP6a-iRFP::KAN *rtn2*::mCitrineV163A/SCFP3a-spHIS5
EY2817/ASH98	*MAT***a**	*TPK1*^{M164G} *TPK2*^{M147G} *TPK3*^{M165G} *msn4*Δ::TRP1 *MSN2*-mCherry
		NHP6a-iRFP::KAN *dcs2*::mCitrineV163A-spHIS5
EY2818/ASH99	*MAT*α	*TPK1*^{M164G} *TPK2*^{M147G} *TPK3*^{M165G} *msn4*Δ::LEU2 *MSN2*-mCherry
		NHP6a-iRFP::KAN *dcs2*::SCFP3A-spHIS5
EY2819/ASH100	diploid	*TPK1*^{M164G} *TPK2*^{M147G} *TPK3*^{M165G} *msn4*Δ::TRP1/LEU2 *MSN2*-mCherry
		NHP6a-iRFP::KAN *dcs2*::mCitrineV163A/SCFP3a-spHIS5
EY2820/ASH101	*MAT***a**	*TPK1*^{M164G} *TPK2*^{M147G} *TPK3*^{M165G} *msn4*Δ::TRP1 *MSN2*-mCherry
		NHP6a-iRFP::KAN *tkl2*::mCitrineV163A-spHIS5
EY2821/ASH102	*MAT*α	*TPK1*^{M164G} *TPK2*^{M147G} *TPK3*^{M165G} *msn4*Δ::LEU2 *MSN2*-mCherry
		NHP6a-iRFP::KAN *tkl2*::SCFP3A-spHIS5
EY2822/ASH103	diploid	*TPK1*^{M164G} *TPK2*^{M147G} *TPK3*^{M165G} *msn4*Δ::TRP1/LEU2 *MSN2*-mCherry
		NHP6a-iRFP::KAN *tkl2*::mCitrineV163A/SCFP3a-spHIS5
EY2823/ASH104	*MAT***a**	*TPK1*^{M164G} *TPK2*^{M147G} *TPK3*^{M165G} *msn4*Δ::TRP1 *MSN2*-mCherry
		NHP6a-iRFP::KAN *ddr2*::mCitrineV163A-spHIS5
EY2824/ASH105	*MAT*α	*TPK1*^{M164G} *TPK2*^{M147G} *TPK3*^{M165G} *msn4*Δ::LEU2 *MSN2*-mCherry
		NHP6a-iRFP::KAN *ddr2*::SCFP3A-spHIS5
EY2825/ASH106	diploid	*TPK1*^{M164G} *TPK2*^{M147G} *TPK3*^{M165G} *msn4*Δ::TRP1/LEU2 *MSN2*-mCherry
		NHP6a-iRFP::KAN *ddr2*::mCitrineV163A/SCFP3a-spHIS5
EY2826/ASH127	*MAT***a**	*TPK1*^{M164G} *TPK2*^{M147G} *TPK3*^{M165G} *msn4*Δ::TRP1 *MSN2*-mCherry
		NHP6a-iRFP::KAN *ald3*::mCitrineV163A-spHIS5
EY2827/ASH128	*MAT*α	*TPK1*^{M164G} *TPK2*^{M147G} *TPK3*^{M165G} *msn4*Δ::LEU2 *MSN2*-mCherry
		NHP6a-iRFP::KAN *ald3*::SCFP3A-spHIS5
EY2828/ASH129	diploid	*TPK1*^{M164G} *TPK2*^{M147G} *TPK3*^{M165G} *msn4*Δ::TRP1/LEU2 *MSN2*-mCherry
		NHP6a-iRFP::KAN *ald3*::mCitrineV163A/SCFP3a-spHIS5
EY2829/ASH142	*MAT***a**	*TPK1*^{M164G} *TPK2*^{M147G} *TPK3*^{M165G} *msn4*Δ::TRP1 *MSN2*-mCherry
		NHP6a-iRFP::KAN *hxk1*::mCitrineV163A-spHIS5 *snf6*Δ::URA3
EY2830/ASH143	*MAT*α	*TPK1*^{M164G} *TPK2*^{M147G} *TPK3*^{M165G} *msn4*Δ::LEU2 *MSN2*-mCherry
		NHP6a-iRFP::KAN *hxk1*::SCFP3A-spHIS5 *snf6*Δ::URA3
EY2831/ASH144	diploid	*TPK1*^{M164G} *TPK2*^{M147G} *TPK3*^{M165G} *msn4*Δ::TRP1/LEU2 *MSN2*-mCherry
		NHP6a-iRFP::KAN *hxk1*::mCitrineV163A/SCFP3a-spHIS5 *snf6*Δ::URA3
EY2832/ASH145	*MAT***a**	*TPK1*^{M164G} *TPK2*^{M147G} *TPK3*^{M165G} *msn4*Δ::TRP1 *MSN2*-mCherry
		NHP6a-iRFP::KAN *sip18*::mCitrineV163A-spHIS5 *snf6*Δ::URA3
EY2833/ASH146	*MAT*α	*TPK1*^{M164G} *TPK2*^{M147G} *TPK3*^{M165G} *msn4*Δ::LEU2 *MSN2*-mCherry
		NHP6a-iRFP::KAN *sip18*::SCFP3A-spHIS5 *snf6*Δ::URA3
EY2834/ASH147	diploid	*TPK1*^{M164G} *TPK2*^{M147G} *TPK3*^{M165G} *msn4*Δ::TRP1/LEU2 *MSN2*-mCherry

		NHP6a-iRFP::KAN *sip18*::mCitrineV163A/SCFP3a-spHIS5 *snf6*Δ::URA3
EY2835/ASH148	*MAT***a**	*TPK1*^{M164G} *TPK2*^{M147G} *TPK3*^{M165G} *msn4*Δ::TRP1 *MSN2*-mCherry
		NHP6a-iRFP::KAN *hxk1*::mCitrineV163A-spHIS5 *gcn5*Δ::URA3
EY2836/ASH149	*MAT*α	*TPK1*^{M164G} *TPK2*^{M147G} *TPK3*^{M165G} *msn4*Δ::LEU2 *MSN2*-mCherry
		NHP6a-iRFP::KAN *hxk1*::SCFP3A-spHIS5 *gcn5*Δ::URA3
EY2837/ASH150	diploid	*TPK1*^{M164G} *TPK2*^{M147G} *TPK3*^{M165G} *msn4*Δ::TRP1/LEU2 *MSN2*-mCherry
		NHP6a-iRFP::KAN *hxk1*::mCitrineV163A/SCFP3a-spHIS5 *gcn5*Δ::URA3
EY2838/ASH151	*MAT***a**	*TPK1*^{M164G} *TPK2*^{M147G} *TPK3*^{M165G} *msn4*Δ::TRP1 *MSN2*-mCherry
		NHP6a-iRFP::KAN *sip18*::mCitrineV163A-spHIS5 *gcn5*Δ::URA3
EY2839/ASH152	*MAT*α	*TPK1*^{M164G} *TPK2*^{M147G} *TPK3*^{M165G} *msn4*Δ::LEU2 *MSN2*-mCherry
		NHP6a-iRFP::KAN *sip18*::SCFP3A-spHIS5 *gcn5*Δ::URA3
EY2840/ASH153	diploid	*TPK1*^{M164G} *TPK2*^{M147G} *TPK3*^{M165G} *msn4*Δ::TRP1/LEU2 *MSN2*-mCherry
		NHP6a-iRFP::KAN *sip18*::mCitrineV163A/SCFP3a-spHIS5 *gcn5*Δ::URA3

A.2.2 Medium and solutions

Low fluorescence medium supplemented with amino acids but lacking leucine and tryptophan was used in all experiments including for microscopy, nucleosome mapping and microarray. Per liter, this medium contains: 20 g glucose (2% glucose), 5 g $(NH_4)_2SO_4$, 1 g KH_2PO_4, 500 mg $MgSO_4{\cdot}7H_20$, 100 mg NaCl, 100 mg $CaCl_2{\cdot}2H_2O$, 500 µg H_3BO_3, 40 µg $CuSO_4$, 100 µg KI, 200 µg $FeCl_3$, 400 µg $MnSO_4$, 200 µg $Na_2MoO_4{\cdot}2H_2O$, 400 µg $ZnSO_4$, 2 µg biotin, 400 µg calcium pantothenate, 2 mg myo-inositol, 400 µg niacin/nicotinic acid, 200 µg *p*-aminobenzoic acid, 400 µg pyroxidine·HCl, 400 µg thiamine·HCl, 30 mg L-isoleucine, 150 mg L-valine, 40 mg adenine, 20 mg L-argine, 20 mg L-histidine, 30 mg L-lysine, 20 mg L-methionine, 50 mg L-phenylalanine, 200 mg L-threonine, 30 mg L-tyrosine and 20 mg uracil.

The inhibitor, 1-NM-PP1, was stored as a 1000x DMSO stock at -20°C and added to medium just before an experiment. For microscopy, a tube with a 20 mg/mL concanavalin A (Con A) (Type IV, Sigma-Aldrich) solution containing 50 mM $CaCl_2$ and 50 mM $MnCl_2$ stored at -20°C was gently and slowly thawed on ice just before each experiment. To this 200 µL solution was added 200 µL phosphate-buffered saline (PBS, at pH 6.5) and 600 µL

ddH_2O. The final Con A solution therefore contains 4 mg/mL concanavalin A.

A.2.3 Microarray analysis

The goal of this experiment was to determine genes whose activation in response to 1-NM-PP1 depends exclusively on Msn2 under our experimental conditions. To achieve this the genome-wide expression levels in response to 3 μM 1-NM-PP1 were analyzed at 0, 10, 20 or 40 min timepoints in a diploid strain with Msn2 present (ASH019 *TPK1*^{M164G} *TPK2*^{M147G} *TPK3*^{M165G} *msn4*Δ::TRP1/LEU2 *MSN2*-mCherry) and compared to a diploid strain lacking Msn2 (ASH013 *TPK1*^{M164G} *TPK2*^{M147G} *TPK3*^{M165G} *msn4*Δ::TRP1/LEU2 *msn2*Δ::natMX). Cells were grown overnight at 30°C in low fluorescence medium until they reached an $OD_{600\,nm}$ of 0.15 and 1-NM-PP1 was added to a final concentration of 3 μM. At timepoints 0, 10, 20 and 40 minutes, 20 mL cell culture was added directly to 30 mL cold methanol solution (-30°C) and incubated in a dry ice/ethanol bath for 20 minutes. The cells were collected by centrifugation and gently washed once with ice cold sterile water. The cells were then resuspended in RNAlater solution (Ambion). For each sample, $5 \cdot 10^7$ cells were used to isolate total RNA with the RNeasy Mini kit (QIAGEN). The integrity of the RNA was then verified on an agarose gel. All subsequent steps were performed exactly as previously described (Zhou & O'Shea, 2011). These step involve complementary DNA synthesis (cDNA) and Cy3 and Cy5 labeling (GE Biosciences), competitive hybridization to Agilent 8x15K S. cerevisiae two-color expression microarrays (G2509F, AMADID #019838, Array #251983810070), extracting Cy3 and Cy5 intensities using an Aon 5000B scanner and GenePix 5.1 software and Lowess and quantile normalization, which was performed in `MATLAB` (2011a, the MathWorks). The results are shown in Appendix Figure A.1C.

A.2.4 Reporter gene selection

To select genes that respond strongly to Msn2, but show no response to 1-NM-PP1 in the absence of Msn2 under our conditions, genes that showed at least 5-fold induction when Msn2 is present but less than 2-fold induction when Msn2 is not present were selected using the microarray data. This gave 22 genes. *RTN2* was also included because it showed 17.64-fold induction in the Msn2-mCherry strain, but only 2.21-fold induction in the *msn2*Δ strain. This gave 23 candidate genes. Since some genes are autoregulatory and since they differ widely in size, the endogenous ORF was replaced in all cases with either CFP or YFP. This necessarily means that genes that are essential or show severe deletion phenotypes must be excluded. Furthermore, in order to get good signal-to-noise in time-lapse microscopy, the genes need to be strongly induced, so the genes that induced significantly above the 5-fold threshold were the focus (Appendix Figure A.1C). Thus, the ORF was replaced with CFP and YFP and diploid strains formed by mating for the following genes: *SIP18*, *ALD3*, *TKL2*, *RTN2*, *DDR2*, *DCS2*, *HXK1*, *GDB1*, *GND2*, *SPI1*, *HBT1*, *UIP4*. Reporter gene expression in response to a 50 min pulse with 3 μM 1-NM-PP1 was used to examine gene expression. *GDB1*, *GND2*, *SPI1*, *HBT1* and *UIP4* all showed too low expression for reliable detection in the microscope and were therefore eliminated from this study. This left 7 promoters, which were then systematically characterized (Figure 2.1C and Appendix Figure A.1D). These 7 promoters have all been previously shown to directly bind Msn2 at their promoters in response to osmotic stress (Huebert *et al.*, 2012).

A.2.5 *In vivo* nucleosome mapping (MNase-Seq)

First nucleosomes in the diploid wildtype (ASH79) strain were mapped and compared the promoter nucleosome occupancy in the wildtype strain to the seven diploid strains

where each of the native ORFs have been replaced with the CFP/YFP reporters (ASH91: *HXK1*; ASH94: *SIP18*; ASH97: *RTN2*; ASH100: *DCS2*; ASH103: *TKL2*; ASH106: *DDR2*; ASH129: *ALD3*). Although nucleosome occupancy show slight variation between the wild-type strain and the reporter strains (ORF::CFP/YFP), the variation is small and in fact comparable to the variation observed between full biological replicates between the wildtype strain (Appendix Figure A.9D). Furthermore, the variation observed is mostly in terms of relative occupancy, and not the actual positioning of the nucleosomes. Thus, this shows that nucleosome occupancy at the promoter is robust and does not change when the native ORF is replaced with a reporter gene.

With this crucial control, it is therefore possible to use the same strain (ASH79) to map nucleosome remodeling dynamics genome-wide. The experimental protocol was essentially identical to what was previously described (Zhou & O'Shea, 2011). Briefly, 6 L of diploid cells (ASH79) was grown overnight at 30°C in low fluorescence medium (-TRP -LEU) and then split into six 1 L cultures. 40, 30, 20, 10, 5 and 0 min before the cultures reached an $OD_{600\ nm}$ of 0.150 1-NM-PP1 was added to a final concentration of 3 μM. Cells were then crosslinked with 1% formaldehyde (final concentration) for 15 minutes at room temperature and quenched for 5 minutes with 125 mM glycine (final concentration). Cells were collected by centrifugation and immediately washed (10 mM Tris pH 7.5, 100 mM NaCl). The cell pellet was then dried and snap frozen in liquid nitrogen.

The frozen pellet was thawed and 200 μL lysis buffer was added (50 mM HEPES, pH 7.5, 150 mM NaCl, 2 mM EDTA, 1% Triton X-100, 0.1% Sodium deoxycholate, complete protease inhibitor cocktail tablets (Roche cComplete Mini version 10, 1 tablet per 10 mL buffer)). The cells were then mechanically lysed with glass beads and bead beating. The cell pellets were then washed twice with MNase reaction buffer (10 mM Tris pH 7.5, 50

mM NaCl, 5 mM $MgCl_2$, 1 mM $CaCl_2$, 1 mM 2-mercaptoethanol), resuspended in 750 µL MNase buffer and digested to primarily mononuclesomes with 0.75-1.5 U of MNase at 37°C for 30 minutes. Subsequently, samples were quenched by addition of 15 µL EDTA (500 mM). Debris was removed by centrifugation and 16 µL SDS solution (20%) and 30 µL proteinase K (10 mg/mL) were added to the supernatant. Crosslinks were then reversed and proteins digested by incubation at 65°C overnight.

The DNA was then purified twice by phenol/chloroform/isoamy alcohol extraction (25:24:1) and followed by precipitation in 1 mL ethanol at -20°C. Precipitated DNA was resuspended in RNase A (0.2 mg/mL in TE buffer) and residual RNA removed by digesting for 1 hour at 37°C. The samples were then purified using the PCR Purification Kit (Qiagen) and run on a 1.5% agarose gel for 60 minutes. The mononucleosome bands at ca. 150 bp were excised and purified on a Freeze 'N Squeeze DNA gel extraction column (BioRad). The DNA was then collected by ethanol precipitation. Sequencing libraries were prepared following the Illumina Multiplexed paired-end protocol. Adapters with a different index (0 min: ATCACG, 5 min: CGATGT, 10 min: TTAGGC, 20 min: TGACCA, 30 min: ACAGTG and 40 min: GCCAAT) for each timepoint were ligated onto the nucleosomal DNA fragments and the sequencing library amplified by 8 cycles of PCR.

Sequencing libraries were sequenced from both ends on an Illumina HiSeq 2000 machine generating 179 million paired-end reads of 100 bp each. We obtained between 24 and 32 million paired-end reads for each timepoint. The paired-end reads were aligned to the 2008 version of the Saccharomyces Cerevisiae genome (sacCer2) using Bowtie (version 0.12.7 (Langmead *et al.*, 2009)) allowing for 2 mismatches in the first 40 bp of the read. More than 90% of the reads were mapped to the yeast genome.

Based on previous work (Zhou & O'Shea, 2011) we restricted our analysis to reads of

between 100 and 200 bp and equated the center of the read to the nucleosome dyad. We thus aligned the center of each sequenced nucleosomal DNA fragment on the genome and extended 73 bp on both sides to generate mono-nucleosome coverage. The occupancy score was subsequently normalized. Our nucleosome maps closely match previous maps (Zhou & O'Shea, 2011) despite differences in culturing conditions, strain background etc. and were highly correlated with each other (Pearsons correlation coefficient generally: $\rho \geq 0.95$).

A.2.6 Microfluidic device fabrication

The high-throughput device developed here was inspired by a previously reported low-throughput device (Hersen *et al.*, 2008). A custom transparency film (PageWorks) was used as a mask with standard tools of photolithography to generate a master pattern with negative-tone UV photoresist (SU-8 2100) (MicroChem Corporation) on 4″ silicon wafers. Microfluidic devices were made by mixing and degassing polydimethylsiloxane (PDMS) and curing agent (Dow Corning), pouring this on the master wafer, curing it at 65°C and pealing it off. Holes were then punched for inlets and outlets (Harris Uni-Core 2.00). Following oxygen plasma activation at ca. 300 torr, the PDMS device was then bonded to custom cover slides (High Precision No. 1.5H, 60x85 mm size, Marienfeld GmbH). Finally, "adapter tubing" was inserted (polyethylene tubing with 1.57OD and 1.14ID, Warner Instruments) into the inlets and outlets, sealed with PDMS and the entire device incubated overnight at 50°C. Each device contains 5 channels that can be independently loaded and modulated. The channel width was 400 μm and the channel height measured to 111 μm. The length of each channel is ca. 5.5 cm. Each PDMS device made in this way was used for only a single time-lapse experiment.

A.2.7 Time-lapse microscopy

Yeast cells were grown overnight for at least 12 h at 30°C in flow fluorescence medium (-TRP, -LEU) until they reached an $OD_{600\,nm}$ of 0.1, quickly collected by suction filtration and resuspended in fresh medium. Before loading, all channels in the microfluidic device were washed with 70% ethanol, ddH2O and then loaded with the Con A solution (4 mg/mL) and incubated at room temperature for at least 20 min. The Con A containing microfluidic device was then quickly washed with fresh medium and cells resuspended in fresh medium were then loaded into each channel of the microfluidic device and immobilized on the glass slide by incubation for 5 min and washed again with fresh medium.

To two flasks containing low fluorescence medium (-TRP, -LEU) and pre-warmed overnight to 30°C, the appropriate concentration of 1-NM-PP1 was added and these were connected to the five 3-way electrovalves (LFYA1228032H Y-valve in perfluoroelastomer, the Lee Company) using PE tubing (0.034″ID x 0.050″OD, Instech Solomon). In turn, ismaprene tubing (ID 0.51 mm x OD 0.85 mm, IDEX Health & Science) was used to connect the valves to the five inlets in the microfluidic device and the outlets on the PDMS device connected to a waste flask with PE tubing. The flow rate was ca. 1 μL/s per channel and driven by gravity (ca. 32 cm). The microfluidic device was loaded on a Zeiss AxioObserver Z1 inverted microscope with an EM-CCD camera (Evolve, Photometrics) and incubation chamber. The entire system was kept at 30°C to avoid introducing air-bubbles. Furthermore, after cells were loaded in the microfluidic device and the flow started, cells were allowed ca. 45 min before the time-lapse acquisition was started.

16 bit tif images were acquired with an oil-immersion objective, (63x, NA 1.4, oil Ph3, Plan-Apochromat). In each time-lapse movie 2 fields of view were acquired for each of the five microfluidic channels giving 10 fields of view in total. The microscope stage automatically

moves between each of the 10 positions, maintains the focal plane (Zeiss Definite Focus) and acquires images consisting of phase-contrast (10 ms), YFP (50 ms, Zeiss Colibri LED at 505 nm excitation using Zeiss filter cube HE 46 (EX BP 500/20, BS FT 515, EM BP 535/30), intensity: 100%), CFP (100 ms, Zeiss Colibri LED at 445 nm using Zeiss filter cube HE 47 (EX BP 436/25, BS FT 455, EM BP 480/40), intensity: 100%), iRFP (400 ms, Sutter DG-4 lamp using filter cube 32 Alexa fluor 680/Cy5.5 (EX BP 665/45, BS FT 695, EM BP 725/50)), RFP (3 x 400 ms z-stack series (focal plane ± 1.75 μm), Zeiss Colibri LED at 590 nm using Zeiss filter cube HE 64 (EX BP 587/25, BS FT 605, EM BP 647/70), intensity: 100%) at an EM gain of 65 and using filtersets optimized for each fluorescent channel. CFP and YFP exposure times were chosen so as to maximize the signal-to-noise ratio without ever saturating the camera. 64 frames were acquired with 2.5 min intervals and 1-NM-PP1 was always added right after the 3rd frame was acquired such that 3 frames before inhibitor treatment were acquired. This corresponds to the 0 min timepoint. Thus, all experiments run from -5 min to 152.5 min. The entire multidimensional acquisition routine was controlled with AxioVision 4.8 (Zeiss).

The electrovalves independently control whether normal medium or medium containing 1-NM-PP1 is delivered to each microfluidic channel and can be electronically switched within milliseconds such that medium inside each microfluidic channel is changed within seconds. It took 27 s to image two fields of view in each microfluidic channel and this time was therefore used as a delay before delivering 1-NM-PP1 to each subsequent channel. The electrovalves were controlled by custom-written `MATLAB` code (2011a, the MathWorks) and synchronized with the time-lapse acquisition software. Once set up, the entire experiment is thus automated. The custom-written code that was used to control and program the electrovalves is available upon request.

Using perfluoroelastomer based electrovalves and ismaprene tubing proved critical, because many other materials absorb and slowly release 1-NM-PP1.

A.2.8 Msn2 modulation range in time-lapse experiments

To systematically dissect how different promoters decode transcription factor dynamics, the following experiments were performed. For the four amplitudes 100 nM, 275 nM, 690 nM and 3 μM corresponding to roughly one, two, three quarters of and maximal nuclear localization, single pulses of Msn2 nuclear localization with durations of 10, 20, 30, 40 and 50 min were used. This gives a total of 20 experiments (4 amplitudes x 5 durations). For oscillatory input, the amplitude was fixed at 690 nM. All pulses had a duration of 5 min. For pulse number modulation 2, 3, 4, 5, 6 and 8 pulses were used and the pulse interval was 5 min. For pulse interval modulation four 5-min pulses at 690 nM 1-NM-PP1 were used and the interval between the pulses either 5 min, 7.5 min, 10 min, 15 min or 20 min. Thus, in total 30 experiments were performed for each promoter. 7 natural promoters and 2 chromatin remodeling mutants containing the *HXK1* reporter were examined. All experiments were done at least in biological triplicate, so in total more than 810 time-lapse experiments were performed following more than 1620 fields-of-view over the 160 min time-lapse experiment. The full data sets are shown in Appendix Figure A.1D, Appendix Figures A.2-A.5 and Appendix Figure A.9A.

A.2.9 Single-cell source data

Single-cell raw data is published alongside this manuscript online on the *Molecular Systems Biology* website (www.nature.com/msb) as source data. The source data is in the comma separated value file format (csv) and compressed as a zip file. Please see the accom-

panying READ ME file.

A.2.10 Image analysis and quantification of single-cell time traces

Custom-written image processing code written in `MATLAB` (2011a, the MathWorks) was used to segment, track and quantify single cells (available upon request). Briefly, the three mCherry images were combined by a maximum intensity projection of the 3 z-stacks. All 5 image types were then background subtracted as follows: all pixels that did not contain cells were automatically identified and the peak of this background pixel distribution histogram (i.e. the mode) was then subtracted from each fluorescent image for each timepoint. Using the mode, rather than the mean or median, to subtract the background is more robust and this background subtraction method has also been used elsewhere (Gordon *et al.*, 2007).

The segmentation algorithm proceeds as follows. By underthresholding smoothed iRFP and mCherry images, all pixels inside cells were identified. For each of these pixels then, a library of 637 ellipses (different combinations of ellipse a and b values and different angles) were then scored for how well they fit the phase ring around each yeast cell in the phase contrast images and the best ellipse saved for each pixel. Although this is computationally expensive, each frame can be segmented in parallel on a computing cluster and the segmentation algorithm is extremely robust and runs essentially without segmentation errors.

Once the best ellipses had been calculated, segmentation and tracking proceeded by picking the highest-scoring ellipses subject to the following criteria: minimal overlap with other cells, minimal distance between closest pair of cell centroids, minimal differences between ellipse shapes (a and b values) between frames and minimal distance between centroids of the same cell between frames. The criteria were chosen in an extremely conservative way, such

that although some cells were lost there were basically no segmentation and tracking errors. Cells that were out of focus were manually removed. CFP and YFP reporter expression was quantified by measuring the mean pixel intensity inside each cell in each frame. The mean intensity inside each cell during the first few frames before 1-NM-PP1 was added was defined as zero and gene expression quantified as the increase in fluorescence over the mean of the initial fluorescence inside the cell due to autofluorescence. Photobleaching adjustments were performed as follows. The change in fluorescence per cell between frame $n+1$ and frame n depends on two processes: photobleaching and changes in FP concentration. Since the rate of photobleaching is known, the percentage decrease in fluorescence can be accounted for and the increase in fluorescence calculated as:

$$\text{Production}\left([\text{FP}(n+1)]\right) = [\text{FP}(n+1)] - [\text{FP}(n)] + \text{PpF} \cdot [\text{FP}(n)] \tag{A.1}$$

Where, PpF stands for Photobleaching per Frame and it was experimentally determined to be 0.0229 for YFP and 0.00570 for CFP. Thus, by integrating this production vector, we can obtain the CFP and YFP reporter expression as a function of time adjusted for photobleaching. The photobleaching rate for each reporter was independently measured by inducing several strains and quickly acquiring many CFP, YFP, mCherry and iRFP frames. The resulting photobleaching curves were then fit to $A(n) = A_0 e^{-cn}$, where n is the frame number.

For Msn2-mCherry, photobleaching was negligible and images not adjusted. The nuclear localization in each cell is quantified as the mean intensity of the 15 brightest pixels inside each cell. This nuclear quantification method is essentially the same as that previously described (Cai *et al.*, 2008; Hao & O'Shea, 2012) and was found to be the most robust between several of the methods that were tested. The minimum value before 1-NM-PP1 was added was used as a baseline and all nuclear localization thus quantified relative to this.

Although modest cell-to-cell variability is observed in the Msn2-mCherry nuclear localization in response to the same 1-NM-PP1 treatment, this is largely due to the nucleus moving in and out of focus during the time-lapse acquisition and the observed cell-to-cell variability decreases with the number of z-stacks taken. Thus it appears, that the Msn2-mCherry level inside the cell is remarkably constant between cells. This is also consistent with the small correlation that was observed between single-cell YFP expression and Msn2 AUC (Appendix Figure A.7E-G). Nuclei were segmented by thresholding the iRFP images.

For all diploid strains, blank runs without inhibitor treatment were recorded to ensure that no reporter expression was observed without inhibitor treatment and to measure the photobleaching rate of the autofluorescence in each fluorescent channel to also adjust for this. In total, 100,549 single cells were segmented, tracked and quantified for 64 frames in this study.

A.2.11 Nuclear import and export of Msn2-mCherry

To obtain a continuous function that describes the nuclear level of Msn2 as a function of time for the model, high-temporal resolution (30 s) microscopy experiments were performed to see how the nuclear Msn2 level increases with time after 1-NM-PP1 addition and decreases with time after 1-NM-PP1 removal. This is well-fit by exponential functions in both cases. That is, import is given by $A\left(1-e^{-c_1 t}\right)$ where A described the maximal amplitude for that particular 1-NM-PP1 concentration and export is given by $Be^{-c_2 t}$, where B is the nuclear Msn2 amplitude just before 1-NM-PP1 removal. The nuclear Msn2 level was 313.2 AU, 744.5 AU, 1107.8 AU and 1410.1 AU for the 1-NM-PP1 concentrations 100 nM, 275 nM, 690 nM and 3 μM, respectively. For the three lower concentrations, it was measured that $c_1 = 0.60$ and $c_2 = 0.60$. However, at 3 μM the inhibitor takes longer to be washed out and $c_1 = 1.07$

and $c_2 = 0.29$. This is also why there is a slight "kink" in the amplitude modulation and Msn2 AUC modulation simulation figures (Figure 2.2D, E) — as the amplitude increases so the nuclear export rate of Msn2 decreases slightly leading to slightly longer nuclear durations as well.

A.2.12 Deterministic model (Figure 2.2A)

The model is described by the following 6 ordinary differential equations:

$$\frac{\mathrm{d}P_{\mathrm{unbound}}}{\mathrm{d}t} = d_1 P_{\mathrm{bound}} - k_1[\mathrm{Msn2}(t)]P_{\mathrm{bound}} \tag{A.2}$$

$$\frac{\mathrm{d}P_{\mathrm{bound}}}{\mathrm{d}t} = k_1[\mathrm{Msn2}(t)]P_{\mathrm{bound}} + d_2 P_{\mathrm{active}} - \left(d_1 + \frac{k_2[\mathrm{Msn2}(t)]^n}{K_{\mathrm{d}}^n + [\mathrm{Msn2}(t)]^n}\right) P_{\mathrm{bound}} \tag{A.3}$$

$$\frac{\mathrm{d}P_{\mathrm{active}}}{\mathrm{d}t} = \frac{k_2[\mathrm{Msn2}(t)]^n}{K_{\mathrm{d}}^n + [\mathrm{Msn2}(t)]^n} P_{\mathrm{bound}} - d_2 P_{\mathrm{active}} \tag{A.4}$$

$$\frac{\mathrm{d}[\mathrm{mRNA}]}{\mathrm{d}t} = \frac{k_3[\mathrm{Msn2}(t)]^n}{K_{\mathrm{d}}^n + [\mathrm{Msn2}(t)]^n} P_{\mathrm{active}} - d_3[\mathrm{mRNA}] \tag{A.5}$$

$$\frac{\mathrm{d}[\mathrm{YFP}]}{\mathrm{d}t} = k_4[\mathrm{mRNA}] - (d_4 + k_5)\,[\mathrm{YFP}] \tag{A.6}$$

$$\frac{\mathrm{d}[\mathrm{mYFP}]}{\mathrm{d}t} = k_5[\mathrm{YFP}] - d_4[\mathrm{mYFP}] \tag{A.7}$$

The input is the function $[\mathrm{Msn2}(t)]$ which describes the level of Msn2 in the nucleus as a function of time. Based on this, the time evolution of each of the six other variables is obtained by numerical solution of the model in `MATLAB` (2011a, the MathWorks) using `ode45` (Runge-Kutta). P_{unbound}, P_{bound} and P_{active} describe the probability of each of these three promoter states as a function of time. Thus each takes a value between 0 and 1, the sum of the three is always 1 and initially, $P_{\mathrm{unbound}}(t = 0) = 1$. Although the three promoter states have been annotated as unbound, bound and active, it should be stressed that these are not mechanistically or biochemically well-defined states. Instead, three is the minimum number of promoter states required to accurately account for the behavior of all of the natural Msn2 target promoters. A Hill function is used here to describe binding of the transcription factor

to the promoter because it is a compact and easily interpreted function that can account for the amplitude dependence (K_{d}) and sensitivity (n) and be related to DNA binding affinity of the transcription factor.

The amplitude threshold used for clustering in Figure 2.2B, is mainly determined by K_{d} and n and to a lesser extent the ratio of k_1 to d_1. Similarly, the promoter activation timescale (Figure 2.2B) is mainly governed by k_1, d_1 and k_2, d_2. A full discussion of how these two properties are calculated is given below. Also important, promoter "memory-effects" are governed by d_1 and d_2. These parameters determine how quickly the promoter de-activates, which is crucial if multiple pulses are used. If the promoter only deactivates very slowly, the next pulse will begin with some probability in the bound and active promoter states and thus contribute more to transcription than the previous pulse. This effect has also been termed the head start effect (Hao & O'Shea, 2012).

Once the promoter is activated, i.e. P_{active} is populated, transcription can take place which leads to the production of mRNA. The promoter strength (or the rate of transcription) is given by k_3. The mRNA transcripts are degraded with rate constant d_3 and translated with rate constant k_4 to give pre-matured YFP. In order to become fluorescent, YFP must mature (chromophore oxidation and cyclization) which takes place with rate constant k_5 and converts pre-mature YFP into mature and fluorescent YFP. Fluorescent proteins are extremely stable *in vivo*, but their concentration diluted due to cell growth explaining the apparent degradation rate d_4. However, at the timescale of these experiments the effect of YFP degradation (dilution) is minor.

In total, 12 different but related models were investigated including a previously described model (Hao & O'Shea, 2012). Some had two promoter states and some had three (for a discussion on the effects of including different numbers of promoter states see also

(Neuert *et al.*, 2013)). In some transcription was simply proportional to P_{active}, whereas in others like the one described above transcription is modeled as a Hill function (which is a convenient mathematical way to account for the observation that transcription ceases almost immediately after Msn2 exits the nucleus). To quantify the relative performance of the different models, the residual sum of squares from the fitting is used. That is, in all cases the fitting is done in the least-squares sense and it was ensured that the model got no predictions very wrong. The model described in Figure 2.2A performed by far the best and two key insights were obtaining from distinguishing between the 12 models:

- 3 promoter states is necessary to fit the slow promoters: Having only 2 promoter states is mostly acceptable for the LF promoters (the fit is only slightly improved by adding an additional state), but having 3 promoter states is crucial for the slow HS promoters in order to account for their delay/refractory period. *SIP18* for instance will filter out all input at 690 nM up until 20 min (Figure 2.2C, top, red line/dots). If the 2 state models were used, the model would not properly be able to account for this. That is, to account for a long (20-30 min) delay in activation, at least 3 promoter states are needed.

- Having the transcription step be dependent on [Msn2(t)] is essential (we use a Hill function because it has a clear value between 0 and 1). Biologically, this means that transcription shuts off more or less immediately after Msn2 exists the nucleus. That is, that transcription requires Msn2 to be bound at the promoter or that without nuclear Msn2 the promoter immediately deactivates. An alternative way of accounting for this is to introduce a 4th promoter state (a transcriptionally active state) that deactivates very quickly, but to avoid over-fitting as much as possible the number of free parameters was minimized.

As mentioned above, the model contains three promoter states because no model with fewer states could accurately account for the slow promoters. But again it should be emphasized that each promoter state is a phenomenological variable and not biochemically well-defined. For example, if a promoter contains 4 Msn2 binding sites and each site can be independently occupied by Msn2, 16 promoter states would be needed to describe the system. Additionally, if nucleosomes are taken into account and each state is allowed to recruit RNA pol II with different kinetics, it quickly becomes evident that the number of states and parameters in such a model vastly exceeds anything that can realistically be constrained by even very rich data sets such as those presented here. Furthermore, such models would be different for different promoters, which makes quantitative comparisons of parameters between promoters difficult. Thus, the model presented here instead represents the simplest unified model that can accurate account for all the different promoters studied here. Although this means that each state is not biochemically well-defined, it has the advantage of providing a unified quantitative framework in which comparisons between different promoters and specific parameters can be made.

A.2.13 Amplitude threshold and the promoter activation timescale

Although the qualitative differences in amplitude threshold and promoter activation timescale between the HS, *RTN2* and LF promoters are clear from Figure 2.1C and Appendix Figure A.1D, extracting quantitative measures of these two key properties greatly facilities the analysis of and comparison between promoters.

As stated in the figure legend of Figure 2.2B, the two properties are defined as follows. The amplitude threshold is defined as the nuclear Msn2-mCherry level required to reach half the P_{active} level obtained at 3 μM 1-NM-PP1 and at steady-state (the maximal nuclear

Msn2-mCherry level) and the promoter activation timescale is defined as the time (min) it takes to reach half the steady-state P_{active} level at 690 nM 1-NM-PP1.

To calculate the amplitude threshold, Msn2 enters the nucleus at $t = 0$ and with amplitude A and the model is then simulated until it reaches steady-state. The P_{active} level is recorded and compared to the P_{active} level in response to 3 μM 1-NM-PP1 ([Msn2] = 1401.1, the maximal level) at steady state. The amplitude A that gives half the P_{active} level of 3 μM 1-NM-PP1 is then defined as the amplitude threshold. Thus, if this value is low (as for *DCS2*), this indicates that the promoter saturates at low amplitudes, which is likely because the promoter has a high binding affinity for Msn2. If, however, this value is high (as for *SIP18*), this indicates that very high levels of Msn2 are required to activate the promoter. The inferred amplitude thresholds were (in AU units of Msn2 nuclear localization) 942, 716, 724, 770, 444, 374 and 496 for *SIP18*, *ALD3*, *TKL2*, *RTN2*, *DDR2*, *DCS2* and *HXK1*, respectively. Other methods of calculating the amplitude threshold are possible. For example, using the raw data rather than model simulations, how gene expression scales with amplitude for a single time-point can be calculated. Using a single 50 min pulse and linear interpolation between the 4 measured amplitudes, the amplitude necessary for 50%-of-maximal activation can be calculated: 989, 887, 791, 886, 593, 437 and 409 for *SIP18*, *ALD3*, *TKL2*, *RTN2*, *DDR2*, *DCS2* and *HXK1*, respectively. This gives the same overall trend. But methods like these are very sensitive to noise in a particular data point and had a 40 min pulse been chosen instead each individual number might vary by 20-30% although the trend is the same. Thus, the simulated amplitude method is the most robust measure and is mainly determined by K_{d} and n and to a lesser extent the ratio of k_1 to d_1.

To calculate the promoter activation timescale, Msn2 enters the nucleus at $t = 0$ and with a single amplitude A and the model is then simulated until it reaches steady-state.

The P_{active} level is recorded as a function of time and compared to the steady-state value at that amplitude. The time it takes to reach half the steady-state P_{active} level, is then defined as the promoter activation timescale. The promoter activation timescale is therefore a function of the amplitude. Here the Msn2 nuclear localization corresponding to 690 nM 1-NM-PP1 (1107.8 AU) is used as the amplitude to calculate the promoter activation timescale. This is chosen, because this is the same 1-NM-PP1 concentration as the one used for all oscillatory Msn2 input. However, the activation timescale depends only weakly on the Msn2 amplitude and the trend and clustering of the promoters is invariant with the amplitude. The promoter activation timescales were 25.3 min, 23.4 min, 26.4 min, 10.1 min, 4.1 min, 2.8 min and 1.3 min for *SIP18*, *ALD3*, *TKL2*, *RTN2*, *DDR2*, *DCS2* and *HXK1*, respectively. The promoter activation timescale measures how quickly the steady-state P_{active} level is reached after Msn2 enters the nucleus and is mainly limited by the slowest promoter transition step ($P_{\text{unbound}} \rightarrow P_{\text{bound}}$ or $P_{\text{bound}} \rightarrow P_{\text{active}}$). The timescales of these steps, in turn, are governed by k_1, d_1 and k_2, d_2, respectively. As for the amplitude threshold, other measures based directly on the raw data are possible. For example, given a particular amplitude how gene expression changes with duration can be considered. Using 690 nM and linear interpolation between the measured timepoints, the promoter activation timescale could also be defined as the timepoint where the gene expression output is 10% of the 50 min output: then the result is 20.7 min, 18.0 min, 16.3 min, 11.9 min, 12.0 min, 10.5 min and 3.8 min for *SIP18*, *ALD3*, *TKL2*, *RTN2*, *DDR2*, *DCS2* and *HXK1*, respectively. However, this involves setting an arbitrary threshold and uses gene expression as a proxy for promoter activation, which is not a true comparison. So although the trend is similar, this measure is much more arbitrary. And this raw-data measure fluctuates by 2- to 3-fold dependent on which threshold is set and which concentration is used, although the trend between promoters is robust. As

mentioned before, this is likely because gene expression is a very poor proxy for promoter transition kinetics. Finally, and as previously mentioned, the simulated promoter activation timescale depends only weakly on the amplitude and is thus a far more robust measure and, importantly, the model-inferred promoter activation timescale trend is in qualitative agreement with the raw data in Figure 2.1C and Appendix Figure A.1D.

A.2.14 Model fitting to natural Msn2 promoters and parameter estimation

The seven promoter specific parameters, k_1, d_1, k_2, d_2, K_d, n and k_3, were obtained by fitting the entire dataset of 30 experiments (Appendix Figure A.1D) to the model. Briefly, this was done by stochastically generating parameter combinations and using these as initial guesses for least-squares curve fitting in `MATLAB` (2011a, the MathWorks) using the function `lsqcurvefit` and the function `ode45` to numerically solve the system of differential equations for the fitting. Continuous Msn2 time-traces corresponding to the Msn2-mCherry input in each of the 30 experiments were used as input and the model simulated YFP traces as output and fitted to the raw YFP data for each promoter. The fitting was done in the least-square sense so as to minimize the sum of squared residuals. To ensure that the best fit and parameter combinations were obtained for each promoter, the fitting was run on a computing cluster for months. The parameters for each promoter are given in Appendix Table A.2. The accuracy of the fit for each promoter and for all 30 time-lapse experiments, was estimated by comparing the raw YFP data to the model simulated YFP. As can be seen in Appendix Table A.2, all fits had R^2-values of 0.95 or above.

The remaining parameters were fixed. The translation rate was fixed to $k_4 = 15.0$.

The mRNA degradation rate, d_3, was measured as follows: Cells were grown overnight

Table A.2: Parameters for deterministic model (units of min^{-1} where applicable).

	SIP18	*ALD3*	*TKL2*	*RTN2*	*DDR2*	*DCS2*	*HXK1*	*HXK1* *snf6*Δ	*HXK1* *gcn5*Δ
k_1	2.2591	2.5703	0.1360	0.6181	4.7580	3.8559	3.9647	4.9946	4.7947
d_1	13.4385	10.5560	2.0460	4.1825	9.5081	3.7523	3.9265	9.4200	9.5687
k_2	0.0756	0.3187	0.6541	0.6402	4.0526	0.9998	7.5391	0.0873	0.2913
K_d	1904.0	978.7	1283.0	1144.5	2369.0	249.0	109.9	419.6	478.9
n	1.5153	2.4766	1.1110	1.2790	0.8969	2.2091	1.3087	1.1154	1.4224
d_2	0.0291	0.0218	0.0239	0.0802	0.1640	0.3951	33.9755	0.1260	0.3231
k_3	21.4708	0.9248	1.5637	3.0337	4.9356	0.6945	10.2952	6.1205	4.2074
R^2	0.984	0.964	0.965	0.972	0.949	0.980	0.985	0.977	0.955
rss	$3.7 \cdot 10^7$	$2.3 \cdot 10^7$	$1.3 \cdot 10^7$	$5.6 \cdot 10^7$	$9.0 \cdot 10^8$	$4.9 \cdot 10^7$	$2.4 \cdot 10^8$	$1.2 \cdot 10^8$	$2.5 \cdot 10^8$

at 30°C in flow fluorescence medium (-TRP, -LEU) until they reached an $\text{OD}_{600\text{ nm}}$ of 0.1. They were then induced with 3 μM 1-NM-PP1 for 45 min, filtered and resuspended in fresh medium and samples collected over 8 timepoints: 0, 2.5, 5, 7.5, 10, 15, 20 and 30 min. Sample collection, RNA extraction (QIAGEN RNeasy Kit) and cDNA synthesis was done as described under Microarray analysis. The mRNA half-life was then determined by qPCR (SYBR®Green PCR Master Mix, Applied Biosystems) using primers targeting both the YFP and CFP transcripts:

Forward: 5'-TTGTTCACTGGTGTTGTTCCA-3'

Reverse: 5'-AGCGTCACCTTCACCTTCAC-3'

and using primers targeting the *TAF10* transcript as control, since *TAF10* has previously been shown not to change in abundance upon perturbations (Teste *et al.*, 2009). Several biological replicates were performed and the data fit to Ae^{-ct} and the rate constant for mRNA decay found to be within $[0.069; 0.139]$ and this range used as a range for the ODE fitting.

Similarly, the fluorescent protein maturation time, k_5, was measured as follows: Cells were

grown overnight at 30°C in flow fluorescence medium (-TRP, -LEU) until they reached an $OD_{600\ nm}$ of 0.1 and loaded in the microfluidic device as for time-lapse microscopy. They were exposed to 3 μM for 45 min and the medium then instantly switched to medium containing 100 μg/mL cycloheximide. Time-points were taken every minute for 90 min at new fields-of-view. This avoids photobleaching cells and therefore only an increase in fluorescence is observed. Several biological replicates were performed and the data fit to $A\,(1 - e^{-ct})$. We define the maturation time, as the time it takes for half of all fluorophores to mature. The maturation time was ca. 8-10 min for mCitrineV163A at 30°C and 1-2 min longer for SCFP3A. For the ODE fitting the mean plus/minus 2 standard deviations is used as the range, i.e. $[0.0504; 0.114]$.

Finally, the YFP degradation/dilution rate, d_4, was obtained from a range of $[0.001; 0.08]$.

The fitting was performed in two steps. First using these ranges, only k_4, d_3, k_5 and d_4 were allowed to vary and all other parameters held fixed and these globally fitted to all 7 promoters (i.e. all 210 experiments). The following values were then obtained: $k_4 = 15$, $d_3 = 0.08$, $d_4 = 0.001$ and $k_5 = 0.06$ in units of min^{-1}. These were therefore used for all 7 promoters, and also the chromatin remodeling complex mutants of *HXK1*. Secondly, keeping these 4 global parameters fixed, the 7 promoter-specific parameters (green parameters in Figure 2.2A) were obtained by fitting to the full 30-experiment data set for each promoter. We found that multiple parameter sets k_4, d_3, k_5 and d_4 could fit the data reasonably well, but that the green, promoter-specific parameters were not very sensitive to which of the k_4, d_3, k_5 and d_4 parameter sets were used.

A.2.15 Noise and transcription factor dynamics: oscillations versus a single pulse

In Figure 2.4C, the total gene expression noise for oscillations and for a single pulse is compared. For oscillations, eight 5 min pulses separated by 5 min intervals at 690 nM 1-NM-PP1 was used, whereas for a single pulse a single 40 min pulse at 690 nM 1-NM-PP1 was used. This keeps the total Msn2 AUC, amplitude and total nuclear duration constant — that is, it keeps the Msn2 input constant. However, this necessarily means that the gene expression means might not be constant between the two conditions. In this example the gene expression means for the eight 5 min pulses are 599.1 AU, 314.3 AU, 529 AU, 5271 AU, 2080 AU, 2284 AU and 5652 AU and the means for the single 40 min pulse are 1474 AU, 1688 AU, 1101 AU, 8373 AU, 2274 AU, 2724 AU and 5881 AU for *SIP18*, *ALD3*, *TKL2*, *RTN2*, *DDR2*, *DCS2* and *HXK1*, respectively. Thus, except for *DCS2*, *RTN2* and *HXK1* where the differences are small, the oscillatory input generally shows lower mean expression. However, in the case of *RTN2* and *DCS2* for example, the differences in mean expression are small but the differences in noise substantial. So the differences in mean expression cannot on their own account for the higher gene expression noise for oscillatory input.

As described in the main text, Tostevin *et al.* found that oscillations can lead to lower gene expression noise than single pulse input based on a simple theoretical model (Tostevin *et al.*, 2012). However, this discrepancy with our experimental results is more due to differences in comparison. Tostevin *et al.* considered the steady-state response, whereas in this work we look at the response to a transient single pulse or a limited number of oscillations. More importantly, however, Tostevin *et al.* made the comparison for constant gene expression means. To achieve constant means, the transcription factor amplitude was significantly higher for oscillations than for the constant input and the total nuclear duration significantly

smaller for oscillations than for the constant input. Since the rate of promoter activation in Tostevin *et al.*'s model is proportional to the transcription factor amplitude, this means that the promoter activation timescale is faster for oscillations than for constant input. Consistent with the results presented here, the promoter activation timescale is a major determinant of gene expression noise (Figure 2.6C) and the finding by Tostevin *et al.* that oscillations with higher transcription factor amplitude (and hence faster promoter activation timescale) yields lower gene expression noise than constant input with lower transcription factor amplitude (and hence slower promoter activation timescale), is fully consistent with the results presented here.

Thus, if the comparison between oscillations and a single pulse are to be made for constant mean expression, this necessarily means that the total duration, the amplitude and/or the Msn2 AUC will be different. On the other hand, if the comparison is made for constant Msn2 amplitude, total duration and Msn2 AUC, this necessarily means that the mean expression might differ. Thus, no perfect comparison is possible. Experimentally, we find in this work that the total noise for constant Msn2 input is higher for oscillatory Msn2 input than for single pulse Msn2 input.

A.2.16 Simplified model (Figure 2.5A)

The "simplified" model described in Figure 2.5A has two distinct advantages over the full deterministic model in Figure 2.2A: it is much simpler, which makes it possible to understand the effect of each individual parameter on noise and gene expression behavior and being simpler, it is analytically tractable. The model is described by the following 4

possible reactions:

$$P_0 \xrightarrow{\frac{k_1[\mathrm{TF}(t)]^n}{K_\mathrm{d}^n+[\mathrm{TF}(t)]^n}} P_1 \tag{A.8}$$

$$P_1 \xrightarrow{d_1} P_0 \tag{A.9}$$

$$X \xrightarrow{\frac{k_2[\mathrm{TF}(t)]^n}{K_\mathrm{d}^n+[\mathrm{TF}(t)]^n}P_1} X+1 \tag{A.10}$$

$$X \xrightarrow{d_2 \cdot X} X-1 \tag{A.11}$$

where X is used to denote mRNA. The promoter can be found in either the inactive (P_0) or active (P_1) state and $P_0(t)$ and $P_1(t)$ describe the probability of finding the promoter in its active or inactive state as a function of time, respectively. Nucleocytoplasmic translocation of the transcription factor, $[\mathrm{TF}(t)]$, is modeled as a step function.

The above model is analytically tractable. First, the case of a single pulse is considered. That is, $[\mathrm{TF}(t)] = \mathrm{TF}$ for $0 \leq t \leq T$ and $[\mathrm{TF}(t)] = 0$ otherwise. Then the probability of the promoter being active is

$$\frac{\mathrm{d}P_1}{\mathrm{d}t} = \frac{k_1 \mathrm{TF}^n}{K_\mathrm{d}^n + \mathrm{TF}^n} - \left(\frac{k_1 \mathrm{TF}^n}{K_\mathrm{d}^n + \mathrm{TF}^n} + d_1 \right) P_1 \quad \text{for} \quad 0 \leq t \leq T \tag{A.12}$$

since $P_0 + P_1 = 1$ and where times $t > T$ are ignored since no transcription can then take place anyway. Then:

$$P_1(t) = \frac{\frac{k_1 \mathrm{TF}^n}{K_\mathrm{d}^n+\mathrm{TF}^n}}{\frac{k_1 \mathrm{TF}^n}{K_\mathrm{d}^n+\mathrm{TF}^n} + d_1} \left(1 - e^{\left(\frac{k_1 \mathrm{TF}^n}{K_\mathrm{d}^n+\mathrm{TF}^n} + d_1 \right) t} \right) \quad \text{for} \quad 0 \leq t \leq T \tag{A.13}$$

Next how the mean mRNA changes with time, $\langle X \rangle$, is considered. Here the system is considered when the transcription factor is nuclear and after T when the transcription factor has left the nucleus:

$$\frac{\mathrm{d}\langle X \rangle}{\mathrm{d}t} = \frac{k_2 \mathrm{TF}^n}{K_\mathrm{d}^n + \mathrm{TF}^n} P_1(t) - d_2 \langle X \rangle \quad \text{for} \quad 0 \leq t \leq T \tag{A.14}$$

$$\frac{\mathrm{d}\langle X \rangle}{\mathrm{d}t} = -d_2 \langle X \rangle \quad \text{for} \quad t > T \tag{A.15}$$

Solving this system, the following is obtained:

$$\langle X\rangle\,(t|0\leq t\leq T)=\frac{\frac{k_1\mathrm{TF}^n}{K_\mathrm{d}^n+\mathrm{TF}^n}\frac{k_2\mathrm{TF}^n}{K_\mathrm{d}^n+\mathrm{TF}^n}}{\frac{k_1\mathrm{TF}^n}{K_\mathrm{d}^n+\mathrm{TF}^n}+d_1}\left(\frac{1-e^{-d_2t}}{d_2}-\frac{e^{-\left(\frac{k_1\mathrm{TF}^n}{K_\mathrm{d}^n+\mathrm{TF}^n}+d_1\right)t}-e^{-d_2t}}{d_2-\frac{k_1\mathrm{TF}^n}{K_\mathrm{d}^n+\mathrm{TF}^n}-d_1}\right) \quad \text{(A.16)}$$

$$\langle X\rangle\,(t|t>T)=\frac{\frac{k_1\mathrm{TF}^n}{K_\mathrm{d}^n+\mathrm{TF}^n}\frac{k_2\mathrm{TF}^n}{K_\mathrm{d}^n+\mathrm{TF}^n}}{\frac{k_1\mathrm{TF}^n}{K_\mathrm{d}^n+\mathrm{TF}^n}+d_1}\left(\frac{1-e^{-d_2T}}{d_2}-\frac{e^{-\left(\frac{k_1\mathrm{TF}^n}{K_\mathrm{d}^n+\mathrm{TF}^n}+d_1\right)T}-e^{-d_2T}}{d_2-\frac{k_1\mathrm{TF}^n}{K_\mathrm{d}^n+\mathrm{TF}^n}-d_1}\right)e^{-d_2(t-T)} \quad \text{(A.17)}$$

These equations describe how the mRNA level changes with time. However, gene expression is quantified as the mRNA AUC. This expression is readily found by solving:

$$\text{mRNA AUC}=\int_0^\infty\langle X(t)\rangle\mathrm{d}t=\int_0^T\langle X(t)\rangle\mathrm{d}t+\int_T^\infty\langle X(t)\rangle\mathrm{d}t \quad \text{(A.18)}$$

The above illustration was for a single pulse. However, the same approach will yield an analytical solution for any number of pulses with any pulse interval. Thus, it is simple to investigate how the mean expression changes with transcription factor amplitude, duration, pulse number, pulse length and pulse interval as shown in Appendix Figure A.8. In order to investigate how the mRNA AUC noise changes with transcription factor amplitude, duration, pulse number, pulse length and pulse interval (Appendix Figure A.8), the model must also be solved for the variance: $\sigma_X^2(t)=\langle X^2(t)\rangle-\langle X(t)\rangle^2$. To solve for $\langle X^2(t)\rangle$, the chemical master equation can be multiplied by X^2 and summed up. Following this standard approach (Thattai & van Oudenaarden, 2001; Tostevin *et al.*, 2012), this system can be analytically solved for the noise. However, the resulting expressions are unwieldy even for a single pulse and unmanageable for multiple pulses and are therefore not presented here. Instead, for multiple pulses, exact discrete time stochastic simulations are used to simulate the system. For a single pulse the simulation results match the analytical result and for multiple pulses the noise is much more easily obtained with simulations. For simulating the model, exact discrete-time stochastic simulations are used because this is convenient when the rates are

changing with time. Briefly, these proceed as follows: The algorithm requires a discrete time-vector, with very short time steps. For each time step then, the probability that each of the elemental reactions occur is calculated. Whether a reaction occurs or not is then determined by picking a random number and comparing this to the elemental reaction probabilities. Based on this, the next time-step is considered and the elemental reaction probabilities updated accordingly. This is continued until end of the time-vector is reached. Provided that the time step interval is chosen to be small enough that the combined probability of all elemental reactions is always less than one, this is exact. A full discussion of discrete time stochastic simulation algorithms is given elsewhere (Sandmann, 2008).

A.2.17 *in silico* promoters for the simplified model (Figure 2.5A)

Four *in silico* promoters representative of the four classes (HS, LS, LF and HF) were generated with the following parameters: $k_1 = d_1 = 0.0167$ (HS, LS), $k_1 = d_1 = 0.5$ (HF, LF), $K_\mathrm{d} = 75$, $n = 8$ (HS, HF), $K_\mathrm{d} = 20$, $n = 2.5$ (HS, HF), $k_2 = 30$ (HS), $k_2 = 12$ (LS), $k_2 = 3$ (LF), $k_2 = 8$ (HF), $d_2 = 0.12$ min^{-1}(for all). Thus, both slow promoters have the same k_1 and d_1, and both fast promoters have the same k_1 and d_1. Similarly, both high amplitude threshold promoters have the same K_d and n, and both low amplitude threshold promoters have the same K_d and n. The transcription rate, k_2, was different for all four *in silico* promoters, but chosen such that differential gene expression is possible at an absolute level.

It should be stressed that these are just examples and that a large range of other parameter combinations could equally well have been chosen to yield differential expression between the four promoters. Furthermore, low/high and slow/fast are continuous scales. For instance, intermediate values also exist and are those employed as well there are 9 promoter types (LS,

IS, HS, LF, IF, HF, LI, II, HI), where I stands for intermediate, and here some differential expression is also possible although to a lesser extent. Thus, in this work four promoter classes are considered and it is shown that four gene expression programs can be encoded in the dynamics of a single transcription factor. However, this is not an absolute maximum — instead it is a number where strong differential gene expression can be achieved solely on the basis of the amplitude threshold and the promoter activation timescale. A third dimension, feedback or something else could possibly expand on the number of gene expression programs that can be encoded in the dynamics of a single transcription factor.

A.2.18 Synthesis of 1-NM-PP1

Although commercially available, 1-NM-PP1 is expensive and large quantities were needed. Therefore, a large-scale synthesis of 1-NM-PP1 was undertaken. Full synthetic details have not previously been reported. However, the synthesis reported here is loosely based on previous literature (Bishop *et al.*, 1999; Hanefeld *et al.*, 1996).

2-(naphthalen-1-yl)acetyl chloride

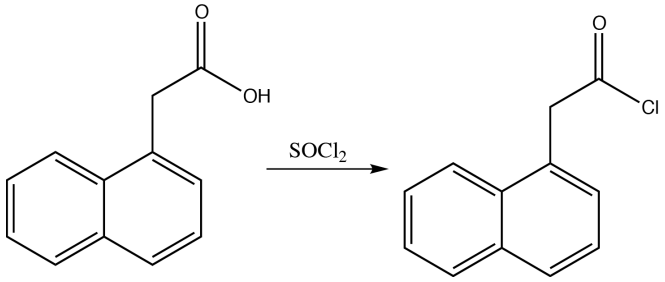

To a flame-dried flask under nitrogen was added 1-naphthaleneacetic acid (16.76 g, 90 mmol, 1 eq.). The flask was fitted with a reflux condenser leading into a bubbler filled with paraffin oil and connected to an empty wash bottle from which the outlet, via an inverse funnel, lead into a 200 mL 20% (w/v) NaOH solution.

The flask was cooled on ice and vigorously stirred as thionyl chloride (13.08 mL, 180 mmol, 2 eq.) was added. The solution was then refluxed at 80°C for 2 h until bubbling had fully stopped, indicating the completion of the reaction.

The remaining excess thionyl chloride was then distilled off using vacuum distillation apparatus with a liquid nitrogen trap under reduced pressure to give a brown oil. The oil was dissolved in 50 mL dry THF and used for the subsequent step without further purification.

5-amino-1-(tert-butyl)-3-(naphthalen-1-ylmethyl)-1H-pyrazole-4-carbonitrile

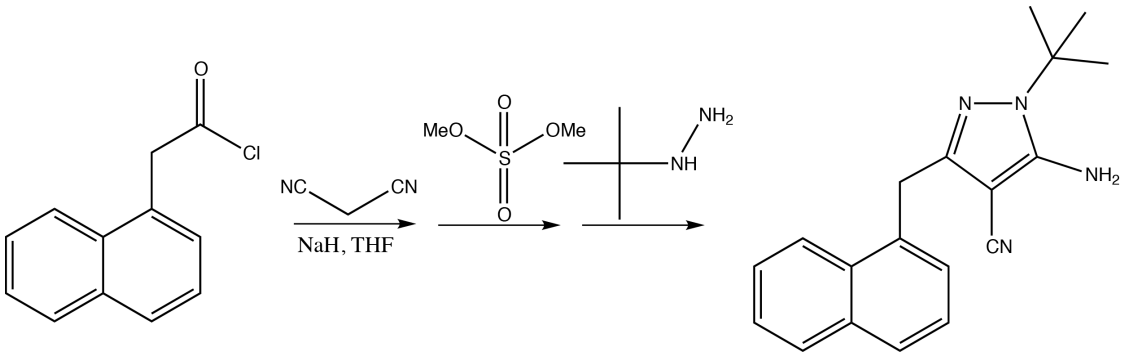

Malononitrile (5.94 g, 90 mmol, 1 eq.) was dissolved in 150 mL dry THF in a flame-dried flask under nitrogen. Sodium hydride (60% suspension in oil, 9.00 g, 225 mmol, 2.5 eq.) was added slowly and portionwise to the solution cooled on ice. 1-naphtylacetyl chloride prepared from above was dissolved in 50 mL dry THF and slowly added on ice. The resulting suspension was then stirred for 1 h at room temperature.

Dimethylsulfate (12.9 mL, 45 mmol, 1.5 eq.) was added and the solution was refluxed at 80°C for 1.5 h until TLC analysis indicated the completion of the reaction. The suspension was cooled on ice and triethylamine (37.8 mL, 270 mmol, 3 eq.) and then tertbutylhydrazine hydrochloride (11.91 g, 135 mmol, 1.5 eq.) were added. The solution was then refluxed overnight at 77°C.

Solvents were removed in vacuo and the residue partitioned between 100 mL DCM and 150 mL water. The aqueous layer was further extracted twice with 100 mL DCM and the combined organics dried over magnesium sulfate and solvents removed in vacuo to give a dark red oil which was purified by column chromatography (340 g Biotage silica column, 20% to 100% DCM gradient in hexanes) to give the product as a pale yellow solid (13.64 g, 50% yield) after drying under high vacuum.

^{1}H NMR (500 MHz, $CDCl_3$-*d*) δ/ppm 1.61 (9 H, $CH(C\underline{H}_3)_3$, s), 4.18 (2 H, $N\underline{H}_2$, br. s.), 4.36 (2 H, $C\underline{H}_2$, s), 7.42 - 7.53 (4 H, Ar<u>H</u>, m), 7.77 (1 H, Ar<u>H</u>, d, J = 8.3 Hz), 7.85 (1 H, Ar<u>H</u>, d, J = 7.8 Hz), 8.30 (1 H, Ar<u>H</u>, d, J = 7.8 Hz).

^{13}C NMR (126 MHz, $CDCl_3$-*d*) δ/ppm 29.4, 32.4, 60.0, 78.2, 114.8, 124.7, 125.7, 125.8, 126.0, 127.6, 127.8, 128.8, 132.3, 134.0, 134.1, 149.8, 150.6.

HRMS (ESI$^+$): $C_{19}H_{21}N_4^+$ ([M+H]$^+$) requires 305.1761: found 305.1763.

1-(tert-butyl)-3-(naphthalen-1-ylmethyl)-1H-pyrazolo[3,4-d]pyrimidin-4-amine (1-NM-PP1)

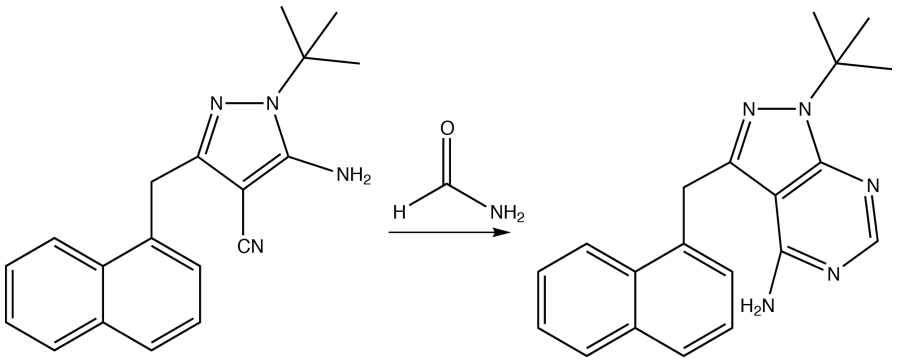

To the pyrazole (10.0 g, 32.9 mmol) in a 2-necked round-bottom flask fitted with a reflux condenser was added 200 mL formamide under nitrogen. The resulting solution was then stirred at 190°C overnight (16 h). The solution was cooled to room temperature and 100 mL water was added to give a cloudy solution. The precipitates were collected by filtration

and dried. The solids were resuspended in ethanol (400 mL) and one spoonful of activated charcoal added. The resulting slurry was then heated to reflux for 15 min to decolorize and then filtered whilst hot. The ethanol solution was concentrated to about 50 mL and 200 mL water added and the precipitated solids collected by filtration and dried under high vacuum to give 9.84 g of a pale brown powder (95% pure by NMR). To remove trace impurities, the crude product was recrystallized from 120 mL of a toluene:cyclohexane (2:1) mixture. The collected product was washed with hexane and then dissolved in 100 mL boiling ethanol and added dropwise to a vigorously stirred 250 mL ice-cold water solution to induce precipitation of the white product. The precipitates were washed with water and dried under high vacuum (0.050 mbar for 18 h) at 40°C to give the product 1-NM-PP1 (7.64 g, 70% yield, >99% pure by NMR) as a cream colored powder.

^{1}H NMR (500 MHz, $CDCl_3$-*d*) δ/ppm: 1.85 (9 H, $CH(C\underline{H}_3)_3$, s), 4.76 (2 H, $C\underline{H}_2$, s), 4.86 (2 H, $N\underline{H}_2$, br. s.), 7.20 (1 H, Ar<u>H</u>, d, J = 8.3 Hz), 7.35 - 7.44 (1 H, Ar<u>H</u>, m), 7.51 - 7.63 (2 H, Ar<u>H</u>, m), 7.81 (1 H, Ar<u>H</u>, d, J = 8.3 Hz), 7.87 - 7.96 (1 H, Ar<u>H</u>, m), 8.22 (1 H, Ar<u>H</u>, d, J = 7.3 Hz), 8.27 (1 H, Ar<u>H</u>, s).

^{13}C NMR (126 MHz, $CDCl_3$-*d*) δ/ppm: 29.5, 33.0, 60.3, 101.4, 123.7, 125.8, 126.1, 126.4, 126.8, 128.4, 129.1, 132.1, 134.1, 134.2, 140.8, 154.7, 154.9, 157.9.

HRMS (ESI^+): $C_{20}H_{22}N_5^+$ ($[M+H]^+$) requires 332.1870: found 332.1872.

A.3 Appendix A references

Bishop AC, Kung CY, Shah K, Witucki L, Shokat KM, Liu Y (1999) Generation of monospecific nanomolar tyrosine kinase inhibitors via a chemical genetic approach. *J Am Chem Soc* **121**: 627-631

Cai L, Dalal CK, Elowitz MB (2008) Frequency-modulated nuclear localization bursts coordinate gene regulation. *Nature* **455**: 485-490

Filonov GS, Piatkevich KD, Ting LM, Zhang JH, Kim K, Verkhusha VV (2011) Bright and stable near-infrared fluorescent protein for in vivo imaging. *Nat Biotechnol* **29**: 757-U133

Gordon A, Colman-Lerner A, Chin TE, Benjamin KR, Yu RC, Brent R (2007) Single-cell quantification of molecules and rates using open-source microscope-based cytometry. *Nat Methods* **4**: 175-181

Grote A, Hiller K, Scheer M, Munch R, Nortemann B, Hempel DC, Jahn D (2005) JCat: a novel tool to adapt codon usage of a target gene to its potential expression host. *Nucleic Acids Res* **33**: W526-W531

Hanefeld U, Rees CW, White AJP, Williams DJ (1996) One-pot synthesis of tetrasubstited pyrazoles — Proof of regiochemistry. *J Chem Soc Perk T* **1**: 1545-1552

Hao N, O'Shea EK (2012) Signal-dependent dynamics of transcription factor translocation controls gene expression. *Nat Struct Mol Biol* **19**: 31-47

Hersen P, McClean MN, Mahadevan L, Ramanathan S (2008) Signal processing by the HOG MAP kinase pathway. *P Natl Acad Sci USA* **105**: 7165-7170

Huebert DJ, Kuan PF, Keles S, Gasch AP (2012) Dynamic Changes in Nucleosome Occupancy Are Not Predictive of Gene Expression Dynamics but Are Linked to Transcription and Chromatin Regulators. *Mol Cell Biol* **32**: 1645-1653

Kremers GJ, Goedhart J, van Munster EB, Gadella TWJ (2006) Cyan and yellow super fluorescent proteins with improved brightness, protein folding, and FRET Forster radius. *Biochemistry* **45**: 6570-6580

Langmead B, Trapnell C, Pop M, Salzberg SL (2009) Ultrafast and memory-efficient alignment of short DNA sequences to the human genome. *Genome Biol* **10**

Neuert G, Munsky B, Tan RZ, Teytelman L, Khammash M, van Oudenaarden A (2013) Systematic Identification of Signal-Activated Stochastic Gene Regulation. *Science* **339**: 584-587

Raser JM, O'Shea EK (2004) Control of stochasticity in eukaryotic gene expression. *Science* **304**: 1811-1814

Sandmann W (2008) Discrete-time stochastic modeling and simulation of biochemical networks. *Comput Biol Chem* **32**: 292-297

Sheff MA, Thorn KS (2004) Optimized cassettes for fluorescent protein tagging in Saccharomyces cerevisiae. *Yeast* **21**: 661-670

Teste MA, Duquenne M, Francois JM, Parrou JL (2009) Validation of reference genes for

quantitative expression analysis by real-time RT-PCR in Saccharomyces cerevisiae. *BMC Mol Biol* **10**

Thattai M, van Oudenaarden A (2001) Intrinsic noise in gene regulatory networks. *P Natl Acad Sci USA* **98**: 8614-8619

Tostevin F, de Ronde W, Ten Wolde PR (2012) Reliability of frequency and amplitude decoding in gene regulation. *Phys Rev Lett* **108**: 108104

Zhou X, O'Shea EK (2011) Integrated Approaches Reveal Determinants of Genome-wide Binding and Function of the Transcription Factor Pho4. *Mol Cell* **42**: 826-836

Appendix B

Supplementary information for Chapter 3

B.1 Supplementary figures for Chapter 3

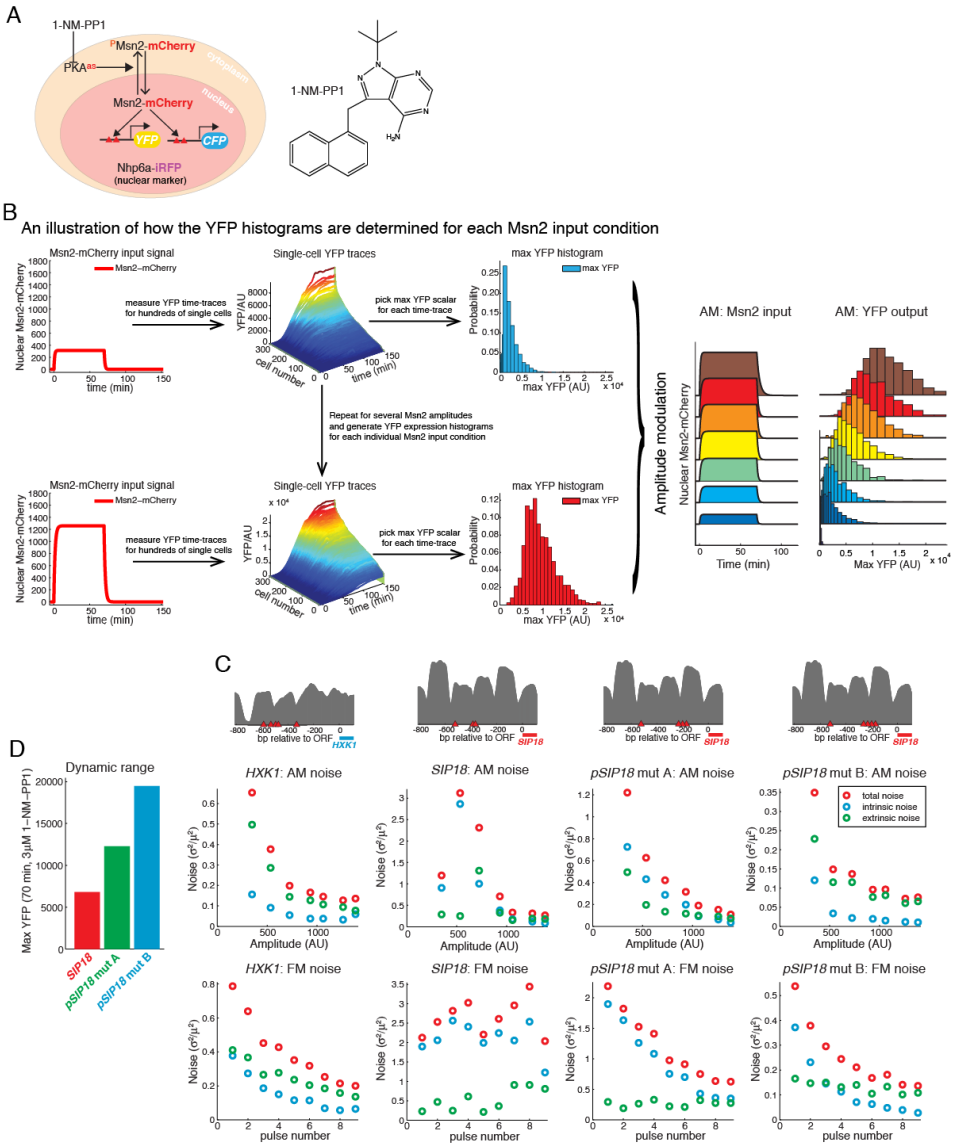

Figure B.1: *How time-lapse data is converted to histograms and promoter maps and noise data*
(A) Overview of strains. Msn2 was C-terminally tagged with mCherry. A nuclear protein, NHP6a, was C-terminally tagged with iRFP (Filonov *et al.*, 2011; Hansen & O'Shea, 2013). All three catalytic subunits of PKA were mutated M→G mutation (*TPK1*^{M164G} *TPK2*^{M147G} *TPK3*^{M165G}). These mutations render all three PKA subunits sensitive to the small molecule 1-NM-PP1 (Bishop *et al.*, 2000; Hao & O'Shea, 2012; Zaman *et al.*, 2009). Thus, when 1-NM-PP1 is added, PKA is inhibited, Msn2-mCherry gets dephosphorylated, and translocates into the nucleus where it can bind to and activate target genes. To visualize gene expression, the ORFs of target genes were replaced with YFP (mCitrineV163A) and CFP (SCFP3A) on homologues chromosomes in diploid cells, as has been described previously (Hansen & O'Shea, 2013; Kremers et al., 2006). The synthesis of 1-NM-PP1 has been described previously (Hansen & O'Shea, 2013).
(B) An illustration of how the YFP histograms are obtained for each condition. For a specific amplitude or frequency (not shown), the response of ∼1000 cells is measured (only ∼300 cells shown here for ease of visualization). For each single cell time-trace a moving average smoothing filter is applied to remove any technical noise and the maximal YFP value is determined after the trace has reached a plateau. This is repeated for all single cells and a YFP histogram is generated by binning. The procedure is then repeated for all the Msn2 conditions (e.g. the no input and all the AM conditions) to generate a full single-cell dose-response (right). This data is then used to calculate the maximal mutual information with respect to amplitude modulation, I_{AM}.
(C) Promoter nucleosome occupancy maps. The upstream promoter region (-800 to 0 bp from ATG site) is shown for each promoter. Msn2 binding sites (STRE 5'-CCCCT-3') are shown in red triangles and nucleosome occupancy data (grey) is from (Hansen & O'Shea, 2013). The *SIP18* promoter has three Msn2 binding sites. The most upstream site is non-functional removing it does not affect gene induction. The two sites (close to -400 bp) are required — removing these two sites abolishes gene induction. *pSIP18 mut A* and mut B have three and four new binding sites, respectively, in between the two nucleosomes close to the transcription start site.
(D) Dynamic range and noise. Removing the two WT Msn2 binding sites and replacing them with three or four binding sites, respectively, substantially increases the dynamic range (defined as the response to a 70 min pulse at 3 μM 1-NM-PP1). How the total (red), intrinsic (blue) and extrinsic (green) noise scales with the Msn2 amplitude (for a 70 min pulse; top) or the frequency (at 690 nM 1-NM-PP1; bottom) for all four promoters is shown. The y-axis scale is different in each case.

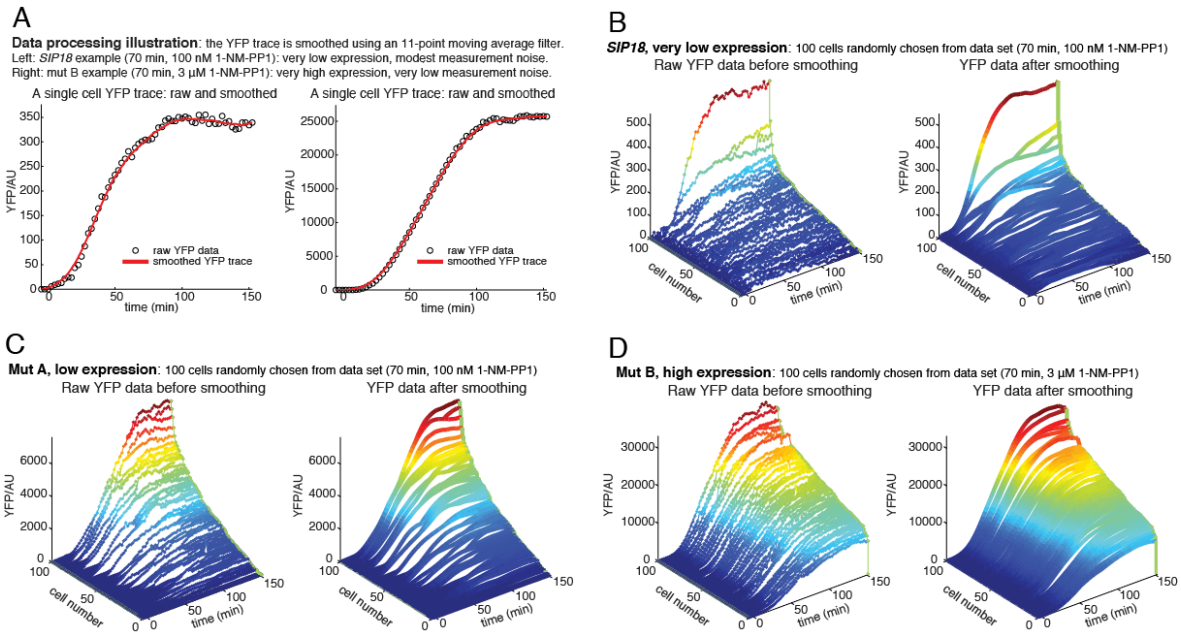

Figure B.2: *Data processing and control of measurement noise*
(A) Data processing illustration. Controlling measurement noise is important, because high measurement noise will cause measurements of mutual information to be underestimates. To minimize effects of measurement noise coming e.g. from improper focusing by the microscope, autofluorescence and camera noise, slight errors in cell segmentation and other sources, multiple YFP measurements are made. For each single cell, the YFP level is measured 64 times at 2.5 min time resolution. In general, measurement noise is modest at very low YFP expression — in part due to cellular autofluorescence — but negligible at high YFP expression. As an example of very low YFP expression, a single cell time trace is shown on the left (*SIP18*, 70 min, 100 nM 1-NM-PP1). By smoothing the raw data (black circles), an accurate estimation of the YFP level can be obtained (red line). As an example of very high YFP expression, a raw and smoothed single cell time trace is shown on the right (mut B, 70 min, 3 µM 1-NM-PP1).
(B) Example of raw data at very low YFP expression (*SIP18*, 70 min, 100 nM 1-NM-PP1). Raw YFP time-traces of 100 randomly chosen single cells are shown on the left and the same YFP time-traces, after smoothing as illustrated in **A)**, are shown on the right. Although the raw YFP data suffers from modest measurement noise, the actual YFP level can be accurately estimated by smoothing.
(C) Example of raw data at low YFP expression (mut A, 70 min, 100 nM 1-NM-PP1). Raw YFP time-traces of 100 randomly chosen single cells are shown on the left and the same YFP time-traces, after smoothing as illustrated in **A)**, are shown on the right.
(D) Example of raw data at high YFP expression (mut B, 70 min, 3 µM 1-NM-PP1). Raw YFP time-traces of 100 randomly chosen single cells are shown on the left and the same YFP time-traces, after smoothing as illustrated in **A)** , are shown on the right. Furthermore, all raw single-cell time-trace data for *HXK1* (15259 cells), *SIP18* (21242 cells), *pSIP18* mut A (18203 cells), *pSIP18* mut B (17655 cells), 1x reporter diploid (21236 cells) and 2x reporter diploid (19222 cells) is available from Dryad Digital Depository (Hansen & O'Shea, 2015).

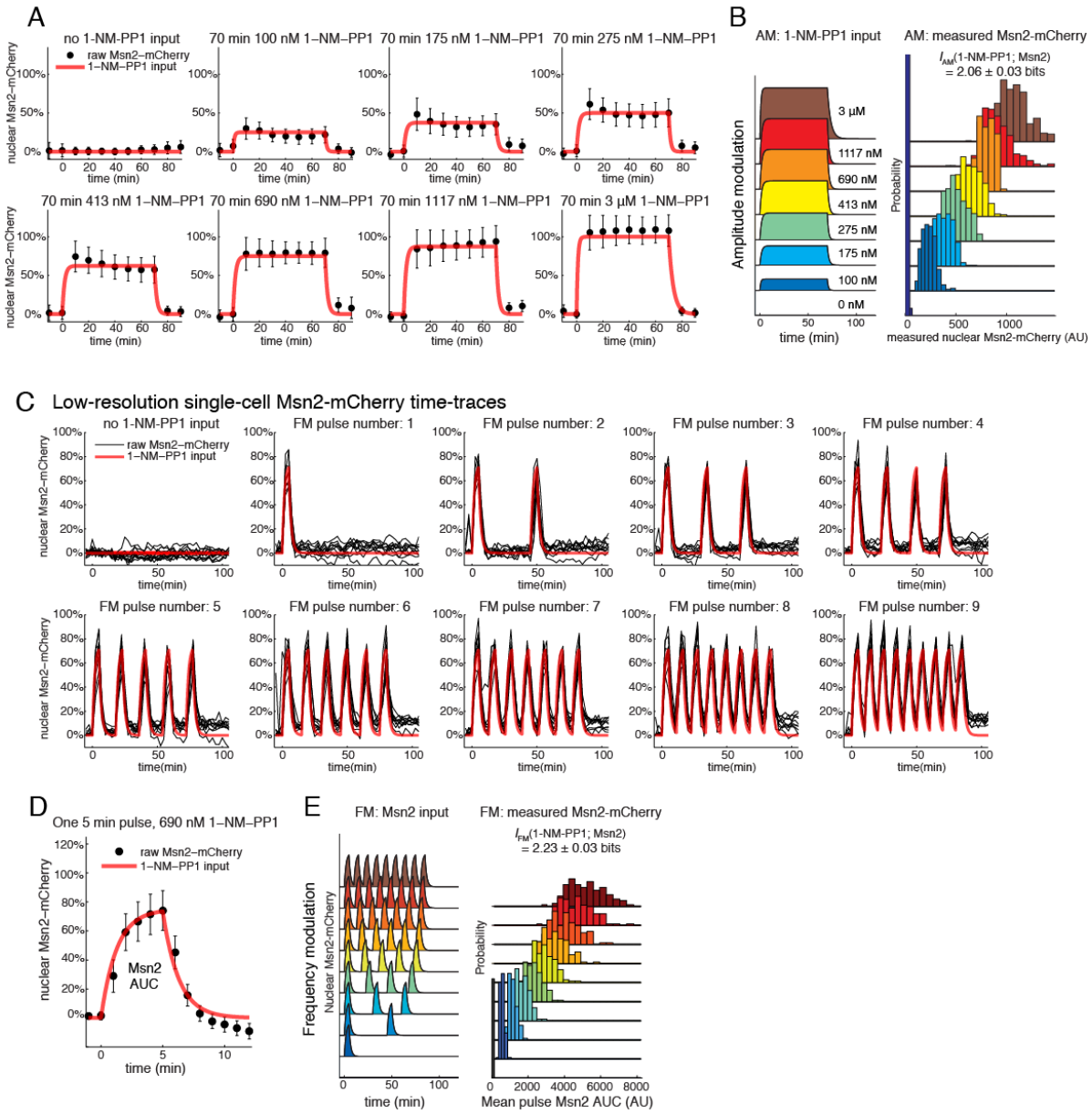

Figure B.3: *Input noise and variability in Msn2 abundance*
The figure legend for this figure is given in the main text in section B.2.1.

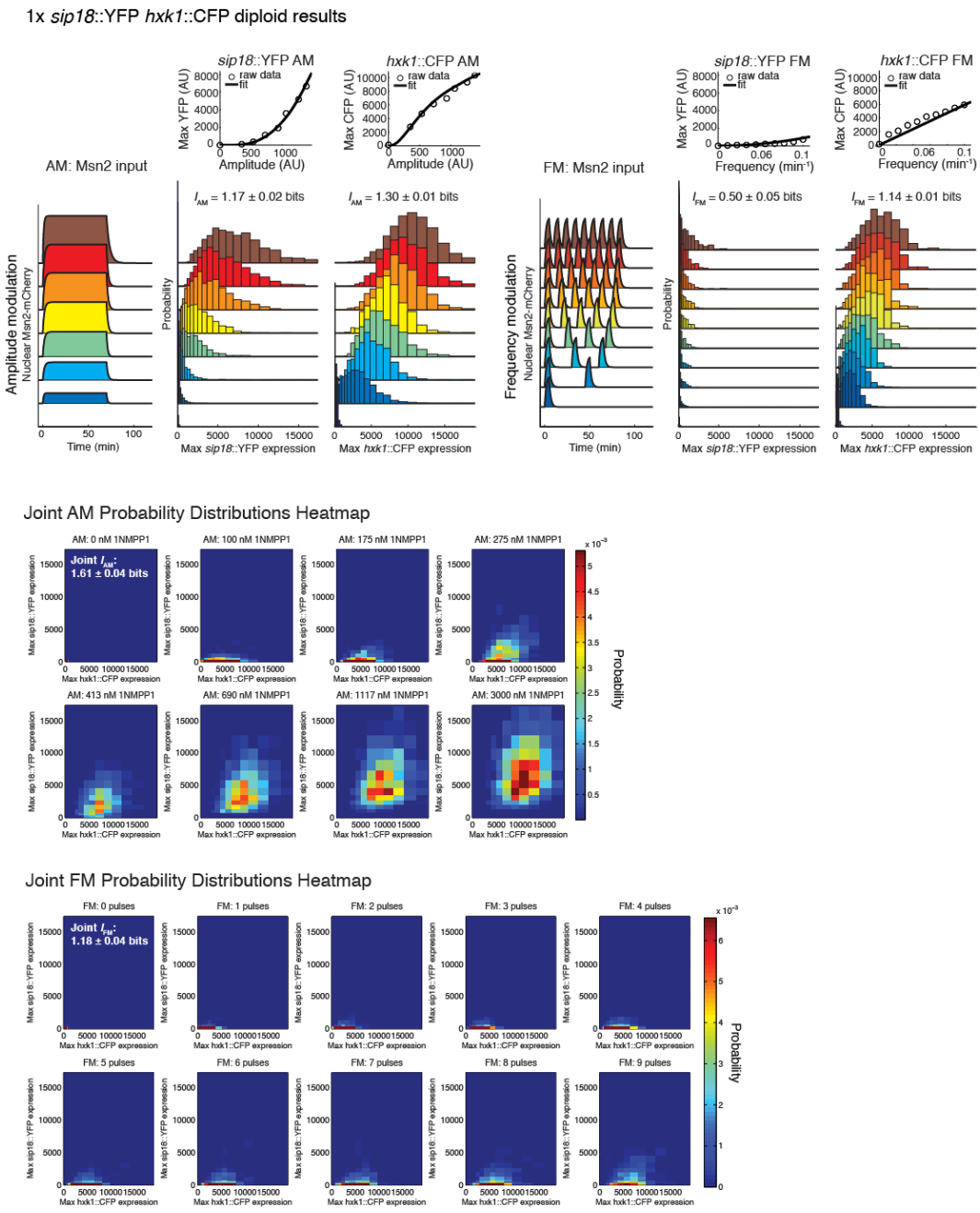

Figure B.4: *Summary of results for 1x reporter diploid*
This figure shows single and joint distribution histograms for the 1x reporter diploid (*sip18*::YFP *hxk1*::CFP).
Top panel, left: Cells containing both the *sip18*::YFP and *hxk1*::CFP reporters were exposed to either no activation or a 70-min pulse of seven increasing amplitudes from ca. 25% (100 nM 1-NM-PP1) to 100% (3 µM 1-NM-PP1) of maximal Msn2-mCherry nuclear localization and single-cell gene expression was monitored. For each single-cell time-trace, YFP expression is converted to a scalar by taking the maximal YFP value after smoothing. For each Msn2-mCherry input (a fit to the raw data is shown on the left (AM: Msn2 input)), the gene expression distribution is plotted as a histogram of the same color on the right for *HXK1* and *SIP18*. The population-averaged dose-response (top) is obtained by calculating the YFP histogram mean for each Msn2 input condition.
Top panel, right: Cells containing both the *sip18*::YFP and *hxk1*::CFP reporters were exposed to either no activation or from one to nine 5-min pulses of Msn2-mCherry nuclear localization (ca. 75% of maximal nuclear Msn2-mCherry, 690 nM 1-NM-PP1) at increasing frequency. All calculations were performed as described above.
Middle panel: The discretized joint AM distribution is shown with *sip18*::YFP on the y-axis and *hxk1*::CFP on the x-axis. The color of each bin corresponds to the probability — dark blue means unoccupied and red corresponds to the highest probability. The single-cell time-traces were converted to scalars as illustrated in Figure B.1B. Each individual subplot corresponds to a different condition (Msn2 amplitude) and the data has been binned such that the low expression bins are much smaller and therefore harder to see on the plot.
Bottom panel: Same as for the joint AM distribution in the middle panel except for the joint FM distribution. Each subplot now corresponds to a specific frequency (and thus number of pulses).

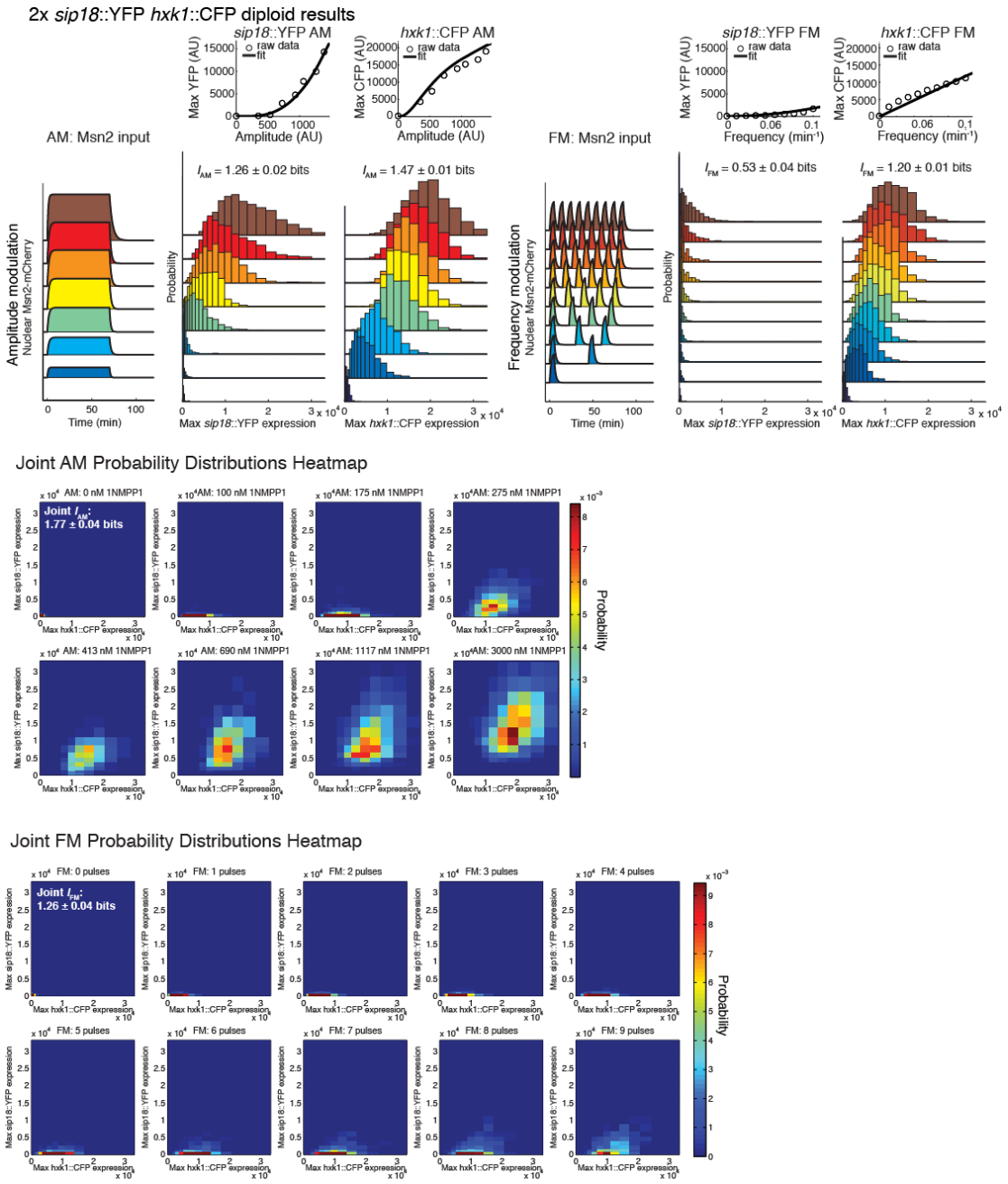

Figure B.5: *Summary of results for 2x reporter diploid*
This figure shows single and joint distribution histograms for the 2x reporter diploid (2x *sip18*::YFP 2x *hxk1*::CFP).
Top panel, left: Cells containing both the 2x *sip18*::YFP and 2x *hxk1*::CFP reporters were exposed to either no activation or a 70-min pulse of seven increasing amplitudes from ca. 25% (100 nM 1-NM-PP1) to 100% (3 μM 1-NM-PP1) of maximal Msn2-mCherry nuclear localization and single-cell gene expression monitored. For each single-cell time-trace, YFP expression is converted to a scalar by taking the maximal YFP value after smoothing. For each Msn2-mCherry input (a fit to the raw data is shown on the left (AM: Msn2 input)), the gene expression distribution is plotted as a histogram of the same color on the right for *HXK1* and *SIP18*. The population-averaged dose-response (top) is obtained by calculating the YFP histogram mean for each Msn2 input condition.
Top panel, right: Cells containing both the 2x *sip18*::YFP and 2x *hxk1*::CFP reporters were exposed to either no activation or from one to nine 5-min pulses of Msn2-mCherry nuclear localization (ca. 75% of maximal nuclear Msn2-mCherry, 690 nM 1-NM-PP1) at increasing frequency. All calculations were performed as described above.
Middle panel: The discretized joint AM distribution is shown with 2x *sip18*::YFP on the y-axis and 2x *hxk1*::CFP on the x-axis. The color of each bin corresponds to the probability — dark blue means unoccupied and red corresponds to the highest probability. The single-cell time-traces were converted to scalars as illustrated in Figure B.1B. Each individual subplot corresponds to a different condition (Msn2 amplitude) and the data has been binned such that the low expression bins are much smaller and therefore harder to see on the plot.
Bottom panel: Same as for the joint AM distribution except for the joint FM distribution. Each subplot now corresponds to a specific frequency (and thus number of pulses).

B.2 Materials and methods

B.2.1 Figure legend for Figure B.3

(A) Variability in Msn2 abundance. One source of noise in our system is non-genetic cell-to-cell variability in Msn2 abundance. Msn2 is a low-abundance protein: there are only a few hundred molecules in each cell (Ghaemmaghami *et al.*, 2003). Therefore, precisely measuring Msn2 abundance is challenging. Furthermore, the nucleus moves in and out of focus during time-lapse acquisition. To estimate the variation in Msn2 abundance, cells (pSIP18 mut B) were grown in the microfluidic device and exposed to a 70-min pulse of either 0, 100 nM, 175 nM, 275 nM, 413 nM, 690 nM, 1117 nM or 3 μM 1-NM-PP1. Msn2-mCherry nuclear localization was measured using a 5-frame z-stack series of 0, ± 1.2 μm, ± 2.4 μm above and below the focal plane using a 500 ms exposure time and imaging every 10 min. Msn2-mCherry fluorescence was corrected for photobleaching. We collected two frames before and after 1-NM-PP1 exposure to calculate the baseline level of Msn2 before 1-NM-PP1 treatment. In **(A)**, we show the mean and standard deviation for each timepoint for each concentration.

(B) To calculate mutual information between 1-NM-PP1 input and Msn2-mCherry dynamics, we use the data from **(A)** and calculate $I_{\mathrm{AM}}(1-NM-PP1;Msn2) = 2.06 \pm 0.03$ bits. We quantify Msn2-mCherry localization in absolute units as the mean nuclear Msn2 level across the seven measurements while Msn2 is nuclear — this also corresponds to the total time-integrated nuclear level of Msn2 (Msn2 'Area Under the Curve' or AUC). In total, we measured 2996 single cells. Using Msn2 variability in response to 3 μM 1-NM-PP1, we estimate the cell-to-cell variability of Msn2 to be CV∼15%. However, given measurement noise we stress that CV∼15% and $I \sim 2.06$ bits are likely over- and underestimates, respec-

tively. Note that Msn2 is a low abundance protein (Ghaemmaghami *et al.*, 2003). Previous proteomic studies showed that essentially no yeast proteins have CV¡10% (Newman *et al.*, 2006). Therefore, Msn2 is among the least variable low abundance proteins in yeast.

(C) This figure is plotted using data from Figure 3.2 for *HXK1*. In red is shown the input and in black are shown traces from 10 representative single cells. We did not do a finely spaced z-stack series for this experiment, which is necessary to accurately quantify the concentration of Msn2 in the nucleus — this causes too much photobleaching to be compatible with imaging at reasonable temporal resolution (2.5 min here). Nonetheless, as can be seen, the black traces faithfully track the input with limited noise. For each cell plotted above, we also measured *hxk1*::CFP and *hxk1*::YFP gene expression.

(D) To accurately quantify Msn2-mCherry dynamics during FM input, we acquired a finely spaced z-stack series at high time-resolution (1 min). This causes too high photobleaching to be compatible with sustained time-lapse imaging. Therefore, we are only able to collect data at this resolution for a single 5-min pulse. The mean (black dots) and standard deviation (error bars) for 132 single cells (*pSIP18* mut B) is shown. As can be seen, Msn2-mCherry accurately tracks the microfluidic 1-NM-PP1 input with limited noise also during FM input. In a population of cells, Msn2 translocates to the nucleus in every single cell during 1-NM-PP1 exposure.

(F) To calculate mutual information between 1-NM-PP1 input and Msn2-mCherry dynamics, we use the data from **(D)** and estimate $I_{\mathrm{FM}}(1-NM-PP1; Msn2) = 2.23 \pm 0.03$ bits. Given measurement noise, this is likely an underestimate. We quantify Msn2-mCherry localization in absolute units as the total nuclear Msn2 level across the ten measurements while Msn2 is nuclear (five during the pulse, five after the pulse) — this also corresponds to the total time-integrated nuclear level of Msn2 (Msn2 'Area Under the Curve' or AUC).

With data from **(D)**, we measure the distribution of cell-to-cell variability for a single 5-min pulse. To calculate $I_{\mathrm{FM}}(1-NM-PP1; Msn2)$, we then extrapolate by multiplying the AUC probability distribution by the pulse number of each experiment since Msn2 tracks the 1-NM-PP1 input as faithfully for the first pulse as for the subsequent pulses. Ideally, one would measure the Msn2 AUC at 1-min time resolution and with finely spaced z-stacks throughout the entire time-lapse experiment, but this is not technically possible due to photobleaching.

B.2.2 Strain construction

All strains used in this study are listed in Table B.1. The diploid strains containing fluorescent reporters for the *SIP18* (ASH94/EY2813) and *HXK1* (ASH91/EY2810) promoters have been described previously (Hansen & O'Shea, 2013; Chapter 2). These and all other *Saccharomyces cerevisiae strains* used in this study are from an ADE^{+} strain in the W303 background ($MAT\mathbf{a}$ (EY0690) and $MAT\boldsymbol{\alpha}$ (EY0691) *trp1 leu2 ura3 his3 can1* GAL^{+} psi^{+}). Standard methods for growing and genetically manipulating yeast was used throughout this study and all manipulations were performed in the same manner in both haploid mating types unless otherwise stated. Mating was performed by mixing haploids and selecting for diploids on SD -TRP -LEU plates. All genetic manipulations were verified by PCR.

To generate the *pSIP18* promoter mutants, the relevant segment of the promoter was replaced by *URA3* and followed by replacing the *URA3* fragment with a PCR generated fragment containing the relevant mutations and counter-selection against *URA3*. The full sequence of the wild-type *SIP18* promoter and the mutant promoters are listed below.

>> wt *SIP18* promoter
GCTCACTTTTTGTTGGTCTGTATTCATTCTGGATGTCTTGGTTGTAGAAATTTCTTTTATTG
GTTCATTAAAGTCAAGGTAAATGGCGAGAACTAGAATAGAGTTTTATTCTTTTTACCGTTAT
ATAGATAATTCTAGCCGGGGGCGGTCG**CCCCT**GAGATTCCCGACATCAGTAAGACATAGTAC

TGTACGATTACTGTACGATTAATCTATCCACTTCAGATGTTCAACAATTCCTTTTGGCATTA
CGTATTAATACTTCATAGGATCGGCACCCTCCCTTAAGCCT**CCCCT**AAATGCTTTCGGTA**CC**
CCTTTAAGACAACTATCTCTTAACCTTCTGTATTTACTTGCATGTTACGTTGAGTCTCATTG
GAGGTTTGCATCATATGTTTAGGTTTTTTTGGAAACGTGGACGGCTCATAGTGATTGGTAAA
TGGGAGTTACGAATAAACGTATCTTAAAGGGAGCGGTATGTAAAATGGATAGATGATCATGA
ATACAGTACGAGGTGTAAAGAATGATGGGACTGAGAGGGCAATTATCATCCCTCAGAATCAA
CATCACAAACATATATAAAGCTCCCAATTCTGCCCCAAAGTTTTGTCCCTAGGCATTTTTAA
TCTTTGTATCTGTGCTCTTTACTTTAGTAGAAAGGTATATAAAAAAGTATAGTCAAG

>> *pSIP18* mut A promoter
GCTCACTTTTTGTTGGTCTGTATTCATTCTGGATGTCTTGGTTGTAGAAATTTCTTTTATTG
GTTCATTAAAGTCAAGGTAAATGGCGAGAACTAGAATAGAGTTTTATTCTTTTTACCGTTAT
ATAGATAATTCTAGCCGGGGGCGGTCG**CCCCT**GAGATTCCCGACATCAGTAAGACATAGTAC
TGTACGATTACTGTACGATTAATCTATCCACTTCAGATGTTCAACAATTCCTTTTGGCATTA
CGTATTAATACTTCATAGGATCGGCACCCTCCCTTAAGCCTCAACTAAATGCTTTCGGTA*CA*
*ACT*TTAAGA*CAACT*ATCTCTTAACCTTCTGTATTTACTTGCATGTTACGTTGAGTCTCATTG
GAGGTTTGCATCATATGTTTAGGTTTTTTTGGAAACGTGGACGGCTCATAGTGATTGGTAAA
TGGGAGTTA**CCCCT**AAACGTATCTTAAAGGGA**CCCCT**ATGTAAAATGGATAG**CCCCT**CATGA
ATACAGTACGAGGTGTAAAGAATGATGGGACTGAGAGGGCAATTATCATCCCTCAGAATCAA
CATCACAAACATATATAAAGCTCCCAATTCTGCCCCAAAGTTTTGTCCCTAGGCATTTTTAA
TCTTTGTATCTGTGCTCTTTACTTTAGTAGAAAGGTATATAAAAAAGTATAGTCAAG

>> *pSIP18* mut B promoter
GCTCACTTTTTGTTGGTCTGTATTCATTCTGGATGTCTTGGTTGTAGAAATTTCTTTTATTG
GTTCATTAAAGTCAAGGTAAATGGCGAGAACTAGAATAGAGTTTTATTCTTTTTACCGTTAT
ATAGATAATTCTAGCCGGGGGCGGTCG**CCCCT**GAGATTCCCGACATCAGTAAGACATAGTAC
TGTACGATTACTGTACGATTAATCTATCCACTTCAGATGTTCAACAATTCCTTTTGGCATTA
CGTATTAATACTTCATAGGATCGGCACCCTCCCTTAAGCCTCAACTAAATGCTTTCGGTA*CA*
*ACT*TTAAGA*CAACT*ATCTCTTAACCTTCTGTATTTACTTGCATGTTACGTTGAGTCTCATTG
GAGGTTTGCATCATATGTTTAGGTTTTTTTGGAAACGTGGACGGCTCATAGTGA**CCCCT**AAA
TGGGAGTTA**CCCCT**AAACGTATCTTAAAGGGA**CCCCT**ATGTAAAATGGATAG**CCCCT**CATGA
ATACAGTACGAGGTGTAAAGAATGATGGGACTGAGAGGGCAATTATCATCCCTCAGAATCAA
CATCACAAACATATATAAAGCTCCCAATTCTGCCCCAAAGTTTTGTCCCTAGGCATTTTTAA
TCTTTGTATCTGTGCTCTTTACTTTAGTAGAAAGGTATATAAAAAAGTATAGTCAAG

To remove the Msn2 binding site (STRE 5'-CCCCT-3'), the two central Cs were replaced by As (5'-CCCCT-3' $\rightarrow$ 5'-CAACT-3'), as shown in underlined italic text in the above sequences. The most upstream site in the SIP18 promoter appears to be non-functional — deleting it has no effect on gene induction. Conversely, the two sites between -350 and -400 nt appear to be solely responsible for gene induction — deletion of both sites completely

abolishes gene induction.

Mut A and Mut B have 3 and 4 new STRE sites, respectively, instead of the 2 STREs in the WT promoter. The position was chosen to be closer to the transcription start site, but in the largely nucleosome free region between two nucleosomes (Figure B.1C).

The same manipulations were performed in both mating types and all microscopy experiments were conducted in diploid strains (Mut A: EY2969/ASH191; Mut B: EY2967/ASH189).

To generate the 1x and 2x reporter diploid strains (1x: EY2972/ASH194; 2x: EY2975 /ASH197), strain EY2811/ASH92 (*MAT***a** *sip18*::mCitrineV163A-HIS) and strain EY2809 /ASH90 (*MAT*$\boldsymbol{\alpha}$ *hxk1*::SCFP3A-HIS) were used as base strains.

In EY2811, the *HXK1* ORF was replaced by *URA3* to generate EY2970/ASH192, which was used for the 1x reporter diploid, and *URA3* further replaced by a PCR fragment containing SCFP3A followed by the *ADH1* terminator and the *spHIS5* selection marker (from a pKT vector) using counter-selection against *URA3*. This gave strain EY2973/ASH195, which was used for the 2x reporter diploid.

Likewise, in EY2811 the *SIP18* ORF was replaced by *URA3* to generate EY2971/ASH193, which was used for the 1x reporter diploid, and *URA3* further replaced by a PCR fragment containing mCitrineV163A followed by the *ADH1* terminator and the *spHIS5* selection marker (from a pKT vector) using counter-selection against *URA3*. This gave strain EY2974/ASH196, which was used for the 2x reporter diploid.

Furthermore, the 1x reporter diploid (EY2972/ASH194) was generated by mating EY2970 /ASH192 and EY2971/ASH193 and the 2x reporter diploid (EY2975/ASH197) generated by mating EY2973/ASH195 and EY2974/ASH196. In the 1x reporter diploid, no WT copies of the *SIP18* and *HXK1* genes are present to ensure that, in the case the encoded protein product could have an autoregulatory effect, this complication would be avoided.

Finally, we note that 1-NM-PP1 mediated gene induction of *HXK1* and *SIP18* is specific to Msn2. In an *msn2*Δ-deletion strain, neither *HXK1* nor *SIP18* are induced by 1-NM-PP1 (Hansen & O'Shea, 2013) and both promoters have been shown to directly bind Msn2 in ChIP experiments (Elfving *et al.*, 2014; Huebert *et al.*, 2012).

All strains are available upon request and all strains are derived from EY0690 and EY0691. A list of the strains is given in table B.1.

Table B.1: List of strains for Chapter 3.

Strain	**Type**	**Strain genotype**
EY0690	*MAT***a**	W303 *trp1 leu2 ura3 his3 can1 GAL*$^{+}$ *psi*$^{+}$ (not generated in this study)
EY0691	*MAT*$\boldsymbol{\alpha}$	W303 *trp1 leu2 ura3 his3 can1 GAL*$^{+}$ *psi*$^{+}$ (not generated in this study)
EY2811/	*MAT***a**	*TPK1*^{M164G} *TPK2*^{M147G} *TPK3*^{M165G} *msn4*Δ::TRP1 *MSN2*-mCherry
ASH89		NHP6a-iRFP::KAN *hxk1*::mCitrineV163A-spHIS5 (not generated in this study)
EY2812/	*MAT*$\boldsymbol{\alpha}$	*TPK1*^{M164G} *TPK2*^{M147G} *TPK3*^{M165G} *msn4*Δ::LEU2 *MSN2*-mCherry
ASH90		NHP6a-iRFP::KAN *hxk1*::SCFP3A-spHIS5 (not generated in this study)
EY2813/	diploid	*TPK1*^{M164G} *TPK2*^{M147G} *TPK3*^{M165G} *msn4*Δ::TRP1/LEU2 *MSN2*-mCherry
ASH91		NHP6a-iRFP::KAN *hxk1*::mCitrineV163A/SCFP3a-spHIS5 (not generated in this study)
EY2811/	*MAT***a**	*TPK1*^{M164G} *TPK2*^{M147G} *TPK3*^{M165G} *msn4*Δ::TRP1 *MSN2*-mCherry
ASH92		NHP6a-iRFP::KAN *sip18*::mCitrineV163A-spHIS5 (not generated in this study)
EY2812/	*MAT*$\boldsymbol{\alpha}$	*TPK1*^{M164G} *TPK2*^{M147G} *TPK3*^{M165G} *msn4*Δ::LEU2 *MSN2*-mCherry
ASH93		NHP6a-iRFP::KAN *sip18*::SCFP3A-spHIS5 (not generated in this study)
EY2813/	diploid	*TPK1*^{M164G} *TPK2*^{M147G} *TPK3*^{M165G} *msn4*Δ::TRP1/LEU2 *MSN2*-mCherry
ASH94		NHP6a-iRFP::KAN *sip18*::mCitrineV163A/SCFP3a-spHIS5 (not generated in this study)
EY2964/	*MAT***a**	*TPK1*^{M164G} *TPK2*^{M147G} *TPK3*^{M165G} *msn4*Δ::TRP1 *MSN2*-mCherry
ASH139		NHP6a-iRFP::KAN *sip18*::mCitrineV163A-spHIS5 *pSIP18* mut A 3 STREs
EY2965/	*MAT***a**	*TPK1*^{M164G} *TPK2*^{M147G} *TPK3*^{M165G} *msn4*Δ::TRP1 *MSN2*-mCherry
ASH140		NHP6a-iRFP::KAN *sip18*::mCitrineV163A-spHIS5 *pSIP18* mut B 4 STREs
EY2966/	*MAT*$\boldsymbol{\alpha}$	*TPK1*^{M164G} *TPK2*^{M147G} *TPK3*^{M165G} *msn4*Δ::LEU2 *MSN2*-mCherry
ASH188		NHP6a-iRFP::KAN *sip18*::SCFP3A-spHIS5 *pSIP18* mut B 4 STREs
EY2967/	diploid	*TPK1*^{M164G} *TPK2*^{M147G} *TPK3*^{M165G} *msn4*Δ::TRP1/LEU2 *MSN2*-mCherry
ASH189		NHP6a-iRFP::KAN *sip18*::mCitrineV163A/SCFP3a-spHIS5 *pSIP18* mut B 4 STREs
EY2968/	*MAT*$\boldsymbol{\alpha}$	*TPK1*^{M164G} *TPK2*^{M147G} *TPK3*^{M165G} *msn4*Δ::LEU2 *MSN2*-mCherry
ASH190		NHP6a-iRFP::KAN *sip18*::SCFP3A-spHIS5 *pSIP18* mut A 3 STREs
EY2969/	diploid	*TPK1*^{M164G} *TPK2*^{M147G} *TPK3*^{M165G} *msn4*Δ::TRP1/LEU2 *MSN2*-mCherry
ASH191		NHP6a-iRFP::KAN *sip18*::mCitrineV163A/SCFP3a-spHIS5 *pSIP18* mut A 3 STREs
EY2970/	*MAT***a**	*TPK1*^{M164G} *TPK2*^{M147G} *TPK3*^{M165G} *msn4*Δ::TRP1 *MSN2*-mCherry
ASH192		NHP6a-iRFP::KAN *sip18*::mCitrineV163A-spHIS5 *hxk1*::URA3
EY2971/	*MAT*$\boldsymbol{\alpha}$	*TPK1*^{M164G} *TPK2*^{M147G} *TPK3*^{M165G} *msn4*Δ::LEU2 *MSN2*-mCherry
ASH193		NHP6a-iRFP::KAN *hxk1*::SCFP3A-spHIS5 *sip18*::URA3
EY2972/	diploid	*TPK1*^{M164G} *TPK2*^{M147G} *TPK3*^{M165G} *msn4*Δ::TRP1/LEU2 *MSN2*-mCherry NHP6a-iRFP::KAN
ASH194		*sip18*::mCitrineV163A-spHIS5 *hxk1*::URA3 / *hxk1*::SCFP3A-spHIS5 *sip18*::URA3 (1x diploid)
EY2973/	*MAT***a**	*TPK1*^{M164G} *TPK2*^{M147G} *TPK3*^{M165G} *msn4*Δ::TRP1 *MSN2*-mCherry
ASH195		NHP6a-iRFP::KAN *sip18*::mCitrineV163A-spHIS5 *hxk1*::SCFP3A-spHIS5
EY2974/	*MAT*$\boldsymbol{\alpha}$	*TPK1*^{M164G} *TPK2*^{M147G} *TPK3*^{M165G} *msn4*Δ::LEU2 *MSN2*-mCherry

ASH196		NHP6a-iRFP::KAN *hxk1*::SCFP3A-spHIS5 *sip18*::mCitrineV163A-spHIS5
EY2975/	diploid	*TPK1*^{M164G} *TPK2*^{M147G} *TPK3*^{M165G} *msn4*Δ::TRP1/LEU2 *MSN2*-mCherry
ASH197		NHP6a-iRFP::KAN **2x** *sip18*::mCitrineV163A-spHIS5 **2x** *hxk1*::SCFP3A-spHIS5 (2x diploid)

B.2.3 Microfluidic modulation of Msn2 dynamics

Each of the five electrovalves independently control whether normal medium or medium with 1-NM-PP1 is delivered to each of the five microfluidic channels where the cells are grown. The channels are controlled using custom-written MATLAB software (available upon request), which allows the valves to be switched within milliseconds. Due to dead volume, it takes a few seconds to wash out the previous medium after valve switching. It took 27 s to image two fields-of-view in each channel, so the 1-NM-PP1 delivery program, which was synchronized with the time-lapse acquisition software (AxioVision), incorporates this delay.

For the amplitude modulation experiments, 1-NM-PP1 was added to each channel for 70 min at the following concentrations: 100 nM, 175 nM, 275 nM, 413 nM, 690 nM, 1117 nM, 3 μM. For the frequency modulation experiments a concentration of 690 nM 1-NM-PP1 was used together with the following pulse sequences: one 5-min pulse; two 5-min pulses separated by a 40-min interval; three 5-min pulses separated by 25-min intervals; four 5-min pulses separated by 17.5-min intervals; five 5-min pulses separated by 13-min intervals; six 5-min pulses separated by 10-min intervals; seven 5-min pulses separated by 7.86-min intervals; eight 5-min pulses separated by 6.25-min intervals; nine 5-min pulses separated by 5-min intervals.

B.2.4 Measurement noise and data processing

Measurement noise is a major concern for information theoretical calculations and can lead to underestimates of mutual information. To control and minimize effects of noise, the

following data processing pipeline was employed. For each single-cell, a time-trace of 64 YFP measurements is made (2.5 min interval). As can be seen in Figure B.1B and Figure B.2 from the single-cell YFP traces, YFP generally reaches a plateau around or after the 100 min time-point (element 43 in the YFP vector). So the maximal YFP level in the cell is measured approximately 20 times before the experiment ends (element 64 in the YFP vector). Although there is slight noise in each measurement of the YFP level as shown in Figure B.2A (black circles), because YFP is independently measured ∼20 times after it has reached a plateau, the actual YFP level can accurately be determined by smoothing (Figure B.2A, red line). The YFP trace is smoothed using an 11-point moving average filter and the vector is subsequently converted to a scalar by taking the maximal YFP value in the [33;64] range of elements. The scalar YFP value (Figure B.1B) is used for all information theoretical calculations.

As illustrated in Figure B.2A-D, measurement noise makes a bigger contribution at very low YFP expression levels (Figure B.2A-B), but is negligible at high YFP expression (Figure B.2A, D). The following factors, among others, contribute to measurement noise: microscope focusing — each time-point, the microscope must return to the same exact focal plane, which does not always happen; cellular autofluorescence — the cell is naturally autofluorescent, especially in the cyan region, and this autofluorescence background can fluctuate and is difficult to precisely subtract at very low expression levels; instrumentation variability — e.g. noise coming from the EM-CCD camera or the LED excitation source; day-to-day experimental variability — e.g. from slight differences in how a protocol was carried out; automated image analysis — the image segmentation algorithm is very conservative, but slight errors in cell segmentation are occasionally observed.

Nonetheless, the overall measurement noise is very low.

B.2.5 Supplementary source data

Raw single-cell time-trace data for *HXK1* (15259 cells), *SIP18* (21242 cells), *pSIP18* mut A (18203 cells), *pSIP18* mut B (17655 cells), 1x reporter diploid (21236 cells) and 2x reporter diploid (19222 cells) is available online at Dryad Digital repository (Hansen & O'Shea, 2015) as a zip-compressed folder containing data in the CSV format. There is a READ ME file together with the source data explaining the format.

B.3 References

Bishop, A.C., Ubersax, J.A., Petsch, D.T., Matheos, D.P., Gray, N.S., Blethrow, J., Shimizu, E., Tsien, J.Z., Schultz, P.G., Rose, M.D., *et al.* (2000). A chemical switch for inhibitor-sensitive alleles of any protein kinase. *Nature* **407**: 395-401.

Elfving, N., Chereji, R.V., Bharatula, V., Bjorklund, S., Morozov, A.V., & Broach, J.R. (2014). A dynamic interplay of nucleosome and Msn2 binding regulates kinetics of gene activation and repression following stress. *Nucleic Acids Res* **42**: 5468-5482.

Filonov, G.S., Piatkevich, K.D., Ting, L.M., Zhang, J.H., Kim, K., & Verkhusha, V.V. (2011). Bright and stable near-infrared fluorescent protein for in vivo imaging. *Nat Biotechnol* **29**: 757-U133.

Hansen, A.S., & O'Shea, E.K. (2013). Promoter decoding of transcription factor dynamics involves a trade-off between noise and control of gene expression. *Molecular Systems Biology* **9**.

Hansen, A.S., & O'Shea, E.K. (2015). Data from: Limits on information transduction through regulation of signaling dynamics. Dryad Digital Repository.

Hao, N., Budnik, B.A., Gunawardena, J., & O'Shea, E.K. (2013). Tunable Signal Processing Through Modular Control of Transcription Factor Translocation. *Science* **339**: 460-464.

Hao, N., & O'Shea, E.K. (2012). Signal-dependent dynamics of transcription factor translocation controls gene expression. *Nat Struct Mol Biol* **19**: 31-39.

Hersen, P., McClean, M.N., Mahadevan, L., & Ramanathan, S. (2008). Signal processing by the HOG MAP kinase pathway. *P Natl Acad Sci USA* **105**: 7165-7170.

Huebert, D.J., Kuan, P.F., Keles, S., & Gasch, A.P. (2012). Dynamic Changes in Nucleosome Occupancy Are Not Predictive of Gene Expression Dynamics but Are Linked to Transcription and Chromatin Regulators. *Mol Cell Biol* **32**: 1645-1653.

Kremers, G.J., Goedhart, J., van Munster, E.B., & Gadella, T.W.J. (2006). Cyan and yellow super fluorescent proteins with improved brightness, protein folding, and FRET Forster radius. *Biochemistry* **45**: 6570-6580.

Zaman, S., Lippman, S.I., Schneper, L., Slonim, N., & Broach, J.R. (2009). Glucose regulates transcription in yeast through a network of signaling pathways. *Mol Syst Biol* **5**.

Appendix C

Supplementary theory for Chapter 3

C.1 Introduction

In this document, we describe in detail how all information theoretical calculations are performed. In Section C.2, we define mutual information and explain how it is computed with empirical data and adjusted for bias. In Section C.3, we describe how joint mutual information, in the case where we consider two reporters, is computed. In Section C.4, we describe the algorithm we use to estimate the intrinsic mutual information. We also go through the steps used to test and verify the algorithm *in silico*. Finally, Section C.5 contains references.

C.2 Mutual information for a single reporter

C.2.1 Shannon entropy and mutual information for a single reporter

We consider the transcription factor (TF) input - gene expression output relationship for a dose-response type relationship. E.g. we consider the YFP gene expression response to different amplitudes or frequencies of TF input in single cells. For each cell we quantify the YFP gene expression response as a scalar and then bin the responses into appropriately sized bins such that we have a discrete probability distribution (Response output) for each TF input (Signal).

Considering all signals (all TF inputs), we can calculate the total Shannon entropy (H) of the responses (R) by summing over all bins i:

$$H(R) = -\sum_i P(R_i) \log_2(R_i) \tag{C.1}$$

Next, to proceed towards defining mutual information, we compute the conditional entropy of the YFP response given the signal

$$H(R|S) = -\sum_j P(S = s_j) \left(\sum_i P(R = r_i|S = s_j) \log_2 (P(R = r_i|S = s_j)) \right) \tag{C.2}$$

Then finally, mutual information in bits is given by:

$$MI(R;S) = H(R) - H(R|S) \tag{C.3}$$

C.2.2 Maximal mutual information for a single reporter

The mutual information is a function of the signal distribution, $P(S)$. To determine the maximal mutual information, $I(R;S)$, we need to find the signal distribution, $P(S)$,

that maximizes the mutual information, $MI(R;S)$. In other words, the maximal mutual information, I, is defined as:

$$I(R;S) = \max_{P(S)} [MI(R;S)] \quad \text{for} \quad \sum_i P(S_i) = 1; \quad P(S_i) \geq 0 \tag{C.4}$$

This is an optimization problem and $P(S)$ can be numerically determined such that the maximal mutual information, $I(R;S) = \max_{P(S)} [MI(R;S)]$, is obtained using the iterative Blahut-Arimoto algorithm (Blahut, 1972; Arimoto, 1972). The maximal mutual information can be thought of as the information capacity and is the upper bound on mutual information.

C.2.3 Computing mutual information with empirical data

To calculate the maximal mutual information for individual promoters with respect to amplitude or frequency modulation, we must first discretize the data. For each promoter we obtain single-cell time-lapse responses to each signal input (e.g. amplitude of Msn2 or frequency of Msn2). To convert the single-cell time-series into a scalar, we smooth the YFP time-series using moving-average smoothing to minimize the effect of technical noise. All single-reporter analysis uses YFP reporter expression rather than CFP reporter expression, since YFP suffers from lower technical noise. Following smoothing, the maximal YFP value for each single cell is used for calculating mutual information. Thus, the time-series is converted into a scalar.

Calculations of maximal mutual information, I, using discretized data are biased by binning and undersampling (Cheong *et al,* 2011). However, for each promoter we are able to obtain ∼15,000-20,000 single cell responses yielding on average more than 1,000 single cell responses per condition. Thus, for the single-reporter calculations we are far away from the seriously undersampled regime. Likewise, binning can introduce bias (Figure C.1). If the data is binned too coarsely, differences in the single cell responses are no longer adequately

captured and the estimated I is an underestimate. Conversely, if the data is binned into so many bins that there are not enough cells to accurately estimate the probability density of each response bin, undersampling becomes important and the estimated I is an overestimate.

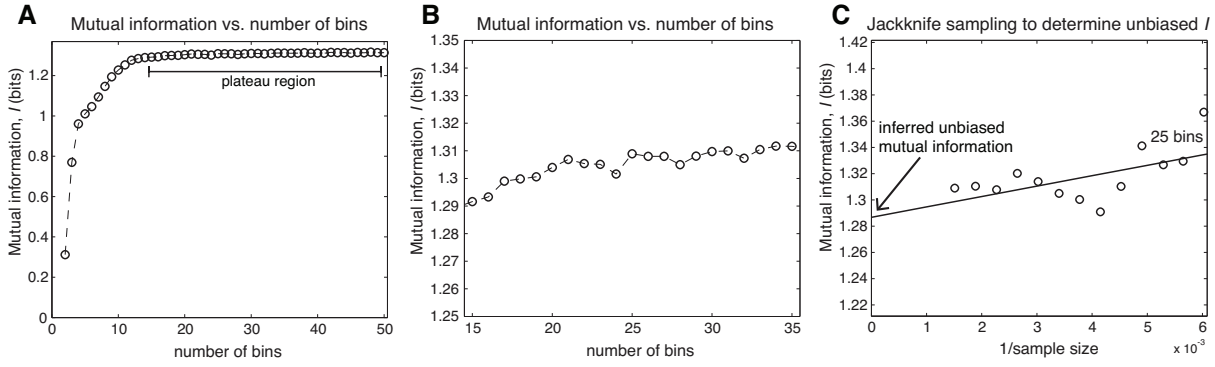

Figure C.1: *Correcting I for bias*
A) Using *HXK1* I_{AM} as an example, how I scales with the number of bins is plotted. After around 12-14 bins, a plateau region is reached.
B) A zoom-in plot of **A)** from 15 to 35 bins.
C) An illustration of how jackknife sampling is used to correct for undersampling and infer an unbiased I.

Methods are available to deal with both the issue of binning and undersampling. Here we largely follow the approach used previously by Cheong, Levchenko and co-workers (Cheong *et al,* 2011) and also described by Bialek and co-workers (Strong *et al,* 1998; Slonim *et al,* 2005). This method is also known as the "direct method". To determine the optimal number of bins, we plot I as a function of the number of bins (Figure C.1). As shown in Figure C.1A, below 10 bins the binning is so coarse that substantial information is lost and I is a serious underestimate. After around 12-14 bins, I reaches a plateau. I should be calculated in the plateau region (Cheong *et al,* 2011; Slonim *et al,* 2005). For all single reporter calculations of I, we follow the approach of Cheong *et al.* and report I_{AM} and I_{FM} for a promoter as the mean I calculated using 15 to 35 bins (the region shown in Figure C.1B), inclusive, and the error in the I estimate as the standard deviation using 15 to 35 bins, inclusive. The only exception is *SIP18* where we used 15 to 25 bins, inclusive.

To correct for undersampling, we consider a series expansion of I in terms of inverse

powers of sample size, N, (Cheong *et al,* 2011):

$$I_{\text{biased}} = I_{\text{unbiased}} + \frac{k_1}{N} + \frac{k_2}{N^2} + ... \approx I_{\text{unbiased}} + \frac{k_1}{N} \tag{C.5}$$

where I_{unbiased} is the desired maximal mutual information corrected for undersampling, N is the number of cells per condition (sample size) and k_i are coefficients. Since we have on average around or above 1000 cells per conditions, we can ignore all terms of second order and higher and I_{unbiased} is therefore approximately a linear function of the inverse sample size. We estimate the linear function in equation (C.5) using jackknife sampling as has been done previously (Cheong *et al,* 2011). We sampled fractions of the data ranging from 100% to 25% without replacement and computed I in each case by optimizing $P(S)$ using the Blahut-Arimoto algorithm to obtain the maximal mutual information. Figure C.1C shows an example using *HXK1* data and 25 bins. As is evident, even with 25 bins, we have so many single cell responses that undersampling is minimal and the difference between I_{unbiased} and I_{biased} is only ~ 0.02 bits.

As mentioned above, to determine I_{AM} and I_{FM} of individual promoters we perform jackknife sampling to estimate C_{unbiased} using 15 to 35 bins, inclusive, and report I as the mean and the error as the standard deviation. In the case of *SIP18* and *HXK1*, we can also estimate the error in our measurement by comparing I_{AM} and I_{FM} obtained in the *sip18*::YFP/*sip18*::CFP and *hxk1*::YFP/*hxk1*::CFP strains with I_{AM} and I_{FM} obtained from the 1x *sip18*::YFP/*hxk1*::CFP strain:

Here AM refers to the maximal mutual information with respect to amplitude modulation and FM refers to the maximal mutual information with respect to frequency modulation. As is evident from the table C.1, the estimates of I_{AM} and I_{FM} between strains are very similar. We note that these are different yeast strains in slightly different genetic backgrounds. Thus, the fact that the *SIP18* and *HXK1* I_{AM} and I_{FM} values have such low estimated errors and

Table C.1: I_{AM} and I_{FM} for *SIP18* and *HXK1*

I	*gene*::YFP/*gene*::CFP strain	1x *sip18*::YFP/*hxk1*::CFP strain
$I_{\mathrm{AM}}(sip18\text{::YFP}; S)$	1.21 ± 0.03 bits	1.17 ± 0.02 bits
$I_{\mathrm{FM}}(sip18\text{::YFP}; S)$	0.52 ± 0.06 bits	0.50 ± 0.05 bits
$I_{\mathrm{AM}}(hxk1\text{::CFP/YFP}; S)$	1.30 ± 0.01 bits	1.30 ± 0.01 bits
$I_{\mathrm{FM}}(hxk1\text{::CFP/YFP}; S)$	1.11 ± 0.01 bits	1.14 ± 0.01 bits

agree so well between different yeast strains in different genetic backgrounds measured during independent experiments, gives us high confidence in the measurements. Further, this shows that measurements of I for natural genes are robust between different clones and robust to slight variation in genetic background.

C.2.4 Comments on how to interpret maximal mutual information

Information theory was developed by Claude Shannon as a mathematical theory of communication to quantify information transmission for engineering applications (Shannon, 1948; Cover & Thomas, 2006). Accordingly, the concept of a channel capacity was originally introduced for a discrete, memoryless channel and is precisely defined in information theory. Here we consider the TF input - YFP output relationship as a noisy channel in the sense that each individual input is converted to a noisy distribution of YFP output. This TF-YFP channel differs from the discrete memoryless channel considered by Shannon in several important ways (Bowsher & Swain, 2014). For example, the TF-YFP channel is a single-use channel, whereas a communication channel is used repeatedly. In fact, one of the central results in information theory, the noisy-channel coding theorem, applies only to repeated use and states that all rates, R, (e.g. in bits per second) below channel capacity, C, are achievable. Thus, the noisy channel coding theorem and other theorems in information theory do not hold in our case. Furthermore, as is clear from equation (C.3), the mutual information

depends on $P(S)$, the distribution of signals or inputs. While in engineering applications the distribution of inputs that maximizes the mutual information can conceivably be chosen by the user, in the case of a cell responding to environmental perturbations like stress or changes in hormone or growth factor levels, $P(S)$ is presumably experienced rather than chosen by the cell.

Thus, while the channel capacity, C, is defined as the maximal mutual information, we refer to the quantity as maximal mutual information or I in this study. I still provides an upper bound on the maximal mutual information transmissible and should be interpreted as such. We choose not to refer to it as mutual information, because mutual information has a $P(S)$-dependence. Similarly, we choose not to refer to it as channel capacity because channel capacity has a precise definition in the context of engineering applications that does not, strictly speaking, apply in cellular signaling.

Furthermore, Shannon considered the transmission of discrete signals, whereas here we consider dynamic signal transduction. In other words, we consider information transmission between a dynamic input signal ([Msn2(t)]) and a dynamic output response ([YFP(t)]). When applying concepts from information theory such as the Data Processing Inequality (DPI) to dynamic signaling events, care has to be taken. As we will discuss in further detail in the next sections, if scalars are used to represent dynamic signals this can lead to an underestimation of the actual amount of information transduced.

Given these caveats, how then should we interpret the calculations of I? Entropy can be thought of as a measure of uncertainty and mutual information quantifies the reduction in uncertainty about the input (e.g. the TF amplitude) that is gained from measuring the output (e.g. YFP level). Thus, the calculated I is the maximal reduction in uncertainty about the TF input that can be gained by measuring the YFP output. This is often interpreted

in terms of distinguishable states such that e.g. $I = \log_2(3) = 1.59$ bits means that the cell can distinguish, without error, three different inputs (Bowsher & Swain, 2014; Levchenko & Nemenman, 2014). However, this is not always the case. For example, $I = 1.59$ bits, does not guarantee that the cell can distinguish three different inputs without error. Similarly, it is possible to have a situation where it is possible to distinguish three different inputs with a low error, even though I is much less than 1.59 bits.

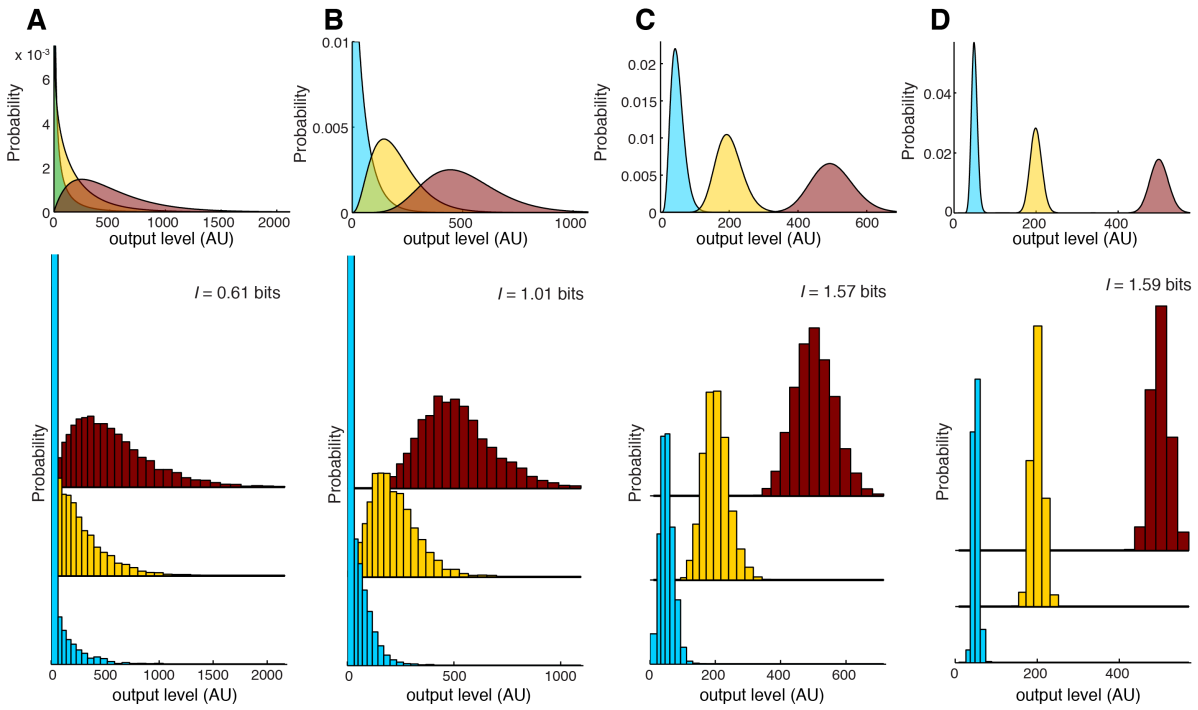

Figure C.2: *Interpreting I*
Illustration of how to interpret I. Gamma distributions were simulated with different variances. The means are 50 (blue), 200 (yellow) and 500 (red) in all cases, but the variances were different. In each case, I was calculated. The gamma distribution b values were 250 **(A)**, 56 **(B)**, 7.5 **(C)** and 1 **(D)**.

To illustrate this, consider the distributions in Figure C.2 (this example is adapted from Figure 1 in (Bowsher & Swain, 2014)). As shown in this example (Figure C.2), even $I = 0.61$ bits allows some inference about the input from observing the output. In Figure C.2B, $I \geq 1$ bits, but no two inputs can be distinguished without error. The overlap between the blue and red distributions is small and thus the inference error will be small, but this does

illustrate that $I \geq 1$ bits, does not necessarily allow for distinguishing two inputs without error. Likewise, even though $I \sim 1$ bits and not 1.59 bits ($\log_2(3)$) in Figure C.2B, it is clearly possible to distinguish the three inputs, albeit with significant error. Therefore, when interpreting the value of I it is important to also consider the shape of the probability distributions. Finally, comparing Figure C.2C and Figure C.2D, we see that even though the difference in I is only 0.02 bits, the difference in the output variability given the input is quite high. More lengthy discussions on how to interpret bits are given in (Bowsher & Swain, 2014; Levchenko & Nemenman, 2014).

C.2.5 Comments on using a scalar for computing mutual information

For each single cell we measure a YFP time-trace. Specifically, the YFP level is measured 64 times in each single cell during an experiment at 2.5 min intervals. For all information theoretical calculations we use a YFP scalar rather than a YFP vector. We use a moving-average filter to smooth the YFP trace and then pick the maximal YFP value after the YFP trace has reached a plateau. Smoothing and picking a single value greatly reduces effects from measurement noise. However, the shape of the YFP trace also contains information: e.g. when the YFP trace begins to rise, how steeply it increases, when it reaches a plateau etc. If all of these effects were included in the calculations, the calculated I would be higher. However, we posit that the max YFP level, that is, the YFP level after the time-trace has reached a plateau, is the most biologically relevant quantity. When a cell is exposed to a particular stress or signal, the goal is presumably to make the right protein in the right amount. In all likelihood, the shape of the protein production rate curve matters much less than the final level of the protein. Thus, for all information theoretical calculations in this

work we use only the final maximal YFP level.

Nevertheless, we did consider how alternative quantification schemes would affect calculations of I. The simplest alternative measure is to use the YFP level at a specific timepoint. However, as shown in Figure C.3 if we use YFP at 120 min (Figure C.3B) or at 150 min (Figure C.3C), this has a minimal effect on I_{AM} compared to using the maximal YFP value (Figure C.3A). Another alternative, is to the use the YFP production rate, i.e. $\frac{\mathrm{d\ YFP}}{\mathrm{d}\ t}$. For this calculation we use the maximal YFP production rate (i.e. the rate when $\frac{\mathrm{d}^2\ \mathrm{YFP}}{\mathrm{d}\ t^2} = 0$). As shown in Figure C.3D, if the production rate is used for calculation of I, we get a much lower value of I. This is consistent with the production rate being a poorer measure of gene expression.

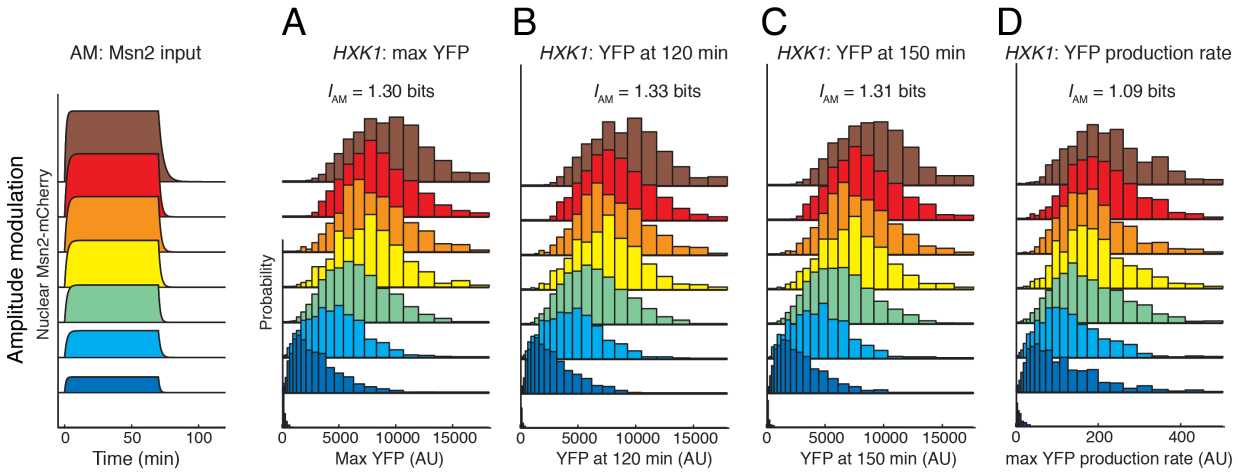

Figure C.3: *Alternative YFP measures for calculating I*
To illustrate different methods for calculating I we use *HXK1* with respect to amplitude modulation as an example.
A) Calculating I_{AM} using max YFP.
B) Calculating I_{AM} using the YFP value at 120 min.
C) Calculating I_{AM} using the YFP value at 150 min.
D) Calculating I_{AM} using the maximal YFP production rate. We define the maximal production rate as the average rate of YFP production from 5 min before to 5 min after the maximal rate. The maximal rate timepoint was determined by differentiating the YFP trace after smoothing.

C.2.6 Comments on applying the Data Processing Inequality

A central result in information theory and a major motivation behind this work is the Data Processing Inequality (DPI). The DPI states that in a network of transmission events,

once information has been lost, it cannot be recovered as is also observed in a game of 'broken telephone'. In other words, post-processing cannot increase information.

More formally, consider a Markov chain $X_1 \rightarrow X_2 \rightarrow X_3$. The DPI states that if X_2 is already known, then observing X_3 provides no additional information about X_1 and observing X_1 gives no additional information about X_3. That is:

$$I(X_1; X_3) \leq I(X_1; X_2) \tag{C.6}$$

More generally, for a Markov chain $X_1 \rightarrow X_2 \rightarrow X_3 \rightarrow X_4 \rightarrow ... \rightarrow X_n$, the DPI states that:

$$I(X_1; X_n) \leq ... \leq I(X_1; X_4) \leq I(X_1; X_3) \leq I(X_1; X_2) \tag{C.7}$$

In the context of our work, we use the DPI to argue that it does not matter how much information can be encoded and transduced upstream during stress exposure. Assuming that the purpose of the cell is to make the right stress response protein in the right amount, measuring YFP levels provides an overall measure of the information transduction of the entire pathway. In other words, even if high information transduction upstream of Msn2 is observed ($I(\text{Msn2}; X)$), the overall pathway cannot transduce more information than the final decoding step ($I(\text{YFP}; \text{Msn2})$. Thus, according to the DPI a pathway cannot transmit more information than the capacity of its 'weakest link'. Therefore, by quantifying information transduction across a pathway's weakest link, we can place an upper limit on information transduction across the entire pathway.

However, while the DPI is very intuitive, its application to dynamic networks is more complicated. To understand why, consider the central dogma TF $\rightarrow$ mRNA $\rightarrow$ YFP, where we use YFP to denote the protein being produced and a TF is activating the gene. According to the DPI, $I(\text{TF}; \text{YFP}) \leq I(\text{TF}; \text{mRNA})$. However, if snapshot measurements of TF, mRNA

and YFP are used, this can cause an apparent breakdown of the DPI if the mRNA has a much shorter life-time than the protein (which is typically the case in a cell). For example, if the mRNA has a lifetime of a few minutes and the protein a lifetime of several hours, a snapshot measurement of the mRNA reflects the transcription activity during recent minutes, whereas the protein reflects the integrated mRNA level over the past few hours. To illustrate this point, consider Figure C.4, which shows two stochastic simulation runs for the standard random telegraph gene expression model. As can be seen, snapshot measurements of mRNA copy number are much less reliable measurements of total promoter activity than is the protein copy number after its plateau (after ∼75 min).

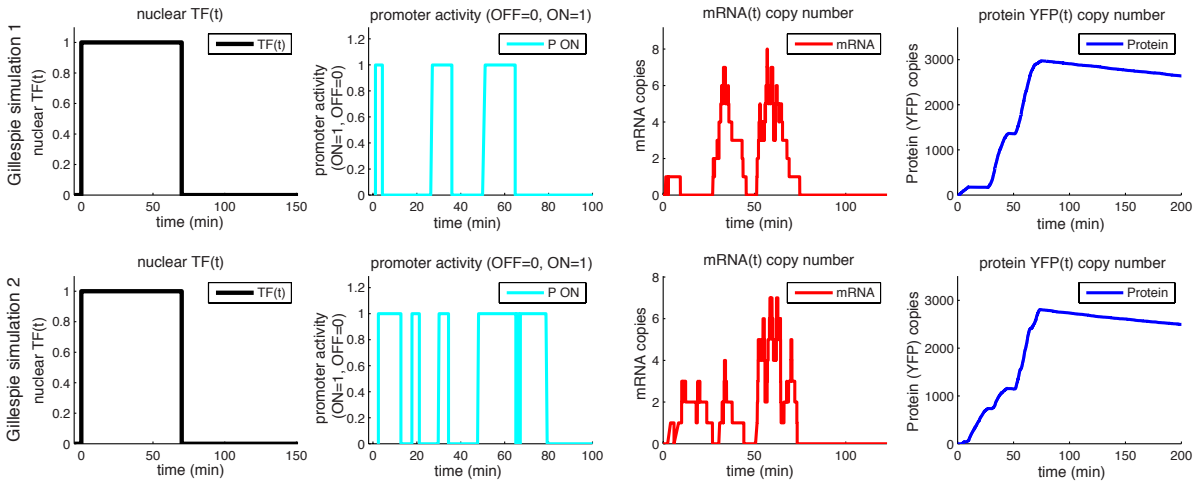

Figure C.4: *Stochastic simulation of the random telegraph model*
To illustrate the importance of dynamics, consider two simulation runs of the standard random telegraph gene expression model. First panel, a 70 min pulse of nuclear TF. Second panel, when the promoter is active (ON) as a function of time. Third panel, mRNA copy number as a function of time. Fourth panel, protein copy number as a function of time. Two simulations runs are shown for comparison.

Therefore, if snapshot measurements were used to characterize the mRNA and YFP distributions under different levels of TF, it would be possible to observe $I(\mathrm{TF};\mathrm{YFP}) \geq I(\mathrm{TF};\mathrm{mRNA})$ in apparent violation of the DPI. Of course, the DPI always applies, but for a dynamic pathway the time-dimension must be included: $\mathrm{TF}(t) \rightarrow \mathrm{mRNA}(t) \rightarrow \mathrm{YFP}(t)$. In other words, had the full time trajectory been included in calculations of mutual information, $I(\mathrm{TF};\mathrm{YFP}) \leq I(\mathrm{TF};\mathrm{mRNA})$ would hold as expected.

This highlights an important distinction between how much information a response contains and which part of the response actually provides information that is useful to the cell. As discussed above, we use a scalar to quantify the maximal YFP concentration after it has reached its plateau. If we had also included the shape of the YFP time-trace, higher information would have been measured. But as mentioned, we posit that the maximal YFP concentration is the biologically relevant quantity. In particular, for a stress response TF such as Msn2 which generally induces proteins that are enzymes rather than regulators, the downstream effects (e.g. enzymatic activity) is determined by protein concentration alone. Therefore, applying the DPI we can establish an upper bound on the pathway's ability to regulate the YFP concentration of a single gene.

This holds provided that the YFP concentration is the correct and biologically relevant measure. If a downstream decoding module existed that could read out the dynamics of YFP production, just using the YFP concentration would underestimate information transduction. Therefore, our claim that we have established an upper limit on the promoter information transduction capacity of a single gene holds if, and only if, our assumption that the biologically relevant output measure is the maximal protein concentration is correct.

C.3 Joint mutual information for two reporters

C.3.1 Joint mutual information for two reporters

Next, we consider the case where we have two different reporters for two different genes in the same cell responding to the same TF input signal. E.g. now we have *gene1*::YFP (R_1) and *gene2*::CFP (R_2). We can calculate the mutual information and I for each individual reporter as described above, but here we are interested in how much additional information

can be transmitted when we consider not just one, but both reporters in the same cell. E.g. if we already know *gene1*::YFP, how much additional information do we obtain from the additional channel, *gene2*::CFP.

Applying the chain rule for mutual information, the mutual information of two reporters responding to the same signal is given by:

$$MI\left(R_1, R_2; S\right) = MI\left(R_1; S\right) + MI\left(R_2; S|R_1\right) \tag{C.8}$$

Or equivalently:

$$MI\left(R_1, R_2; S\right) = MI\left(R_2; S\right) + MI\left(R_1; S|R_2\right) \tag{C.9}$$

Considering equation (C.8) we already know the single reporter mutual information $MI\left(R_1; S\right)$ from equation (C.3). Thus, only $MI\left(R_2; S|R_1\right)$ remains to be determined. $MI\left(R_2; S|R_1\right)$ represents the additional information we obtain, already knowing $MI\left(R_1; S\right)$, from also knowing the response of the second reporter, R_2.

To compute $MI\left(R_2; S|R_1\right)$, we use:

$$\begin{aligned} MI\left(R_2; S|R_1\right) = \sum_i \sum_j \sum_k & P\left(R_1 = r_i, R_2 = r_j, S = s_k\right) \\ & \cdot \log_2 \left(\frac{P\left(R_1 = r_i\right) P\left(R_1 = r_i, R_2 = r_j, S = s_k\right)}{P\left(R_1 = r_i, R_2 = r_j\right) P\left(R_1 = r_i, S = s_k\right)} \right) \end{aligned} \tag{C.10}$$

Thus, from equations (C.3) and (C.10), we can calculate the additional mutual information gain from an extra reporter according to (C.8).

C.3.2 Joint maximal mutual information for two reporters

As for a single reporter (equation (C.4)), the maximal joint mutual information is defined as:

$$I\left(R_1, R_2; S\right) = \max_{P(S)} \left[MI\left(R_1, R_2; S\right)\right] \quad \text{for} \quad \sum_i P(S_i) = 1; \quad P(S_i) \geq 0 \tag{C.11}$$

Whereas before $P(R, S)$ was a 2D matrix, $P(R_1, R_2, S)$ is now a 3D matrix. To determine the maximal mutual information, $I(R_1, R_2; S)$, we consider the conditional response data, $P(R_1, R_2|S)$. As before, we need to find $P(S)$ that maximizes $I(R_1, R_2; S)$. To do so we convert $P(R_1, R_2|S)$ into a 2D matrix and, as before, apply the iterative Blahut-Arimoto algorithm (Blahut, 1972; Arimoto, 1972) to obtain $P(S)$ and hence $I(R_1, R_2; S)$.

C.3.3 Computing joint mutual information with empirical data

As in the single reporter case, we must correct for bias due to binning and undersampling. When considering two reporters, the issue of undersampling is rather more pertinent. If the number of bins for *sip18*::YFP (R_1) is n and the number of bins for *hxk1*::CFP (R_2) is also n, then the total number of bins is n^2 and hence, with the same number of total cells, the number of cells available for estimating the probability density of each bin is much smaller than in the single reporter case. Thus, calculations of mutual information are now prone to bias due to undersampling. To correct for bias, we follow the same approach as in the single reporter case (an example using the 1x reporter diploid with *sip18*::YFP *hxk1*::CFP is shown in Figure C.5).

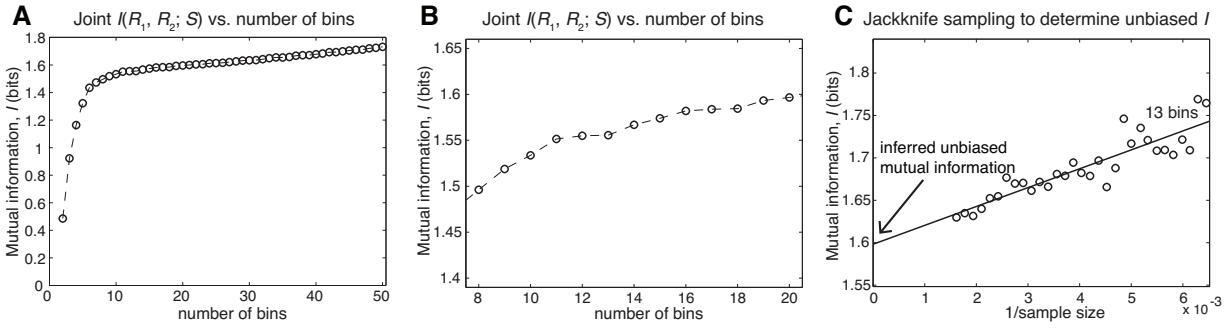

Figure C.5: *Bias correction for joint mutual information,* $I(R_1, R_2; S)$
A) Using the 1x reporter diploid *sip18*::YFP *hxk1*::CFP joint maximal mutual information with respect to amplitude modulation as an example, how $I_{\text{AM, joint}}$ scales with the number of bins is plotted.
B) A zoom-in plot of **A)** from 8 to 20 bins.
C) An illustration of how jackknife sampling is used to correct for undersampling and infer an unbiased I_{joint}.

As shown in Figure C.5A, for the joint $I(R_1, R_2; S)$, there is less of a plateau region

Table C.2: $I_{\text{AM, joint}}(R_1, R_2; S)$ and $I_{\text{FM, joint}}(R_1, R_2; S)$ for *SIP18* and *HXK1*

I	1x *sip18*::YFP/*hxk1*::CFP strain	2x *sip18*::YFP/*hxk1*::CFP strain
$I_{\text{AM, joint}}(R_1, R_2; S)$	1.61 ± 0.04 bits	1.77 ± 0.04 bits
$I_{\text{FM, joint}}(R_1, R_2; S)$	1.18 ± 0.04 bits	1.26 ± 0.04 bits
$I_{\text{AM+FM, joint}}(R_1, R_2; S)$	1.67 ± 0.04 bits	1.83 ± 0.03 bits

compared to the single reporter $I(R; S)$ (Figure C.1A). This indicates undersampling and is caused by the n^2 number of bins in the joint case. Nonetheless, we consider I_{joint} between 8 and 20 bins as shown in Figure C.5B and calculate the joint $I(R_1, R_2; S)$ for 8 to 20 bins, inclusive, corrected for bias using jackknife sampling and the series expansion (Figure C.5C and equation (C.5)) and report $I(R_1, R_2; S)$ as the mean and its error as the standard deviation. Thus, the approach is identical to the bias correction for a single reporter and similar to previously reported bias correction approaches (Cheong *et al,* 2011). The results, after bias correction, are summarized in table C.2. In conclusion, having two copies of each gene instead of just one leads to a small, but robust increase in I_{joint}.

C.4 Determining intrinsic mutual information

C.4.1 Intrinsic and extrinsic contributions to gene expression noise

It is well-known that gene expression is noisy in the sense that a group of genetically identical cells exposed to the same perturbation or signal will exhibit significant cell-to-cell variability in their gene expression responses. In terms of information transduction this leads to a loss of information.

The sources of gene expression noise can be classified into two broad sources: intrinsic and extrinsic noise (Elowitz *et al,* 2002; Swain *et al,* 2002; Hilfinger & Paulsson, 2011). To experimentally distinguish these two sources of gene expression variability, the dual-reporter

system was developed (Elowitz *et al,* 2002). Using diploid yeast, equivalent CFP and YFP gene expression reporters are placed on the homologous chromosomes at the same locus. Thus, the two reporters are in identical genetical contexts. Extrinsic noise is then defined as variability caused by the shared intracellular environment, such as differences in the number of RNA Pol II complexes, Msn2 molecules, ribosomes or cell cycle phase between cells, which affect both CFP and YFP within the same cell equally. The remaining variability, which is not accounted for by the shared environment, is then defined as intrinsic noise and could stem from stochastic TF binding or chromatin remodeling at individual promoters (Elowitz *et al,* 2002; Swain *et al,* 2002; Hilfinger & Paulsson, 2011).

Mathematically, noise is defined as $\eta^2 = \frac{\sigma^2}{\mu^2}$. Using dual CFP and YFP reporters, gene expression noise can be decomposed into its intrinsic and extrinsic parts:

$$\eta^2_{\text{total}} = \frac{\langle \text{CFP}^2 + \text{YFP}^2 \rangle - 2\langle \text{CFP} \rangle \langle \text{YFP} \rangle}{2\langle \text{CFP} \rangle \langle \text{YFP} \rangle} \tag{C.12}$$

$$\eta^2_{\text{extrinsic}} = \frac{\langle \text{CFP} \cdot \text{YFP} \rangle - \langle \text{CFP} \rangle \langle \text{YFP} \rangle}{\langle \text{CFP} \rangle \langle \text{YFP} \rangle} \tag{C.13}$$

$$\eta^2_{\text{intrinsic}} = \frac{\langle (\text{CFP} - \text{YFP})^2 \rangle}{2\langle \text{CFP} \rangle \langle \text{YFP} \rangle} \tag{C.14}$$

Finally, we note that $\eta^2_{\text{tot}} = \eta^2_{\text{int}} + \eta^2_{\text{ext}}$.

C.4.2 Effect of extrinsic noise on mutual information

Ideally, mutual information and the information transduction capacity of a promoter would be measured in the same cell. That is, using I_{AM} as an example, the ideal experiment would involve exposing the same cell to different amplitudes of Msn2 translocation and

measuring a gene expression response each time and repeating this thousands of times in each single cell. However, this is not experimentally feasible: each experiment takes ~ 3 hours and there is the issue of adaptation, which means the first response will be different from the second.

Instead, to measure I, we must take populations of cells and expose them to a single amplitude of Msn2 translocation and repeat this experiment multiple times to obtain enough cells for each amplitude and to obtain data for different conditions (i.e. different amplitudes). However, this means that the measured I might be an underestimate.

To illustrate this point, consider the cell cycle. It is known that the cell cycle can affect gene expression variability (Zopf *et al,* 2013). Thus, when we measure the gene expression response to a Msn2 signal across a cell population with unsynchonized cell cycle phases, part of the variability that we observe is really due to cell cycle variability, rather than anything due to the PKA/Msn2 signaling pathway. While it is possible to determine the cell cycle phase and therefore condition each cell's response on the initial cell cycle phase, this is very labor intensive, but more importantly the cell cycle is only one of a huge number of known and unknown extrinsic factors. Thus, we need a method that can correct for all extrinsic effects, without having to specify each individual source of extrinsic noise, and estimate a purely intrinsic I.

The importance of extrinsic effects on single cell dose-responses was highlighted in recent work from Toettcher, Lim and Weiner (Toettcher *et al,* 2013). Using optogenetics to control Ras activation (input) and microscopy to measure nuclear translocation of ERK (output), Toettcher *et al.* was able to measure full dose-responses in single cells because of the rapid response time and the lack of adaptation of their system. The key finding was that the single cell dose-responses exhibited much lower variability than the dose-response obtained from

averaging over a population of cells. Rephrasing this in an information theoretic framework, this work experimentally demonstrates that single cells condition on extrinsic factors and that I measured across a cell population could be a serious underestimate of the true I.

C.4.3 An algorithm to estimate the intrinsic mutual information

Using the dual CFP/YFP reporters in the same cell, we can calculate intrinsic and extrinsic noise. To determine the intrinsic maximal mutual information, I_{int}, we need to determine the full gene expression probability distribution in the absence of extrinsic noise. This is an intractable problem and the intrinsic noise component has to be carefully interpreted (Hilfinger & Paulsson, 2011; Shahrezaei *et al,* 2008). Here we present an algorithm to infer an approximate I_{int}. The approach is outlined in Figure C.6. We stress that this approach is approximate and that it is not possible to analytically determine the gene expression distribution in the absence of extrinsic noise. Nonetheless, comparisons using stochastic simulations validate the approach and indicate that the error is small.

In the following we go through each step in the algorithm. First, for each condition we fit the raw empirical distribution of YFP gene expression responses to a gamma distribution. That is, if X is the random variable representing the YFP response, then $X \sim \Gamma(a, b)$. We choose a gamma distribution because it is a highly flexible distribution with positive support. More importantly, a gamma distribution has been justified in terms of theoretical stochastic models of gene expression (Friedman *et al,* 2006), statistical inference approaches (Zechner *et al,* 2014) and shown to be able to fit 1009 out of 1018 protein distributions across the *E. coli* proteome (Taniguchi *et al,* 2010). Finally, we found that our empirical YFP responses were well-fit by gamma distributions. An example of the gamma fit to a raw empirical YFP distribution is shown in Figure C.6 (black fit to red histogram). An obvious case where a

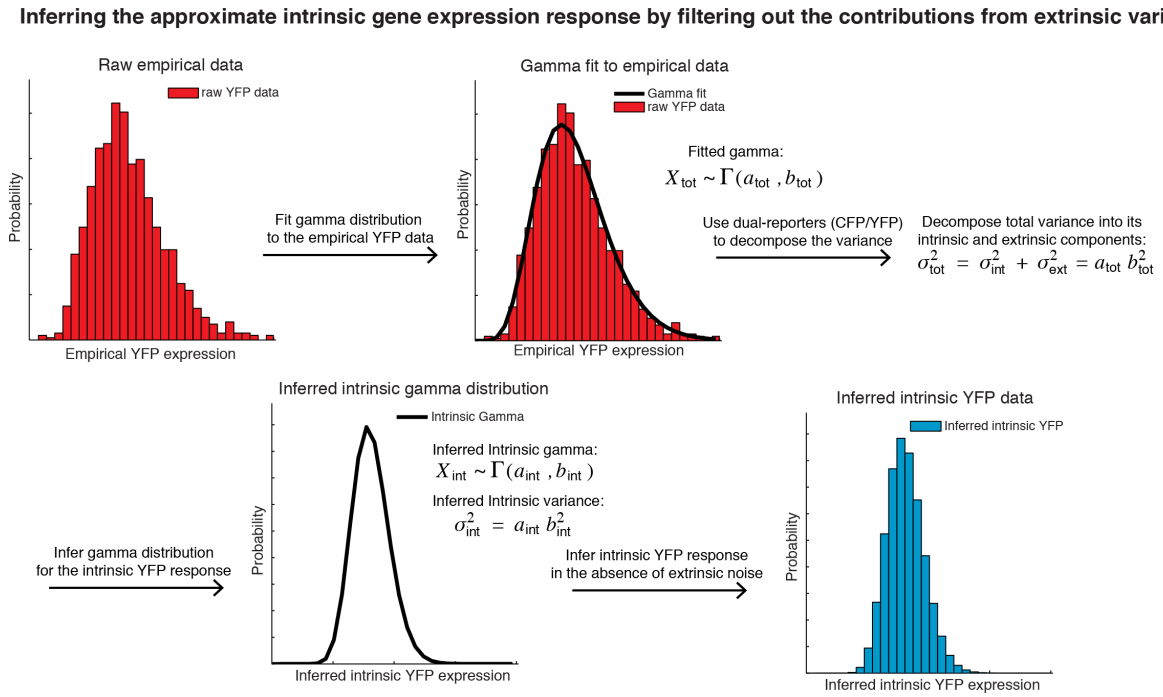

Figure C.6: *Inferring an estimate of I_{int}*
The raw empirical YFP distribution (red) is fitted to a gamma distribution. While keeping the mean constant, a new gamma distribution is inferred where the variance is now equal to the intrinsic variance. This distribution is then used for calculating the I_{int}.

single gamma distribution would be insufficient would be a bimodal distribution, but we do not observe any bimodal responses.

Let $X_{\text{tot}} \sim \Gamma(a_{\text{tot}}, b_{\text{tot}})$ represent the YFP response in the presence of extrinsic noise and $X_{\text{int}} \sim \Gamma(a_{\text{int}}, b_{\text{int}})$ the YFP response in the absence of extrinsic noise. To determine a_{int} and b_{int}, we first calculate the intrinsic variance from the empirical CFP and YFP data according to equation (C.14):

$$\sigma^2_{\text{int}} = \eta^2_{\text{int}} \langle \text{CFP} \rangle \langle \text{YFP} \rangle = \frac{1}{2} \langle (\text{CFP} - \text{YFP})^2 \rangle \tag{C.15}$$

In addition to assuming that both X_{tot} and X_{int} are gamma distributed, we also assume that the mean is unchanged. For gamma distributions, $E(X) = ab$ and $\text{Var}(X) = ab^2$. Thus, we require $a_{\text{tot}} b_{\text{tot}} = a_{\text{int}} b_{\text{int}}$. If we define $k = \frac{\sigma^2_{\text{tot}}}{\sigma^2_{\text{int}}}$, we therefore get:

$$a_{\text{int}} = k a_{\text{tot}} \tag{C.16}$$

$$b_{\text{int}} = \frac{b_{\text{tot}}}{k} \tag{C.17}$$

Thus, if $X \sim \Gamma(a, b)$ then $X_{\text{int}} \sim \Gamma\left(a\frac{\sigma^2_{\text{tot}}}{\sigma^2_{\text{int}}}, b\frac{\sigma^2_{\text{int}}}{\sigma^2_{\text{tot}}}\right)$, where σ^2_{int} is defined in equation (C.15). We use the `MATLAB` function `gamfit` to fit a gamma distribution to the raw data and calculate a and b.

Next and using *HXK1* with respect to amplitude modulation as an example, we then repeat the above procedure for each amplitude and discretize the intrinsic gamma distribution using the same bins as for the empirical YFP distribution. An example is shown in Figure C.7.

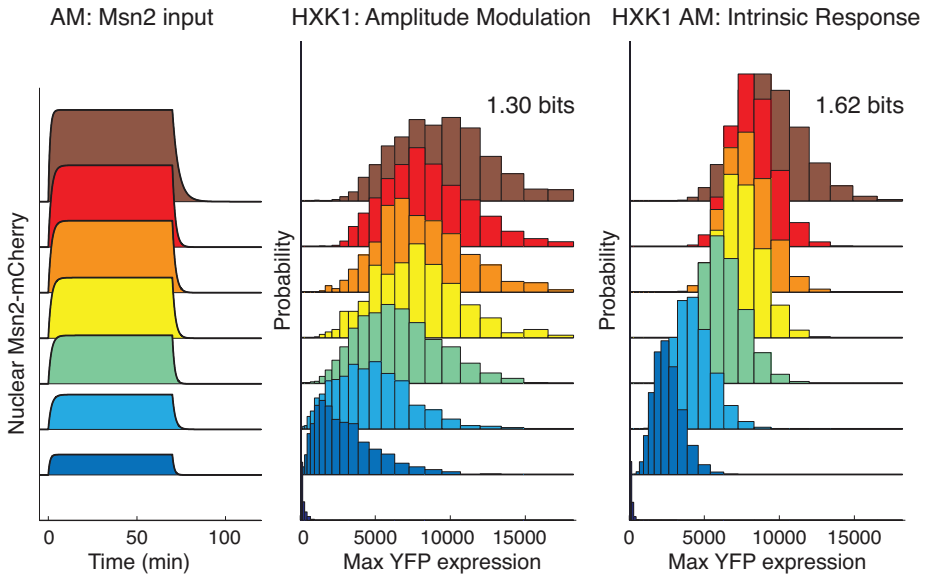

Figure C.7: *Inferring the approximate intrinsic gamma distribution*
Using *HXK1* with respect to amplitude modulation as an example, the empirical YFP response distributions are plotted next to the intrinsic gamma distribution. The empirical I_{raw} and the inferred approximate I_{int} are listed as well.

Finally, having determined the intrinsic gamma distribution, I_{int} is calculated according to equation (C.4) using the Blahut-Arimoto algorithm as previously. As shown in Figure C.7 the intrinsic response distributions for *HXK1* are significantly more narrow and I_{int} significantly greater than I_{raw}.

It is important to note that it is not possible to analytically determine the intrinsic distributions from filtering extrinsic noise out of the empirical distribution (Hilfinger & Paulsson, 2011). Here we approximate both the total and intrinsic distributions as gamma distributions and make several important assumptions that cannot rigorously be justified. In the next section we test the algorithm on simulated data to determine how well the algorithm can estimate the true I_{int}.

C.4.4 Testing the algorithm with simulated data and linear gene expression models

To systematically test the algorithm and estimate the error in the estimation of I_{int} we took the following approach. For the 5 linear models shown in Figure C.8, we used the Gillespie algorithm (Gillespie, 1977) to simulate stochastic gene expression, with two reporter genes per cell, for thousands of cells and several conditions (e.g. different TF amplitudes), with or without extrinsic noise. We model extrinsic noise by letting rate constants differ between cells (Shahrezaei *et al,* 2008; Zechner *et al,* 2014). We then apply the algorithm to the data with extrinsic noise, calculate the inferred I_{int} and compare this to I_{int} obtained from the data with only intrinsic noise. Below, we go through each step in detail.

To test the generality of our approach, we test it using five different gene expression models (Figure C.8). Model 1 and 2 are versions of the classic 2-state random telegraph model (Ko 1991; Peccoud & Ycart, 1995) with transcription either dependent or independent of [TF(t)], respectively. Model 3 (Zechner *et al,* 2014) and model 5 (Rieckh & Tkacik, 2014) are 3-promoter state versions of the random telegraph model and model 4 includes a refractory state (Zechner *et al,* 2014).

In the following we will use model 1 to illustrate the steps. To model multiple conditions,

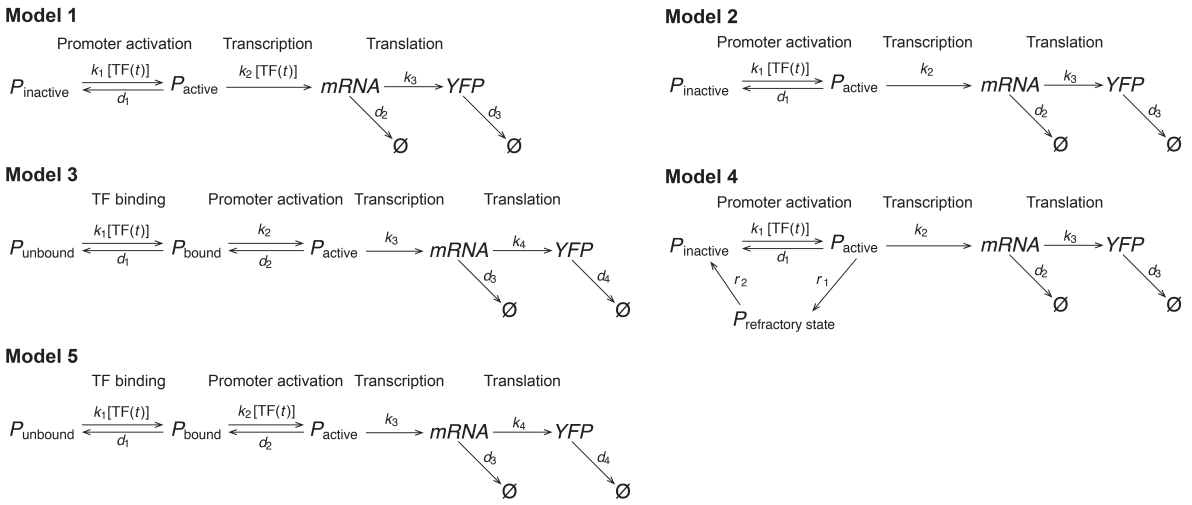

Figure C.8: *Linear gene expression models*
The I_{int} algorithm was tested using data simulated with the 5 linear models above.

we vary the transcription rate from 0.025 min^{-1} to 3 min^{-1} in 10 steps. Previous approaches have used the assumption that all extrinsic noise comes from translation (Zechner *et al,* 2014). Since for our purpose another direct source of extrinsic variability is variation in Msn2 levels between cells, we model extrinsic noise as coming from translation and [TF(t)]. Thus, for each simulated cell we pick k_3 (model 1) and [TF(t)] from a gamma distribution. Since the upper bound for a gamma distribution is ∞, it will occasionally happen that unphysically large or small values of k_3 (model 1) and [TF(t)] are picked and we therefore set a lower and upper threshold of half and twice the mean, respectively. If values above or below this threshold are picked, we re-pick until a physically plausible value is picked. Furthermore, to both simulate cases where intrinsic and extrinsic noise dominates we repeat the simulations where k_3 and [TF(t)] are picked from a gamma distribution with low variance (such that intrinsic noise dominates) and from a gamma distribution with high variance (such that extrinsic noise dominates). Finally, to find I in the absence of extrinsic noise, we also perform simulations where [TF(t)] and all the rate parameters have fixed values. This gives the true I_{int}.

For each condition we use 2000 iterations, corresponding to 2000 simulated cells, over 10 conditions, corresponding to 10 amplitudes of a 70 min pulse. To test generality, we simulate both a slower ($k_1 = d_1 = 0.1$ min^{-1} for model 1) and a faster ($k_1 = d_1 = 0.5$ min^{-1} for model 1) promoter (slower promoters exhibit substantially higher gene expression noise and therefore, all other things being equal, have lower I (Hansen & O'Shea, 2013)).

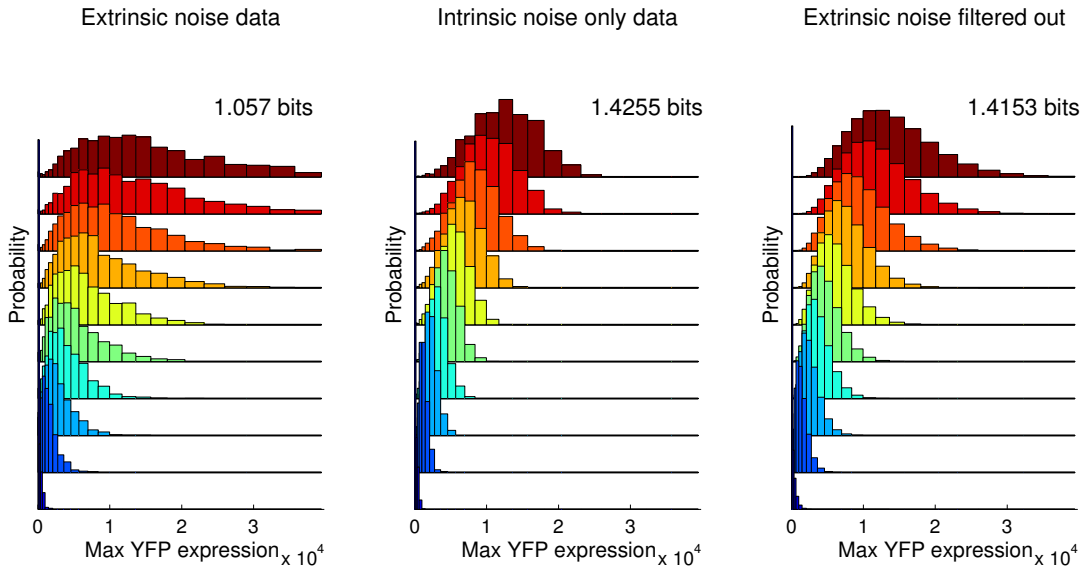

Figure C.9: *Example of the algorithm on simulated data using a linear model*
Using model 1 and a slow promoter, data with a high level of extrinsic noise was simulated over 10 conditions (left), such that extrinsic noise dominates over intrinsic noise at higher expression. The same system was simulated without extrinsic noise (center) and the corresponding I calculated. Finally, the algorithm was applied to the data with extrinsic noise (left) and intrinsic distributions were inferred (right) and used to estimate I_{int}. As can be seen, the inferred I_{int} is a slight underestimate.

Figure C.9 shows an example of a typical model simulation over the 10 conditions. The true I_{int} (center), is obtained from simulations without extrinsic noise (1.426 bits). The algorithm is then applied to data with extrinsic noise (left) and used to infer an estimate (1.415 bits) of the true I_{int} (right).

Figure **??** summarizes the results from simulations over 5 different conditions for each of the 5 models. Figure **??**A shows I with and without extrinsic noise. The parameters were chosen such that I would be in the 1-2 bit range as we observe experimentally. Figure **??**B shows the error in the inferred I_{int} for each of the 4 conditions with extrinsic noise.

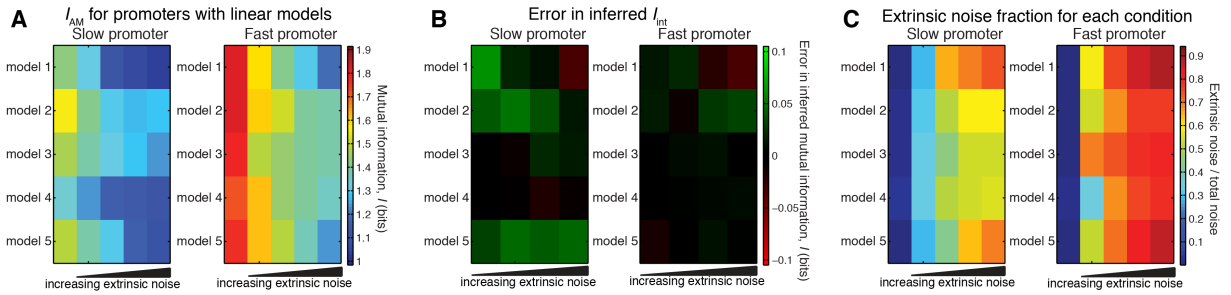

Figure C.10: *Testing the algorithm using simulated data and linear models*
A) For each of the 5 linear models, two promoters (slow and fast) were simulated without and with increasing amounts of extrinsic noise and I determined.
B) For the 4 conditions with extrinsic noise, the error in the estimated I_{int} was determined for each promoter.
C) The fraction of the total noise that is extrinsic for each simulated condition (shown is the fraction for the amplitude that yields maximal expression)

The algorithm generally underestimates the true I_{int}. However, the error is very small. In all cases, the error is less than 5% and the average error is less than 2%. This should be compared with an error from the simulations of around 1%. Finally, as shown in Figure **??**C we choose the level of extrinsic noise (shown only for the maximum expression condition) to vary over a range of levels. For the experimental data, extrinsic noise always dominates at the 70 min 3 μM 1-NM-PP1 condition, but to different extents: it vastly dominates for p*SIP18* mut B, but less so for *SIP18*. Thus, the extrinsic noise was similarly varied for the simulations.

C.4.5 Testing the algorithm with simulated data and nonlinear gene expression models

To exhaustively test the algorithm, we repeated the above approach of simulating 5 models with and without extrinsic noise and then applying the algorithm to the extrinsic noise data and testing how well it matches the true I_{int} using also nonlinear models. To fully account for the nonlinear dependence of gene expression on the Msn2 amplitude, nonlinear functions such as the Hill function are necessary (Hansen & O'Shea, 2013). Thus, we consider the same 5 models as in Figure C.8 but this time with a nonlinear Hill function-type

dependence on the nuclear Msn2 concentration as shown in Figure C.11.

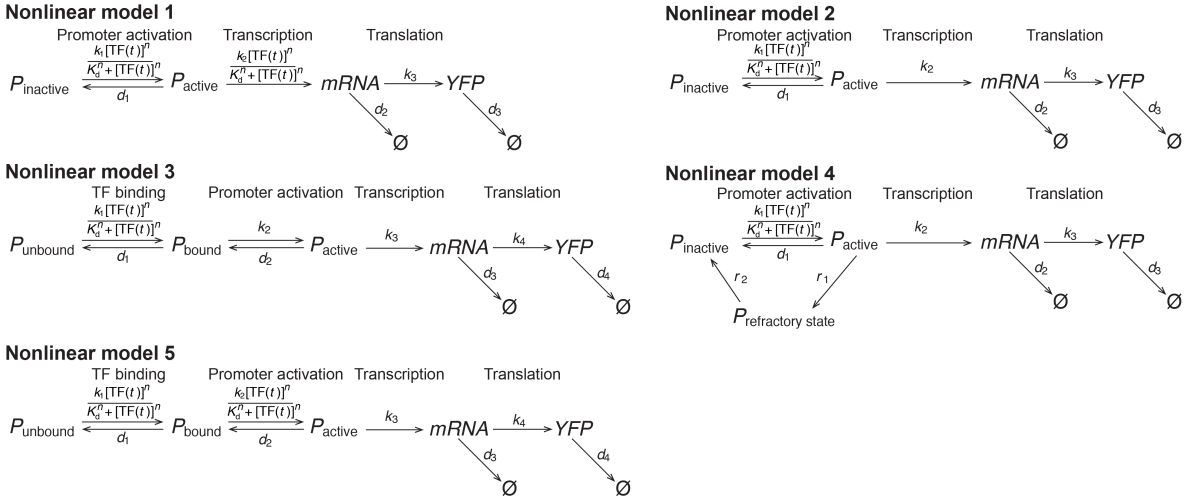

Figure C.11: *Nonlinear gene expression models*
The I_{int} algorithm was further tested using data simulated with the 5 nonlinear models above.

Without repeating the previous section, for the nonlinear models we followed exactly the same approach as for the linear model simulations. For the Hill function we picked, $K_d = 1.5$ and $n = 1.5$ (this level of moderate cooperativity is consistent with our previous observations (Hansen & O'Shea, 2013)) and we now allow the TF concentration to increase with each of the 10 conditions up until a final value of 10 in the same arbitrary units as the K_d is given in. As before, we model extrinsic noise by picking the TF concentration and the translation rate (k_3 in model 1) from a gamma distribution and for each model we consider both a slow and a fast promoter. As before, we summarize the simulation results as a heatmap (Figure C.12).

As shown in Figure C.12, the error is always small also for the nonlinear models. In fact, as for the linear models the algorithm tended to slightly underestimate the true I_{int}, but again, the error was always less than 5% and the average error was less than 2 %.

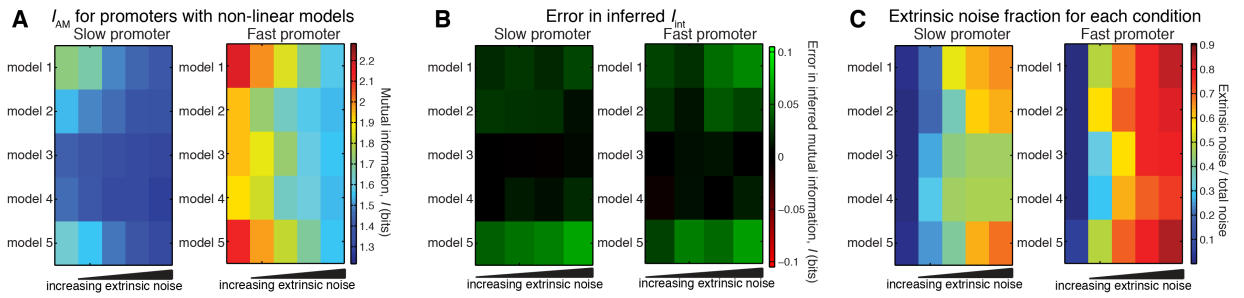

Figure C.12: *Testing the algorithm using simulated data and nonlinear models*
A) For each of the 5 nonlinear models, two promoters (slow and fast) were simulated without and with increasing amounts of extrinsic noise and I determined.
B) For the 4 conditions with extrinsic noise, the error in the estimated I_{int} was determined for each promoter.
C) The fraction of the total noise that is extrinsic for each simulated condition (shown is the fraction for the amplitude that yields maximal expression)

C.4.6 Comments on the algorithm

Taken together, we have considered 5 linear and 5 nonlinear gene expression models and a slow and a fast promoter for each and in each case four different levels of extrinsic noise. In every one of these 80 simulations we find that the error is always below 5% (in bits) and the mean error is less than 2%. As mentioned under most conditions the extrinsic noise can be precisely measured, but it is not possible to obtain the full intrinsic probability distribution (Hilfinger & Paulsson, 2011). Yet, based on the model simulations our algorithm seems to work very well and gives negligible error. One possibility is that the various approximations cancel each other out. Regardless, we do not make claims about the precise I_{int} of a specific Msn2-dependent promoter, but rather roughly of what order it is. E.g. for *SIP18*, I_{int} was inferred to be ca. 1.51 ± 0.07 bits. Given the error range of our algorithm, we cannot with certainty say what the exact value it, but we can say that it is almost certainly less than 2 bits and therefore that signal intensity information cannot be amplitude transmitted through the *SIP18* gene without significant associated error.

Table C.3: Empirical I_{int}

Promoter	I_{raw}	I_{int}
HXK1: AM	1.30 ± 0.02 bits	1.61 ± 0.02 bits
HXK1: FM	1.11 ± 0.01 bits	1.36 ± 0.02 bits
SIP18: AM	1.21 ± 0.03 bits	1.51 ± 0.07 bits
SIP18: FM	0.52 ± 0.06 bits	0.76 ± 0.07 bits
pSIP18 mut A: AM	1.42 ± 0.01 bits	1.59 ± 0.02 bits
pSIP18 mut A: FM	0.88 ± 0.02 bits	0.96 ± 0.02 bits
pSIP18 mut B: AM	1.55 ± 0.01 bits	2.00 ± 0.02 bits
pSIP18 mut B: FM	1.39 ± 0.01 bits	1.69 ± 0.02 bits

C.4.7 Computing I_{int} with empirical data

To estimate I_{int} using empirical data we apply the algorithm as explained above and shown in Figure C.7. The results are shown in table C.3. To estimate the error in I_{int}, we follow the same approach as for the empirical I_{raw} shown in Figure C.1 to correct for bias due to binning and undersampling. That is, we perform jackknife sampling to estimate C_{unbiased} (equation (C.5)) using 15-35 bins, inclusive, and report I_{int} as the mean and the error as the standard deviation.

C.5 References

Arimoto, S. (1972). An algorithm for computing the capacity of arbitrary discrete memoryless channels. *IEEE Trans. Inform. Theory.*

Blahut, R. E. (1972). Computation of channel capacity and rate-distortion functions. *IEEE Trans. Inform. Theory.*

Bowsher, C.G. & Swain, P.S. (2014). Environmental sensing, information transfer, and cellular decision making. *Curr Opin Biotech*, 28, 149-155.

Cheong, R., Rhee, A., Wang, C. J., Nemenman, I. & Levchenko, A. (2011). Information transduction capacity of noisy biochemical signaling networks. *Science*, 334, 354-358.

Cover, T. M. & Thomas, J. A. (2006). Elements of information theory. *Wiley*.

Elowitz, M. B., Levine, A. J., Siggia, E. D. & Swain, P. S. (2002). Stochastic gene expression in a single cell. *Science*, 297, 1183-1186.

Friedman, N., Cai, L. & Xie, X. S. (2006). Linking stochastic dynamics to population distribution: an analytical framework of gene expression. *Physical review letters*, 97, 168302.

Gillespie, D. T. (1977). Exact stochastic simulation of coupled chemical reactions. *The journal of physical chemistry*, 81, 2340-2361.

Hansen, A. S. & O'Shea, E. K. (2013). Promoter decoding of transcription factor dynamics involves a trade-off between noise and control of gene expression. *Molecular systems biology*, 9.

Hilfinger, A. & Paulsson, J. (2011). Separating intrinsic from extrinsic fluctuations in dynamic biological systems. *Proceedings of the National Academy of Sciences*, 108, 12167-12172.

Ko M. S. H. (1991). A stochastic model for gene induction. *Journal of Theoretical Biology*, 153, 181-194.

Levchenko, A. & Nemenman, I. (2014). Cellular noise and information transmission. *Curr Opin Biotech*, 28, 156-164.

Peccoud J. & Ycart B. (1995). Markovian Modeling of Gene Product Synthesis. *Theor Popul Biol*, 48, 222-234.

Rieckh, G. & Tkacik, G. (2014). Noise and information transmission in promoters with multiple internal states. *Biophysical journal*, 106, 1194-1204.

Shahrezaei, V., Ollivier, J. F. & Swain, P. S. (2008), Colored extrinsic fluctuations and stochastic gene expression. *Molecular Systems Biology*, 4.

Shannon, C. E. (1948), A mathematical theory of communication. *Bell System Technical Journal*, 27, 379-423 and 623-656.

Slonim, N., Atwal, G. S., Tkacik, G. & Bialek, W. (2005). Information-based clustering. *Proceedings of the National Academy of Sciences of the United States of America*, 102, 18297-18302.

Strong, S. P., Koberle, R., de Ruyter van Steveninck, R. R. & Bialek, W. (2005). Entropy and Information in Neural Spike Trains. *Physical Review Letters*, 80, 197-200.

Swain, P. S., Elowitz, M. B. & Siggia, E. D. (2002). Intrinsic and extrinsic contributions

to stochasticity in gene expression. *Proceedings of the National Academy of Sciences*, 99, 12795-12800.

Taniguchi, Y., Choi, P. J., Li, G. W., Chen, H., Babu, M., Hearn, J., Emili, A. & Xie, X. S. (2010). Quantifying E. coli proteome and transcriptome with single-molecule sensitivity in single cells. *Science*, 329, 533-538.

Toettcher, J. E., Weiner, O. D. & Lim, W. A. (2013). Using optogenetics to interrogate the dynamic control of signal transmission by the Ras/Erk module. *Cell*, 155, 1422-1434.

Zechner, C., Unger, M., Pelet, S., Peter, M. & Koeppl, H. (2014). Scalable inference of heterogeneous reaction kinetics from pooled single-cell recordings. *Nature methods*, 11, 197-202.

Zopf, C. J., Quinn, K., Zeidman & J., Maheshri, N. (2013). Cell-cycle dependence of transcription dominates noise in gene expression. *PLoS computational biology*, 9, e1003161.

Appendix D

Preliminary results for understanding how promoter architecture influences promoter decoding of Msn2 dynamics

D.1 Abstract

In this appendix, we briefly outline ongoing studies on understanding how promoter architecture influences promoter decoding of transcription factor dynamics. In Chapter 2 we have shown the promoters fall into different classes based on their amplitude threshold and activation timescale. This therefore raises the question of which promoter *cis*-elements control how a promoter decodes transcription factor dynamics and thus, which class a promoter falls into. We hypothesized that the number and location of Msn2 binding sites (STREs: 5'-CCCCT-3') relative to nucleosomes in the promoter would be a major factor. In this appendix, we very briefly describe our preliminary studies on the *SIP18* promoter.

D.2 Preliminary results

D.2.1 Inferring the amplitude threshold and activation timescale for mutant promoters

In Chapter 2 we have systematically studied how seven wildtype promoters decode Msn2 dynamics using diploid strains with dual CFP/YFP reporters. This allows us to also dissect intrinsic and extrinsic contributions to noise. However, studying the response of dual-reporter diploid strains in response to thirty different dynamical Msn2 inputs is very labor-intensive and not necessary to determine the promoter class. Instead, we sought a way to determine promoter class from just five experiments (i.e. five dynamical Msn2 inputs) in haploid strains.

Thus, we sought a limited set of experiments from which we could infer an approximate amplitude threshold and activation timescale. As shown in figure D.1, with just five experiments this is possible. By comparing the $\frac{x_{175\ \mathrm{nM}}}{x_{690\ \mathrm{nM}}}$- and $\frac{x_{690\ \mathrm{nM}}}{x_{3\ \mu\mathrm{M}}}$-ratios, we can infer an approximate amplitude threshold: for a high threshold promoter such as *SIP18*, these ratios are very low, whereas for a low amplitude threshold promoter such as *HXK1*, these ratios are much higher.

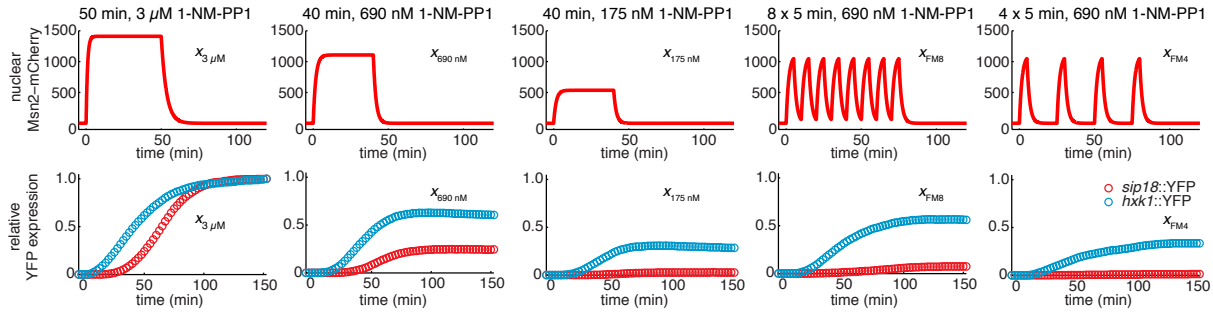

Figure D.1: *Inferring amplitude threshold and activation timescale from a limited set of experiments*
With just five experiments it is possible to infer approximately the promoter class. For example, promoters with a high amplitude threshold (*SIP18*; red), completely filter out low amplitude input ($x_{175\ \mathrm{nM}}$), whereas promoters with a low amplitude threshold still induce strongly in response to low amplitude input (*HXK1*; blue). Similarly, fast promoters (*HXK1*; blue) induce significantly in response to oscillatory input (x_{FM8} and x_{FM4}), whereas slow promoters (*SIP18*; red) effectively filter out oscillatory input.

Similarly, by comparing the $\frac{x_{\mathrm{FM8}}}{x_{690\ \mathrm{nM}}}$- and $\frac{x_{\mathrm{FM4}}}{x_{\mathrm{FM8}}}$-ratios, we can infer an approximate acti-

vation timescale: a slow promoter such as *SIP18* effectively filters out oscillatory input and have ratios close to zero, whereas for a fast promoter such as *HXK1*, these ratios will be much higher.

Thus, from this limited set of experiments we can qualitatively infer the promoter class and we can use the $x_{3\ \mu\mathrm{M}}$ expression level as a measure of promoter strength.

D.2.2 A simple calibration model for quantitative promoter class inference

To quantitatively infer the amplitude threshold and activation timescale for promoter mutants, we developed a simple calibration approach. We know the precise values for the seven wildtype promoters (Figure 2.2B). Thus, we used the limited set of experiments shown in Figure D.1 and developed a simple calibration model that can quantitatively infer the amplitude threshold and activation timescale from just these five experiments.

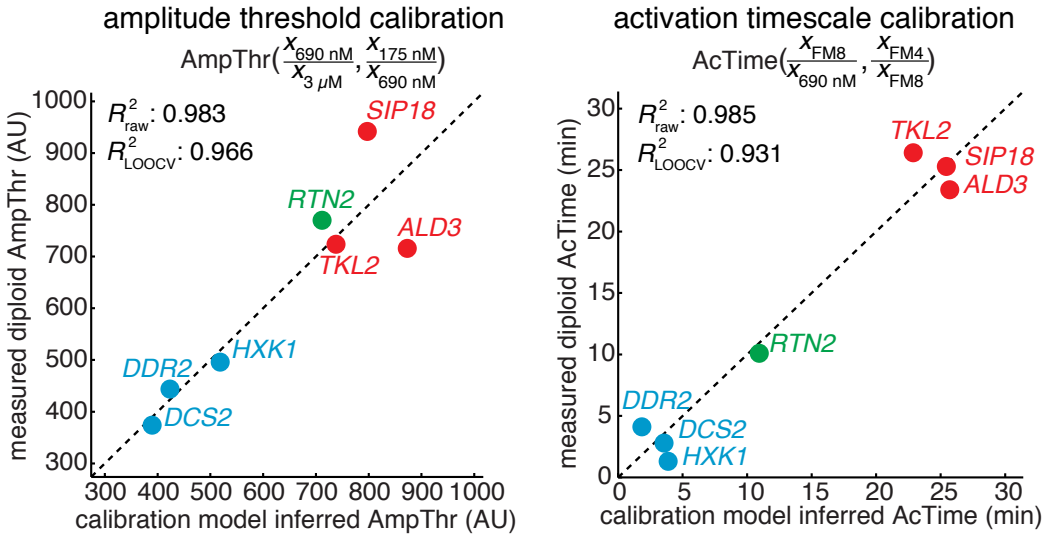

Figure D.2: *A calibration model for inferring amplitude threshold and activation timescale*
Left: Actual amplitude threshold (Figure 2.2B) is plotted vs. calibration model inferred amplitude threshold. The calibration model uses just two fitted parameters to avoid overfitting.
Right: Actual promoter activation timescale (Figure 2.2B) is plotted vs. calibration model inferred activation timescale. The calibration model uses just three fitted parameters to avoid overfitting.

Our calibration model uses only two and three fitted parameters to infer the amplitude

threshold and activation timescale, respectively. Nonetheless, it can account for more than 98% of the variance (Figure D.2). However, one has to be careful because provided that the model is complicated enough, any dataset can be fit. Furthermore, the goal is not to fit an existing dataset, but rather to be able to reliable infer information about uncharacterized mutants. Thus, it is crucial to avoid overfitting. To estimate how much the calibration model is overfit, we use Leave-One-Out Cross Validation (LOOCV). LOOCV is a standard statistical technique for estimating overfitting. In LOOCV, we hide a single promoter, fit the model to the remaining six promoters and then use this model to infer the seventh and hidden promoter. We then repeat this procedure for all seven promoters. Using these errors, we can calculate a coefficient of determination corrected for overfitting R^2_{LOOCV}. As shown in (Figure D.2), our calibration model is not strongly overfit. We can therefore use it to quantitatively infer the amplitude threshold and activation timescale of promoter mutants from the limited set of experiments shown in Figure D.1.

D.2.3 How Msn2 binding site number and location affects promoter class

Having developed and verified a calibration model for inferring promoter class, we next made a series of mutants of the *SIP18* promoter. We divided the *SIP18* promoter into four regions: A, B, C and D. The wildtype promoter has two Msn2 binding sites in region C. First, we considered a null mutant with these two binding sites removed (null mutant; Figure D.3. The null mutant was not active. This indicates that the two wildtype binding sites in region C are required and that the more upstream site (-524 bp) is not functional on its own.

Next, we made a series mutants with either 2, 3 or 4 binding sites in regions A, B, C or D. Furthermore, we made "spread-out" mutants with 3 or 4 binding sites spread between

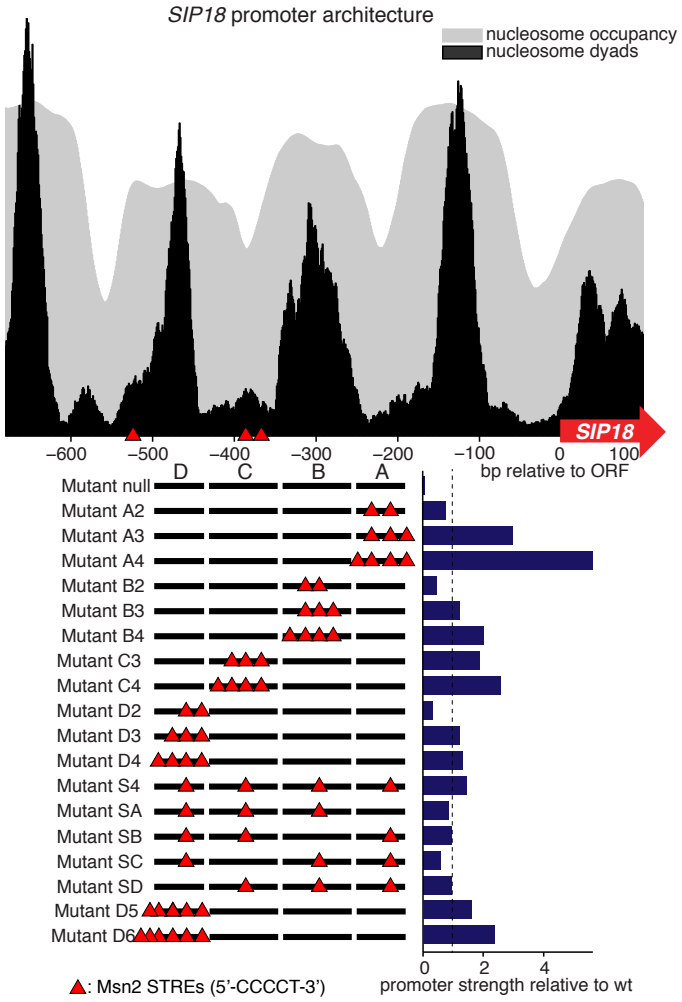

Figure D.3: *pSIP18 promoter mutants*
Twenty *SIP18* promoter variants are shown. The promoter was divided into four regions (A, B, C and D) and the location and number of Msn2 binding sites systematically varied. The nucleosome occupancy and position is also shown using MNase-Seq data from Figure 2.7E.

regions A, B, C and D Figure D.3. Finally, we made extreme versions in region D with 5 and 6 Msn2 binding sites.

Having constructed these 19 promoter mutants, we tested their class by measuring their expression level in response to the five experiments shown in Figure D.1. We then applied the calibration model and inferred the amplitude threshold and activation timescale for each mutant (Figure D.4). As is evident from Figure D.4, it is possible to change both the amplitude threshold and activation timescale simply by modulating the number and location of the Msn2 binding sites in the promoter (Figure D.3). The most dramatic change

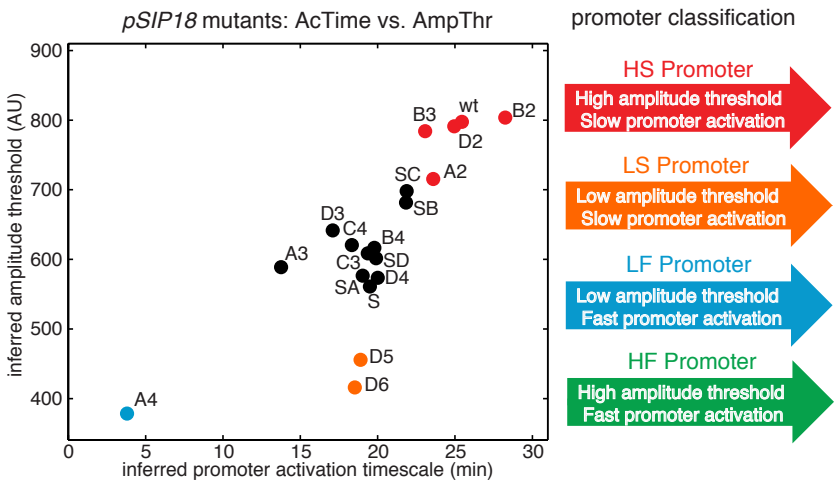

Figure D.4: *Promoter class for pSIP18 mutants*
Clustering of the twenty *SIP18* promoter variants. The promoters are clustered according to their inferred amplitude threshold and activation timescale and colored according to promoter class.

is observed for mutant A4 (Figure D.4). Whereas the wildtype *SIP18* promoter has two binding sites in the C region, mutant A4 has four binding sites in the nucleosome free A region. The much lower amplitude threshold is consistent with mutant A4 having twice the number of binding sites in a region not occluded by nucleosomes. The much faster amplitude threshold appears to be in part due to the binding sites being closer to the transcription start site. This shows that we can convert between the HS and LF classes simply by changing 18 nucleotides in the promoter.

Also notable, mutants D5 and D6 fall into the LS class. This class was not observed among the wildtype promoters studied in Chapter 2 (Figure 2.2B). Considering the D mutants, it appears that the amplitude threshold can be decoupled from the activation timescale. As the number of Msn2 binding sites in the D region is increased, the amplitude threshold strongly decreases, whereas the activation timescale is not strongly affected. Thus, this shows that the LS class, which was previously missing, does exist.

D.2.4 A quantitative relationship between promoter architecture and promoter class

From figure D.4, it is clear that changing the location and number of Msn2 binding sites significantly changes the amplitude threshold and activation timescale of the promoter. But can we quantitatively understand this relationship?

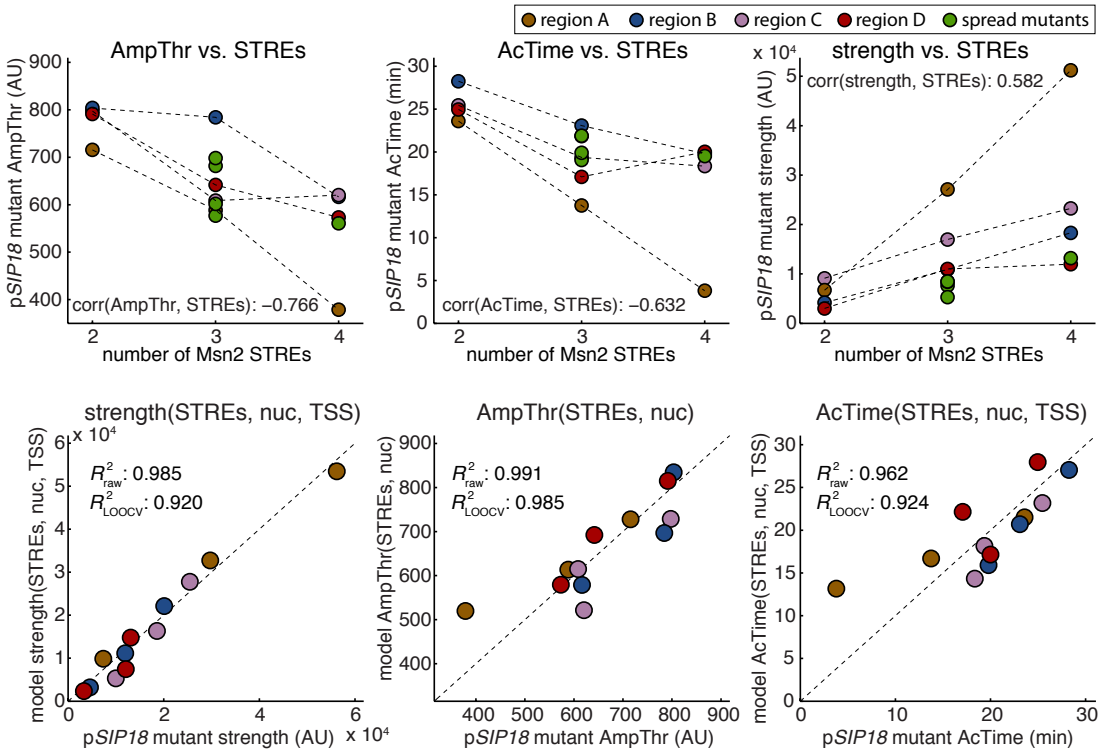

Figure D.5: *Quantitative relationships between promoter architecture and class*
Top panels: How amplitude threshold, activation timescale and promoter strength scales with the number of Msn2 binding sites (STREs).
Bottom panels. Left, a simple model quantitatively explains strength based on three variables: number of STREs, nucleosome occupancy over STREs and distance from transcription start site (TSS). Middle, a simple model quantitatively explains amplitude threshold based on two variables: number of STREs and nucleosome occupancy over STREs. Right, a simple model quantitatively explains activation timescale based on three variables: number of STREs, nucleosome occupancy over STREs and distance from TSS.

First, we studied the simple relationship between the number of binding sites and promoter amplitude threshold, activation timescale and strength (Figure D.5; top panel). As the number of binding sites increases, the amplitude threshold decreases. This is likely because the affinity for Msn2 increases with the number of binding sites. Similarly, as the number of binding sites increases, the activation timescale generally decreases, although there are

significant differences between the different promoters. Finally, promoter strength increases with the number of binding sites although also here, we observe a strong dependence on the location of the binding sites.

From this analysis, it is clear that the differences we observe in strength, amplitude threshold and activation timescale can partly be explained simply by the number of binding sites (Figure D.5; top panel). But on its own, the number of binding sites is not sufficient. We hypothesized that the location and the nucleosome occupancy over the binding sites would also play important roles.

To test this, we developed simple models for the promoter strength, amplitude threshold and activation timescale based on three variables: number of Msn2 binding sites (STREs); distance to the transcription start site (TSS); and nucleosome occupancy over the binding sites (nuc). Using simple non-linear phenomenological models with three or four fitted parameters, based on these variables we can explain more than 90% of the variance we observe in the promoter strength, amplitude threshold and activation timescale for the mutants with 2-4 binding sites in regions A, B, C and D (Figure D.5; bottom panel).

In conclusion, just three mechanistic variables - the number, location and accessibility of Msn2 binding sites - are sufficient to quantitatively explain the observed promoter class of *SIP18* promoter mutants.

D.3 Discussion

In this appendix, we have briefly outlined some of the results of our ongoing project to understand the relationship between promoter architecture and class at a mechanistic level. We find that a combination of three variables can quantitatively explain the behavior of the promoter mutants. Thus, the number of binding sites, their location relative to the

transcription start site and the nucleosome occupancy over the sites appear to determine the promoter class. Furthermore, we have shown that promoter class is tunable — by exploiting this relationship, we can independently tune the amplitude threshold and activation timescale of a promoter.

From Msn2 first enters the nucleus until the first mRNA is produced, a series of steps need to take place at the promoter. In Figure D.6, we present a speculative, simplified mechanistic model for the differences we see.

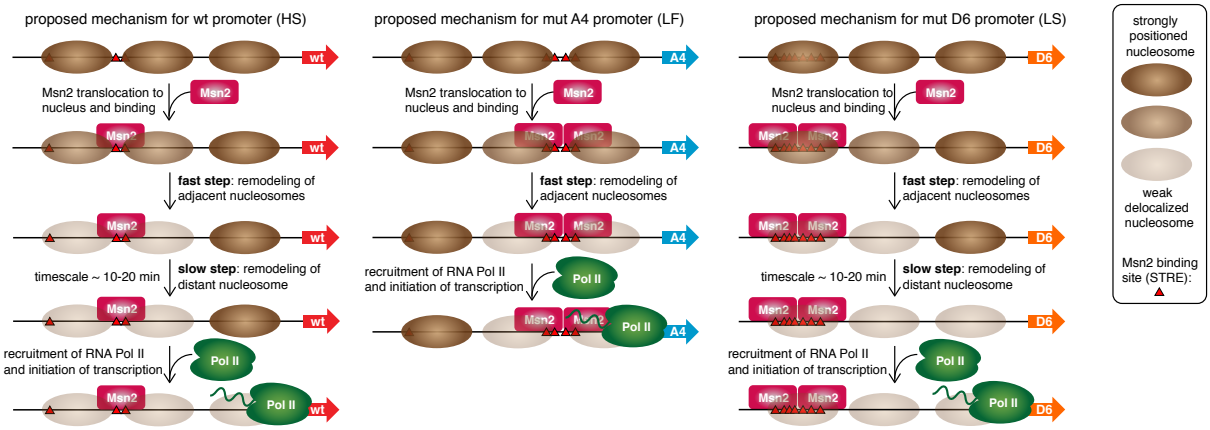

Figure D.6: *A speculative mechanistic model for transcriptional control at promoters*
A speculative mechanistic model for *SIP18* promoter variants: the wildtype promoter (left), mutant A4 (middle) and mutant D6 (left).

Why is mutant D6 slow and mutant A4 fast, even though D6 contains two more Msn2 binding sites? The main difference between these mutants is the distance to the transcription start site (Figure D.6). Presumably, for transcription initiation to take place, it is necessary to recruit RNA Pol II and its associated factors to the transcription start site. For this to happen, the nucleosome occupying this region must be remodeled. Thus, a possible explanation would be if nucleosome remodeling adjacent to where Msn2 is bound is fast, but nucleosome remodeling distal to where Msn2 is bound is slow. If this is correct, the wildtype and D6 mutants are slow because although they quickly remodel nucleosomes adjacent to where they bind, remodeling of the nucleosome occupying the transcription start site is slow.

Conversely, in the A4 mutant Msn2 binds immediately adjacent to the transcription start site and remodeling of this nucleosome is therefore fast.

While this model is speculative and further experiments will be necessary to definitely test it, the model is nonetheless consistent with the data and provides a mechanistic explanation for the differences in promoter class that we observe. This project is in progress and we are currently conducting further experiments on mutants A4 and D6.